Ways to stop mirrors from moving unnecessarily: design of advanced gravitational wave detectors

Von der Fakultät für Mathematik und Physik der Gottfried Wilhelm Leibniz Universität Hannover zur Erlangung des Grades

Doktor der Naturwissenschaften

Dr. rer. nat.

genehmigte Dissertation

von

MSc.-Phys. Vaishali Badrish Adya

2018

REFERENT:

Prof. Dr. Karsten Danzmann

Leibniz Universität Hannover

KORREFERENTIN:

Prof. Dr. Michèle Heurs

Leibniz Universität Hannover

KORREFERENT:

Prof. Dr. Andreas Freise

The University of Birmingham

TAG DER DISPUTATION:

27.04.2018

Diese Arbeit wurde angefertigt am

Max-Planck-Institut für Gravitationsphysik (Albert-Einstein-Institut)
und Institut für Gravitationsphysik, Leibniz Universität Hannover,
Callinstraße 38, 30167 Hannover

To my grandparents

Nomenclature

AEI	Max Planck Institute for Gravitational Physics (Albert Einstein Institute) based in Hannover and Golm, Germany
AIGO	Australian International Gravitational Observatory
AlGaAs	Aluminum Gallium Arsenide
ASD	Amplitude spectral density
BHD	Balanced homodyne detection
BS	Beam splitter
Caltech	California Institute of Technology
CARM	Common arm cavity degree of freedom
CDS	Control and Data acquisition System
DARM	Differential arm cavity degree of freedom
DC	In this thesis, DC refers to zero frequency
dof	degree of freedom
DFO	Dark fringe offset
ET	Einstein Telescope
ESD	Electro Static Drive
EOM	Electro-optic modulator
FINESSE	Frequency domain interferometer simulation software
FSR	Free spectral range
FWHM	Full width at half maximum
GAS	Geometric Anti Spring
GEO 600	GW detector with 600 meters arm length in Germany
GW	Gravitational Waves
GWD	Gravitational Wave Detector

HF	High frequency
HR	Highly reflective
ITM	Input Test Mass
ETM	Enput Test Mass
KAGRA	KAmioka, GRAvitational wave detector
LASTI	LIGO advanced systems testing interferometer at MIT
LIGO	Laser Interferometer Gravitational-Wave Observatory
LIGOWA	Laser Interferometer Gravitational-Wave Observatory Washington(Hanford)
LIGOLA	Laser Interferometer Gravitational-Wave Observatory Louisiana(Livingston)
LG_{33}	Laguerre Gauss modes
LF	Low frequency
$M_{\odot}$	Solar mass
MICH	Michelson degree of freedom
MIT	Massachusetts Institute of Technology
PDH	Pound-Drever-Hall
PRCL	Power recycling degree of freedom
PRM	Power recycling mirror
RF	Radio frequency
rms	Root-Mean-Square
SAS	Seismic Attenuation System
SAT	Single Arm Test
SPI	Suspension Platform Interferometer
SQL	Standard Quantum Limit
SRCL	Signal recycling degree of freedom
SRM	Signal recycling mirror
TAMA 300	Japanese GW detector with 300 meters arm
TEM	Transverse electromagnetic
ugf	Unity gain frequency
Virgo	GW detector with 3km arm length based in Italy

Abstract

Now that we have entered an era of gravitational wave astronomy, gravitational wave detectors are expected to detect several events a month (or more) in the near future. The current ground based detectors are undergoing upgrades, and future gravitational wave detectors, using exotic techniques and aiming at better sensitivity with lower noise contributions, are under consideration. To maintain strain sensitivity, precise control of various interferometric degrees of freedom in the detectors is required.

The core work of this thesis involves the analysis of a sensing and control scheme for a third generation gravitational wave observatory, the Einstein Telescope (ET). A novel technique that will allow us to sense all the longitudinal degrees of freedom of the interferometer independently has been proposed in this thesis. Assuming conservative servo designs, a shot noise limited displacement noise budget for the low frequency part of ET (ET-LF) has been simulated using the simulation tools FINESSE and SimulinkNb. It is thus shown that the control scheme does not inject additional sensing noise from auxiliary degrees of freedom into the measured gravitational wave strain channel. The simulated demonstration of the controllability of ET-LF with the new GHz control scheme is an important finding as current detectors are limited by control noise in the low frequency ($< 10\,\mathrm{Hz}$) regime.

The new technology should be tested thoroughly to ensure that it can be incorporated into detectors. The new sensing scheme proposed for ET-LF can be tested and tweaked for low noise operation at the AEI 10 m prototype before transferring the technology to full-scale detectors. In this thesis, a control scheme was developed to independently sense and control the three longitudinal degrees of freedom of the AEI 10 m prototype using a GHz sub-carrier. The sum of the control noise from all the loops was shown to be below the quantum noise limit predicted for the AEI 10 m prototype.

The sensing scheme presented for ET-LF could also be tested in GEO 600 since this detector presently suffers from signal recycling cavity length (SRCL) control noise. Different fundamental questions may be addressed by deploying the new sensing scheme at AEI 10 m prototype versus GEO 600. While the scheme implemented through the input port of the interferometer at the AEI 10 m prototype would allow us to understand the influence of cavity stability parameters on control signals, the scheme implemented through the dark port of GEO 600 (as proposed for ET-LF) provides answers for the mitigation of the SRCL control noise in the interferometer.

Keywords: gravitational wave detectors, interferometer simulations, control noise

Zusammenfassung

Nun, da wir in eine Ära der Gravitationswellenastronomie eingetreten sind, wird erwartet, dass die Detektoren in naher Zukunft regelmäßig mehrere Ereignisse pro Monat (oder mehr) entdecken werden. Die jetzigen bodengestützten Detektoren werden derzeit modernisiert, und zukünftige Gravitationswellendetektoren, die exotische Techniken verwenden und auf eine wesentlich höhere Empfindlichkeit abzielen, befinden sich in der Planung. Sie alle erfordern eine präzise Regelung verschiedener interferometrischer Freiheitsgrade in den Detektoren.

Die Kern dieser Arbeit beinhaltet die Analyse eines Mess- und Regelungsschemas für ein Gravitationswellenobservatorium der dritten Generation, das Einstein-Teleskop (ET). Eine neuartige Technik, die es uns ermöglicht, alle Freiheitsgrade des Interferometers unabhängig voneinander zu erfassen, wurde in dieser Arbeit vorgeschlagen. Mit Hilfe konservativer Regler-Designs haben wir ein schrotrauschbegrenztes Noise Budget für den niederfrequenten Teil von ET (ET-LF) mit Simulationswerkzeugen wie Finesse und SimulinkNb simuliert, und zeigen, dass das Regelschema keine zusätzlichen Ausleserauschen von anderen Freiheitsgraden in die Hauptmessdaten injiziert. Die simulierte Demonstration der Regelbarkeit von ET-LF mit dem neuen GHz-Regelungsschema ist eine wichtige Erkenntnis, da heutige Detektoren durch regelungstechnisches Rauschen im niederfrequenten ($< 10\,\mathrm{Hz}$) Bereich begrenzt sind.

Es muss überprüft werden, ob die neue Technologie in Detektoren verwendet werden kann. Das neue, für ET-LF vorgeschlagene Regelungs-Schema kann am AEI 10 m Prototypen getestet und für einen rauscharmen Betrieb optimiert werden, bevor die Technologie auf die Detektoren übertragen wird. In dieser Arbeit wurde ein Regelungsschema entwickelt, um die drei Freiheitsgrade des AEI 10 m Prototypen mit Hilfe eines GHz sub-carriers unabhängig voneinander zu erfassen und zu kontrollieren. Die Summe des Regelungsrauschens aller Regelkreise liegt unter dem für den Prototyp des AEI 10 m vorausgesagten Quantenrauschlimit.

Das für ET-LF vorgestellte Regelungs-Schema könnte auch in GEO 600 getestet werden, da dieser Detektor derzeit Rauschen durch die SRC-Regelung erfährt. Der wesentliche Unterschied zwischen dem Einsatz des neuen Regelungs-Schemas am AEI 10 m Prototypen und GEO 600 ist der Unterschied in den grundlegenden Fragen, die beantwortet werden sollen. Während das Schema, das am Eingangsport des Interferometers am AEI 10 m Prototyp umgesetzt wird, es erlauben würde den Einfluss von Resonatorstabilitätsparametern auf die Regelungssignale zu verstehen, liefert das Schema, welches am Dark Port von GEO 600 (wie für ET-LF vorgeschlagen) implementiert wird, Lösungen für die Mitigation des oben erwähnten durch Regelung verursachten Rauschens im Interferometer.

Stichworte: Grawitationswellendetektoren, Interferometersimulationen, Regelungsrauschen

Acknowledgments

This thesis would not have been possible without the support, advice and motivation provided by various people. Firstly, I would like to thank my parents for raising me to follow my dreams. This one's for you PaMa. I would have never been so motivated to study Physics had it not been for you Malathi Ma'am, Prabha Ma'am and Smitha Ma'am. Shru, thank you for being such an important part of my life. 12 years and counting, our friendship is important to me. To the rest of my family, Mama's, Mami's and Atya's, cousins from both sides of the family thank you for listening to me jabber about Physics and being supportive.

Everyone in Skellefteå, thank you for the lovely Christmas times and being a part of my life. Daniel T aka Danni, what would I do without you? From the northern lights to warm Italy, every trip with you has been such a wonderful experience. You've made me a better person and for that, aoouuii.

I would also like to thank Karsten Danzmann and Harald for hiring me as a PhD student and being phenomenal mentors. A special thanks to Harald who has always motivated me to be a good scientist. Your abilities to guesstimate solutions to problems are unrivaled. Even though you won't let me call it so, the new sensing scheme will always be the Lück lock.

Conor, Tobin, you were the best post-docs a young, dumb, new PhD student could have asked for. Without you, I would have never been able to get this far. Fu, thank you for saving me from the terrible street light. The little piece of tape still continues to serve its purpose. The entire prototype group has my cordial thanks for being a wonderful group to work with. Gerald, thank you for going bouldering with me to make sure I am not glued to my computer all the time and taking the time to drink tea with me and helping me during this thesis writing phase. Sina, all the hat building and crafting and Christmas markets would have been so boring without you.

Katha, how would I even get through this PhD without you? I do not have enough words to thank you for being my best friend and keeping me sane and listening to me (even if i repeated the same stories a thousand times). Germán, Thomas, Daniel P, thank you for giving me refuge in your office when I needed it and also sharing several bags of Snyders of Hannover; it added the spice to my writing. The rest of the 'Mensa-crew' and 'lecture-week peeps', Heather, Steffen, Marina, Amrit-junge, Lisa, Victor, Colin, Stefan, Melanie, little Luna, thank you for making

lunch time/lecture week a fun-time. Ramon-San, Daniel P, thank you for all the coffees shared and PhD stories swapped.

I cannot not thank my fellow fellows Heather (you were such a fabulous room-mate and such a good friend), Karl (all the fries, coffee and grocery runs), Pep, Joe, Evan (for being the calm in the fellows storm). A special shout out to all the Hanford folk, Amber, Kim, Rick, Mike, Fred, Sheila, Greg, Jeff K, Kiwamu, Chandra, Nutsinee, Marc, Daniel Sigg, TJ, Christine, Corey and absolutely everyone else on the site who made my fellow time not only enjoyable but teaching me valuable science. Jenne, thank you for letting me be the little coffee stalker and letting me drive the machine. GW170608 would not be so special for me otherwise. Kiyomi and Rick, you gave me a home away from home during my time at Hanford and for that I am indebted to you.

Miriam, Juliane, you are such amazing women! I am so glad you are my friends. I promise we will have our girl's night soon. Thank you Syl and Divya for letting me join in on the Papier-mâché fun! That black hole simulator is the best there is!

Whenever there was FINESSE question, I could count on DDB and DanielT to help me with it. Thank you for that and being so patient with me. Thank you Sean, Stefan and Ken for making my visits to Glasgow fun and productive. I must take this opportunity to thank all the other Brummies for letting me be a part of the crew. Serena, you have been such a delight to hang out with. Thank you for all the pub times we've had and here's to many more.

For proof reading this thesis and helping me translate my abstract into German I would like to thank Holger, Fu, Ken, Benno, Emil, Daniel P, Janis, Aparna, David, Harald, Johannes, Germán, Sean, Suresh, Tom Dent and Daniel T. All remaining mistakes are my fault.

Kirsten and Emma, thank you for the copious amounts ok cake, marmalade, breads, warm socks, the list is endless. You both are the best!

My non-institute friends Jake, Karo, Vitor, Andrew, Jenny, Ajay, Ashwini, Priyanka, Bala, Swathi, Vinay, Monish, Supreeth, Kumar, thank you for keeping me sane and spending time with me.

Also, dear Mr.Coffee Machine in Appelstße 11A, you are the best.

Two pages are not enough to thank all the people who have made this thesis a reality and been a part of my life. If I have forgotten to mention you here, I apologise; everyone I have come across during my time as a PhD student has influenced me and for that, I am grateful to you.

Contents

Chapter 1

Introduction to GWs

1.1 Introduction

The general theory of relativity proposed by Einstein in 1916 [1], predicted the existence of gravitational waves (GWs) which were described to be perturbations of the space-time metric. In simpler terms, a passing gravitational wave would change the proper distance between two free masses. Einstein however postulated that the amplitude of GWs would be too small to be measured experimentally. These 'disturbances' were predicted to propagate at the speed of light and are produced by accelerated bodies with a time-varying quadruple moment. Nearly a century after this prediction, in 1979, the Hulse-Taylor binary system was observed. The loss of kinetic energy of this rotating binary neutron star system (PSR B1913+16) was an indirect evidence of gravitational radiation. This observation won Taylor and Hulse the Nobel prize in Physics [2].

The historical direct experimental detection of GWs in 2015 from two merging black holes (GW150914 see section 1.5) was the beginning of 'gravitational wave astronomy' and won Rainer Weiss, Kip S.Thorne and Barry C.Barish the Nobel Prize in Physics in 2017. Apart from confirming the postulates of the general theory of relativity pertaining to gravitational waves. The detections that followed GW150914 opened the doors for multi-messenger astronomy (GW170817, see section 1.5); a collaborative effort of various detectors observing different parts of the electromagnetic spectrum (visible light, x-rays, gamma rays, radio waves and neutrinos) to observe astronomical

sources at the same time thus revealing aspects of the universe never before observed [3].

1.2 Thesis structure and motivations

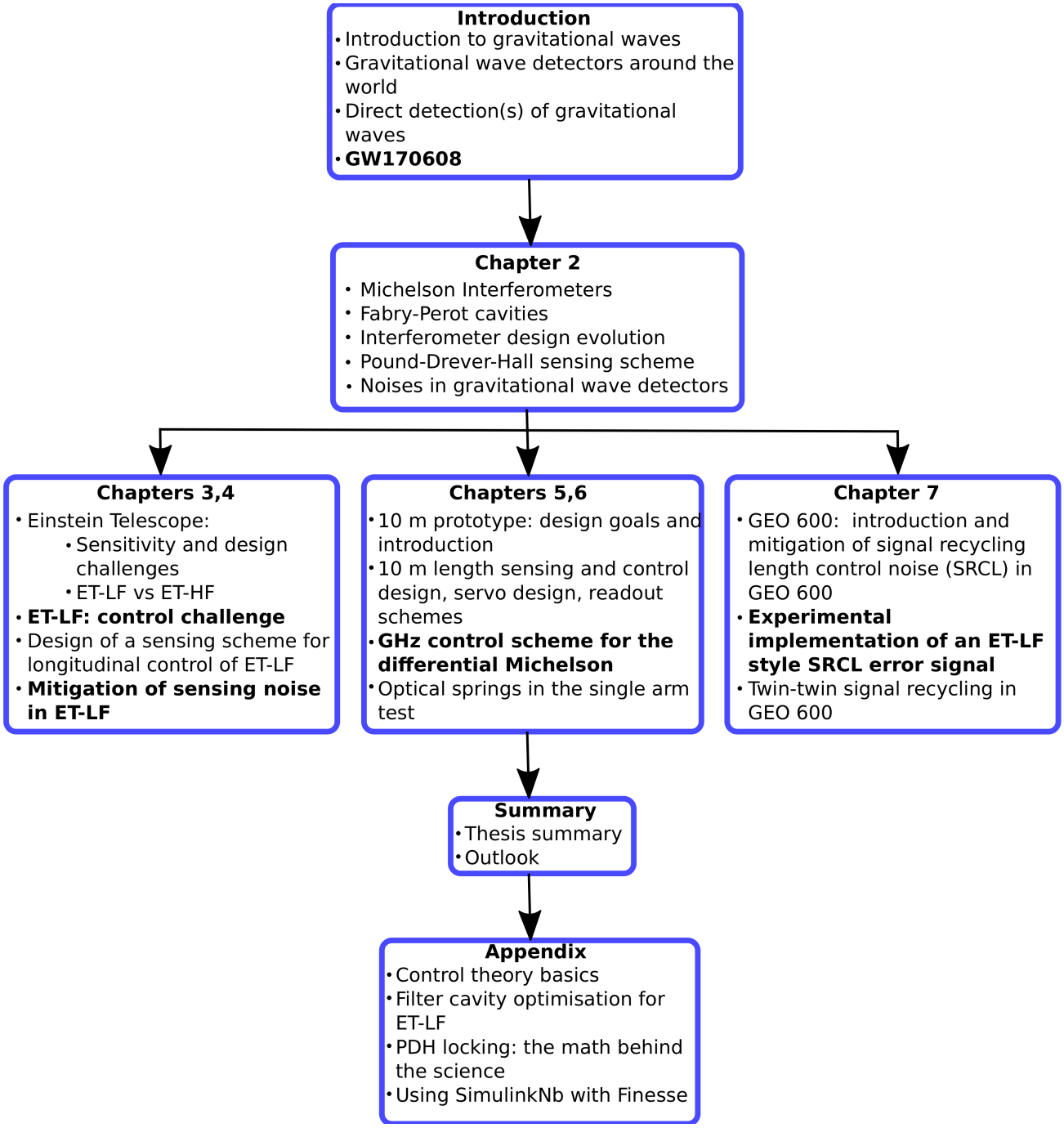

Figure 1.1: Graphical overview of the thesis.

This thesis is focussed on development of sensing and control schemes for advanced gravitational

wave detectors (GWDs) that make the experimental observation of GWs possible. Chapter 1 provides a brief introduction to GWs, GWDs that are currently operational/to be operational around the world. This chapter also presents an insight into the 5 binary black hole mergers and one binary neutron star merger from the two observing runs of the LIGO detectors (advanced Virgo joined the observing run O2 in August 2017). The chapter also only briefly mentions the astrophysics behind GW170608 as I was a part of the rapid response team to assess the detector status at the time of this event.

Chapter 2 describes the working principle of a Michelson interferometer and lays the mathematical foundations for the work presented in the rest of this thesis.This chapter also describes the improvements to the conventional Michelson interferometer design which are the founding steps of the improved sensitivity of the advanced GWDs. Excess noise in GWDs prevent them from reaching their design sensitivity. This chapter highlights some of the noise sources and techniques that are employed in advanced GWDs to mitigate them.

Chapters 3 and 4 highlight the design challenges and technical challenges for the Einstein Telescope (ET). A new sensing and control scheme for the longitudinal control of the low frequency part of ET (ET-LF) is proposed in chapter 4. The new sensing scheme breaks the degeneracy of the error signals in ET-LF; a problem that is not effectively mitigated in current ground based detectors. The low frequency sensitivity of ET-LF also requires control noise arising from feed-back systems to be low. With the help of simulation tool like FINESSE and SimulinkNb, a control loop model was set up to estimate the sensing noise contamination of the gravitational wave readout channel.

One of the places where the sensing scheme highlighted for ET-LF could potentially be tested is the AEI 10 m prototype facility located at the Albert Einstein Institute in Hannover. Chapter 5 describes the facility, the aims and objectives of the AEI 10 m prototype. The results of the numerical modelling of the longitudinal sensing scheme of the AEI 10 m are presented in chapter 6. This chapter also highlights the advantages of balanced homodyne detection as a potential readout scheme for the differential arm motion (DARM) over the currently used DC readout. Servos, which are the heart of a feedback loop, can be designed to shape the overall feedback loop response and this can be used to decouple the different degrees of freedom. The basic principle of the same is presented in this chapter.

GEO 600 is a German-British detector GWD located outside Sarstedt, Germany. GEO 600 has been a pioneer in prototyping technologies for advanced GWDs. The low frequency part of the noise budget of GEO 600 is dominated by the sensing noise of the signal recycling cavity length (SRCL) control error signal. The new sensing SRCL sensing scheme proposed for ET-LF would benefit GEO 600 as well, and is presented chapter 7. The chapter also discusses necessary modifications required to the existing infrastructure of GEO 600 to test the new sensing scheme.

A summary and outlook of this thesis is presented in chapter 8. The appendices following the summary are aimed at providing additional information on some topics described in the thesis. Appendix A gives an introduction to the basics of control theory which is essential for understanding the feedback loops discussed in the main body of the thesis. Appendix B describes the mathematics of the Pound-Drever-Hall sensing scheme. Appendix C briefly describes the optimisation of the parameters of the two filter cavities required for frequency dependent squeezing to improve the quantum noise limited sensitivity of ET-LF. Appendix D details how to use FINESSE with SimulinkNb.

1.3 Gravitational waves

A passing gravitational wave affects the proper distance between free masses. If one were to imagine a ring of free particles as shown in figure 1.2, the GW would stretch and squeeze the space between these particles as shown at the different points in the cycle of the wave. The weak intensity of the gravitational waves and the stiffness of space-time causes the distance to change only by fractional amounts. Massive objects moving at relativistic velocities such as merging black holes or merging neutron stars (which are at distances between a few at a distance of kPc to MPc from the earth) cause length changes on the order of 10^{-21} m.

The strain of a such a gravitational wave is given by,

$$h(r) = \frac{2G}{c^4}\frac{1}{r}\ddot{I} \,, \tag{1.1}$$

where G is the gravitational constant, c is the speed of light, r is the distance from the source and I is the quadrupole moment of the source. $\ddot{I}$ is the second derivative of I with time.

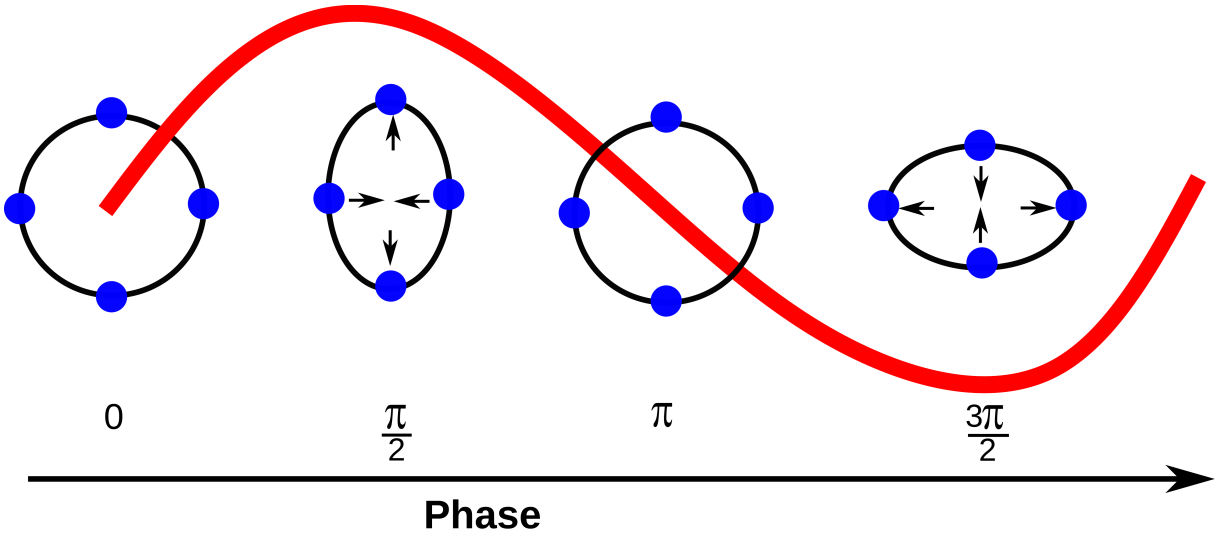

Figure 1.2: The effect of a GW of plus polarisation on a ring of non-interacting particles. The gravitational wave alters the distance between the particles and is represented by the violet wave. Image inspired by [4] [5]. A cross polarisation GW would also stretch and squash the space between the particles but at an angle of 45°in comparison to the plus polarisation. More information can be found in [4].

'h' is a measure of how much the space is distorted by the GW. By measuring the change of a known length due to a GW, the strain can be estimated. This is the basic working principle of all current and planned GWDs. Section 2.1 contains more details on the working of Michelson interferometers which form the heart of the current GWDs.

1.3.1 What sources can we detect?

GWs can be emitted by a wide range of astrophysical events. This section provides a brief overview of sources for GWs that dominate different parts of the frequency spectrum.

- The very low frequency part of the spectrum (below 10^{-5} Hz) is dominated by stochastic sources and super-massive binaries. Stochastic sources refer to the relic GWs from the early evolution of the universe and the super-massive black holes which are at the centres of the galaxies (for example super-massive blackholes at the centre of the Milky way galaxy) [6].

- Low Frequencies (between 10^{-5} Hz to 10 Hz): This part of the spectrum is dominated by extreme mass ratio inspirals, Type IA supernova and galactic binaries [6].

- Frequencies above 10 Hz are dominated by compact binary inspirals, neutron star mergers,

core collapse supernovae and pulsars [6].

For continuous observation of GWs, originating from different sources, a network of GWDs is required which would not only improve sky localisation (which makes electromagnetic followup easier) but also allows observers to track a signal through time. For instance, a BNS merger observed by LISA (Laser Interferometer Space Antenna) can provide the ground based detectors like aLIGO (advanced LIGO), AdV (advanced Virgo), Einstein Telescope (ET) a 'fore-warning' thus the signal can be tracked for periods longer than just the inspiral (see section 1.4 for the current and planned network of gravitational wave detectors and figure 3.2 to see the frequency spectrum covered by various existing/proposed GWDs.).

1.4 Ground-based gravitational wave detectors around the world

Ground based detectors having a detection bandwidth between 30 Hz and 10 kHz have been built over the last 30 years. Currently, there are six large scale GWDs in operation/being commissioned. There are two four kilometer arm length interferometers in the USA, one in Hanford, Washington state and another at Livingston, Louisiana. Both of these detectors have the dual recycled Fabry-Perot Michelson configuration (see section 2.3.3 for more details on the configuration).

LIGO (Laser Interferometer Gravitational wave Observatory) Hanford (LIGOWA) and LIGO Livingston(LIGOLA) currently have the best strain sensitivity of all the detectors: $10^{-23}\,1/\sqrt{\text{Hz}}$ [7].

The Virgo detector (or called advanced Virgo after being upgraded from initial Virgo) in Cascina, Italy is an Italian-French collaboration GWD with a power recycled Michelson configuration (currently). With an arm length of 3 km, this detector joined the LIGO detectors for the observing run O2 in August [8].

TAMA300 [9] was a Japanese GWD located in Tokyo with 300 m arms and belongs to the first generation of detectors. Japan is also home to a more sensitive 3 km long cryogenic KAGRA detector [10] located in Kamioka. KAGRA will use sapphire test masses and is expected to join observing runs in 2019 [11]. The experience gained from KAGRA will be invaluable for third generation detectors like the Einstein Telescope (ET) [12].

Last but not the least, GEO 600 [13], a German-British collaboration detector with 600 m arm length and a dual recycled Michelson interferometer configuration, has high frequency sensitivity comparable to advanced LIGO (with the employment of phase squeezed states for improved shot noise limited sensitivity). Chapter 7 introduces GEO 600 in more detail.

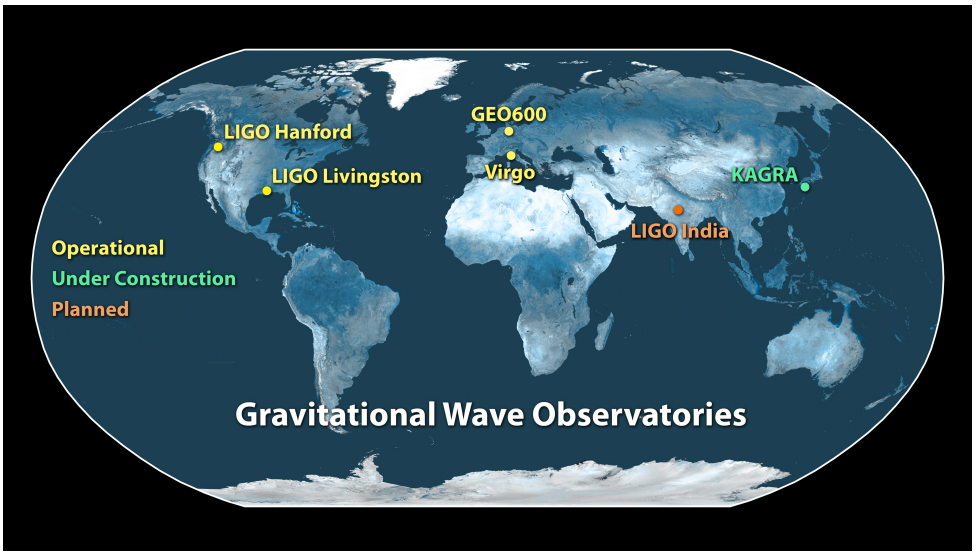

Figure 1.3: Gravitational Wave detectors around the world: Planned, propsed and under construction. Picture courtesy Caltech/MIT/LIGO Lab.

1.5 All detections so far

The first observing run of the advanced LIGO detectors (O1) [14] lasted from September 12, 2015 until January 19, 2016. The peak sensitivity of the detectors was between 30Hz and a few kHz [15]. During this run, two binary black hole mergers (BBHs) and one detection candidate (which had a 1.7σ probability of being a BBH) were discovered.

The second observing run (O2) [16] began on November 30,2016 and ended on August 25, 2017. During the period May 8-26, 2017 for LIGO Livingston (LIGOLA) and May 8-June 8, 2017 for LIGO Hanford (LIGOWA), O2 was suspended for in-vacuum commissioning activities. Advanced Virgo (AdV) joined the O2 on August 1, 2017 and until the end of O2, the two LIGO detectors took coincident data for approximately 117 days and all three detectors (LIGOWA, LIGOLA, AdV) took coincident data for 15 days. During O2, three confirmed BBHs and one BNS were added to the existing list of known gravitational wave sources. The main 'features' of the seven

events are discussed in the section below. The events are named in the year-month-date format that they were discovered for example, GW150914 was observed on September 14, 2015.

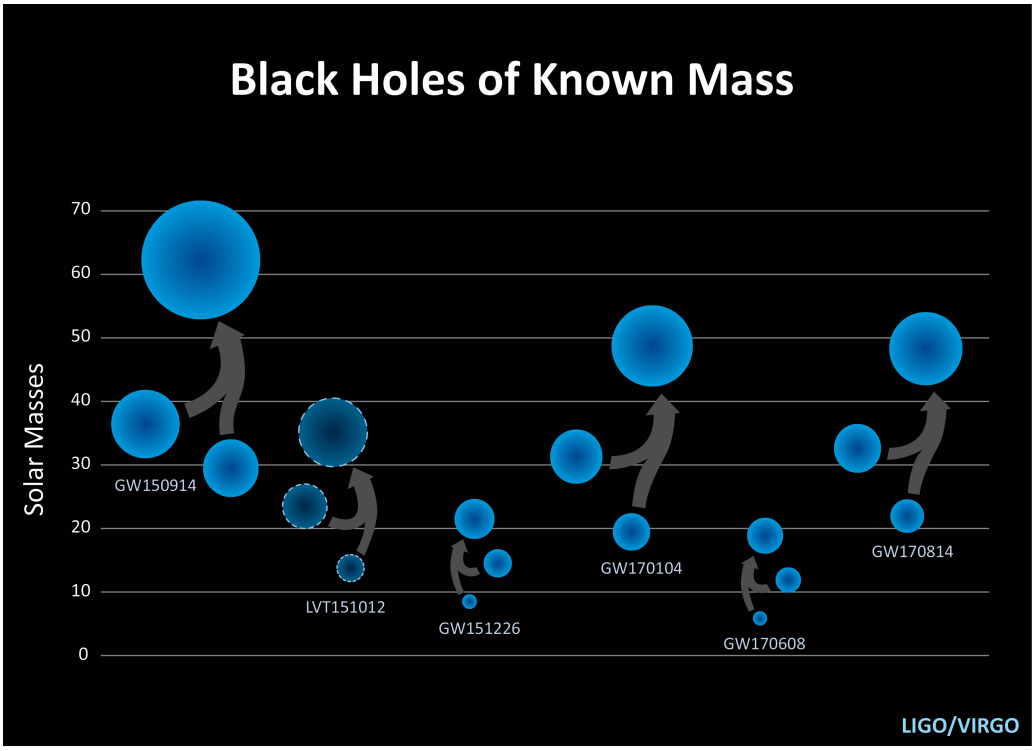

Figure 1.4: Graphical list of known BBH mergers. Picture courtesy LSC/LIGO/Caltech/Sonoma State (Aurore Simonnet)

- GW150914: see section 1.6.

- GW151226: Fondly known as the Boxing day event, this BBH merger resulted in a final black hole of mass $20.8^{+6.1}_{-1.7}\,M_{\odot}$having originated from two black holes with initial masses $14.2^{+8.3}_{-3.7}\,M_{\odot}$and $7.5^{+2.3}_{-2.3}\,M_{\odot}$. This was the second direct detection of merging black holes in O1. This event occurred at a distance of $440^{+180}_{-190}\,$Mpc from earth [17].

- LVT151012: The possibility of LVT151012 being a GW candidate is about 87%. Owing to its lower significance (1.7 σ as opposed to over 5σ for the other events), it has been classified as a LIGO-Virgo-Trigger as opposed to a GW-candidate. The distance of LVT151012 is very uncertain but is estimated to be $1000^{+500}_{-500}\,$Mpc. The initial masses of this 'possible' BBH were estimated to be $23^{+18}_{-6}\,M_{\odot}$and $13^{+4}_{-5}\,M_{\odot}$resulting in a final mass of $35^{+14}_{-4}\,M_{\odot}$ [18].

- GW170104: This was the first confirmed detection of a BBH in O2. This BBH comprised

of two black holes of masses $31.2^{+8.4}_{-6.0}\,M_\odot$ and $19.4^{+5.3}_{-5.9}\,M_\odot$merging into a black hole of mass $48.7^{+5.7}_{-4.6}\,M_\odot$. Having occured 880^{+450}_{-390} Mpc away from earth, this is the farthest confirmed BBH merger to date [19].

- GW170608: see section 1.7.

- GW170814: This BBH merger resulting from two black holes of masses $30.5^{+5.7}_{-3}\,M_\odot$and $25.3^{+2.8}_{-4.2}\,M_\odot$was the first BBH to be measured with three GWDs (LIGOWA, LIGOLA and aVirgo). A first measurement of the polarisation of the GW could be made with this detection along with improved sky localisation (due to three detectors). The final mass of the blackhole from this merger was $53.2^{+3.2}_{-2.5}\,M_\odot$. These two blackholes merged at a distance of 540^{+130}_{-210} Mpc away from earth [20].

- GW170817: This special event towards the end of O2 was the first direct observational evidence for the existence of gravitational waves from a binary neutron star. Having occurred in NGC 4993 at a distance of 40^{+8}_{-14} Mpc, this is the nearest event to have occurred to-date and also the loudest (with a combined SNR of 32.4). This signal was measured by LIGOWA and LIGOLA and the exemption of signal from AdV allowed the restriction of the location in the sky where the BNS could have originated. This event was also the initiator for 'multi-messenger astronomy.' The first EM signal to follow the merger was a short gamma ray burst (GRB 170817A) which was detected 1.7 s after the merger. Using the luminosity distance to NGC 4993 and knowing its optical properties also allowed new constraints to be placed on the Hubble constant. Although new information about the equation of state of a neutron star was not revealed by GW170817, it was possible to set constraints on the tidal deformation of the neutron stars. The possibility of this merger occurring is less than 1 in 80000 years (also called the False-Alarm-rate). More information about the formation of heavy elements such as gold, platinum and other heavy metals through the rapid neutron-capture process resulting from absorption of neutrons during the merger is available in literature [3, 21].

1.6 Nobel prize for GW150914

The Nobel Prize in Physics 2017 was split by three scientists of the LIGO-Virgo scientific collaboration. One half was awarded to Rainer Weiss and the other half jointly to Barry C.Barish and Kip S.Thorne for decisive contributions to the LIGO detector and the observation of gravitational waves.

The discovery of GW150914 was a monumental day in gravitational wave astronomy for all the 1200+ members of the LIGO-VIRGO Collaboration. It was the first direct detection of GW signals from the merger of two black holes and was detected by the LIGOWA and LIGOLA. The estimated masses of the initial black holes are $36^{+5}_{-4}\,M_{\odot}$and $29^{+4}_{-4}\,M_{\odot}$resulting in a final black hole of $62^{+4}_{-4}\,M_{\odot}$with a spin of $0.67^{+0.05}_{-0.07}$. This event is the largest BBH merger to-date. the the total energy radiated by the system in the form of GWs is $3\,M_{\odot}c^2$ [22].

The signal first arrived at LIGOLA and 10 ms later at LIGOWA (the difference comes from the light travel time to traverse the 3000 km between LIGOLA and LIGOWA) .

1.7 GW170608

As mentioned earlier in section 1.5, the Hanford detector was under maintenance from 8 May 2017 until June 8, 2017. During this period, the input test-mass in the X-arm was cleaned with first contact [23] and a lens in the Hartmann wavefront sensor path of the Y-Arm was also swapped [24]. Upon completion of these activities, efforts were made to tune the control loops and go through lock acquistion to bring the interferometer to the 'observing state' [25]. An important aspect after locking the interferometer is to check the low frequency (below 30 Hz) part of the strain sensitivity for contamination from the sensing noise of the angular control loops into the differential arm readout (DARM) which contains the GW information. This noise is mitigated by means of an angle-to-length decoupling script [26].

In the angle-to-length decoupling script (A2L), a dither is applied to the suspension in pitch (or yaw) during a lock [27] and the resultant length signal is measured. If the beam does not point

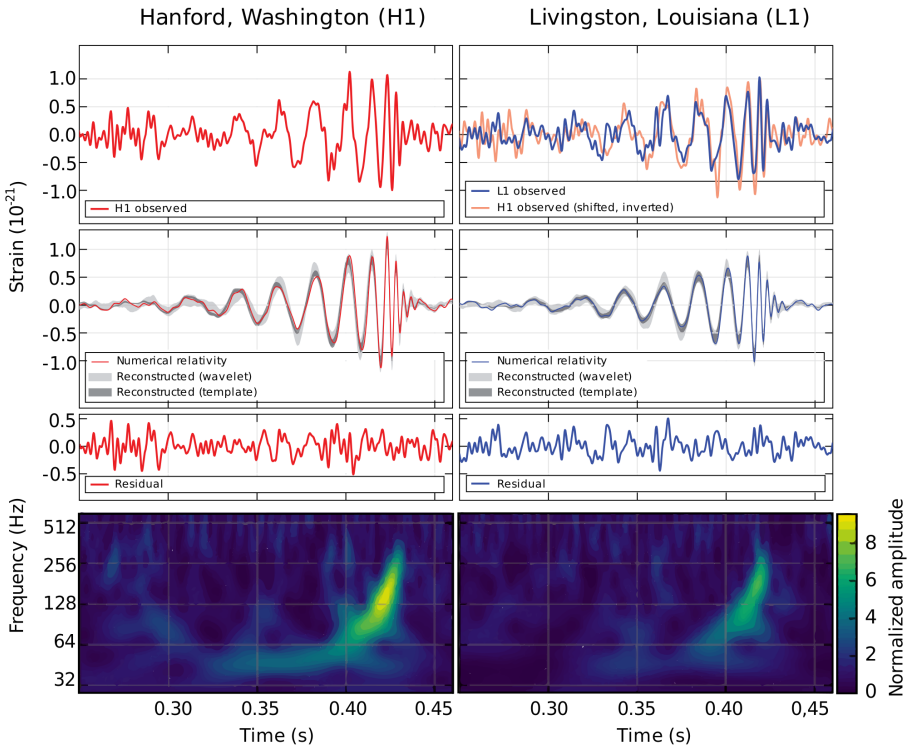

Figure 1.5: The gravitational wave signal from the GW150914 event. All time series shown here are filtered with a 35-350 Hz bandpass filter. The top row shows the H1 (LIGO Hanford) and L1 (LIGO Livingston) time series, the top right panel shows both time series overlapped with the H1 strain shifted by 10 ms to compensate for the delayed signal arrival at the H1 detector, and inverted to account for difference in the relative orientation of the detectors. On both of the panels of the second row traces show the numerical relativity (NR) waveform computed for the system with the GW150914 source parameters (solid black lines), 90% credible region for signal reconstruction based on binary black hole template waveforms (dark gray) and 90% credible region of a strain signal calculated from a combination of sine-Gaussian wavelets (light gray). The third row shows the background noise after the NR waveforms are subtracted from the time series. The time-frequency plots in the bottom row show how the frequency of the signal evolved during the inspiral [22].

to the center of the optic, the angular motion would appear in the length signal of the cavity. The additional coupling from the angular motion of the optic appears as a length signal at the dither frequency. This signal is then subtracted from the length signal by means of feed-forward techniques. By changing the angle to length feed-forward coefficients, the coupling between the angular position of the test-mass mirrors and the strain measurement can be minimised. This is a regular 'maintenance' procedure that is run when this low frequency coupling makes noticeable contributions to DARM.

On the day of GW170608, what started off as an ordinary day during my time as a fellow at

LIGOWA, ended up as one of my fondest memories. After reliably locking LIGOWA to the nominal low noise state (this is when the interferometer is said to be in 'observing' state), A2L decoupling was run which affects the sensitivity of the detector between 19 Hz and 23 Hz. This is the reason for the low frequency cut-off for the analysis of GW170608 to be 30 Hz. Upon being notified of this interesting event, I was a part of the rapid response team which is mostly comprised of the fellows on shift during that period and/new fellows in training (with the support of commissioners and operators), to assess the overall functioning of the interferometer and look for any glitches, blips or abnormalities in the data around the time of the event.

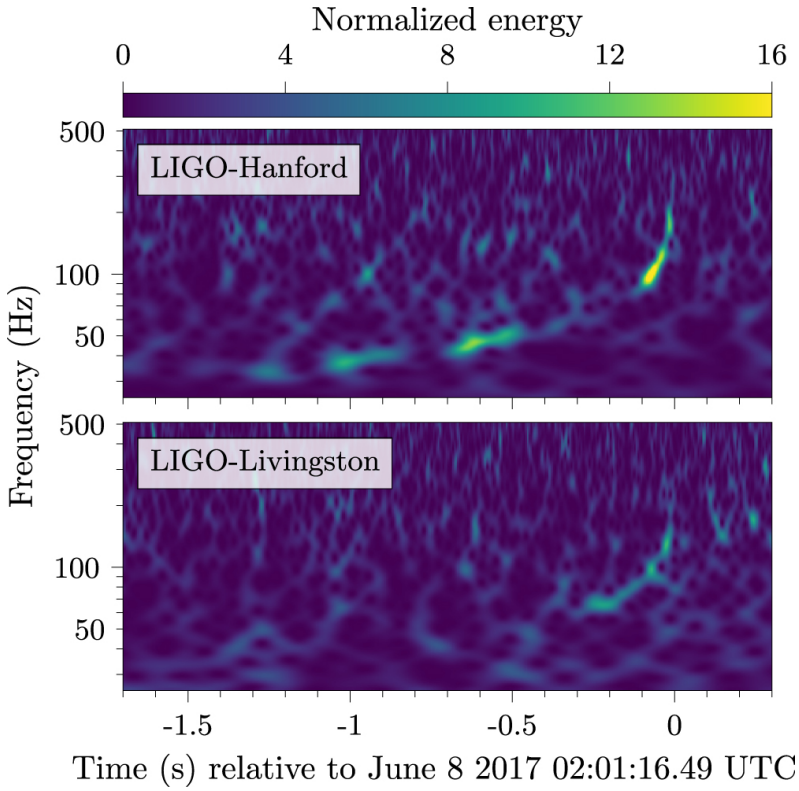

Figure 1.6: Power maps of LIGO strain data at the time of GW170608 in a constant Q sine-Gaussian basis. The characteristic upward-chirping morphology of a binary inspiral driven by GW emission is visible in both detectors, with a higher signal amplitude in LHO. This figure, and all others in this letter, were produced from noise-subtracted data (Section 4 from the paper cited) [28].

GW170608 was found by PyCBC [29], GstLAL [30] and the coherent WaveBurst [31] searches off-line. The false alarm rates predicted by all these searches were 1 in 160000 years, 1 in 3000 years and 1 in 30 years respectively. Having originated from two low mass binary black holes of individual masses $12^{+7}_{-2}\,M_{\odot}$and $7^{+2}_{-2}\,M_{\odot}$, the final mass of the remnant black hole was $18^{+4.8}_{-0.9}\,M_{\odot}$.

The chirp mass, which is estimated from the measured waveform and is a function of the frequency of the signal (chirp frequency) and the first time derivative of the signal, was $7.9^{+0.2}_{-0.2}\,M_{\odot}$for GW170608. This makes GW170608 the lowest measured chirp mass to-date. The uncertainty of GW151226 having a lower mass compared to GW170608 is about 11%.

The low chirp mass of GW170608 can provides insight into the environment of the two merging black holes. The properties of GW170608 are consistent with those of low mass X-ray binaries. Such binary systems where one of the companions is a star emitting X-rays which can be observed by telescopes like Chandra. The mass of GW170608 also suggests that the progenitors of X-ray binaries are unlikely to have a low metallicity environment unlike GW150914 and instead contain large amounts of 'heavy' elements like carbon and nitrogen [28].

Chapter 2

Interferometry 101

The effect of gravitational waves can be measured using a laser interferometer which converts the displacement of test masses due to gravitational waves into phase information which is encoded in a laser beam. Section 2.1 describes this 'transducer' behavior of a Michelson interferometer. Sections 2.2, 2.3 and 2.4 lay the foundations for advanced techniques employed to improve the sensitivity of Michelson interferometers and builds up from the core Michelson interferometer, leading up to the design of advanced detectors like the Einstein Telescope (ET). Section 2.5 outlines the various noise sources that plague advanced GWDs and possible ways of mitigating them.

2.1 Michelson interferometers

The Michelson interferometer converts the differential length change caused by gravitational waves to phase difference at the output port. Modern gravitational wave interferometers are based on the Michelson interferometer, shown in Figure 2.1. The passage of a gravitational wave causes a differential length change (Δl_{GW}) of the two arms of the Michelson interferometer. This is given by:

$$\Delta l_{\mathrm{GW}} = \frac{h L_{\mathrm{arm}}}{2}\,, \tag{2.1}$$

where L_{arm} is the unperturbed arm length of the Michelson interferometer (L_x and L_y in figure 2.1) and h is the strain of the gravitational wave.

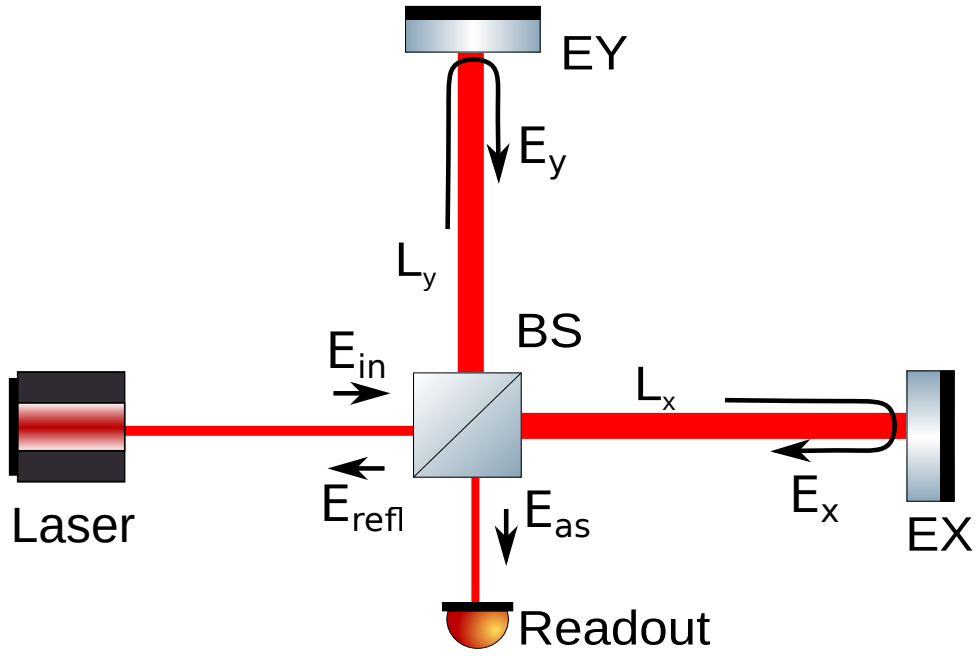

Figure 2.1: Simplified optical layout of a Michelson interferometer with test masses EX and EY at a distance L_x and L_y from the beam splitter (BS). The input laser beam from the main laser is split by BS into two perpendicular paths towards EX and EY. EX and EY are mirrors ('test-masses') with high reflectivities and return the light to BS. The returning beams interfere destructively at the dark port (readout).

The fields in the two arms of the Michelson interferometer after reflection from the mirrors EX and EY are E_x and E_x (figure 2.1). Assuming the beam-splitter splits the incoming electric field (E_{in}) in a 50:50 ratio i.e. $r_{BS} = t_{BS} = \frac{1}{\sqrt{2}}$ the electric field incident on the beam-splitter can be written as:

$$E_{in} = E_0 e^{i\omega t}\,, \tag{2.2}$$

where E_0 and ω are the amplitude and the angular frequency of the input field respectively. It should be noted that here we have assumed that the mirrors EX, EY and the BS are lossless. In practice however, all of the optics have losses and imperfections.

The electric fields that are first reflected (transmitted) at the beam splitter into the arms, and then upon returning are transmitted (reflected) back at the beam splitter appear at the anti-symmetric port. For destructive interference at the dark port ('Readout' in figure 2.1), the field E_{as} can be calculated as the sum between the fields returning from the two arms of the Michelson

interferometer.

$$\begin{aligned} E_{as} &= \frac{i}{2} E_0 \left(e^{-2ikL_x} - e^{-2ikL_y} \right) \ , \\ &= \frac{i}{2} E_0 e^{-2ikL} \left(e^{-ik\Delta L} - e^{ik\Delta L} \right) \ , \\ &= E_0 e^{-2ikL} \sin(k\Delta L) \ , \end{aligned} \tag{2.3}$$

where, k is the wavenumber ($k = \omega/c$) and $\Delta L = L_x - L_y$.

At the readout, the electric field E_{as} cannot be measured directly but instead, the power can be measured with a photodiode as indicated in figure 2.1. Mathematically, the expression for the same is:

$$\begin{aligned} P_{as} &\propto |E_{as}|^2 \, , \\ &\propto |E_0|^2 \sin(k\Delta L) \, , \end{aligned} \tag{2.4}$$

where, $|E_0|^2$ is the DC input laser power henceforth represented as P_{in}.

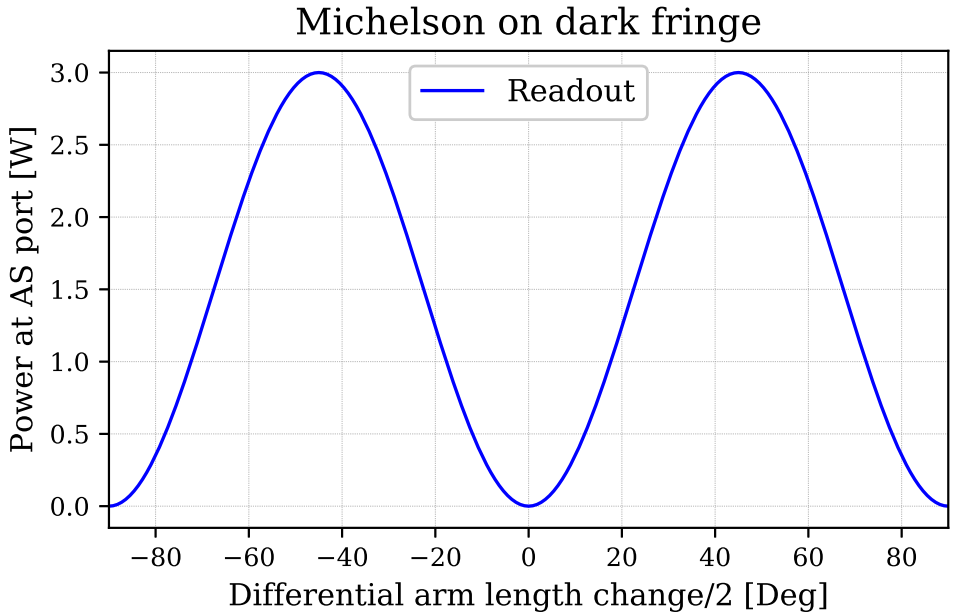

Figure 2.2: For an input power of 3 W, the power at the asymmetric (AS) port is plotted as a function of the differential change in the arm length of the Michelson interferometer.

Figure 2.2 shows the variation of the output power at the dark-port as a function of the differential arm length change (DARM). The Michelson interferometer here is tuned to dark fringe condition, i.e. the light fields interfere destructively at the dark port.

Also, if the microscopic change in the differential arm length due to a passing gravitational wave is $\Delta L = \Delta L + 2hL$. Hence,

$$L_x = L + \frac{\Delta L}{2},$$
$$L_y = L - \frac{\Delta L}{2},$$

where, $\Delta L = \Delta L + 2h\,l$ is the macroscopic change in the differential arm length. The detected power at the dark port due to the passing gravitational wave is now,

$$P_{as} \propto P_{in} \sin(k\Delta L)^2 \,, \tag{2.5}$$

If ΔL is zero, the coupling of h to the readout is not linear but quadratic. In figure 2.2 at the dark fringe, the slope in W/m is zero. Although the slope at mid-fringe (where $P_{as} = P_{in}/2$) is maximal, that is an undesirable operating point as, the laser fluctuations in $\mathrm{P_{in}}$ do not get cancelled [32]. To deal with this conundrum, DC readout was implemented where the arms operate slightly off the dark fringe thereby letting some amount of carrier light to the AS port. More details about the motivation for DC readout can be found in [33].

In practice, we use a control servo to force the differential length of the arms such that the power detected at the photodiode is near zero. The force required to hold the mirrors in this state is directly related to how much the mirrors would have moved in the absence of control and with the help of regular calibration, the measurement of gravitational waves is possible.

2.1.1 Sensitivity of a Michelson interferometer to gravitational waves

The phase sensitivity of the Michelson interferometer to a passing gravitational wave is calculated to be $\frac{dP_{as}}{d\phi_-}$ where $\phi_- = \phi_x - \phi_y$ is the differential phase shift due to a differential change in arm length of the Michelson interferometer. $\phi_x = 2kL_x$ and $\phi_y = 2kL_y$ are the phase accumulated by the light propagating in the X and Y arm of the Michelson interferometer respectively.

Calculating the phase sensitivity (using equation 2.5) gives,

$$\frac{dP_{as}}{d\phi_-} \propto P_{in} \sin(\phi_-) \cos(\phi_-) \ , \tag{2.6}$$

Shot noise (see section 2.5.2) arising due to photon counting statistics, sets a limit on the sensitivity of the Michelson interferometer. The minimum detectable phase in terms of amplitude strain spectral density of a gravitational wave is given by [34],

$$\widetilde{h}_{min} = \frac{1}{2\pi(L_x + L_y)} \sqrt{\frac{hc\lambda}{P_{in}\eta}} \ , \tag{2.7}$$

For an input laser power of 3 W and wavelength 1550 nm traversing an optical path of 10 km (the Michelson arm length $L_x = L_y = 10\,\mathrm{km}$) with the readout photodiode having an efficiency of 0.9 (η) can be calculated using 2.8, corresponds to $2.68{\times}10^{-21}\,1/\sqrt{\mathrm{Hz}}$. The linear amplitude spectral density of a typical gravitational wave signal with amplitude $\widetilde{h}$ in a frequency band $\Delta f{=}\ 100\,\mathrm{Hz}$ is $\approxeq 10^{-23}\,1/\sqrt{\mathrm{Hz}}$ [35] which is a few orders of magnitude lower compared to the sensitivity of the Michelson calculated using equation 2.7. In order to improve the sensitivity, we require longer arm interferometers, more laser power thus prompting design changes to the conventional Michelson interferometer layout.

2.2 Fabry-Perot cavities

A Fabry-Perot cavity is an optical resonator formed by two mirrors for the input laser light. For a cavity length which is an integer number of half-wavelengths, the light interferes coherently with itself every time it bounces off the end mirror. When this happens, the cavity resonates and the amplitude of the circulating light field is amplified. The basic setup of a Fabry-Perot cavity is shown in figure 2.3.

2.2.1 Field equations in a Fabry-Perot cavity

For two mirrors IX and EX having an amplitude reflectivity r_1 and r_2 respectively and separated by a distance L_c, the static electric fields can be calculated similar to the case of the Michelson interferometer. The amplitude transmissivity of IX and EX are represented by t_1 and t_2 respectively. Throughout this thesis, we make the assumption that the cavity length change due to a passing gravitational wave changes slowly compared to the light travel time from one mirror of the cavity to the other. This is known as the long wavelength approximation and is valid due to the underlying assumption that light and gravitational waves travel at the same speed. With the

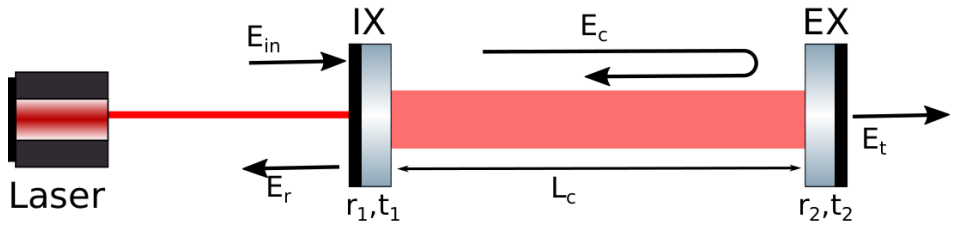

Figure 2.3: Electric field equations for a two mirror Fabry-Perot cavity formed by mirrors IX and EX separated by a distance L_c.

input field, circulating field, transmitted field, directly reflected field denoted as E_c, E_t and E_r respectively,

$$E_{circ} = \frac{it_1 E_{in}}{1 - r_1 r_2 e^{2i\phi}} \,, \tag{2.8}$$

where ϕ is the phase accumulated by the light field during its propagation from IX to EX.

$$\begin{aligned} E_r &= it_2 E_{in} e^{i\phi} E_{circ} \,, \\ &= \left(r_1 - \frac{t_1^2 r_2 e^{2i\phi}}{1 - r_1 r_2 e^{-2i\phi}} \right) \,, \end{aligned} \tag{2.9}$$

$$E_t = -\frac{t_1 t_2 E_{in} e^{-i\phi}}{1 - r_1 r_2 e^{-2i\phi}} \,, \tag{2.10}$$

For all the above equations, we have adopted the convention where transmission through a mirror conveys 90° of phase, i.e. a factor of i.

2.2.2 Characteristics of a Fabry-Perot cavity

Using the equation obtained above, it is possible to design Fabry-Perot cavities that would suit our requirements. In this section we briefly summarise a number of important physical quantities that characterize a Fabry-Perot cavity.

2.2.2.1 Power build up in the cavity

The maximum power built up in the cavity on resonance can be calculated from the build up factor. Examining equation 2.8 again, this factor can be calculated to be:

$$g_{circ} = \left(\frac{t_1}{1 - r_1 r_2} \right)^2 , \tag{2.11}$$

The intra-cavity power can be plotted as a function of the change in length of the Fabry-Perot cavity. The round trip phase accumulated by the light in the cavity determines the resonance condition and is given by:

$$\begin{aligned} \phi_{rt} &= \frac{2\omega L_c}{c} , \\ &= \frac{4\pi L_c}{\lambda} , \end{aligned} \tag{2.12}$$

where λ is the laser wavelength.

The Fabry-Perot cavity increases the light storage time and when implemented into a Michelson interferometer (section 2.4), is equivalent to increasing the length of the Michelson arms by a factor of the cavity gain.

2.2.2.2 Free spectral range

The frequency separation (see figure 2.4) between the resonance peaks is defined as the free spectral range (FSR) of the Fabry-Perot cavity and depends on the macroscopic length of the arm cavity:

$$\text{FSR} = \frac{c}{2L_c} , \tag{2.13}$$

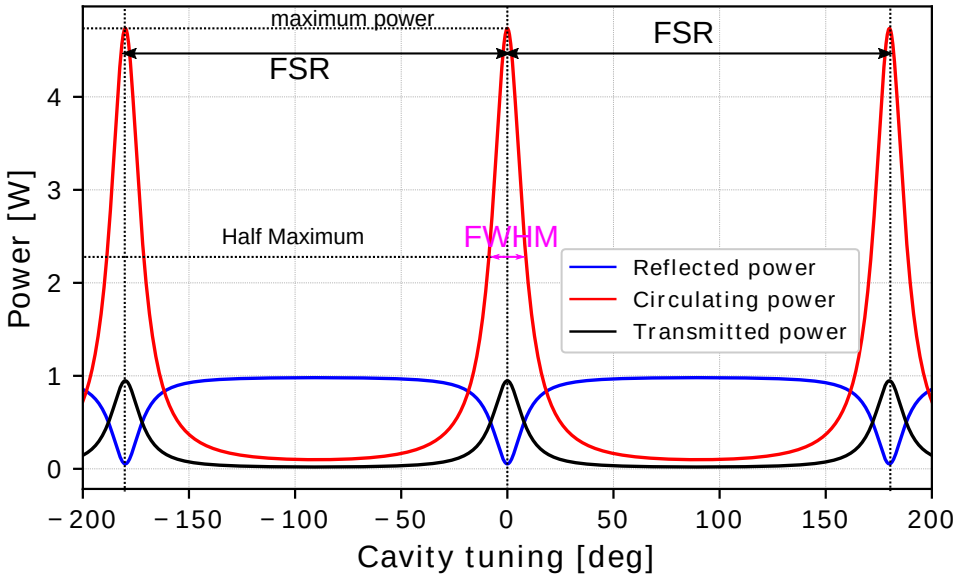

Figure 2.4: Static response of a Fabry-Perot cavity, simulated with FINESSE. A input power of 1 W and reflectivities of 0.7 and 0.8 are assumed for IX and EX respectively with L_c being 10 km. Image inspired by [36].

2.2.2.3 Finesse and linewidth

The finesse (F) of a Fabry-Perot cavity is determined by the losses in the cavity and is a measure of the resonant enhancement of the light field and can be calculated from:

$$F = \frac{\pi\sqrt{r_1 r_2}}{1 - r_1 r_2} \ . \tag{2.14}$$

The line-width of the cavity is the full width at half maximum (FWHM) of the cavity resonance. This quantity is a measure of the filtering effect of the Fabry-Perot cavity. It can be calculated from:

$$\text{FWHM} = \frac{\text{FSR}}{F} \ . \tag{2.15}$$

2.2.2.4 Storage time and cavity pole

A Fabry-Perot cavity can be regarded as a filter for the laser light entering it. We can calculate the cavity pole of such a cavity which is the sideband frequency at which the circulating power in the cavity falls by 3 dB. This is also known as the half width half maximum of the cavity and

can be calculated from the equation:

$$f_p = \frac{\text{FSR}}{2\pi} \frac{(1 - r_1 r_2)}{\sqrt{r_1 r_2}} = \frac{\text{FWHM}}{2} \ . \tag{2.16}$$

The cavity pole essentially originates from the fact that a cavity has a finite storage time.

$$f_p = \frac{1}{2\pi\tau_s} \ , \tag{2.17}$$

where τ_s is the storage time of light in the cavity.

2.2.2.5 Sub-species of Fabry-Perot cavities

Depending on the reflectivities of the mirrors IX and EX, Fabry-Perot cavities can be broadly classified into three categories:

- Over-coupled cavity: $r_1 < r_2$. In this case, the directly reflected field is dominated by the circulating field resonating in the cavity, which leaks out through IX. This field has opposite sign to the prompt reflection, and so the sign of the field reflected from the cavity changes when the cavity is resonant (for example, the arm cavities in a ET-LF are over-coupled).

- Under-coupled cavity: $r_1 > r_2$. In this case, the reflected field is dominated by the field promptly reflected from the input mirror (for example the current power recycling cavity in GEO 600 is under-coupled; see section 7.5 for more details about the consequence of the same).

- Critically coupled cavity: $r_1 = r_2$. For a critically coupled cavity, the promptly reflected field is cancelled by the leakage field, and there is zero reflection. This situation is described as an impedance matched cavity or a critically coupled cavity (for example the power recycling cavity designed for ET-LF is impendance matched to the losses in the interferometer).

2.3 Evolution of the Michelson interferometer

The Michelson interferometer is the most basic configuration and typically is not sensitive enough for continuous measurement of gravitational waves. The shot noise limited strain sensitivity for a Michelson interferometer is given by equation 2.7. In order to increase the sensitivity of the interferometer, one would need to increase the arm length or use extraordinarily high laser powers (which would then lead to other problems like high thermal noise, see section 2.5). A more space-effective solution would be to use optical folding techniques such as using Fabry-Perot cavities in the Michelson interferometer arms thus giving rise to the first evolution in the Michelson configuration.

2.3.1 Fabry-Perot Michelson Interferometer

The Fabry-Perot Michelson interferometer or FPMI has an additional mirror in each arm of the interferometer. This is denoted by IX and IY in figure 2.5 in the panel with the title FPMI. The individual arm length is now denoted by $L_{[x,y]}$ for the X and Y arms respectively and the shorter distance between the beam splitter and the input test masses (IX, IY) is denoted by $l_{[x,y]}$ respectively. The addition of optical cavities to the arms of the Michelson interferometer increase the effective optical length of the arms by a factor

$$\frac{L_{\mathrm{FP}}}{L_{\mathrm{MICH}}} = \frac{2F}{\pi} \ , \tag{2.18}$$

where F, is defined as the finesse of the Fabry-Perot cavity. These Fabry-Perot arm cavities are generally over coupled. The shot noise limited strain amplitude spectral density is calculated by [37]:

$$h(f) = \frac{1}{8FL}\sqrt{\left(\frac{2hc\lambda}{P_{in}}\right)\left(1+\left(\frac{f}{f_p}\right)^2\right)} \ , \tag{2.19}$$

where, $f_p = \frac{c}{4FL}$ is the cavity pole. We also make the assumption that the two arms lengths L_x and L_y are equal and the average of the same is denoted by L.

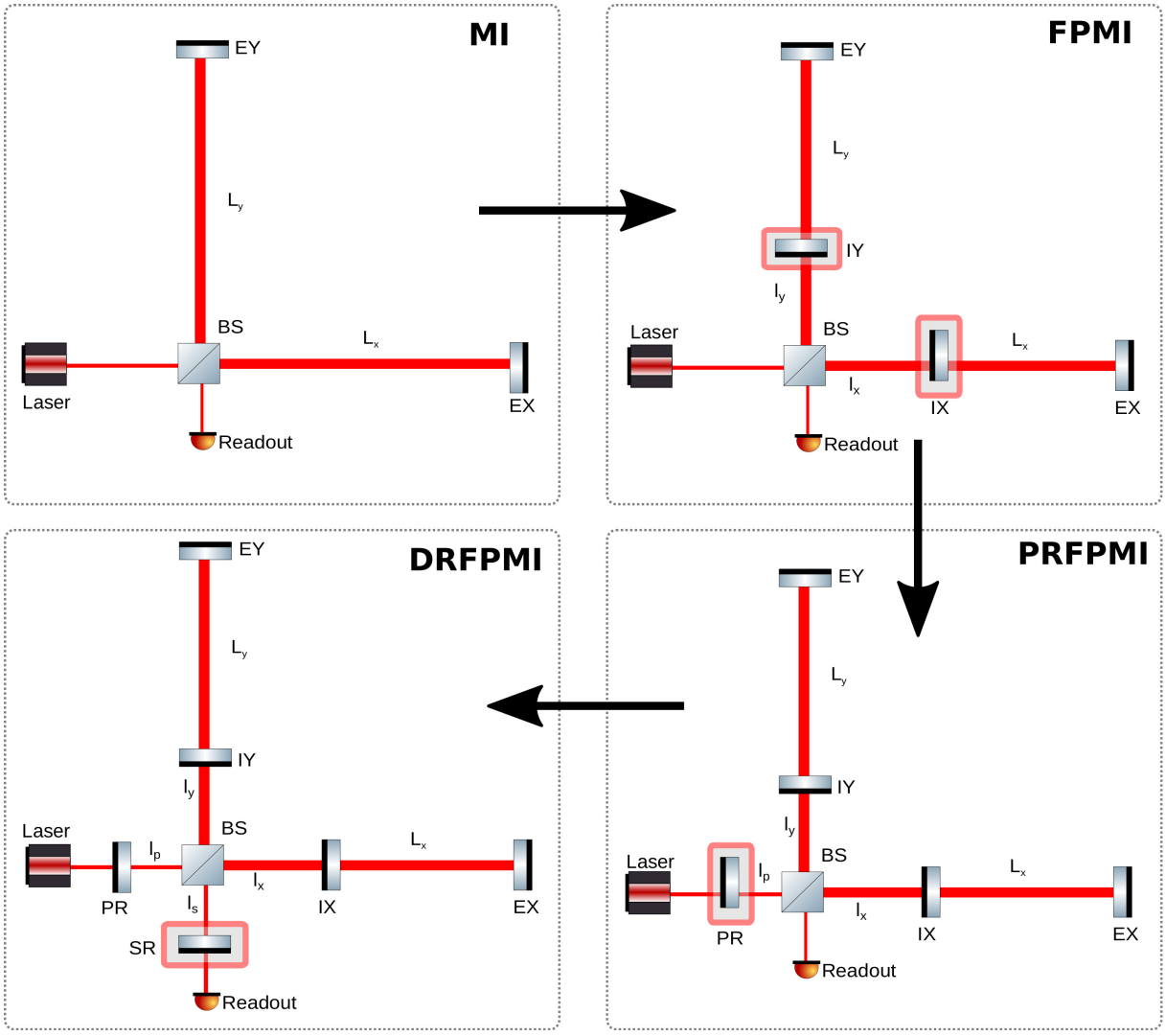

Figure 2.5: Optical configurations for gravitational wave detection and the evolution of a simple Michelson interferometer (MI) to the complex currently favored layout of advanced gravitational wave detectors (Dual Recycled Fabry-Perot Michelson Interferometers).

2.3.2 Power Recycled Fabry-Perot Michelson interferometer

Power recycling is a technique to increase the total circulating power inside the interferometer. This configuration involves adding an additional mirror in the path of the input laser beam. If this configuration is implemented in a FPMI interferometer configuration (as shown in the bottom right panel of figure 2.5), the new configuration is called power recycled Fabry-Perot Michelson interferometer (PRFPMI). Intra-cavity power is maximized by choosing transmission of the power recycling mirror to minimize reflected power. The additional power increase decreases the shot noise thus improving the sensitivity of the interferometer.

The recycling gain (or the factor by which the circulating laser power is increased, G_{PR}) is the ratio of the input laser power and the circulating power in the central part of the interferometer (in other words, the power impinging on the central beam splitter) and be calculated from:

$$G_{PR} = \left(\frac{t_{PR}}{1 - r_{PR}\, r_{MICH}} \right)^2 , \tag{2.20}$$

where, t_{PR} and r_{PR} is the amplitude transmissivity and amplitude reflectivity of the power recycling mirror (denoted by PR in the figure 2.5). r_{MICH} is the amplitude reflectivity of the Michelson interferometer.

The improvement in the shot noise limited sensitivity of the PRFPMI over the FPMI configuration is related as follows:

$$h(f) = \frac{1}{\sqrt{G_{PR}}}\, h(f)_{FPMI} , \tag{2.21}$$

where $h(f)_{FPMI}$ is the shot noise limited sensitivity of the FPMI configuration.

2.3.3 Dual Recycled Fabry-Perot Michelson interferometer

The concept of signal recycling was developed by Meers et.al. in 1980 [38, 39] to increase the storage time of an interferometer for GW signals. The signal sidebands that exit through the output port of the interferometer can be 'recycled' by adding a mirror in the output path thereby forming an additional optical cavity. A dual recycled Fabry-Perot Michelson interferometer (DRFPMI), as shown by the bottom left panel in figure 2.5, is formed by the addition of a signal recycling mirror (SR) to a PRFPMI. This mirror reflects the signal sidebands back into the interferometer. The SR tunes the bandwidth of the interferometer and the reflectivity of the same alters the 'sharpness' of the tuning. Dual recycling thus allows a detector to be constructed which has a high- sensitivity, narrow-frequency response whose peak frequency can be adjusted.

With the addition of this mirror, the simple Michelson interferometer has evolved into the complex DRFPMI configuration. In order to not compromise the sensitivity of the detector, five longitudinal (see section 4.1.2) degrees of freedom (dofs) need to be sensed and controlled along with sixteen angular dofs (2 each for PR, SR and BS; 10 for the arm cavity mirrors). We describe

the longitudinal sensing challenge from the perspective of ET-LF (a DRFPMI configuration) in chapter 4 which is applicable to any of the current operating interferometers.

2.4 Pound-Drever-Hall sensing scheme

The basic principle of all the sensing and control schemes in advanced GWDs, are variants or extensions of the Pound-Drever-Hall (PDH) technique [40]. In a basic PDH setup, the laser light is modulated with an electro-optic modulator (EOM) to produce a pair phase modulation sidebands on the laser carrier (laser beam). These sidebands can be viewed as additional electric fields going into the cavity. While the laser carrier is resonant in the Fabry-Perot cavity, the sideband frequency is chosen to be non-resonant in the same.

Upon reflection from a cavity, the carrier and the two phase modulated sidebands are rotated. The rotation converts phase modulation to amplitude modulation which is measured by the photodiode. Around resonance, for a small mismatch in the frequency of the laser carrier and the cavity length, there is a rather large change in the phase of the reflection. The modulation sidebands which are non-resonant experience a minimal phase change. An error signal can this be obtained by taking demodulating the photodiode signal at the sideband frequency. This error signal is linearly dependent on the carrier phase thus indicating how much the cavity is off resonance for the carrier.

The mathematical aspects of PDH sensing are dealt with in the Appendix B. In advanced GWDs which have multiple degrees of freedom to control to maintain resonance conditions for the interferometer carrier to prevent degradation of the sensitivity, multiple sidebands are used which are subject to individual resonance conditions i.e. the sideband frequencies are chosen to make the sidebands resonant in different cavities. The choosing of these RF-sidebands is described from the perspective of ET-LF in section 4.2.

Several variants of the PDH signal are used for control of the multiple degrees of freedom in an interferometer with the DRFPMI configuration. In the original Pound-Drever-Hall method the beats are between sidebands and carrier, but for complex optical systems such as aLIGO or ET-LF, error signals for control of the the short degrees of freedom of the interferometer

are obtained using double demodulation or the optical beats between the sidebands. The beats between the modulation sidebands reveal the phase shifts they acquire in traversing various parts of the interferometer, and thus reveal the length degrees of freedom. For instance for control of the signal recycling cavity (SRC) length in aLIGO, the error signal is obtained by demodulating at the beat frequency between a sideband resonant in both the recycling cavities and a sideband which is resonant only in the power recycling cavity.

2.5 Noises in GWDs

Noise budgets are instrumental in understanding the noises that affect the sensitivity of the GWD. A simplified, theoretical noise budget for ET-LF is shown in figure 2.7. The design sensitivity of ET-LF requires the ability to measure displacements on the order of 10^{-20} m. It is hence of utmost importance that displacements around this level are not dominated by other noise sources. Noise budgets are an effort to understand and mitigate these noise sources by means of interferometer design. The final noise at the readout is sum of the individual noise sources propagated to the readout port. All the noise sources are calibrated to the units of $1/\sqrt{\text{Hz}}$ to compare it to the gravitational wave strain .

As all the other current GWDs, the measurement band of ET-LF will be dominated by quantum noise. With the help of novel techniques (see section 3.2), thermal noise arising from mirror coatings which limits current GWDs (after quantum noise) is reduced in ET-LF. At lower frequencies (1–7 Hz), seismic noise and thermal noise arising from mirror suspensions dominate. In order to improve the sensitivity beyond the limit set by quantum noise, several new techniques are currently being tested at prototypes around the world including the 10 m prototype at the AEI (Albert Einstein Insitute) [41]. GEO 600, a British-German collaboration GWD located outside Hannover has been using frequency independent squeezing to improve its sensitivity [42].

Some of the noise sources that limit the sensitivity of GWDs are discussed in this section.

We have divided some of the known noise sources into three broad categories: displacement noises, sensing noises and uncategorised noises. We only consider noises that are relevant from the point of view of this thesis.

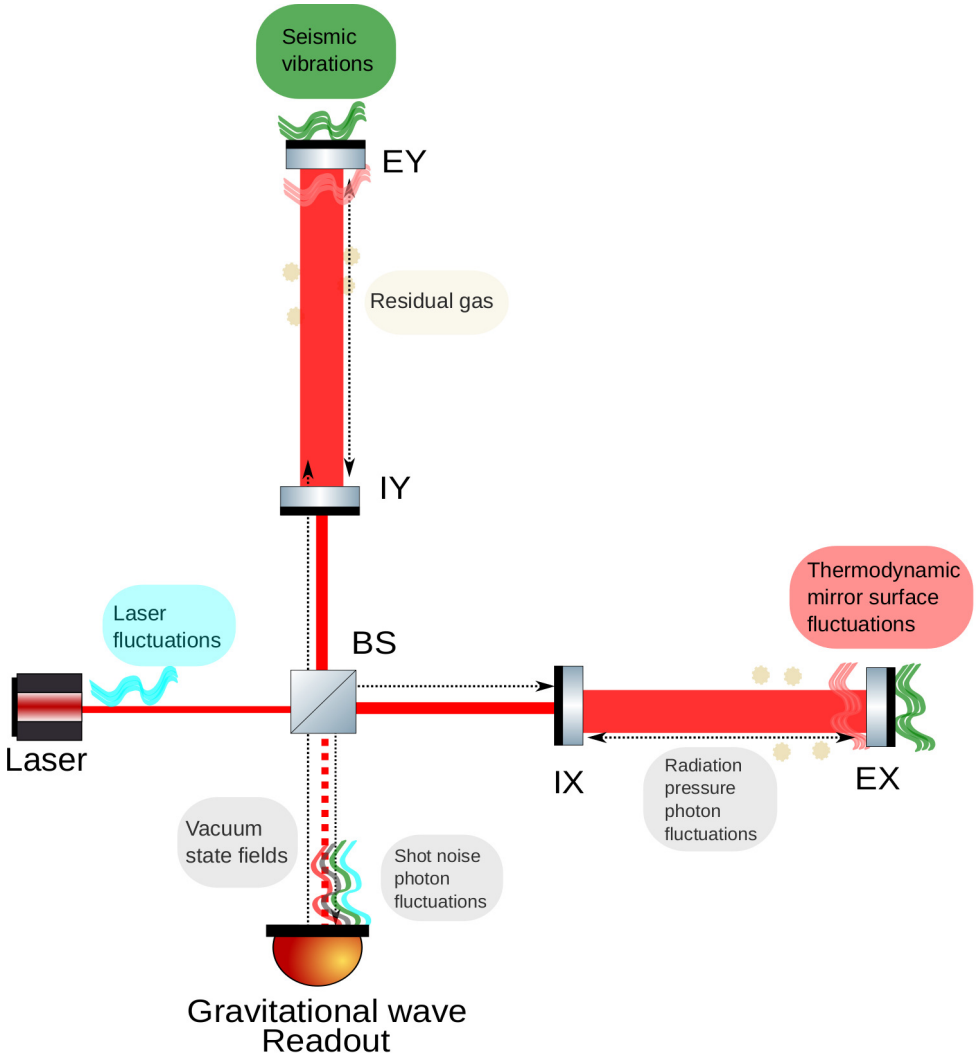

Figure 2.6: Simplified infographic of a GWD with an FPMI configuration to demonstrate the various noise sources that mask the gravitational wave signal at the readout photodiode. The noise sources can be mitigated with the help of careful design of individual components such as mirror coatings, optimised control loops etc.

2.5.1 Displacement noise sources

Displacement noises as the name suggests, displace suspended test mass optics thus causing a spurious differential arm length change which would interfere with the detection of gravitational waves. The main displacement noise sources are listed below.

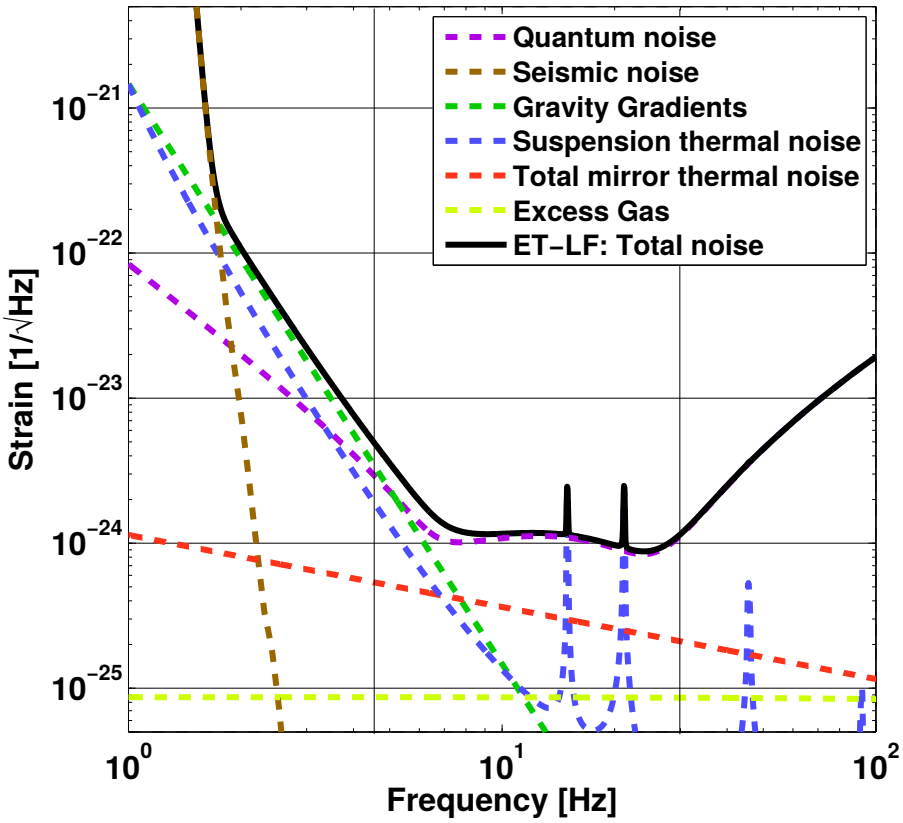

Figure 2.7: ET-D-LF noise budget created using GWINC [12, 43]. The incoherent sum of some of the noise sources that would dominate the low frequency part of the ET interferometer is shown in black.

2.5.1.1 Seismic noise and gravity gradient noise

Seismic excitations due to earthquakes, ocean waves, standing waves on land, man made noise due to trucks or subways (anthropogenic noise), acoustics and vibrations from the vaccum systems and fans are all contributing factors to seismic noise. With the combination of active and passive seismic isolation systems [44, 45] and suspensions [46], the contribution of ground motion is reduced by nearly 10 orders of magnitude in the frequency range of interest.

The concept of seismic isolation system for ET has been developed on the basis of the Virgo super attenuator concept [47] where a futuristic 17 m super-attenuator is divided up into six individual stages of 2 m each. The transfer function for such a system from the horizontal ground motion to the test mass falls off with a factor of $1/f^2$ for each pendulum stage for frequencies above the resonance. In current advanced GWDs, several seismometers and other sensors are placed

around the instrument to monitor the seismic activity and this information is used to improve the duty cycle of the interferometer by making the interferometer more robust to seismic noise below 10 Hz [48].

Gravity gradient noise (GGN), arises from the varying gravitational attraction of the test mass by its surroundings. Mitigation of gravity gradient noise is not yet experimentally demonstrated. The shaping of the ground near the test masses, and using auxiliary witness sensors have shown promise in mitigating GGN. The choice of going underground for ET was made to mitigate these noises [49, 50].

2.5.1.2 Suspension thermal noise

In current advanced detectors like aLIGO, the suspensions for the test masses which isolate the test mass from ground motion utilise fused silica fibres [51] as opposed to previously used wires because the displacement noise in the test mass when using the latter was significantly large in the measurement band (in the 5–50 Hz regime) [52]. With the exception of KAGRA, current advanced GWDs utilise fused silica for its lower mechanical loss factor with high quality factor, leads to a lower displacement noise. Figure 2.7 shows the suspension thermal noise for ET-LF and it is no longer a dominant source in the measurement bandwidth of ET-LF (as ET-LF would use cryogenics and silicon fibers).

Violin modes (shown as spikes in the dotted blue noise curve in the figure 2.7) with a resonant peak in the measurement bandwidth, can pose a significant problem when they ring up. During O2, after the short vent to clean the input test mass in the X-arm, the ringing of the violin modes of some of the suspensions hindered the locking process of the interferometer. Even with damping and control techniques, there were difficulties in damping these modes [53].

2.5.1.3 Quantum radiation pressure noise

There are two kinds of radiation pressure noises: technical radiation pressure noise and quantum radiation pressure noise. Technical radiation pressure noise arises from the power fluctuations of the laser beam impinging on the test mass surface. These power fluctuations couple to the GW

readout and arise from finesse mismatches of the arms, mass imbalances of the test masses and imperfect beam-splitter splitting ratio.

Quantum radiation pressure noise (in combination with quantum shot noise) poses a limit on the sensitivity of the detector. It depends on the laser power incident on the mirrors and the mirror mass. This noise arises from the zero point fluctuations of the vacuum field that enters the interferometer through all open ports [54] (it is almost exclusively the output port). A differential radiation pressure displacement arises between the two arms of the Michelson interferometer due to the Poisson distribution of photons in the individual arms. In other words, the randomly fluctuating number of photons impinging on the test masses leads to random displacement fluctuations.

The displacement noise of a mirror with mass m, illuminated with a laser beam with power P due to radiation pressure is given by [55]:

$$x(f) = \frac{1}{2mc(\pi f)^2}\sqrt{\frac{2hcP}{\lambda}} \ . \tag{2.22}$$

From the above equation, we can see that decreasing the laser power and/or increasing the test mass lowers the quantum radiation pressure noise. This would however increase the quantum shot noise (see 2.5.2 for details on quantum shot noise).

The sensitivity limit of a detector is the cross-over of quantum radiation pressure noise and quantum shot noise and is called the standard quantum limit (SQL). The SQL for two free test masses of mass m, separated by a distance L is given by:

$$h_{SQL} = \sqrt{\frac{4h}{\pi m(\omega L)^2}} \ , \tag{2.23}$$

with units of $1/\sqrt{\text{Hz}}$.

For each input laser power, assuming that the amplitude fluctuations (radiation pressure) and phase fluctuations (shot noise) are uncorrelated, the sum of the same leads to an envelope of minima which is the SQL and this limit has not been experimentally measured. The AEI 10m prototype is a radiation pressure noise limited experiment which is aimed at measuring this. The

experiment is described in Chapter 5.

2.5.1.4 Mirror thermal noise

The highly reflective mirrors used as test masses in the GWDs, are made up of multiple dielectric layers. Thermal excitation of these coatings produces displacement noise which was a limiting noise source in the low frequency (5–50 Hz) in initial GWDs (the coatings make up the bulk of thermal noise and the substrate thermal noise contribution is small). The mechanical loss in the numerous layers of this dielectric coating layers on the test masses are studied extensively [55–57] and are optimised to minimise the coating Brownian noise.

Following Levin's approach [58] for the mirror thermal noise we can express the displacement noise power spectrum of the total thermal noise of a single test mass as:

$$S_x(f) = \frac{8k_BT}{3\pi^2 f}\frac{d}{\omega^2 E}(2\phi_B + \phi_S) \ , \tag{2.24}$$

where ω is the spot size of the beam, E is the Young's modulus of the mirror substrate, ϕ_B and ϕ_S are the bulk and shear modulus of the mechanical loss of the coating material and k_B is the Boltzmann constant. The best samples of fused silica, sapphire, and silicon can have loss angles as low as 10^{-8} [59] or better and as such, do not limit the sensitivity of modern detectors.

Thermal fluctuations can cause fluctuations in the refractive index of the coating layers (thermo-refractive noise) along with change in thermal expansion coefficient of the material of the coatings (thermo-elastic noise). The coating layers can be optimised to cancel out these two noise sources as the origin of these noise sources is the same [60]. The total thermal noise for mirrors is shown by the noise curve in dotted red lines in figure 2.7.

A significant research effort is being invested into crystalline coatings (AlGaAs coatings) [61, 62], cryogenically cooled test-masses (ET-LF, KAGRA) [10, 46]. [5, 63] have investigated the use of grating structures and waveguides as an alternative to the conventional coatings structure used in current GWDs, but these are technically more difficult to implement.

2.5.1.5 Residual gas noise

The residual gas in the vacuum envelope can result in displacement of the optics via the Brownian motion of the gas molecules which would then impinge on the test-masses thus resulting in spurious motion of the test mass which creates displacement noise. This noise arises due to the damping force exerted by the residual gas molecules via exchange of momentum between the gas molecules and the test mass surface. This noise source is shown by a lime green dotted curve in figure 2.7 for ET-LF. At 25 Hz for ET-LF, this noise source is estimated to be an order of magnitude below the quantum noise limit [4].

2.5.2 Sensing noises

Sensing noise as the name suggests arises from the sensing of the state of the interferometer. Sources of sensing noise are in general independent of the arm length and test mass parameters . The two largest contributors of sensing noise are quantum shot noise and electronics noise. Although laser noises (power fluctuations of the laser beam) couple to the GW readout (for a discussion of the same refer [55]) , we do not discuss them in this section. The active control of the length of an optical cavity introduces technical noises like electronic noises, sensor noises into the feed-back control loop and these noises are eventually fed-back to the cavity mirrors. This control noise which arises from imprinting sensing noise on the feed-back signals can couple to the GW readout. In order to not be limited by such control noise, the control system needs to be designed with the appropriate bandwidth, gain and phase margins. In chapter 4, a longitudinal sensing and control scheme was developed for ET-LF.

2.5.2.1 Quantum shot noise

The shot noise component of the total quantum noise limit described in section 2.5.1 originates due to Poisson statistics of the photons arriving at the readout. The quantum vacuum fluctuations that enter the interferometer through the open ports, causes variations in the arrival time of the photons at the photodetectors . In other words, the photodetector sees a fluctuating light power. The spectral density of shot noise has equal power at all frequencies i.e. it is white.

The displacement-equivalent amplitude spectral density for shot noise is given by [55]:

$$x_{shot} = \sqrt{\frac{hc^2}{2\pi P_{in}\omega_0}}\ , \tag{2.25}$$

in m/$\sqrt{\text{Hz}}$, where P_{in} is the input laser power, ω_0 is the angular frequency of the laser carrier.

2.5.2.2 Dark noise

Dark noise is the electronic noise when no light is incident on the photodetector used in the readout. Generally, the use of low noise electronics allows this to not be a limiting noise source. This noise can however pollute the sensing noise signal and thus contribute to the overall electronics noise.

2.5.3 Uncategorised noises

Some noise sources are difficult to classify for instance:

2.5.3.1 Barkhausen noise

The magnetic actuation system [55] suffers from Barkhausen noise and the upconversion of this force noise, can pose a problem and limit the sensitivity of the detector. This magnetic actuation system was used to provide low frequency control forces and for the GW readout channel. The magnetic actuation system has been switched out for a new electrostatic drive (ESD) which does not suffer from the Barkhausen effect in 2010 [64].

2.5.3.2 Cross-couplings

Cross couplings from imperfections in the diagonalisation of the control system leads to imprinting sensing noise of one degree of freedom onto another for example, imperfect angular actuation for the angular control of a dof, leads to perturbations of the differential arm length change (which contains the GW information). As a result of this contamination, there is additional noise in the GW readout. In aLIGO, this noise is mitigated to a large extent by the use of feed-forward

cancellation techniques known as angle-to-length decoupling [27]. Another way is to cut off the feedback of the control signal below the detection band (but this cut-off frequency cannot be chosen to be arbitrarily low as explained in section 6.3.4).

Chapter 3

The Einstein Telescope

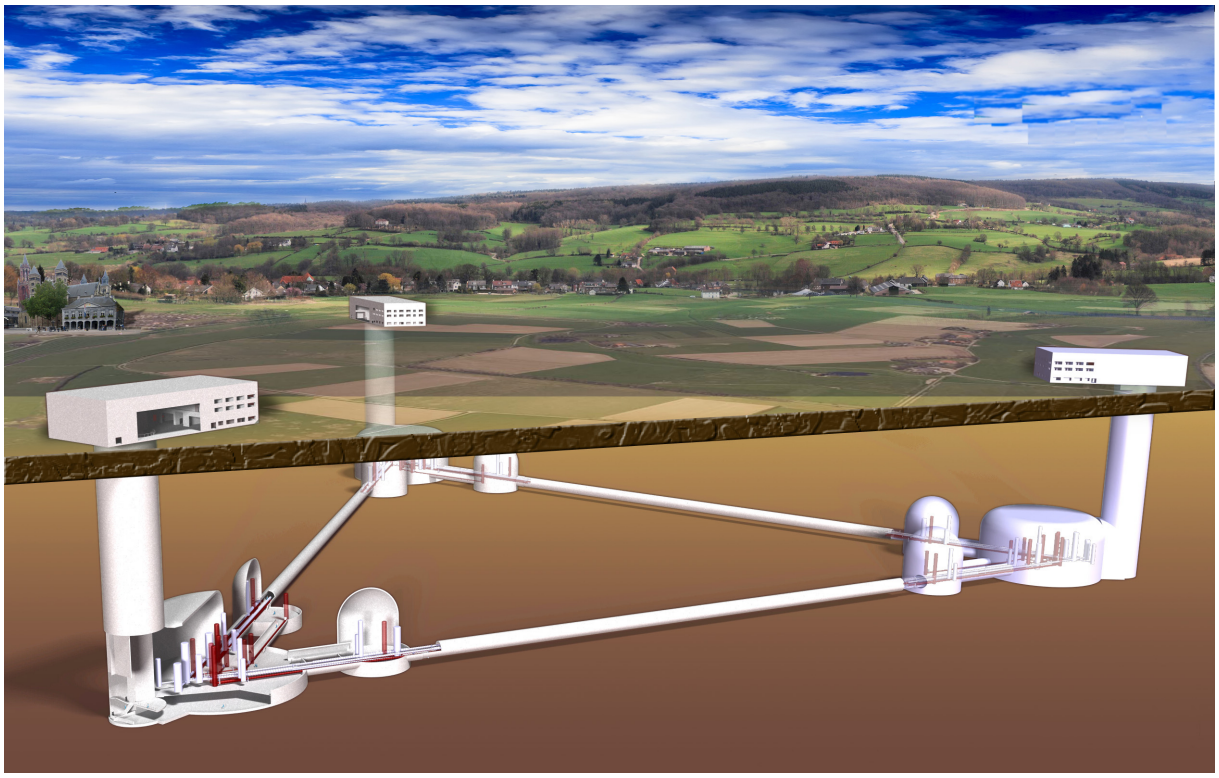

Artists impression of the Einstein Telescope observatory. Picture courtesy Nikef.

3.1 Einstein Telescope : A new facility to do GW observations

In the dawning era of advanced third-generation gravitational wave observatories, the Einstein Telescope (ET) is set to have a target sensitivity an order of magnitude higher than the design sensitivity of current advanced detectors, advanced LIGO (aLIGO) and advanced Virgo (AdV). In the period between 2008-11, the ET design study [12] was completed where the current infrastructures for advanced GWDs were examined. Techniques on how to push the boundaries of the current infrastructures to enhance the sensitivity of ET were examined in the design study.

The conceptual design of ET is envisioned to have three pairs of nested detectors (a total of six interferometers), of 10 km each and with an opening angle of 60°. The three interferometers would help detect both polarisations of a gravitational wave thereby enhancing the ability to estimate source parameters. On average, the sensitivity of the triple 60°detector is slightly better than a single, optimally oriented 90°one by a factor of 0.816 [65]. The triangular infrastructure also maximises the tunnel usage along with the added benefit of polarisation resolution. Null stream signals which would help identify and cancel common noise sources in the interferometers can also be generated in such a configuration. These null stream signals are invaluable for low SNR signals [6] as they contain a combination of both signal and noise. The coherent noises can then be cancelled [66] [67]. Having multiple detectors allows upgrades for parts/whole interferometer without loosing entire sky coverage. LIGOWA (LIGO Hanford) has been previously known to have co-located interferometers for null stream analysis during the period 2000-2010. LIGO detectors at the Hanford site consisted of two interferometers (H1 and H2), 4 km and 2 km long respectively, sharing the same vacuum system.

Current GWDs are limited by seismic noise below 10 Hz and in order to meet the design requirements, ET will be located underground at a depth between 100 m and 300 m. Underground seismic measurements were performed initially for eight sites [12]. Over time, some new potential sites have been identified namely, Son Enattos, Limburg site in the Netherlands border [68].

The observation band of ET-LF is 7–32 Hz. Having good sensitivity at low frequencies gives us improved sky localisation for EM follow-up owing to the longer time scales of observation period. Signals from BBHs of masses greater than 1000 solar masses could potentially be observed for

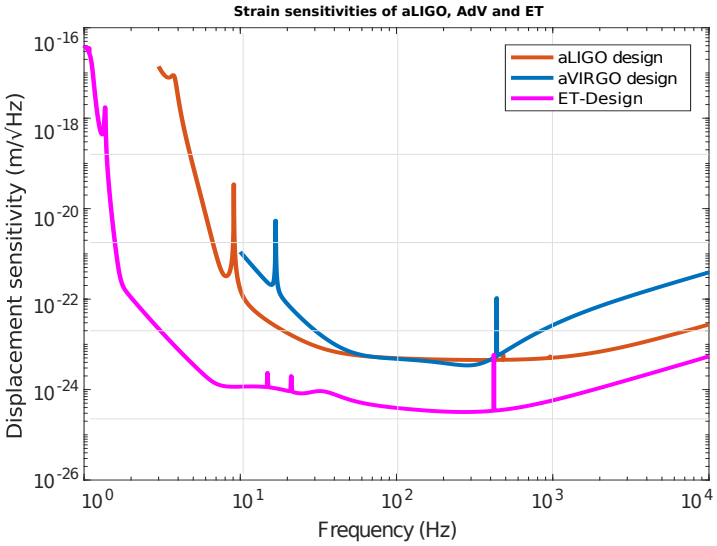

(a) Design Sensitivity of ET

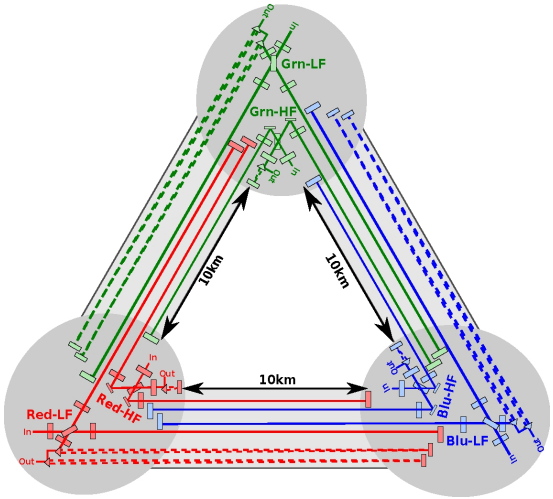

(b) ET xylophone Layout

Figure 3.1: Figure 3.1a shows the design sensitivity for aLIGO, aVIRGO and ET-D. The ET-D curve is a combination of the sensitivity of ET-LF (1–35 Hz) and ET-HF (35–10 kHz). The optical configuration of the ET GW observatory is the figure 3.1b and shows the three tunnels with the main optics and filter cavity optics thus giving the reader a visual picture of the observatory itself. More images can be found in the design study document.

a period of 10^3–10^4 seconds allowing for better parameter estimation. These low frequencies (1–10 Hz) [69] are not investigated by any other detectors and it would put ET (because of ET-LF) in a unique position to discover the unknown. D.Keitel et. al. are currently working on these long inspiral signals which are believed to give us improved parameters for compact binary coalescences (CBC). In the low frequencies, these searches provide us with information about degeneracies with precession and higher modes and improved sensitivity even if the SNR is low. These CBC signals also contain information about ellipticity of orbits before it is radiated away [12] [70].

The high frequency sensitivity of ET would allow us to observe neutron star inspirals [71] paving way for astro-seismological studies of such objects thus allowing us to study the equation of state and the internal structure of neutron stars. These are mere examples for the various benefits of having a detector with the sensitivity capabilities of ET.

In order to show the benefit of having multiple detectors observing different frequency spans, the sensitivities of various detectors to different sources is shown in the figure below [72].

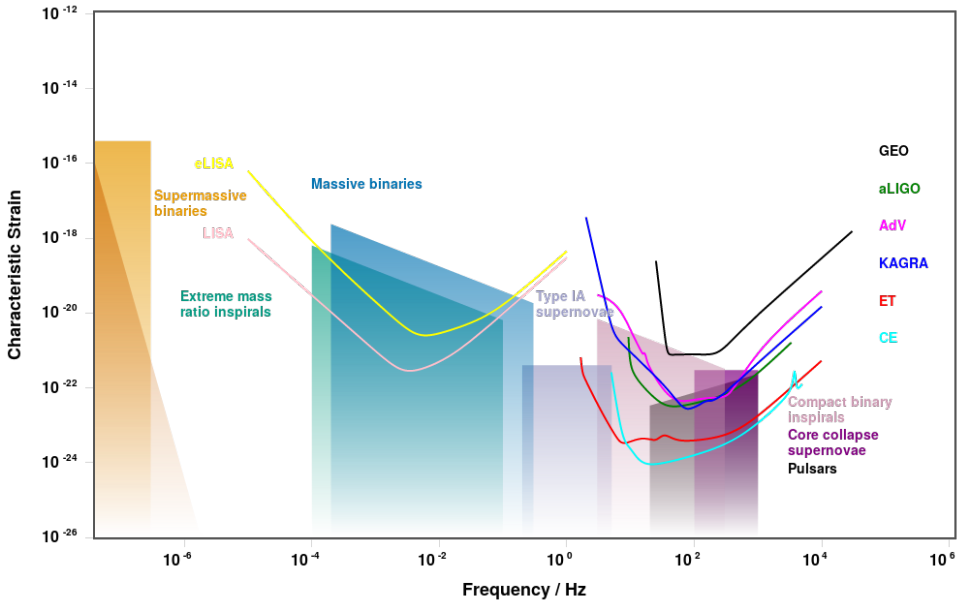

Figure 3.2: Characteristic strain sensitivities of existing and planned gravitational wave detectors. This picture shows the frequency 'gap' covered by the low frequency part of ET thus advocating for a detector sensitive to those frequencies. A network of GWDs (a few have been named in the figure) would open the window to sources unseen in the universe.

3.2 ET technologies

Current detectors are limited by seismic noise and gravity gradient noise at low frequencies, thermal noise at mid-frequencies. Additionally, the sensitivity of the detectors depends on the arm-cavity length (see section 2.3.1). In order to reach the aforementioned design sensitivity, ET will employ dedicated technologies to surpass the limitations of the current second generation detectors.

The interferometer configuration currently assumed for both ET-LF and ET-HF is a standard

dual recycled Fabry-Perot Michelson interferometer [7]. Alternative configurations for ET are under study [65, 73] and a potential configuration where we have one detector as opposed to the layout presented in the design study is under consideration. This design was conceptualised at the ET design study update meeting in Glasgow (2017) [73].

The evolution of the current ET design sensitivity is detailed in [46] and for this thesis, we use the configuration proposed in the design study. The detector arm-length increase from the current 3 km and 4 km (AdV and aLIGO respectively) to 10 km improves the overall sensitivity by a factor of 3.3 . As all ground-based detectors hit the seismic noise and gravity-gradient noise barrier at low frequencies, ET is proposed to be built underground with 17 m (ET-LF) and 21 m (ET-HF) long super attenuators with pre-isolation systems like the AEI 10 m SAS [12] [44]. Gravity-gradient noise can be reduced by a factor of 50 by choosing a seismically quiet site (thus justifying the seismic studies being done currently for ET at various places) and active subtraction. Although this has not yet been demonstrated in the current detectors, simulations [46] [49] have shown promising results in terms of subtraction of this noise by using an array of auxiliary witness sensors.

Thermal noise which limits ground based detectors in the mid-frequency range (see section 2.5.1) can be countered with the use or large beams, crystalline coatings, cryogenics and modifying beam shape for mitigating thermal noise effects in the mid frequency band for example the use of LG_{33} beams as opposed to TEM_{00} beams reduces coating thermal noise by a factor of 1.6 [74]. However, coating thermal noise scaled for a fixed beam size scales inversely with arm length [75] and for many other reasons cited in [63], a significant effort is ongoing in the design of ET [76]. The main driver to employ cryogenics in ET-LF is suspension thermal noise mitigation (see section 2.5.1). Details on the research for thermal noise mitigation for ET are outlined in the design study [12] and [63].

3.2.1 The 'Xylophone' configuration for ET

Radiation pressure and relative shot noise scale oppositely with increasing laser power. High sensitivity can be achieved with low laser power at low frequencies and high laser power at high frequencies. Thermal noise is another limiting factor at low frequencies and requires cryogenic

optics for its mitigation. Cryogenics (200 K) with high laser power (3 MW) are a technical hindrance to work with and hence, in order to avoid a conflict of interest, the ET-facility will be divided into two sets of interferometers, one optimised for high frequency detection (32 Hz–10 kHz) and another one low frequency (1 Hz–32 Hz) GW detection.

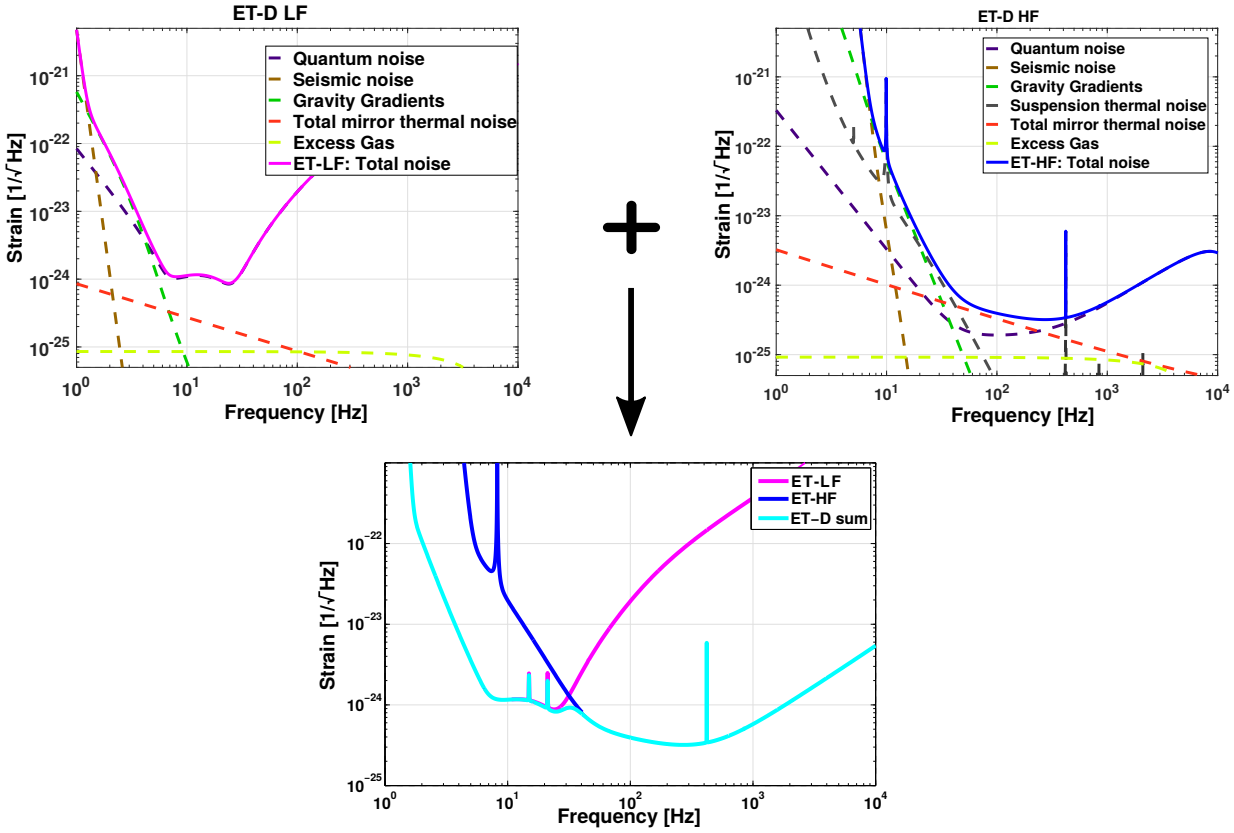

Figure 3.3: Design sensitivities of ET-LF, ET-HF. The overall sensitivity of a single detector of the ET observatory is shown by the curve ET-D sum.

In the following section, the key design differences between ET-LF and ET-HF are discussed.

3.2.2 ET-LF

A configurational difference between ET-LF and ET-HF is the detuning on the signal recycling cavity of ET-LF, the consequences of which are dealt with in the following section. ET-LF is envisioned to use lower laser power with 211 kg masses to combat radiation pressure. As thermal noise is a problem for current advanced detectors, ET-LF would use cryogenic test masses along with silicon optics as opposed to conventional fused silica optics. It has to be noted here that

the wavelength requirements also change for ET-LF as silicon is opaque to 1064 nm. This is the reasoning behind the use of 1550 nm wavelength lasers for ET-LF. ET-LF has narrow band cavities (Finesse c.a 880 and length 10 km) because only a small frequency range has to be covered. According to the Mizuno theorem, a consequence of high sensitivity requirements and low input laser power is low bandwidth cavities [77]. In order to facilitate the reduction in quantum noise, the use of frequency dependent squeezing has also been envisioned for ET-LF with 15 dB of input squeezing (a technology which has been experimentally demonstrated [78]). 17 m long AdV style super-attenuator suspension design have been considered for ET-LF in an effort to lower the suspension resonant frequency and provide isolation from ground motion along with the seismic systems from frequencies as low as 2 Hz. More information about the actual mirror dimensions and beam parameters are detailed in the design study [12].

3.2.3 ET-HF

ET-HF is similar in optical design to current advanced detectors with additional noise mitigating upgrades like the use of LG_{33} modes to reduce coating thermal noise and frequency dependent squeezing to reduce quantum noise. Owing to tuned signal recycling, ET-HF would require only one filter cavity to get the desired rotation of the squeezed states as opposed to ET-LF. The optics for ET-HF are also projected to use advanced technologies to improve the overall detector sensitivity by a factor of 10 over the design sensitivities of the current advanced detectors.

3.3 Detuned ET-LF

The process of detuning the signal recycling cavity for ET-LF involves choosing the bandwidth of the SRC such that the carrier is neither resonant nor anti-resonant. This process modifies the frequency response of the interferometer thereby allowing us to maximise the detector sensitivity to certain frequencies which would be particularly beneficial for certain targeted searches of astrophysical quantities such as pulsars. A sideband is made resonant by choosing a particular length of the SRC coupled with a tuning of the SRM. In detuned SRC, only one sideband is resonant as opposed to resonant sideband extraction, a technique that is detailed in [79] [80].

The detuning ϕ is chosen with respect to the carrier and follows $0 < \phi < \pi/4$ [81]. The signal recycling cavity in case of ET-LF which has a detuning of 0.6 rad (ϕ) or 25 Hz corresponds to a macroscopic detuning of,

$$dx = \lambda\phi/\pi \approx 2.96 \times 10^{-7} m \ . \tag{3.1}$$

This detuning of the SRM, creates an opto-mechanical resonance which occurs due to radiation pressure effects (see 3.4). The combination of these two effects leads to increased sensitivity at certain frequencies. The opto-mechanical peak frequency depends solely on the mass of the mirrors and the input laser power while the optical resonance frequency is the cavity pole of the combined ITMs–SRC cavity. The GW signal sideband is resonantly enhanced below this frequency.

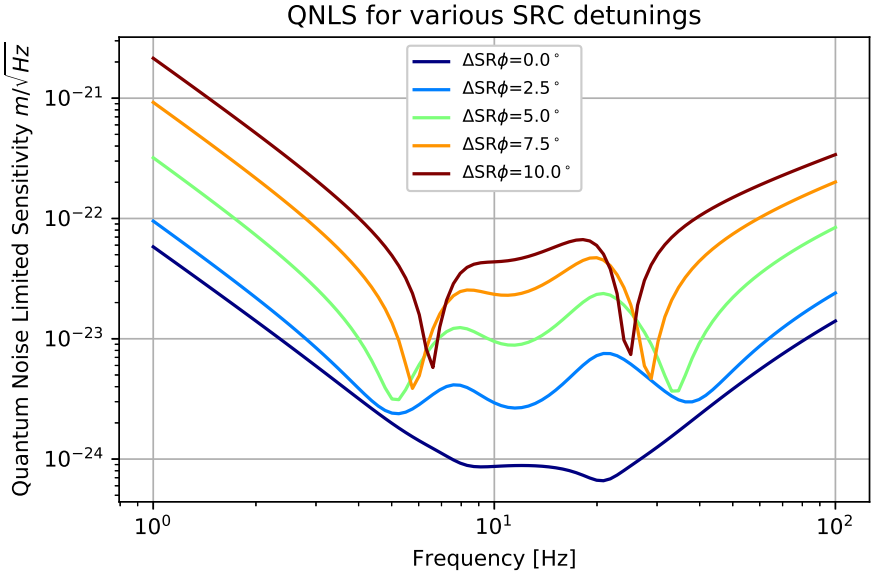

Figure 3.4: Quantum noise limited sensitivity as a function of additional detuning of the signal recycling cavity around its nominal design detuning (indicated by $\Delta SR_\phi = 0$). The readout phases and the filter cavity parameters are not optimised for the individual change in SRC phase.

At low frequencies, the coupling from the sideband imbalance due to detuning becomes a substantial effect in combination with dark fringe offset and was one of the main motivators to opt for BHD as opposed to the conventional DC-Readout (see section 6.4 for more details on the benefits of BHD for DARM readout).

Another important aspect to be noted here is the complexity of the parameter space while optimising the quantum noise limited sensitivity of the interferometer. While changing the

detuning changes the response function of the interferometer, not optimising the filter cavity parameters in conjecture with the homodyne readout angle leads to poor sensitivity at other detunings and the figure is indicative of the same.

Chapter 4

Length sensing and control of ET-LF

This chapter outlines my work on designing and modelling a realistic length sensing and control scheme for one interferometer of the low frequency part of the Einstein Telescope (ET-LF). For a GWD to remain at its peak sensitivity, the interferometer must be kept sufficiently close to its operating point, which is achieved by using a feed-back control system comprising of sensing signals, actuators, servos, etc. The required high sensitivity at low frequencies in combination with a detuned signal recycling cavity make the control problem for ET-LF challenging.

Numerical models are powerful, flexible and cheap tools for in the initial stages of designing a control system. The ET design study does not detail a sensing and control scheme for ET-LF. In section 4.1, I present the challenges in controlling ET-LF and a suitable sensing scheme overcoming the challenges. The shot noise limited displacement noise budget obtained for ET-LF shows that all the longitudinal dofs can be sensed and controlled individually and that ET-LF will be limited by quantum noise only in the observation bandwidth of ET-LF between 7 Hz and 32 Hz.

Details of the design process of the new sensing scheme are described in sections 4.2 and 4.3 and here we choose the modulation frequencies, Schnupp asymmetry, sensing signals etc. . These parameters are not mentioned in the ET design study but are quintessential for any control scheme to work.

In section 4.4 I introduce the principles of linear noise projection. This section also discusses a few components of a control loop such as the sensing matrix, output matrix. These components are important for the noise projection modelling described in section 4.5.

The error signals (obtained in section 4.3) are then used in the steady state control loop model, which is described in section 4.5. A feed-back control system is designed for all the longitudinal dofs to be controlled. This model is then used to project sensing noise from all the dofs into differential arm readout (DARM) to obtain the shot noise limited displacement noise budget for DARM.

In section 4.7, we show that the resulting noise projections from our ET-LF control model agree well with analytical estimations of the shot noise couplings from CARM, MICH, PRCL, and SRCL into DARM.

4.1 ET-LF sensing scheme: motivation and the new sensing scheme

4.1.1 The challenge

- None of the existing large scale detectors with Fabry-Perot arm cavities have been intentionally operated in the detuned regime. GEO 600 [42] is the only gravitational wave detector to have operated (2005 to 2009 [13]) with a detuned SRC [82]. However, in contrast to ET-LF, GEO 600 does not have Fabry-Perot arm cavities. Hence, a different control scheme is required for ET-LF control compared to GEO 600.

- The sensitivity of ET-LF ranges from 7 Hz to 35 Hz [12]. In its current planned DRFPMI configuration, the error signals obtained with existing techniques for the longitudinal control of ET-LF are degenerate i.e. they are highly coupled and cannot be sensed individually.

- In a frequency band of interest, maximal sensitivity can be achieved by maximising the signal to noise ratio (commonly called the SNR). If the optical gain of the signal is poor and the measurement noise associated with it is high, the measurement quantity is obscured by noise and cannot be measured effectively. Control noise which arises from imprinting

sensing noise on the feed-back signals of the different dofs is known to be high at low frequencies [83]. If this noise couples to DARM strongly and is not mitigated, this wold overwhelm the gravitational wave readout thus obscuring the gravitational wave signal.

- Normally, the control band of interferometers overlaps with the observation frequency band to a small extent for instance in aLIGO, the DARM control bandwidth is $\approxeq 50\,\mathrm{Hz}$ [37] and the observation band of aLIGO ranges from 30 Hz to a few kHz with peak sensitivity being achieved at 200 Hz [84]. This is done in order to not contaminate the observation band with control noise as this would degrade the strain sensitivity.

- In ET-LF, the observation band and the control band overlap. In order to judge if control noise arising from the longitudinal control of ET-LF would compromise the sensitivity of ET-LF, in this chapter we estimate the maximum tolerable sensing noise contamination from all the dofs into DARM.

4.1.2 Definitions of the longitudinal dofs in ET-LF

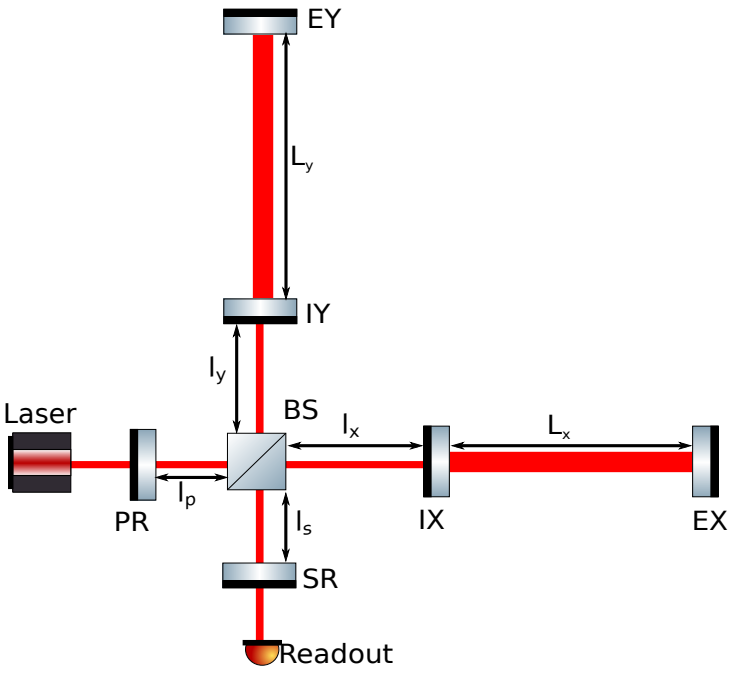

Figure 4.1: Simplified version of a DRFPMI to demonstrate the longitudinal dofs to be sensed and controlled to maintain resonance conditions inside the interferometer.

In an interferometer like ET-LF with a DRFPMI configuration, there are five length degrees of

freedom (figure 4.1) to control:

- CARM = $\frac{L_Y+L_X}{2}$: Common displacement of the arm cavity end mirrors and maintains interferometer carrier resonance conditions in the arm cavities.
- DARM = $\frac{L_Y-L_X}{2}$: Differential displacement of the arm cavity end mirrors (contains 'h' or the gravitational wave information).
- MICH = $l_Y - l_X$: Differential displacement of the arm cavities; determines the fringe condition at the dark port.
- PRCL = $l_P + \frac{l_Y+l_X}{2}$: Length change of the PRC; maximises the power coupled into the interferometer
- SRCL = $l_S + \frac{l_Y+l_X}{2}$: Length change of the SRC; resonance conditions of the SRC tune the interferometer response.

While we have followed the aVIRGO terminology [79], aLIGO defines the CARM and DARM dofs as [85]:

- CARM = $L_Y + L_X$
- DARM = $L_Y - L_X$

In case of a simple cavity, only one longitudinal degree of freedom, the cavity length, is to be sensed and controlled. In case of a simple Michelson interferometer, the differential arm length is the most important dof to be sensed and controlled. The common arm length is not as important. Adding additional mirrors such as power recycling, signal recycling, arm cavity mirrors raises the number of dofs to be sensed and controlled to a total of 5 (1 PRM + 1 SRM + 2 arm cavities + differential Michelson).

4.1.3 The old and new sensing scheme

Since DARM is the gravitational wave channel, it is the main focus when designing a length sensing and control scheme. For to maintain full sensitivity of the interferometer, the other

degrees of freedom (CARM, MICH, PRCL, SRCL) need to be well controlled with low noise signals with minimal coupling to DARM. Any residual motion of these dofs affects DARM owing to the optical coupling in the interferometer.

In the aLIGO sensing scheme [85], DARM is sensed using the DC readout scheme, CARM is sensed using the optical beat between the interferometer carrier and the modulation sideband which is resonant in the PRC (LIGO_$f_1 = 9\,\mathrm{MHz}$) at the sensing port in reflection of the PRC. PRCL and MICH are sensed at a pick off port in the PRC. PRCL is demodulated in-phase with the interferometer carrier at 9 MHz and the error signal for MICH is obtained by quadrature demodulation at 45 MHz (LIGO_f_2). For the SRCL, the error signal is obtained by demodulating at the beat frequency of LIGO_f_1 and LIGO_f_2 at the same port as CARM.

As a preliminary step in the design of a control scheme for ET-LF, the controllability of ET-LF was assessed with the aLIGO sensing scheme. The results of the same were presented in [86]. With this technique it was not possible to obtain decoupled error signals with high optical gain to independently sense and control all the five longitudinal dofs of ET-LF. The high degree of cross coupling made the diagonalisation of the control impossible.

In an effort to decouple these error signals, a new sensing scheme was proposed for ET-LF. This new sensing scheme requires the use of four phase modulation sidebands subject to different resonance conditions in the interferometer. The design choice of these modulation sidebands is explained in section 4.2. Three out of the four phase modulation sidebands are imprinted onto the laser carrier at the input port and are represented by f_1 (blue), f_2 (green), f_3 (bright green) in figures 4.4 and 4.2. A fourth pair of phase modulation sidebands (f_4, brown) are imprinted onto a sub-carrier ($f_{sub-carrier}$, purple) which is frequency shifted from the main interferometer laser. The sub-carrier and f_4 are injected into the interferometer through the dark port of the interferometer.

Conventionally, GWDs use only one output mode cleaner (OMC) in the interferometer output path. This OMC reflects all the modulations sidebands and allows only the interferometer carrier and GW signal sidebands (in case of DC readout) or only the signal sidebands (in case of BHD) to the GW readout port. We propose using a second OMC in reflection of the main OMC (additional OMC, in figure 4.2) to separate sub-carrier and f_4 from the f_1 and f_2 modulation sidebands.

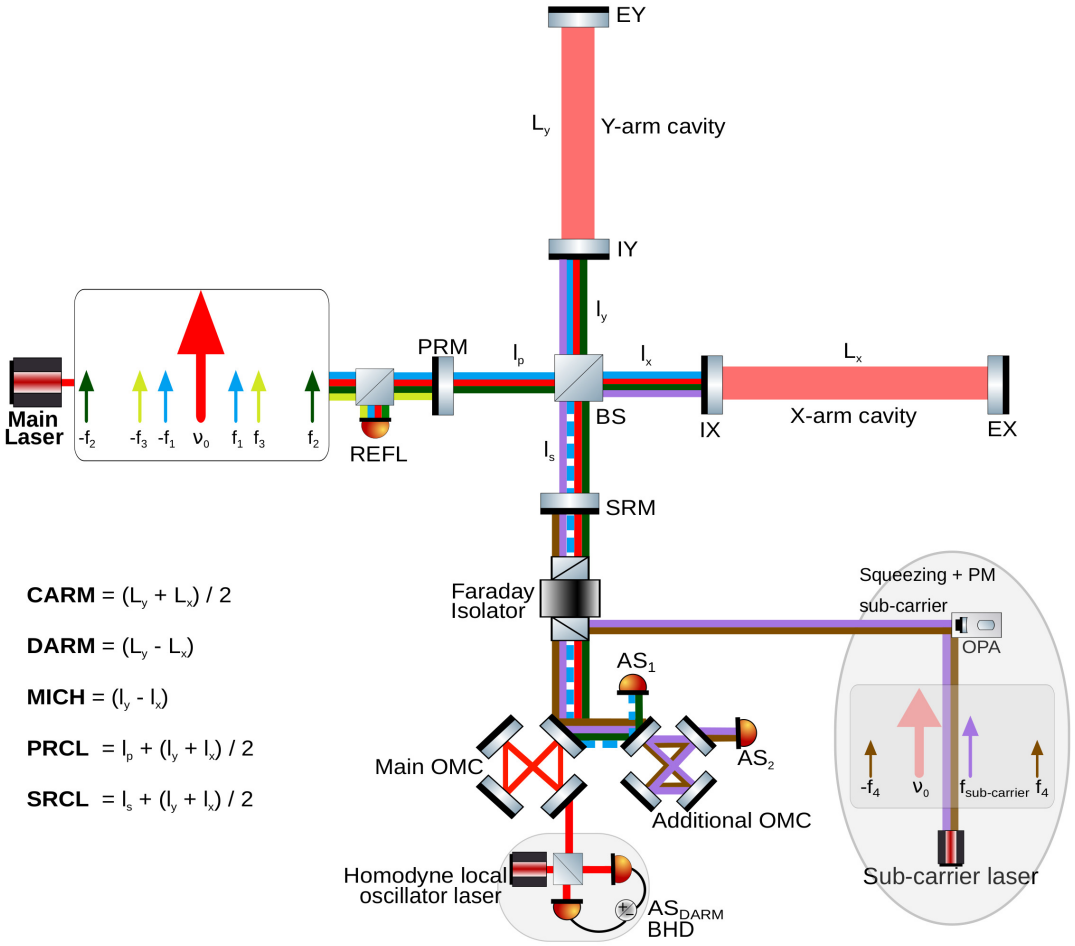

Figure 4.2: Layout of ET-LF where the sidebands are chosen such that the first modulation frequency (f_1: blue) is resonant in the power recycling cavity only and the second modulation frequency of 56.82 MHz (f_2: green) is resonant in both recycling cavities. A third modulation frequency which is not resonant in the interferometer i.e. it is reflected off the PRM, and shown in bright green(f_3). The Schnupp asymmetry is designed to allow the f_1 sidebands to leak into the SRC (dotted blue line). The sub-carrier ($f_{sub-carrier}$) is phase modulated before reflecting it off the OPA and is shown in purple together with its modulation sidebands (shown in brown (f_4)) enter the interferometer through the dark port. The port AS_1 is used for the detection of the MICH signal and AS_2 for the SRCL. The balanced homodyne readout will require an additional output mode cleaner to ensure that the local oscillator is not contaminated by higher order modes but for simplicity, this is not shown in the figure.

Both the sub-carrier and f_4 are transmitted by this additional OMC.

We also propose to use balanced homodyne readout (BHD) [87–89] for DARM. This technique is particularly beneficial for ET-LF as it eliminates the necessity of a dark fringe offset which is mandatory for DC readout. As a consequence of this, the noises that couple to the dark port due to asymmetry in the arms such as laser frequency noise, oscillator phase noise etc. do not cause

problems in ET-LF [90]. For the CARM and MICH error signals, we propose to use the beat between the interferometer carrier and f_1, the beat between f_2 and f_1 respectively.

Two important changes that we have chosen to make for PRCL and SRCL readout are :

- For PRCL, obtain the error signal by demodulating at the optical beat between f_2 and f_3.
- For SRCL, we demodulate at the beat frequency between the sub-carrier frequency and f_4.

The generation of the error signals and readout ports is explained in detail in section 4.3. The error signals are chosen to obtain high gain, decoupled error signals for the control of all dofs. This fundamental difference in the sensing of MICH, PRCL and SRCL between our proposed scheme and the current aLIGO scheme enables us to sense all five dofs individually with high optical gain.

Sensing noise is described in detail in section 2.5.2. It is a technical noise source that is always present in the strain sensing channel and is difficult to minimise. In the absence of technical noise on photodiodes (like photodiode dark noise, photodiode electronics noise), the contamination of the DARM signal by sensing noise from the control loops. The sensing noise associated with each degree of freedom primarily depends on the optical gain of its error signals.

Control loop noise is the noise which is imposed onto the feed-back signals due any noise created in the control loop that is converted to displacement noise by the feed-back loop. Here we only consider the shot noise of the light detected on the photodiode, assuming that we can keep technical noise below that level. A controller or a servo in the feed-back loop cannot distinguish sensing noise from actual disturbances of the plant e.g. seismic noise. As sensing noise only mimics displacements which do not correspond to actual mirror motion, the feed-back of the controller tries to compensate fake motion thereby introducing mirror motion. This sets a fundamental limit on the controlled mirror motion. See [91] for a mathematical derivation of the control loop noise.

Having obtained high gain error signals, a steady state closed feed-back loop system was setup using SimulinkNb to project the sensing noise of all dofs into DARM with linear noise projection techniques (see section 4.5) by making the assumption that we feed-back all the sensing noise with high gain to the mirrors. Figure 4.3 shows the shot noise limited displacement noise budget

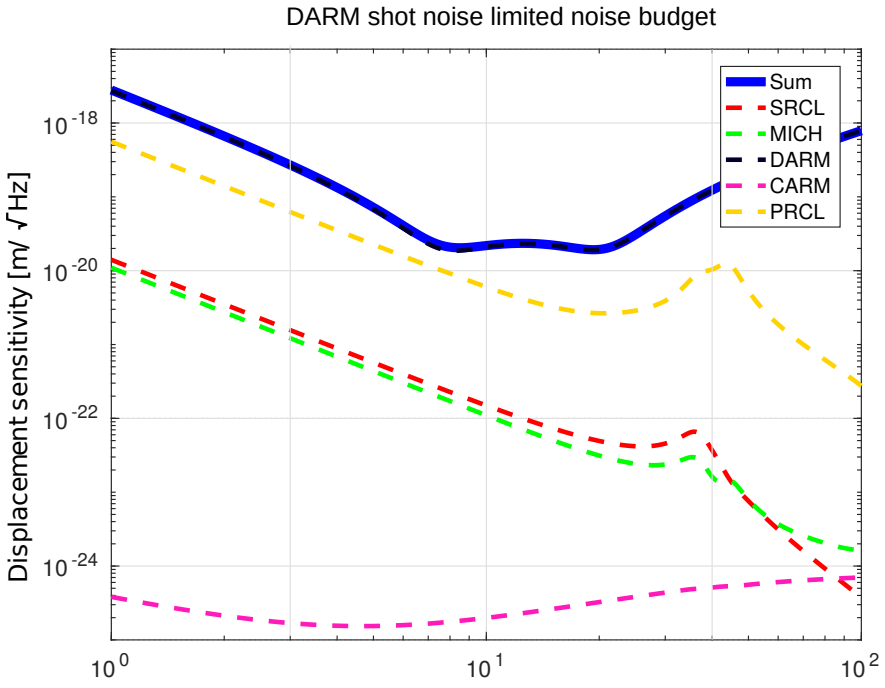

Figure 4.3: Quantum noise budget and the estimated sensing noise couplings from all the dofs into DARM. The blue solid curve is the uncorrelated sum of sensing noise from all the dofs. As we are shot noise limited by DARM alone, the total sum curve and the DARM shot noise curves overlap.

for DARM. It can be seen from this figure that the DARM readout port is shot noise limited by DARM only even if we were to imprint the respective sensing noise to all dofs in the whole observation frequency band of ET-LF.

4.2 Design choices for ET-LF length sensing and control

With FINESSE [92], a simulation model was setup for ET-LF using parameters from the design study [12]. This section describes the choice of the modulation frequencies and Schnupp asymmetry required for the sensing and modelling of ET-LF which are not mentioned in the design study. With information about these static lengths we also revisited the calculations for two already defined parameters: the power transmission of the power recycling mirror and the length of the signal recycling cavity (which had to be re-optimised).

4.2.1 Modulation sidebands: choice and constraints

The frequencies f_1 and f_2 are chosen such that f_1 is resonant in the PRC only and f_2 resonates in both PRC and SRC. In current GWDs, the phase modulated laser beam entering the interferometer is passed through an input mode cleaner/s to benefit from the spatial filtering effects of the mode cleaner/s [7]. For this reason we have placed an additional constraint on the modulation frequencies entering through the input port of the interferometer requiring them to be transmitted through mode cleaners [79]. The design of such mode cleaner/s has not been specified in the ET design study but our choice of modulation frequencies can pass through two mode cleaners having a linear length of 20.541 m and 21.1 m.

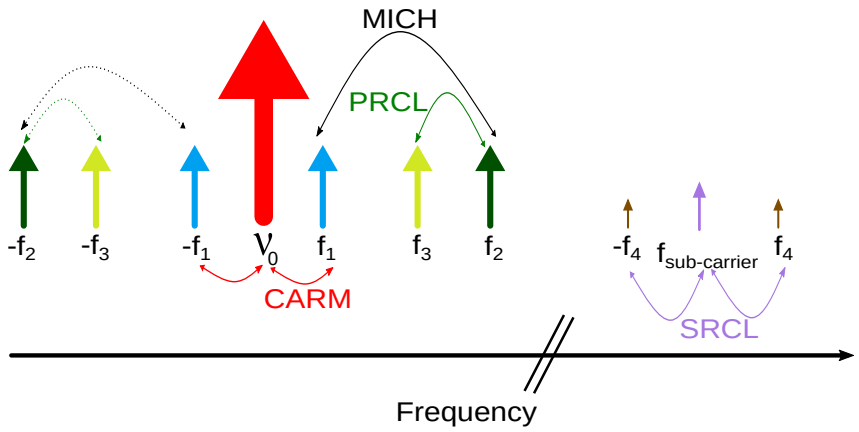

Figure 4.4: The frequency spectrum of input laser light with the auxiliary laser and including the chosen beat signals for the error signals for length control of CARM (solid red), PRCL (solid green), MICH (solid black) and SRCL (solid purple). For simplicity, we have only shown the first order beats of the modulation sidebands with the laser carrier. Some other possibilities of generating the same error signals but with the lower modulation sideband are shown in dashed lines. DARM (not mentioned in the figure) can be sensed via balanced homodyne (BHD) readout.

The FSR of the ET-LF recycling cavities for the length stated in the design study($L_{PRC} = L_{SRC} = 310\,\mathrm{m}$) is,

$$\mathrm{FSR_{PRC}} = \mathrm{FSR_{SRC}} = \frac{c}{2\,L_{PRC/SRC}} = 483\,536\,\mathrm{Hz} \tag{4.1}$$

To produce sidebands which resonate in the PRC (f_1) while not resonating in the arm cavities, we use a frequency which is a integer multiple of the FSR of the PRC i.e ,

$$\begin{aligned} f_1 &= (N) \times \mathrm{FSR_{PRC}}\ , \\ f_1 &\neq M \times \mathrm{FSR_{SRC}}\ , \end{aligned} \tag{4.2}$$

where N and M are positive integers.

Using these conditions, the f_1 sideband frequency was determined to be 11.36 MHz. f_2 was chosen to be a multiple (5 times) of f_1 and resonant in both the recycling cavities [63, 85]. In the case of aLIGO, this choice led to a lower coupling of sensing noise from MICH control to DARM and as we started developing a sensing scheme for ET-LF using the aLIGO sensing scheme, we have used a similar condition for f_2. Thus for f_2,

$$f_2 = 5 \times f_1 \ , \tag{4.3}$$

The FSR of the ET-LF arm cavities is

$$\mathrm{FSR_{Arm}} = \frac{c}{2\,L_{Arm}} = 14\,990\,\mathrm{Hz} \ , \tag{4.4}$$

where c is the speed of light and L_{Arm} is the arm-cavity length.

From equations 4.2, 4.3 and 4.4 we can conclude that if we were to choose an odd multiple of half the FSR of the arm cavities, the f_1 and f_2 sidebands can be made anti-resonant in the arm cavities. However, the linewidth of the arm cavities of ET-LF (which have a finesse of 880) is 17 Hz. Due to this, the higher order harmonics of the modulation sideband (see appendix B) might become resonant in the arm cavities. This can be prevented by adding an additional constraint on the modulation sidebands,

$$f_{1,2} = (N + 0.5 + x) \times \mathrm{FSR_{Arm}} \ , \tag{4.5}$$

where, $|x|$ is $\ll \frac{1}{2}$ and N is an positive integer.

The f_1 sideband leaks into the SRC (dashed blue lines in figure 4.2) via the Schnupp asymmetry [93] (see section 4.2.2) which has been optimised to maximise the transmission of f_2 over f_1 to the SRC. The f_3 and f_4 sidebands are off-resonant in PRC and SRC respectively. While f_3 is injected through the input port of the interferometer, f_4 is injected through the output port together with a frequency shifted carrier of an additional laser (henceforth called sub-carrier).

Parameters	ET-LF	Power at BHD
f_1	11.36 MHz	6.58 nW
f_2	56.82 MHz	20.33 μW
f_3	25.19 MHz	0
f_4	15 MHz	14.73 nW
$f_{sub-carrier}$	1.72 GHz	22.50 μW
P_{in}	3 W	0
$P_{sub-carrier}$	0.2 W	
L_{cav}	10 km	
L_{src}	311.58 m	
L_{prc}	310 m	

Table 4.1: Modulation frequencies and lengths of the recycling cavities and arms. The table also shows the single sideband power in the modulation sidebands at the photodiode used to measure DARM.

The sub-carrier frequency is chosen such that it is resonant in the detuned SRC only i.e. it is a integer multiple of the FSR of the SRC (see equations 4.1, 4.2). For a detector like ET-LF, which would use squeezing to improve the quantum noise limited sensitivity of the interferometer, the injected sub-carrier should not compromise the squeezed states. Also, phase modulation of the sub-carrier with f_4 must occur before the squeezing as phase modulators are notorious sources of noise [94] and squeezed states are very sensitive to phase noise [95].

In section 7.6 and 7.7, a description of the process of imprinting the sub-carrier and f_4 onto the squeezed states and how to remove it before GW readout is provided. For now, it can be assumed that it is desirable to inject the phase modulated sub-carrier such that it is reflected off the cavity (OPA cavity) that produces the squeezed states. The bandwidth of this OPA cavity is generally about 100 MHz [96] and the sub-carrier frequency that would have to be well outside the bandwidth of the OPA cavity. The output mode cleaner which is used to filter out all the modulation sidebands (called main OMC in figure 4.2) also has a bandwidth of 0.3 MHz [7]. In order to prevent contamination of the DARM readout, the sub-carrier must also be outside the bandwidth of the OMC such that it is reflected off the OMC.

Conventionally, only modulation frequencies between 10 MHz and 100 MHz have been used for sensing purposes in GWDs [63]. Frequencies in the GHz regime have not been used for sensing interferometer dofs. However the current generation of signal generators, for instance the signal generators from Rohde and Schwarz [97], can be used to produce frequency shifted sub-carriers

with low single sideband phase noise. The sub-carrier can be generated using an additional laser which is phase locked to the main interferometer laser and then frequency shifted using the signal generator to the desired frequency.

For these reasons, our chosen sub-carrier frequency offset, $f_{sub-carrier}$ is 1.72 GHz and the resonance conditions in the interferometer along with the resonance conditions for f_4 are plotted in figures 4.5a and 4.5b respectively.

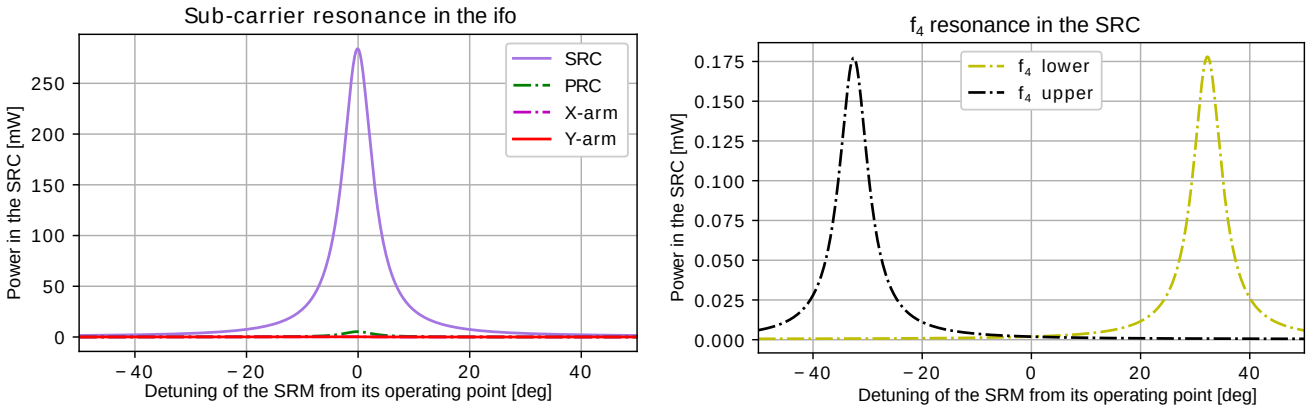

(a) (b)

Figure 4.5: a) Resonance conditions of the sub-carrier in the detuned SRC. The detuning of the SRC for ET-LF is shown by the dashed black line. The 108°detuning of the SRM in FINESSE corresponds to detuning frequency of 25 Hz b) Resonance conditions for upper and lower first order phase modulation sideband f_4 in the SRC

It can be seen from the above figures that while the Schnupp asymmetry allows for f_1 and f_2 to leak into SRC, it also allows a small amount of the sub-carrier also leaks into the PRC. This is not a problem because the ratio of the resonant power of the sub-carrier in the SRC to the PRC is very high.

We have made the assumption that all the modulation frequencies are phase modulated with a modulation depth of 0.1 rad. With this, it was possible to achieve a reasonable amount of power in the modulation sidebands (to the first order) without comprising the power in the interferometer carrier. This parameter is subject ot change during the technical design phase of ET-LF. All the chosen modulation frequencies and the power levels of the sidebands at the photodiode used to sense DARM i.e the power contribution of the sidebands to the shot noise on the DARM photodiode (BHD) are illustrated in Table 4.1.

4.2.2 Schnupp Asymmetry: requirements and choice

To obtain maximal benefit from PRM and SRM a DRFPMI interferometer is typically tuned to dark fringe. For an equal arm length interferometer, this means that the dark port is dark for all frequencies. To obtain error signals for e.g MICH, SRCL control, Lise Schnupp proposed [93] adding an intentional macroscopic length offset to the inner Michelson or MICH. This implies a deviation from the dark fringe condition for the sidebands while maintaining the dark fringe condition for the carrier light. The difference in the lengths of the arms of the Michelson is called the 'Schnupp asymmetry' [93].

Figure 4.6 shows an exaggerated length difference between the X and Y arms of the inner Michelson interferometer.

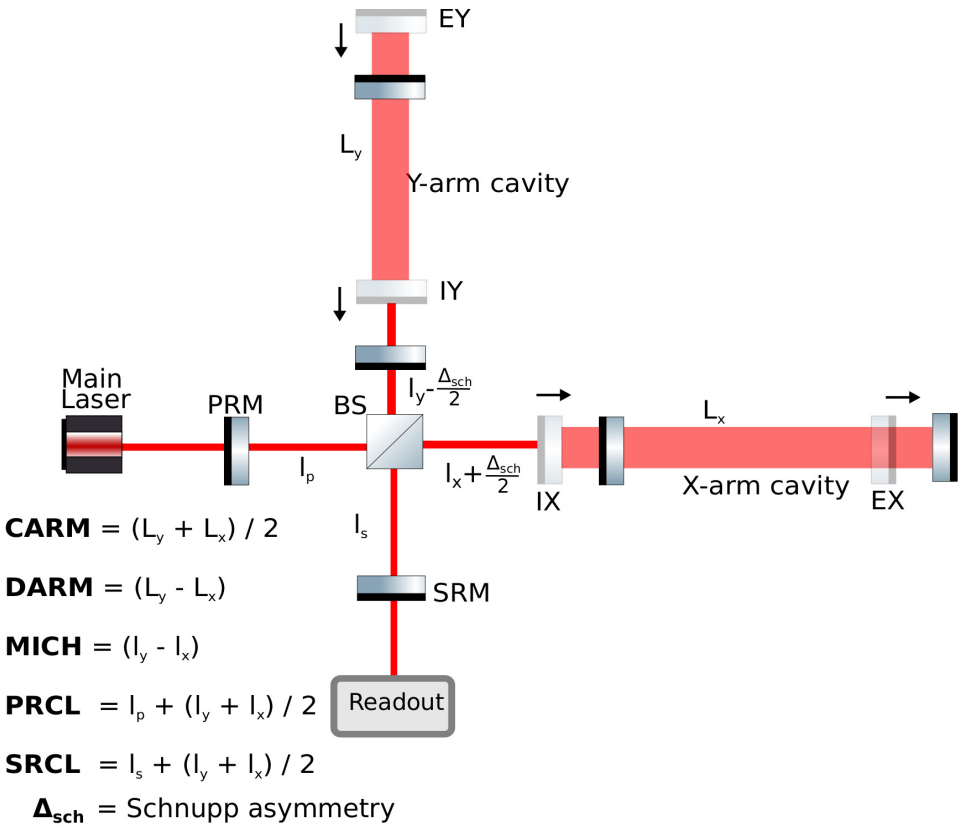

Figure 4.6: The figure above is an exaggeration of the Schnupp asymmetry (black arrows) which is a macroscopic length difference between the arms of the inner Michelson interferometer (MICH) which renders the output port 'not dark' for the modulation sidebands. The symmetric positions of the mirrors (without Schnupp asymmetry) is represented by faded optics.

With the Michelson tuned to the dark fringe for the laser carrier, and given a Schnupp asymmetry of l_{schn} (in units of meters), the amplitude transmission of sidebands (t_{schn}) from the interferometer input to the 'dark port' is

$$t_{schn} = \sin(2\pi\ (f_{rf}/c\, l_{schn})\ , \tag{4.6}$$

where f_{rf} is the frequency of the modulation sideband transmitted to the dark port. From this equation it is possible to calculate the optimal Schnupp asymmetry for a known modulation frequency.

In order to choose a Schnupp asymmetry for ET-LF (this parameter is not optimised in the design study), a plot (see figure 4.7) of the sideband power in the SRC and PRC was made as a function of the Schnupp asymmetry. The solid blue and solid green lines are the resonance conditions of the f_1 and f_2 sidebands in the SRC. The dashed lines show the resonance of f_1 and f_2 in the PRC. The objective of choosing the 4 cm of Schnupp asymmetry (in each arm; shown by the black dotted line) was to maximise the ratio between the powers of the second and first sideband in the SRC. A large Schnupp asymmetry makes the f_1 sideband resonant in the SRC. A practical advantage is that a small Schnupp asymmetry also has lower laser frequency noise coupling to 'h' [85]. A larger Schnupp asymmetry would allow both f_1 and f_2 to be resonant. A control scheme with this condition has been simulated for the sensing and control of the longitudinal dofs in KAGRA [10].

4.2.3 Signal Recycling Cavity Length : change from the design study

Having made the choice where $f_2 = 5\, f_1$ and knowing that the f_1 is resonant in the PRC only, the length of the SRC had to be optimised such the f_2 was resonant in the SRC. Figure 4.8 shows the power in each sideband in the SRC versus SRCL. The black dashed line indicates that our choice of l_s .

The (300+11.58) m ($\frac{l_x+l_y}{2}+l_s$) was found to be more suitable than the baseline design of (300+10) m. It can be seen from the figure 4.8 that at our chosen length, the f_2 sideband is resonantly enhanced in the SRC and at the same length, f_1 is non-resonant. The ratio between the sideband powers at $l_s = 11.585$ m is 673.

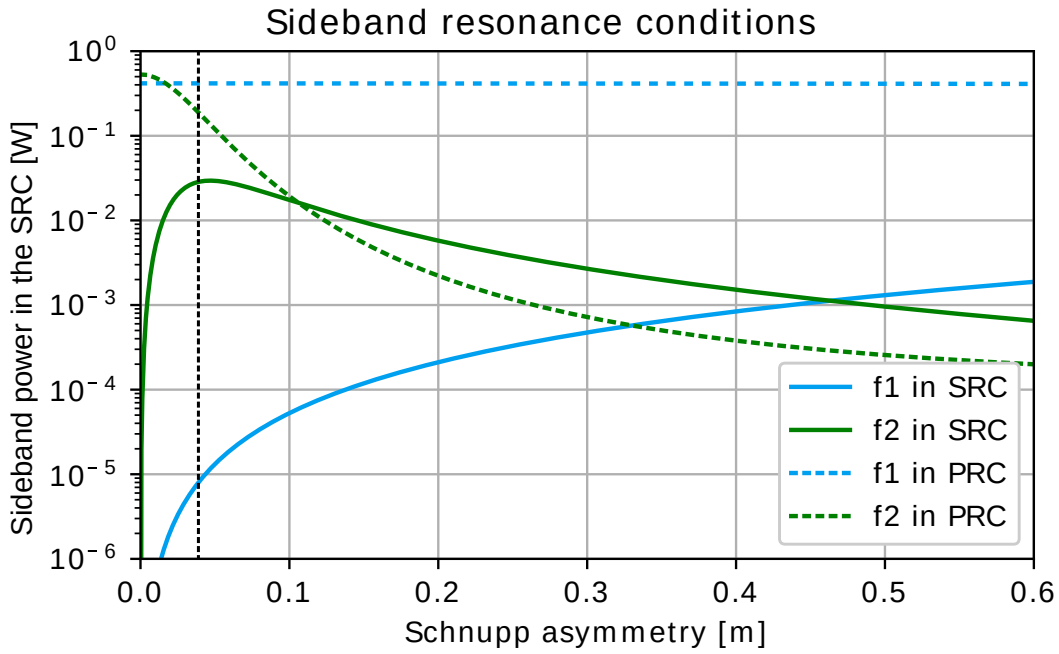

Figure 4.7: The power in the modulation sidebands injected through the input port of the interferometer in the PRC and SRC as a function of Schnupp asymmetry. For small asymmetries, f_2 is coupled into the SRC preferentially over f_1. As f_3 is reflected off the PRM, there is a very small amount this frequency present in the SRC in comparison to the other two modulation sidebands. Our choice of asymmetry (4 cm) is shown by dashed black lines. The ratio of the sideband powers of f_2 and f_1 is 2900.

4.2.4 Impedance matching of the PRC

The power recycling mirror (PRM in figure 4.2) is placed at the input port of the interferometer to increase the amount of the laser carrier in the interferometer. The transmission of this mirror in combination with the losses in the interferometer determines the amount of light reflected back to the laser. The condition in which the losses in the interferometer match the transmission of the PRM, thus leading to a minimal amount of light reflected back towards the laser, is called impedance matching. In order to keep the PRC critically coupled to the interferometer, the ET-LF design study sets the value of the transmission of the PRM to be 4.6%. The plot 4.9 shown below is affirmative of the choice of the transmission of the PRM presented in the design study. The end test masses (ETMs: EX and EY), have a loss of 6 ppm per ETM optic and all the other optics in the model have been assigned a loss of 35 ppm each. The undesirable effect of having an under coupled PRC is discussed in section 7.4.

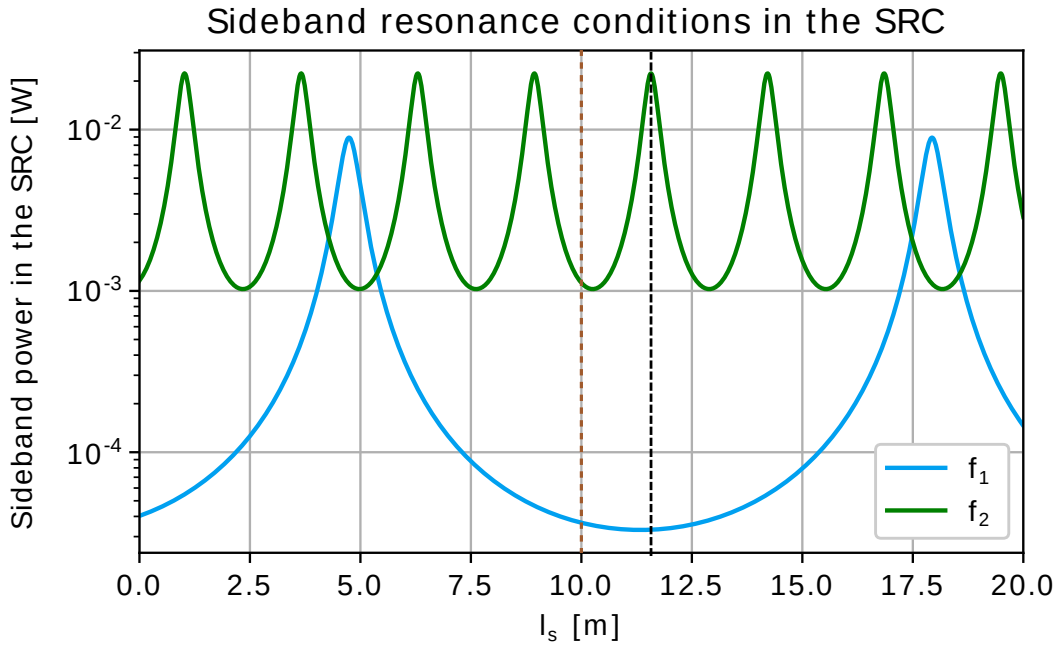

Figure 4.8: The power in the modulation sidebands f_1 and f_2 in the SRC as a function of SRCL (in the figure we have only varied l_s). The black dashed line shows the choice of SRCL used for this study. The design study value for l_s is shown by brown dashed lines.

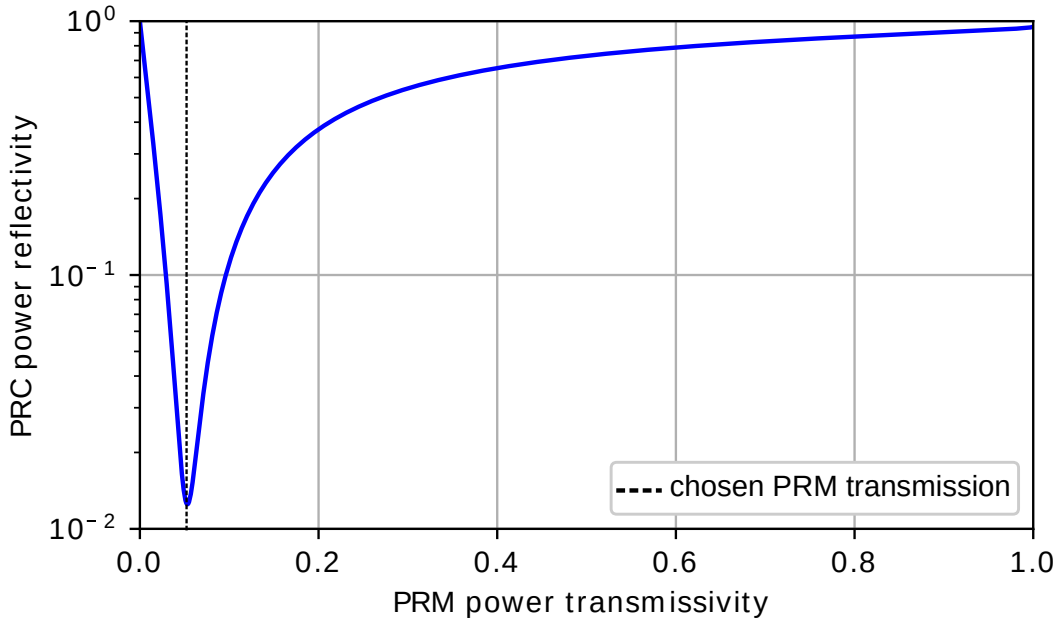

Figure 4.9: Reflected power in the common port of the interferometer for ET-LF as a function of PRM transmissivity. The change in transmission changes the impedance matching of the PRC to the interferometer and for the existing set of parameters (taken from the design study [12]), the aforementioned PRM transmission is the most optimal one.

4.3 Error signal generation and sensing

Lock acquistion is the process of bringing the interferometer from an uncontrolled state (free swinging) to the operating point. For all our simulations we have assumed that the interferometer optics are not free swinging and are around the operating point. A length sensing and control (LSC) loop keeps the interferometer at this operating point. To do so, the control system requires error signals which are a measure of the deviation of a dof from it's operating point. This section describes the sensing ports in the interferometer and also the error signals that can be obtained at these detection ports. The error signals that we have chosen have been optimised for a high signal to noise ratio while minimising the cross-coupling between the dofs.

4.3.1 Readout ports in ET-LF

The main readout ports included in our ET-LF model to measure the error signal are shown in figure 4.2 and are listed below:

- REFL: in reflection of the PRC (AR surface of the PRM). In a realistic setup, this signal can also be derived in reflection of the faraday isolator in the input path of the laser (before it enters the PRC [63]) that would be in place in order to protect the laser from the light reflected back by the interferometer (in particular the carrier). The laser carrier, f_1, f_2, f_3 frequencies are available at this port.

- AS_1: This port is in reflection of the additional OMC (see figure 4.2). The main OMC is designed to only let the carrier pass and to reject all the modulation sidebands. The additional OMC which is placed in reflection of the main OMC, is designed to transmit the only the sub-carrier and f_4 frequencies. The modulation frequencies f_1 and f_2 are available at the sensing port, AS_1.

- AS_2: This port is sensitive to the dofs sensed by the sub-carrier and f_4.

- AS_{DARM} (BHD): This is the 'main' output port of the interferometer and is used for sensing DARM.

Port	Signal	demodulation frequency
REFL	REFL I/Q_1	11.36 MHz
	REFL I/Q_2	56.82 MHz
	REFL I/Q_3	25.19 MHz
	REFL $f_1 f_3$	36.55 MHz
	REFL $f_2 f_3$	82.00 MHz
AS_1	AS_1_$f_2 f_1$	68.17 MHz
AS_2	AS_2_SR	15.00 MHz
BHD	-	-

Table 4.2: Signals measured at each port, with the corresponding demodulation signal. REFL I/$Q_{1,2,3}$ indicate the optical beat between the main interferometer carrier and the modulation sidebands f_1, f_2 and f_3. REFL $f_{1,2}f_3$ refer to the beat signal between the sidebands $f_{1,2}$ and f_3. While it is possible to detect a signal at the sum and difference frequencies of the sidebands, we have only presented the signal obtained from the sum frequencies. Similarly, AS_1_$f_2 f_1$ is the signal obtained at the sum frequency of f_2 and f_1 sidebands. AS_2_SR is however the only signal that uses f_4 and the sub-carrier as opposed to the main interferometer carrier and is sensed at port AS_2.

4.3.2 Generating decoupled error signals in ET-LF

An error signal is an output from the interferometer that can be used to stabilise and control a particular parameter of the system. Error signals in our case are demodulated photodiode outputs (see PDH locking in section 2.4 and appendix B) which are used to control the lengths of the cavities so that they are at the desired operating point. Two main requirements for an error signal are:

- the presence of a zero crossing at the operating point
- Existence of a linear range around the zero crossing

For all error signals (including DC readout signals), there exists a linear regime around the operating point. However, the linear range around the operating point depends on the finesse of the cavity being controlled and is on the order of the line-width of the cavity. If the cavity has a rather high finesse (like the arm cavities), the linear range is rather small and if the cavities have a moderate finesse (like PRC), the linear regime around the operating point is comparatively larger.

On a photodiode (PD) used for sensing the error signal, the total power (P_{det}) detected can be

calculated by

$$P_{det} \propto \underbrace{|a_c|^2}_{\text{large at } \nu_0} + \underbrace{|a_{sb}|^2}_{\text{small}}, \tag{4.7}$$

where a_c and a_{sb} are the complex amplitude of the carrier field (ν_0) and the modulation sideband (f_{sb}) at the detection photodiode (P_{det}). P_{det} is sensitive to a phase difference between a_c and a_{sb}.

At the input port of the interferometer, the phase of the reflected carrier light is dominated by the CARM dof in carrier reflection. The phase of the carrier light transmitted to the dark port is dominated by the DARM dof. Conventionally, error signals for the PRCL, MICH and SRCL dofs are obtained by taking the optical beat of the carrier light with the sideband frequencies or by taking the beat between the modulation sidebands.

The REFL port senses the f_1, f_2, f_3 sidebands, and the interferometer carrier (see figure 4.2). The error signal obtained at this port by demodulating at f_1 contains phase information from the common arm length mismatches. However, the f_1 sideband contains information about the length fluctuations of the PRCL, SRCL and MICH. Owing to the high finesse of the arm cavities, the error signal obtained by demodulating at f_1 is largely dominated by the CARM dof (because the carrier phase shift is enhanced by the arm cavity finesse; see equation 4.4).

The f_2 and f_1 modulation sidebands are resonant in the PRC and thus they are sensitive to changes in PRCL to a similar extent. f_3 however is not resonant in the PRC but is reflected off the PRM. Thus by demodulating at the beat frequency (here we look at the sum frequencies) of either f_3 and f_1 or f_3 and f_2, we obtain a PDH like error signal for PRCL. We have chosen to use the error signal obtained by taking the beat between f_3 and f_2 because of the higher optical gain of the error signal. The higher optical gain is a consequence of the higher modulation frequency. Such a scheme of sensing a dof by taking the beat between the modulation sidebands is called double demodulation and is described in detail in [98].

The dark port ($\mathrm{AS_{DARM}}$, $\mathrm{AS_1}$, $\mathrm{AS_2}$) senses DARM, MICH and SRCL (and also CARM and PRCL to a small extent). It is however, largely dominated by DARM owing to this error signal being enhanced by the arm cavity finesse. For DARM, we propose using balanced homodyne readout [89] at port $\mathrm{AS_{DARM}}$. It has been favored over the conventional DC readout as the power imbalance in the arms due to the dark fringe offset would cause an increased coupling of MICH

and SRCL in DARM at low frequencies [90].

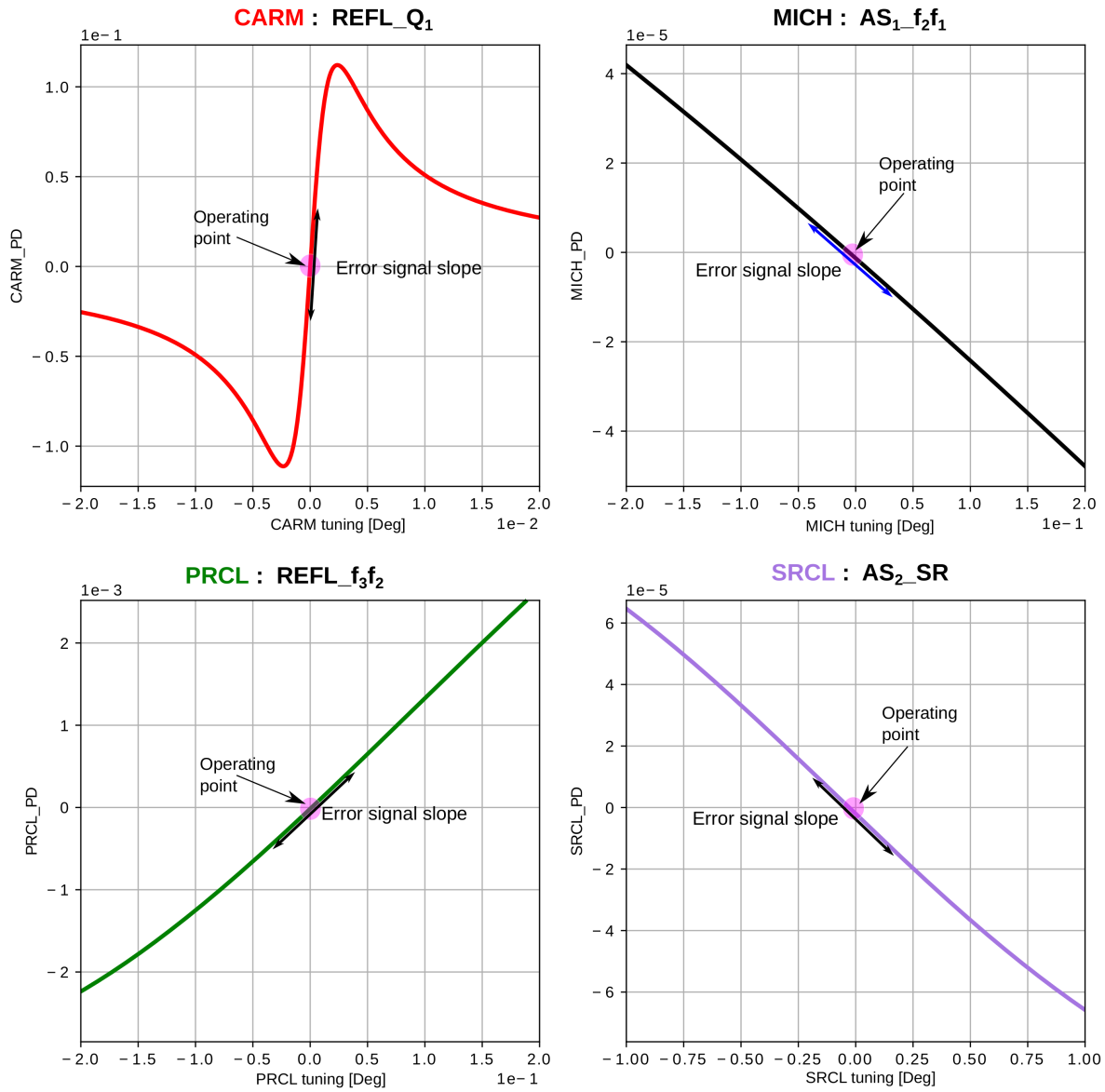

Figure 4.10: Error signals for CARM, MICH, PRCL and SRCL control. The error signal for CARM is sensed at REFL, MICH at AS_1, PRCL at REFL and SRCL at AS_1 (from figure 4.2). The CARM dof which is an arm cavity dof, has the steepest slope owing to its large finesse of the arm cavities and by consequence the smallest linear locking range.

MICH can be sensed at the AS_1 port by demodulating at the beat frequency between f_2 and f_1. f_2 and f_1 are transmitted to the dark port through the Schnupp asymmetry and is thus present at port AS_1 . The difference in frequency between f_1 and f_2 allows us the sidebands to pick up information about the MICH length changes differently. Thus by demodulating at the optical beat frequency between f_1 and f_2, we can obtain we obtain a PDH-like error signal for MICH

control which is not dominated by DARM as neither of the sidebands are resonant in the arm cavities.

The SRCL error signal is overwhelmed by other dofs if we were to use conventional readout techniques [86] owing to the poor finesse of the SRC. To obtain an independent, PDH style error signal for SRCL control (which has a high optical gain), we would require a situation similar to the error signal of PRCL. If a independent phase modulated laser beam were to be injected through the dark port as the main phase modulated laser (shown in red in figure 4.2) such that the phase modulation sidebands are not resonant in the SRC, an error signal for the SRC independent of the other dofs in the interferometer can be obtained. To do so, a phase modulated frequency shifted sub-carrier was injected through the dark port. The sub-carrier is sensitive to changes in SRCL and a PDH error signal can be obtained for SRCL control by demodulating at f_4. Although a simplified version of the new sensing scheme is shown in Figure 4.2, an elaborate explanation of the injection methodology of the sub-carrier and the off-resonant f_4 modulation sidebands is described from the perspective of GEO 600, a GWD with a DRMI configuration in sections 7.6 and 7.7.

4.3.3 Susceptibility of the new SRCL error signal to demodulation phase change

For SRCL control, as mentioned earlier, we have investigated the benefits of both the conventional aLIGO style error signal (conventional error signal) and the error signal obtained by taking the beat between the sub-carrier and f_4 ('new' error signal). The conventional SRCL error signal is obtained by taking the optical beat between f_2 and f_1 at the REFL port (see section 5.4.2 and figure 4.2). The demodulation phase is dependent on a number of parameters like cable length, temperature etc. and cannot be controlled better than 1° [32]. For this reason, it would be advisable to have signals that are not susceptible to changes in demodulation phase to a few degrees.

The conventional error signal (see figure 4.11a) for SRCL is more susceptible to demodulation phase changes in comparison to the 'new' error signal (see figure 4.11b). It must also be noted here that the error signal obtained by the conventional technique is offset from the operating

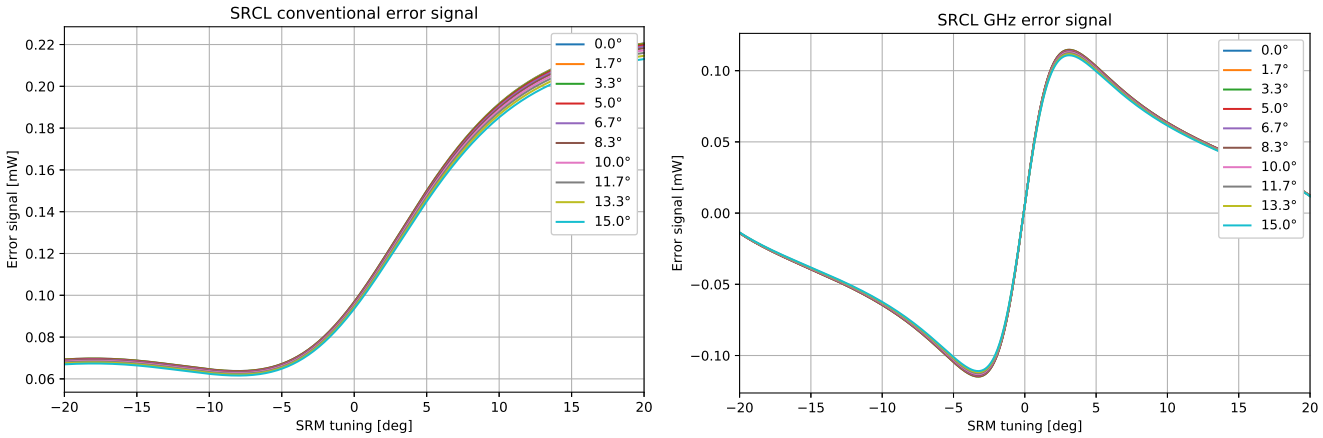

(a) Conventional SRCL signal

(b) 'New' SRCL signal

Figure 4.11: a) SRCL error signal: using aLIGO style sensing b) SRCL error signal: sensed using the sub-carrier. The legend in both plots indicates the change in demodulation phase (in degrees) of the readout photodiode. It must be noted that the conventional SRCL error signal is offset from the operating point of the interferometer owing to the detuning of the SRC.

point of the interferometer due to the detuning on the SRM in ET-LF. As the sub-carrier is frequency shifted resonant in the detuned SRC specifically, the new error signal does not suffer from any offsets.

4.4 Linear noise projection techniques and control loop elements

In the absence of feed-back control, displacement noises like seismic noise, suspension thermal noise etc. cause a displacement of the mirrors from, the required operation points. In the simulations for ET-LF, the focus is entirely on one such displacement noise source, the sensing noise.

Sensing noise is the sum of both the shot noise and technical noise for e.g. electronic noise from the photodiode used for power detection. The level of sensing noise is affected by the light power incident on the photodiode, the readout scheme used, the modulation frequencies used etc. This sensing noise is imposed onto the feed-back signals in the form of control loop noise causing the controlled mirrors to move. For these reasons, the sensing noise can be discussed as the shot noise limited displacement noise. If the optical parameters in the interferometer were to change, the sensing noise calculations in this chapter would also have to be re-calculated.

This section details the linear noise projection technique and a few control loop components to

make a shot noise limited displacement noise budget for one interferometer of ET-LF.

4.4.1 The technique of linear noise projection

Laser interferometers and sensors in general are non linear devices [99]. However, as discussed in section 4.3.2 around the operating point of the interferometer, there exists a linear regime where the interferometer output can be approximated to a linear system. As control systems keep the interferometer close to the operating point, we can justify the use of linear noise projection techniques for determining the limiting noise source in a given frequency band. This technique enables us to estimate the influence e.g. of technical noises coupling into the detector output and finally into the science signal [34]. A noise projection is not a mathematical projection, but instead a mapping of a given signal using a transfer function from the point of injection to the readout [100].

In a second generation GWD like aLIGO, over 300 control loops are required to keep all subsystems at their operating points [101]. Control noise associated with these loops that arises from sensing and feed-back of the actuators, if not designed carefully, affects the science signal. Projecting the control noise to the science signal readout allows us to estimate whether this noise would lead to a degradation of the strain sensitivity. If it would, we could employ techniques to mitigate the limiting noise source. One such technique would be the angle-to-length decoupling in aLIGO (A2L) where the control noise from the loops that maintain the angular positions of the core optics is cancelled from the DARM readout [27].

4.4.2 Sensing matrix

A sensing matrix is a measure of how much of each dof shows up on the measurement sensor or PD. Every element of the sensing matrix gives the optical gain of the error signal in W/m which is a measure of the deviation of a dof from its operating point. It indicates much of each dof shows up on every sensor. In the ideal case, each sensor is only sensitive to a single dof i.e. the sensing matrix is diagonal.

In practice however, the sensing matrix has cross coupling terms. For example, MICH and DARM

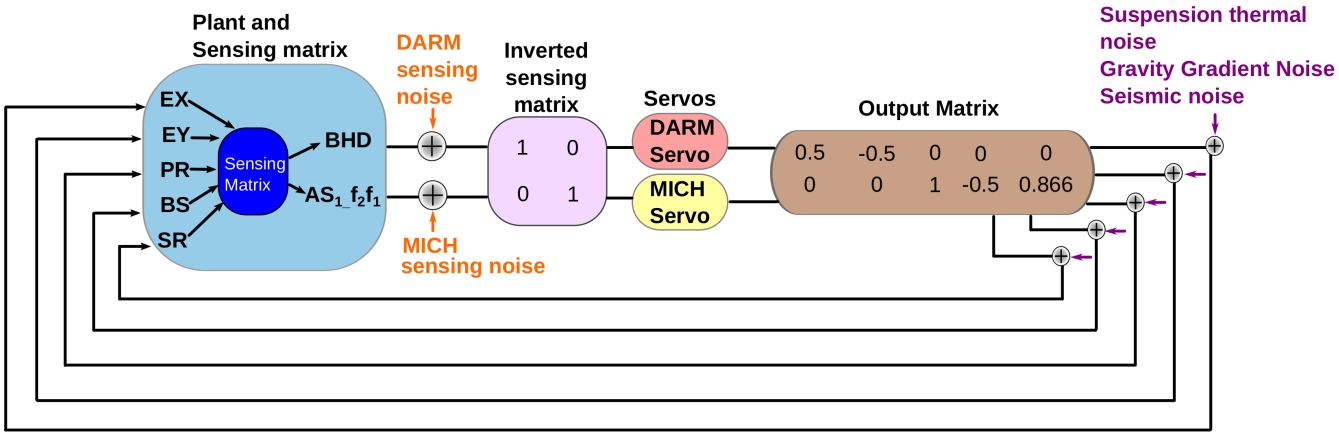

Figure 4.12: Skeletal control loop showing the MICH and DARM dofs. The plant consists of all the transfer functions from mirror motion to the sensor/photodiode. The sensing matrix accounts for the cross-couplings in the optical system. The servos are frequency dependent transfer functions required to shape the control loop response. The output matrix converts the DoFs to an optic basis thus completing the feed-back loop.

are both caused by ITM displacements with the difference being, DARM is enhanced by the arm cavity finesse. By obtaining the error signals as mentioned in section 4.3.2, it was possible to obtain a sensing matrix with high optical gains for the individual degrees of freedom and negligible off-diagonal terms which describe the cross cross-couplings.

Each element of the sensing matrix (M) is the optical gain of a given signal in the signal vector $\overrightarrow{S}$ in units of W/m with respect to the corresponding motion of a degree of freedom $\overrightarrow{L}$.

$$\overrightarrow{S} = M\ \overrightarrow{L}\ , \tag{4.8}$$

where, M is called the sensing matrix.

The table in figure 4.13 suggests the sensing matrix to be diagonal. However, the graphs in the same figure are representative of a realistic sensing matrix and shows us the optical cross-coupling between the dofs. Upon obtaining this sensing matrix, the desired dofs can be obtained by applying the inverse of the matrix (and is shown by the block inverted sensing matrix in figure 4.13).

This cross-coupling between the dofs is frequency dependent, so an idealised sensing matrix as indicated in the figure would only diagonalise the system at one frequency. In the modelling of ET-LF, a frequency dependent sensing matrix has been used. In case of the old sensing scheme,

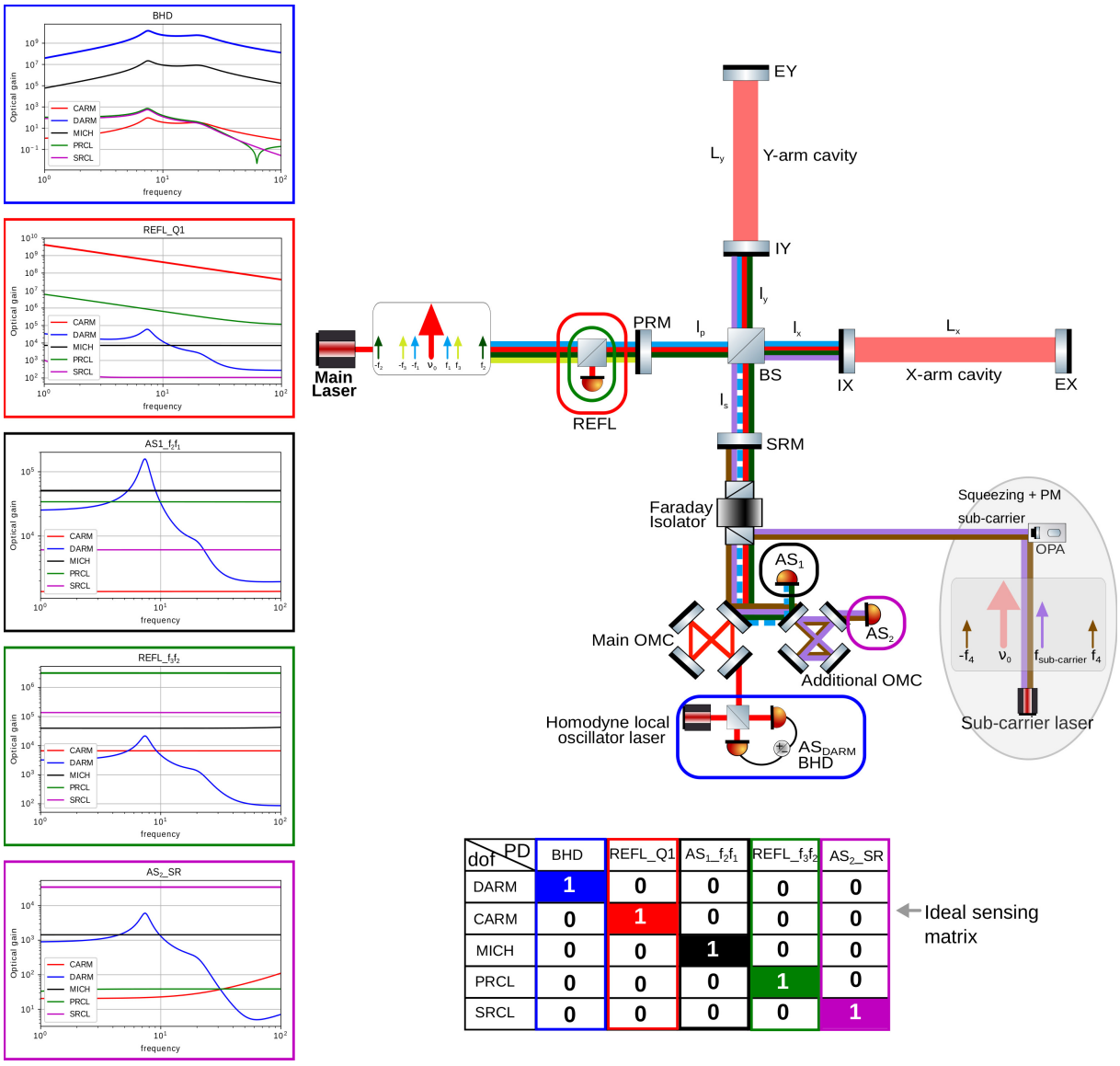

Figure 4.13: The graphical representation of the normalised sensing matrix highlights the error signals chosen to sense the different longitudinal dofs of the interferometer. For example, DARM which is sensed at BHD (AS_{DARM}) has the largest optical gain at that sensing port dominating the other dofs by more than an order of magnitude. While the ideal sensing matrix here suggests the off-diagonal elements to be zero, the graphs show the existence of cross-coupling between the dofs.

the inverted sensing matrix had large off-diagonal elements which would all have to be cancelled via feed-forward techniques with precision. With the new sensing scheme proposed in section 4.1.3, the off-diagonal terms of the sensing matrix have been minimised. For this reason, we use a diagonal inverted sensing matrix. Including the off-diagonal elements in the present ET-LF sensing model would only improve the separation between the error signals and lower the sensing noise contribution from the cross-couplings dofs.

The coloured boxes around the detection ports are indicative of the dof sensed at that port. For instance, CARM (red box) is sensed at the REFL. The frequency dependent entries in the sensing matrix for the REFL port are shown by the transfer functions in the red box. The error signal for CARM is obtained by demodulating the electric fields at the sensing port 'REFL' at the beat frequency of the interferometer carrier and f_1. The '1' in REFL_Q1 is indicative of the modulation frequency used for demodulation (f_1). The error signals can be read out inphase (I) or quadrature (Q) (see appendix B).

The following table explains the titles of the other plots:

Name	Meaning
BHD	DARM; balanced homodyne readout
REFL_Q_1	CARM, beat between interferometer carrier and f_1
AS_1_f_1f_2	MICH; AS_1 port; beat between f_1 and f_2
REFL_f_3f_1	PRCL; REFL port; beat between f_1 and f_3
AS_2_SR	SRCL; AS_2 port; beat between $f_{sub-carrier}$ and f_4

Table 4.3: The error signal readout ports for the longitudinal control of ET-LF.

4.4.3 Output Matrix

As noted in section 4.4, we aim to control the five longitudinal degrees of freedom of the interferometer using linear feed-back techniques. The error signals generated for each dof are processed by individual servos to provide control signals ($\overrightarrow{C}$). The output matrix (N) converts the control signals into feed-back signals for individual mirrors i.e. to an optic basis.

$$\overrightarrow{A} = N\ \overrightarrow{C} \tag{4.9}$$

Table 4.4 is the output matrix N for the longitudinal control of ET-LF. Like the sensing matrix, the output matrix would consist of frequency dependent signals sent out from the actuators to push on the mirrors to complete the linear feed-back loop. For simplicity, we have assumed perfect actuators and used the output matrix as presented in table 4.4.

DoF	DARM	CARM	MICH	PRCL	SRCL
EX	0.5	1	0	0	0
EY	-0.5	1	0	0	0
BS	0	0	1	0	0
PR	0	0	-0.5	1	0
SR	0	0	0.866	0	1

Table 4.4: The output matrix converts the control basis (MICH, PRCL etc.) to the optic basis (BS, PRM, EX, etc.). The conversion of MICH to its optic basis involves geometry and is explained in the section below.

Using the table 4.4, equation 4.9 can be explicitly written as :

$$\begin{pmatrix} A_{EX} \\ A_{EY} \\ A_{BS} \\ A_{PR} \\ A_{SR} \end{pmatrix} = \begin{pmatrix} 0.5 & 1 & 0 & 0.0 & 0 \\ -0.5 & 1 & 0 & 0.3 & 0 \\ 0 & 0 & 1 & 0 & 0 \\ 0 & 0 & -0.5 & 1 & 0 \\ 0 & 0 & 0.866 & 0 & 1 \end{pmatrix} \begin{pmatrix} C_{DARM} \\ C_{CARM} \\ C_{MICH} \\ C_{PRCL} \\ C_{SRCL} \end{pmatrix} \tag{4.10}$$

An interesting point to be made here is the actuation of MICH. MICH was defined as the difference between l_x and l_y (see figure 4.1). When the beam-splitter is actuated, we inadvertently change the length of the PRC and SRC.

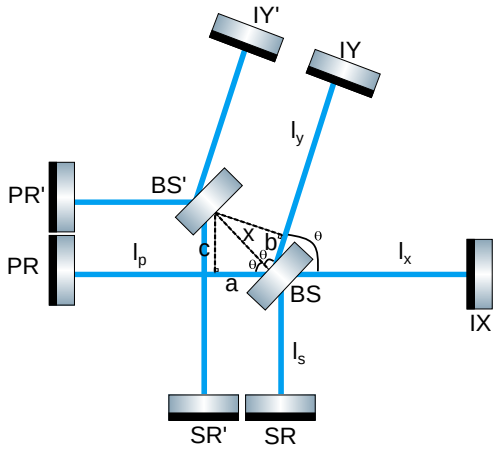

Figure 4.14: Geometrical coupling between MICH, PRCL and SRCL degrees of freedom.

Firstly, we define the convention that we have used for the mirror motion. Using the FINESSE convention,

- The motion of PR is negative in the direction of the BS

- The motion of SR is positive in the direction of the BS

A geometrical coupling between PRCL, SRCL and MICH is intrinsically present, so by moving BS, we inadvertently move PRCL and SRCL.

If BS, PR, SR, IX and IY are the initial positions of the mirrors (for simplicity I have excluded the ETMs, input and output paths of the interferometer), moving the BS which is at an angle of 60° (θ) along the perpendicular x to position BS$'$, we obtain the following relations for l_p, l_s, l_x and l_x (see figure 4.2 for the definition of these lengths).

$$\begin{aligned} \Delta l_p &= -x\,\cos\theta = -x\,\cos 60^\circ = -a\ , \\ \Delta l_s &= x\,\sin\theta = x\,\sin 60^\circ = c\ , \\ \Delta l_x &= x\,\cos\theta = x\,\cos 60^\circ = a\ , \\ \Delta l_y &= -x\,\cos\theta = -x\,\cos 60^\circ = -b\ , \end{aligned} \tag{4.11}$$

where Δl_p, Δl_s, Δl_x and Δl_x are the change in the lengths due to motion of the BS.

These equations tell us that for a motion 'x' of the beam-splitter, the PRC gets shorter by 0.5 $\times$ x and the SRC gets longer by 0.866 $\times$ x and thus to keep the length of MICH constant, PRCL and SRCL as indicated by the output matrix. The output matrix coefficients for MICH control of ET-LF are,

$$\begin{pmatrix} ET:N_{BS} \\ ET:N_{PR} \\ ET:N_{SR} \end{pmatrix} = \begin{pmatrix} 1 \\ -0.5 \\ 0.866 \end{pmatrix} \tag{4.12}$$

Even though it would be relatively easier to feed the MICH error signal to the ITMs (IX, IY), we prefer not to do so to avoid displacement of the arm cavities. It must be noted that the ambiguity in the definition of MICH leads to a difference in the output matrix coefficients used

at aLIGO [85] and aVIRGO [79]:

$$\begin{pmatrix} Virgo : N_{BS} \\ Virgo : N_{PR} \\ Virgo : N_{SR} \end{pmatrix} = \begin{pmatrix} 1/\sqrt{2} \\ 0.5 \\ 0.5 \end{pmatrix} \text{ and } \begin{pmatrix} LIGO : N_{BS} \\ LIGO : N_{PR} \\ LIGO : N_{SR} \end{pmatrix} = \begin{pmatrix} 1/\sqrt{2} \\ 0 \\ 0 \end{pmatrix} \tag{4.13}$$

4.5 Simulating a shot noise limited displacement noise budget for ET-LF

Implementing a full control system into a complex GWD without simulating it before hand and knowing what to expect is a difficult task. In order to test the sensing contamination of DARM if we were to use our proposed sensing scheme, in this section we calculate the shot noise limited displacement noise budget for DARM. To do so, we have made the assumption that the technical noise in the photodetectors used for sensing the different dofs is assumed to be negligible relative to the shot noise. We then use linear noise projection techniques to project possible noise sources to the DARM loop taking into account the cross-couplings due to various feed-back loops.

4.5.1 A complete noise budget for DARM

From figure 4.13, it can be seen that the auxiliary dofs show up on the PD used for DARM sensing. This cross-coupling allows the sensing noise arising from the feed-back control of CARM, PRCL, MICH and SRCL dofs to couple to the DARM loop. Were this additional sensing noise to be large, the sensitivity of the detector would be compromised. If the unity gain frequency (ugf) of all the control loops were to be below the DARM measurement band, and it were possible to roll off the loop response above the ugf steeply, this additional sensing noise would not be an inherent problem.

A steady state control loop model was setup for ET-LF using SimulinkNb [102]. Figure 4.12 shows two of these control loops (for simplicity) namely the MICH and DARM loops. We have however built these loops for CARM, PRCL and SRCL as well. Sensing noise is added to the loop at the point where the error signal for a dof is measured. Seismic noise, gravity gradient

noise and suspension thermal noise are added at the feed-back point. In our modelling described in this section, the servos used in the feed-back loops set the ugf of all the control loops above the DARM measurement band (reminder: for ET-LF this is 25 Hz). Doing so allows us to feed-back all the sensing noise with high gain to the mirrors. This sets an upper limit on the amount of tolerable control loop noise. Details about the ugfs of the individual loops are listed in section 4.5.2.

The estimated displacement noise budget using displacement noises mentioned in the ET design study [12] like seismic noise, suspension thermal noise, gravity gradient noise were projected into DARM. The results of the same are shown in Figure 4.15.

The seismic noise in figure 4.15 (by green dotted lines) is the measured seismic excitation at an underground facility in the Black Forest Observatory [103, 104] which is then passed through an aVIRGO style super-attenuator but 17 m long. The resulting transfer function was presented in [104]. This transfer function can be directly imposed onto the feed-back signal as this is effectively the mirror motion due to seismic noise at the facility which is transmitted by the suspension. For gravity gradient noise (shown by pink dotted lines) and suspension thermal noise (shown by black dotted lines), we have used rough theoretical estimates from [104] and not included any resonance features for the sake of simplicity. During the technical design phase for ET, this work can be re-visited and we can include realistic transfer functions for these noise sources. The quantum noise limit of the interferometer which includes the shot noise arising from sensing DARM is also shown in the figure 4.15 by the red dotted line. The overall sum of the noises is shown by the solid blue trace. As the noise sources are uncorrelated, we can sum them up together as shown in the figure. This plot shows us that between 7–32 Hz, ET-LF will be limited by quantum noise.

Figure 4.3 shows the shot noise limited displacement noise budget for DARM using balanced homodyne readout, including the sensing noise contributions from the other dofs due to the optical cross-coupling mentioned in section 4.4.2. The contributions from the other dofs are smaller than DARM itself across the measurement band, and are expected to be even smaller with more optimised servos which have a lower ugf compared to the ones that we have used. The effect of servo design is presented in section 6.3.4.

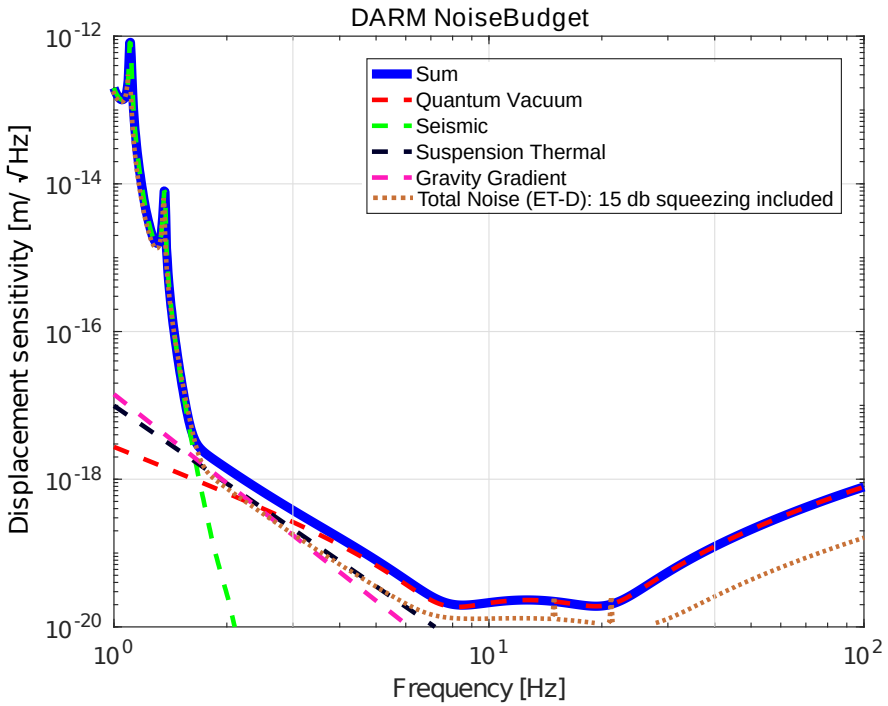

Figure 4.15: Estimated noise budget for one interferometer of ET-LF with an opening angle of 60°. The total noise is the sum of all the uncorrelated noises projected to DARM. The displacement noise sources are only indicative and are subject to change depending on the eventual site for ET-LF. Above 7 Hz, we are limited only by quantum noise limited sensitivity of DARM. For completeness we have included the quantum noise limited sensitivity of ET-LF with 15 dB squeezing taken from [104] for ET-LF with a 60° opening angle.

4.5.1.1 MICH sensing noise in DARM

MICH motion like DARM, produces differential phase signal sidebands. These sidebands are converted to amplitude sidebands at the dark port in the same manner as the differential phase sidebands from the arm-cavities [37]. The effect of the DARM signal sidebands is enhanced by the arm cavity finesse unlike the MICH signal sidebands by a factor of $\frac{2F}{\pi}$. This optical coupling allows the MICH sensing noise to show up in the DARM readout. The coupling path for the MICH sensing noise in DARM is calculated in appendix A (section 8.2).

As described in section 4.4.3, the geometrical coupling between MICH, PRCL and SRCL allows the sensing noise from PRCL and SRCL to show up in DARM. This however is only a second order coupling unlike MICH to DARM which is a first order coupling. The opto-mechanical coupling at 7 Hz allows DARM to dominate MICH at 7 Hz and it can also be seen from figure 4.13, that PRCL error signal is nearly as large as MICH at AS1_$f_1 f_2$. To subtract this inherent

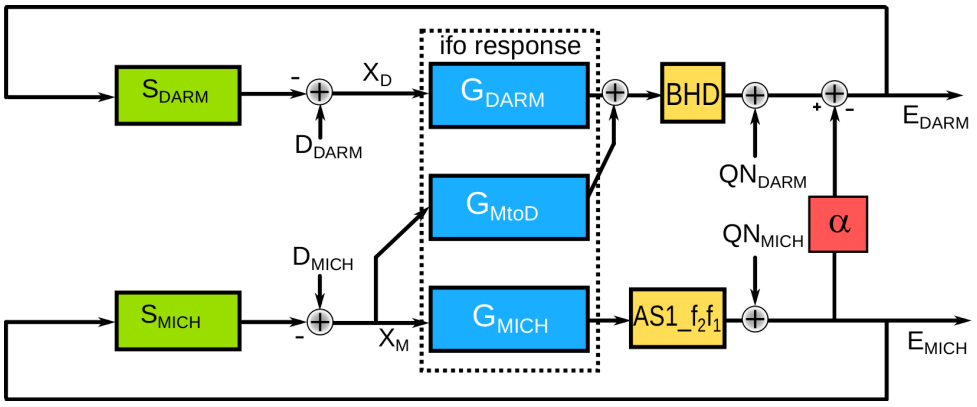

Figure 4.16: Feed forward of MICH into DARM in order to compensate for the optical coupling of MICH via G_{MtoD} in DARM. This block in the feed-back loop is a part of the interferometer response(also called the optical plant, see control theory basics appendix A, section 8.1) and the filter that subtracts this contribution is the α-filter which is also shown in the feed-back loop. The servos used to compensate for the disturbances in DARM and MICH are shown by D_{DARM} and D_{MICH} respectively. The readout photodiodes for the MICH and DARM error signals (E_{DARM} and E_{MICH}) are the yellow blocks in the feed-back loop. The quantum shot noise associated with the sensing MICH and DARM are summed into the loop after the readout photodiodes.

coupling between MICH and DARM, an aVIRGO style α-technique feed-forward filter [105] was also implemented in the MICH control path.

The α feed-forward filter shown in figure 4.16 is frequency dependent and can be measured and fit with fitting algorithms to produce a usable transfer function. However, this transfer function can change with change in readout port, demodulation phase etc. This technique cannot be used for large suppressions and requires tuning over long stretches of time as the transfer functions might vary with time (an example for the drift in transfer function over time was shown in this logbook post by S.Dwyer [106]).

The DARM optical gain is represented by G_{DARM} in the figure and the optical gain of MICH by G_{MICH}. If these two degrees of freedom were completely decoupled, then G_{MtoD} would not exist.

The α filter required is calculated to be;

$$\alpha = \frac{G_{MtoD}}{G_{DARM}} \ . \tag{4.14}$$

The position of the alpha filter in the feed-back loop determines the cancellation of sensing noise or actuation noise [107]. In our case, assuming perfect actuators, we want to mitigate sensing

noise, we use the filter immediately after the sensors and the filter removes the contribution of MICH on the DARM photodiode.

4.5.2 Properties of the control loops

The servos that we have used were tailored to imprint sensing noise onto the feed-back signal. As a rule of thumb all the control loops in our simulation have a ugf $\gg 40\,\text{Hz}$. In this section we describe the stability of the DARM control loop and mention the ugf for the CARM, MICH, PRCL and SRCL loops.

The DARM control loop has a ugf of 52.6 Hz (see figure 4.17a) and a phase margin of 22.3°. The filter used was designed to have high suppression below the unity gain crossing after which the transfer function rolls off.

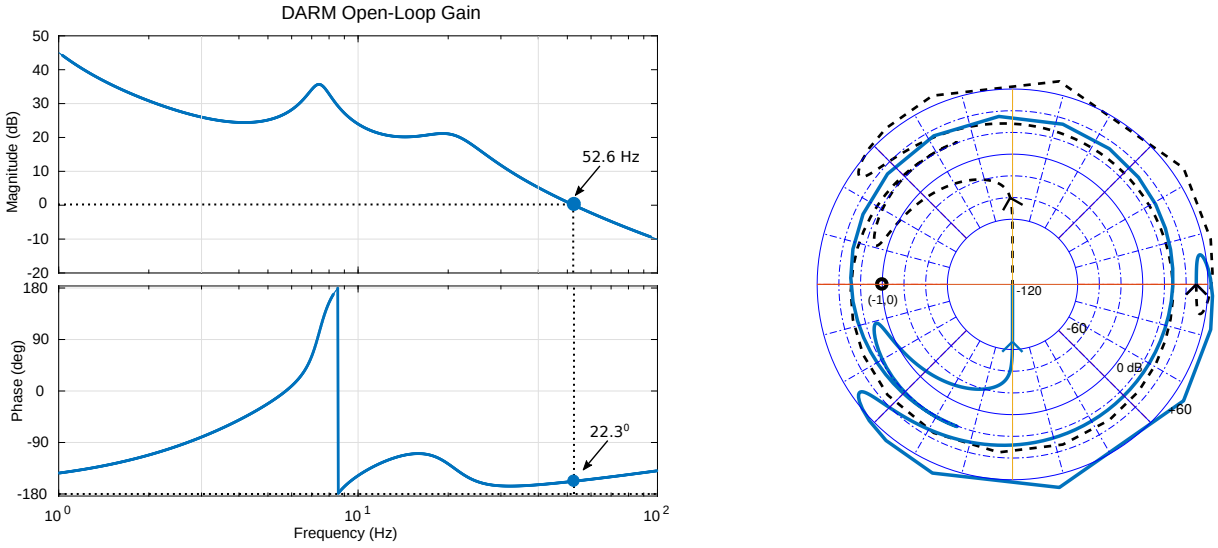

(a) (b)

Figure 4.17: a) Open-Loop gain of DARM including the servo b) Logarithmically scaled Nyquist closed loop stability plot for the DARM control loop.

A Nyquist plot allows us to predict the stability of a closed loop system by observing its open-loop behaviour. Similar to a Bode plot (figure 4.17a is a Bode plot of the DARM loop), a Nyquist plot can also be used to predict the gain and phase margins of the closed loop (see appendix A, section 8.1.1 for control theory basics). The Nyquist stability plot of DARM shown in figure 4.17b is a logarithmic version of an ordinary Nyquist plot generated with a Matlab function accredited to Trond Andresen [108]. There are two poles in the the right half plane (RHP) of the open-loop

system of DARM and there are -2 encirclements around the (-1,0) point thus implying that there are no poles in the RHP of the closed loop system. Owing to this lack of poles in the RHP, the system is predicted to be stable in closed loop.

Table 4.5 shows the open-loop gain and the phase margins for the auxiliary dofs. The CARM loop which is also used as a reference for the laser frequency has a ugf of about 51.1 Hz with a phase margin of 87.2°. In aLIGO, this loop has a high ugf (65 kHz [85] to suppress laser frequency noise). Since this dof is decoupled from DARM to a large extent, its sensing noise projected to DARM is small.

DoF	ET_LF ugf	ET_LF phase margin	aLIGO ugf
CARM	51.1 Hz	87.2°	65 kHz
MICH	44.8 Hz	31.4°	30 Hz
PRCL	42.3 Hz	30.9°	40 Hz
SRCL	49.6 Hz	14.2°	≈20 Hz
DARM	52.6 Hz	22.3°	50 Hz

Table 4.5: Phase margin indicates how far the control loop is from the -180°phase instability. If the phase margin is negative, the feed-back system will oscillate thus being instable. An important criterion for a control loop to be stable is for the loop to have a positive phase margin. The phase margins of the control loops calculated above, indicate that the control loops that we have designed meet this criterion. For comparison purposes, we have included the ugfs for the corresponding loops in aLIGO [37, 85].

The MICH loop has a ugf of about 44.8 Hz and a phase margin of 69°. The PRCL and SRCL loops have a ugf of 42.3 Hz and 49.6 Hz and a phase margin of 30.9°and 14.2°respectively. Upon maturity of the technical design of ET-LF the servos used here can be modified to have a larger stability margin by modifying the ugf and the slope of the servo.

4.6 Estimation of coupling of individual dofs to DARM

The results obtained from SimulinkNb in section 4.5.1 were re-affirmed using the calculations described below.

- The solid blue line in all the plots (figures 4.18, 4.19, 4.20, 4.21) below are the optical gains of the error signals at their readout ports ($OG1_{SRCL}$ in the example equation 4.15). This optical gain is the transfer function of the error signal to the measurement photodiode.

- The magenta line is the optical gain in W/m of the dof at the photodiode used to measure DARM due to optical coupling in the interferometer ($OG2_{\mathrm{SRCL}}$ in the equation 4.16).
- The black line is the quantum noise associated with the dof at its measurement PD having the units $W/\sqrt{Hz}$ (SN_{SRCL} in the equation 4.15).
- The quantum noise of DARM is shown in cyan and has the units $W/\sqrt{Hz}$.
- The shot noise contribution of a dof in DARM is then calculated in $W/\sqrt{Hz}$ using equation 4.16 and compared to the quantum noise of DARM. This quantity is represented by the dark green line in the plots.

An example set of calculations for SRCL control is detailed below. If we were to lock the SRM using the PDH signal detailed in section 4.3.2, the motion of the SRM ($SRCL_{\mathrm{QNLS}}$) after locking is:

$$SRCL_{SNLS}(m/\sqrt{Hz}) = \frac{SN_{SRCL}\,at\,AS_2\,(W/\sqrt{Hz})}{OG1_{SRCL}\,(W/m)}\ , \tag{4.15}$$

The quantity mentioned above is also the shot noise limited sensitivity of SRCL ($SRCL_{SNLS}$).

$$SRCL_{coupling}(W/\sqrt{Hz}) = OG2_{SRCL}\,(W/m) \times SRCL_{SNLS}(m/\sqrt{Hz})\ , \tag{4.16}$$

For a dof not to couple strongly to DARM, the coupling obtained using equation 4.16 should be lower than the shot noise of DARM at AS_{DARM}. In other words, the dark green curve should be below the cyan curve in all the figures.

The contribution of all the dofs except MICH satisfy the aforementioned condition and show that their coupling into DARM is not worrying. The contribution of MICH into DARM was artificially removed using the α-technique mentioned in section 4.5.1.

Conclusion and outlook

In this chapter we have proposed a new technique for controlling SRCL, and shown that it significantly reduces the coupling from SRCL to DARM compared to current control techniques.

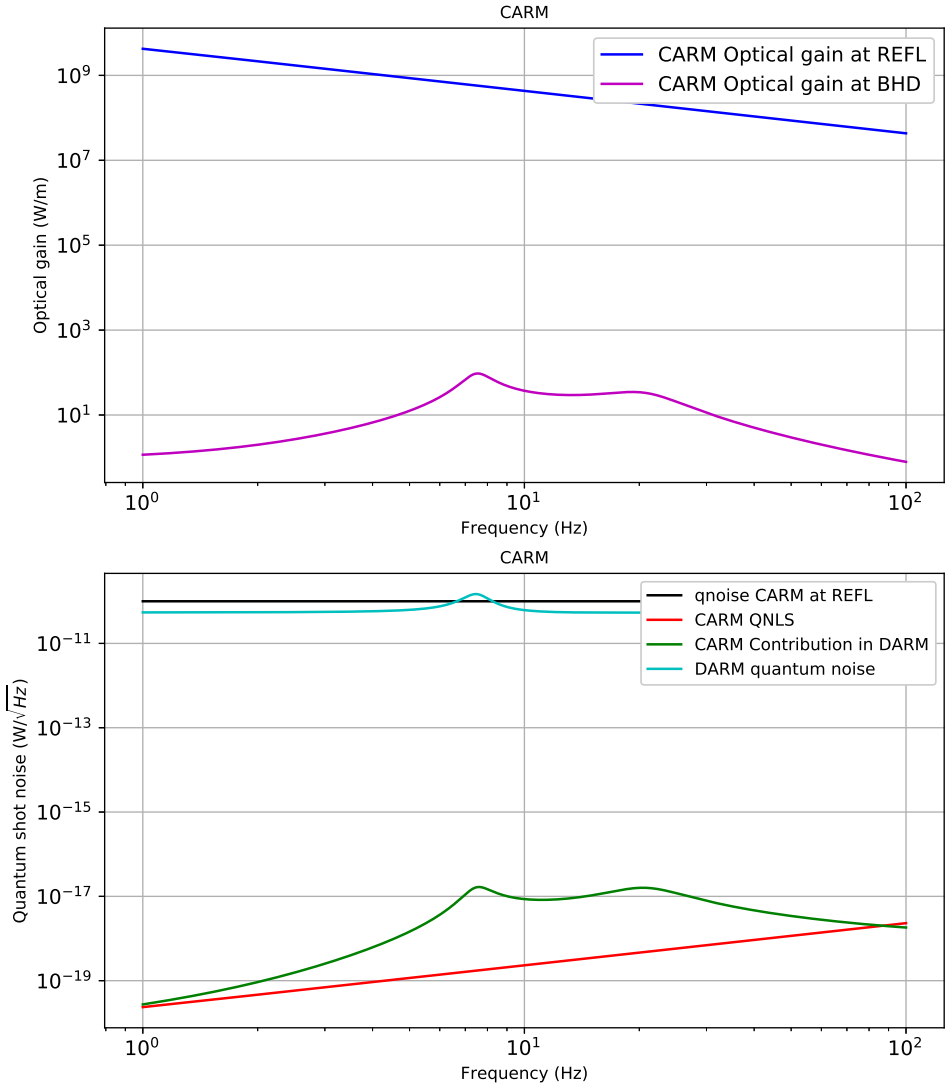

Figure 4.18: CARM contribution to DARM: CARM is readout using the 11.36 MHz and interferometer carrier

We have in this chapter demonstrated a new technique to control detuned ET-LF. By using the optical beat between a frequency shifted carrier produced with a separate laser and a phase modulation sideband not resonant in the signal recycling cavity, we can obtain an error signal with a high optical gain for SRCL control. The error signal so obtained is tolerant to large changes in demodulation phase.

The control scheme proposed for ET-LF is also applicable for ET-HF or as shown in chapter 7, for any interferometer with a DRMI layout to obtain low noise, high gain error signals for SRCL control. The infrastructure setup in terms of FINESSE models and control loop models in this thesis, is transferable to the modelling of ET-HF.

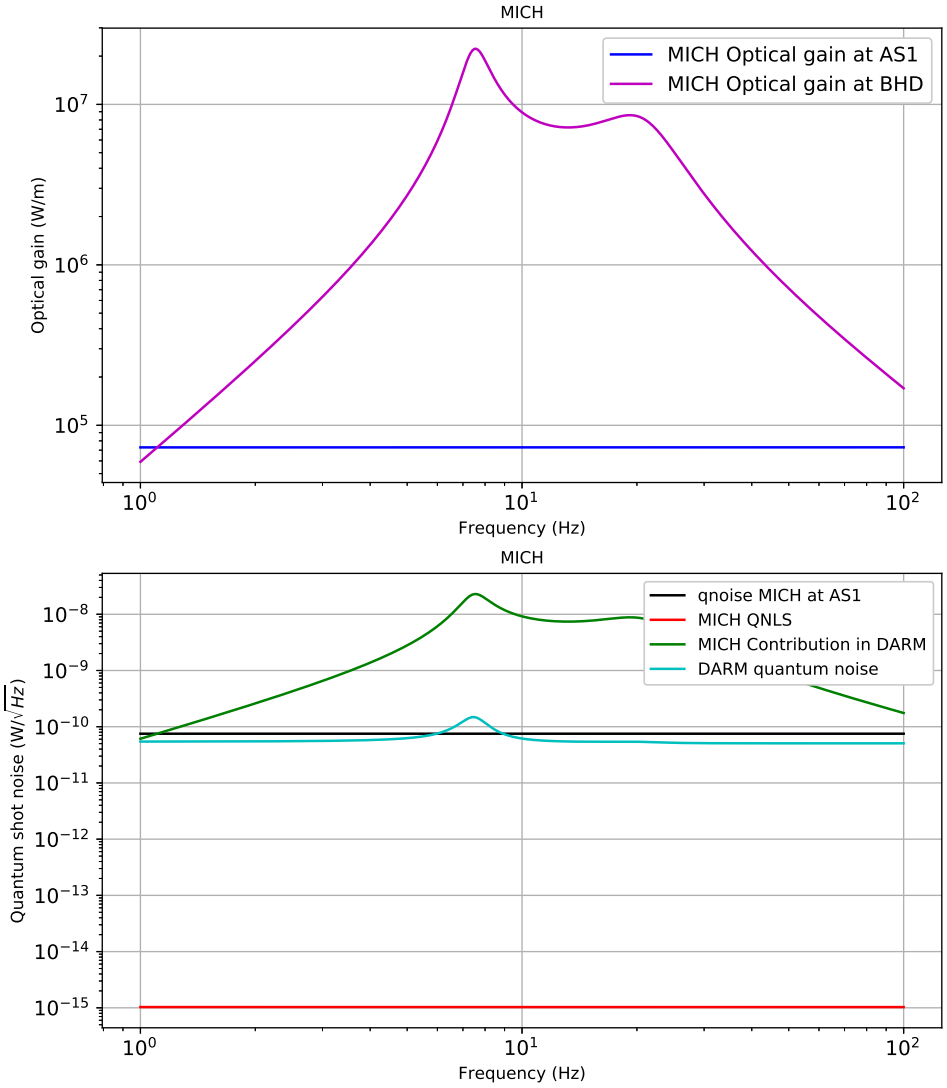

Figure 4.18

Figure 4.19: MICH contribution to DARM: The error signal for MICH is obtained by taking the beat between the 56.82 MHz and the 11.36 MHz sidebands.

Control noise arising from angular control of mirrors limits the sensitivity of current GWDs below 10 Hz [27]. A possible application of this technique which is not explored in this thesis is the generation of high optical gain angular control signals which could eliminate this low frequency noise.

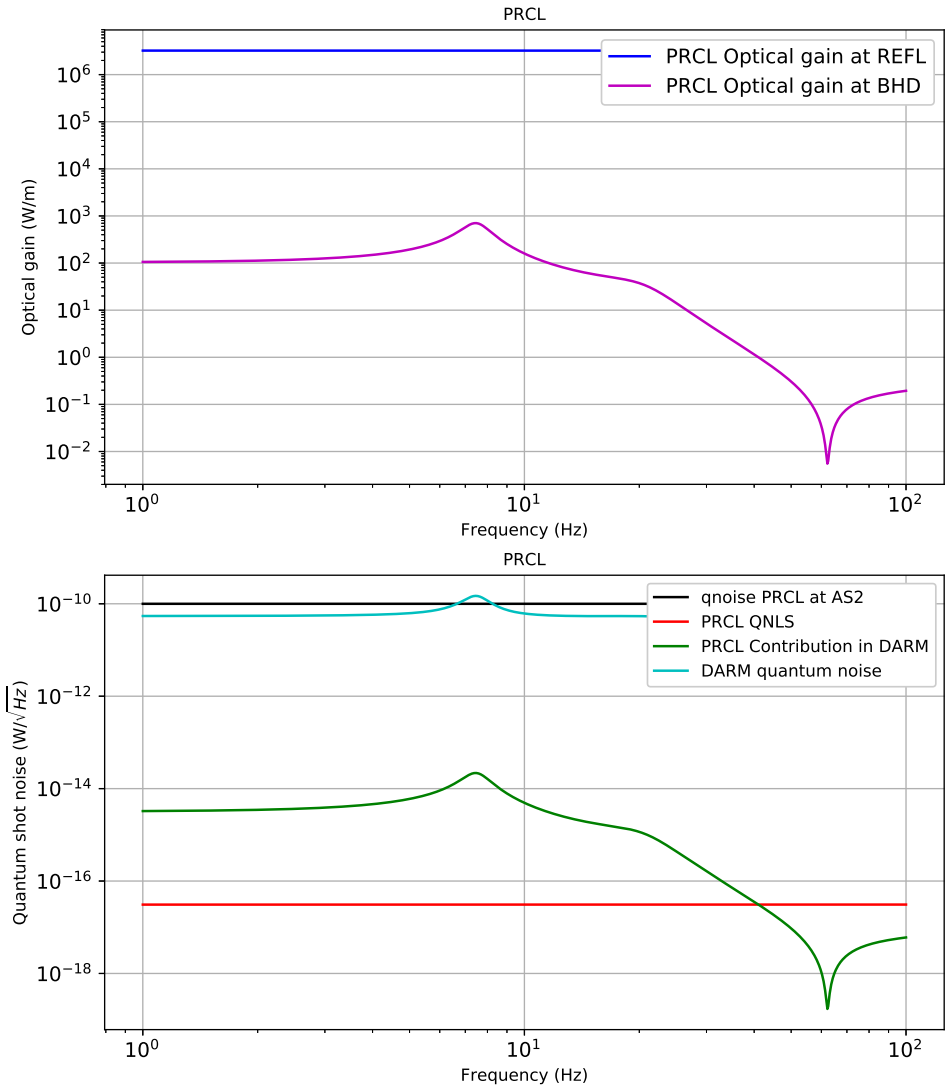

Figure 4.20: PRCL contribution to DARM: PRCL readout is performed using the beat between the 56.82 MHz and the 25.19 MHz sidebands.

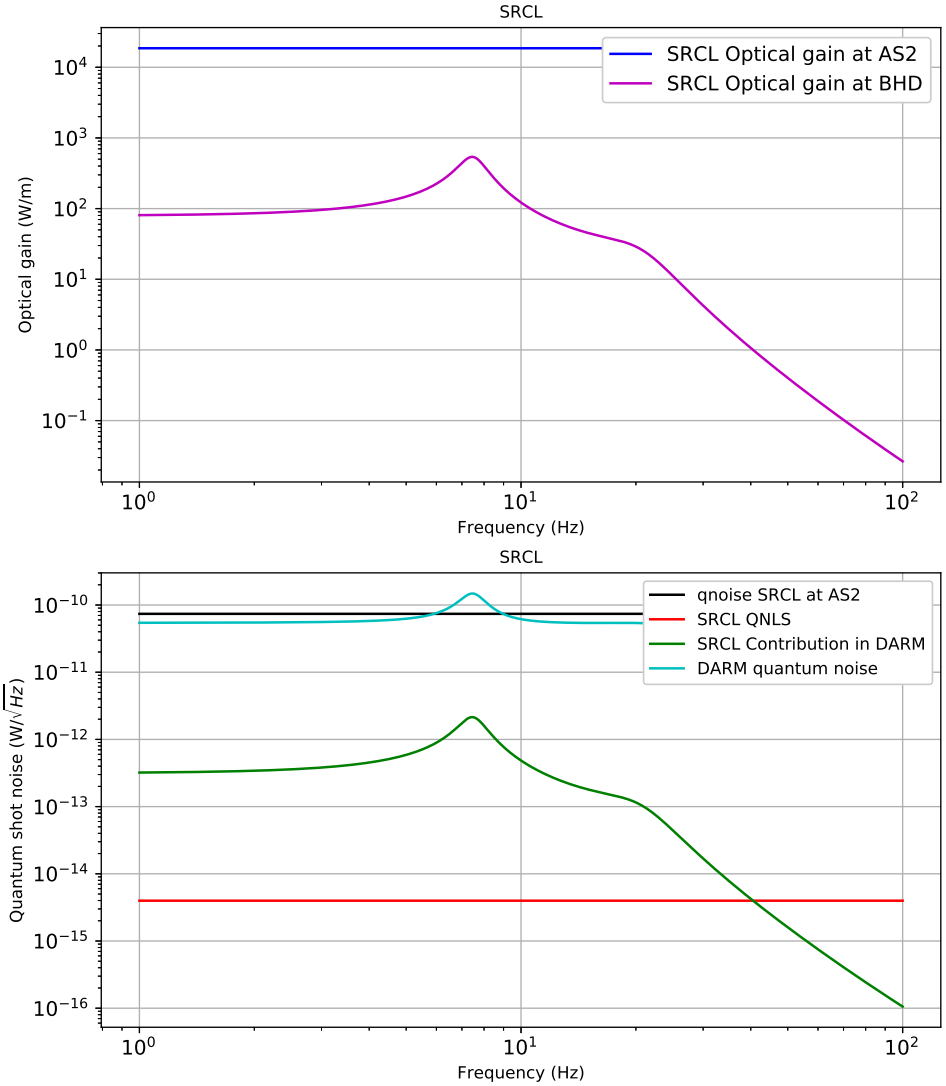

Figure 4.20

Figure 4.21: SRCL contribution to DARM: using the sub-carrier sensing scheme, the beat between the 1.72 GHz sub-carrier and the 15 MHz sideband, the error signal to control SRCL is generated.

Chapter 5

The 10m Prototype facility

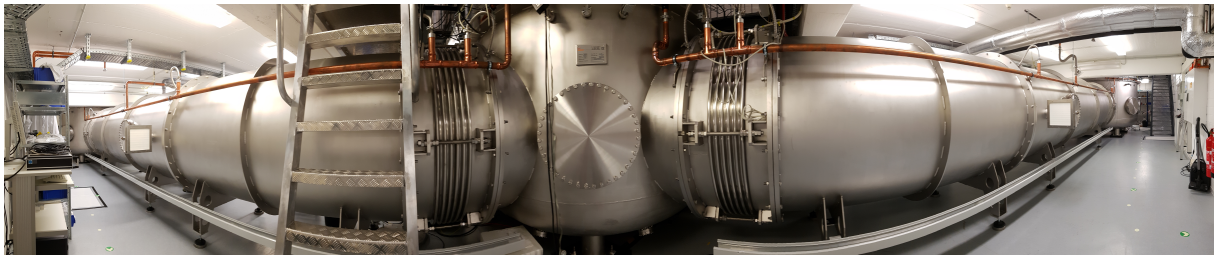

Panaromic view of the AEI 10 m prototype. Picture courtesy Harald Lück.

5.1 The AEI 10 m facility : Design and goals

The Albert Einstein Institute 10 m prototype facility is a test-hub for techniques for advanced gravitational wave detectors. It is similar to advanced gravitational wave detectors in terms of complexity and noise requirements. The AEI 10 m prototype facility is named so for its current optical configuration a 10 m Michelson interferometer with Fabry-Perot cavities in the arms.

The 10 m prototype is one among the many GWD prototypes around the world which have played a crucial role in development of technology quintessential for optimal functioning and sensitivity improvement of advanced GWDs. To name a few such technologies,

- Dual recycling (see section 2.3) was prototyped and thoroughly tested at both the Glasgow University [38] and the Max-Planck-Institut für Quantenoptik in Garching [109, 110]

- The Glasgow University 10 m prototype also houses the ERC proof of principle speedmeter [63].

- The LIGO advanced systems testing interferometer (LASTI) at the Massachusetts Institute of Technology, has prototyped the technology for an in-vacuum squeezer with the Australian National University and this technology is currently being integrated into the LIGO detector sites at both Hanford and Livingston [111, 112]

- Several aspects of sensing and control including the ALS technique for lock acquisitive of the arm cavities were investigated at the Caltech 40m prototype before being installed at the LIGO observatory sites [113, 114]

- Techniques for interferometry at cryogenic temperatures were tested in the scope of the Japanese cryogenic laser interferometer observatory (CLIO) projects [115] and paved the way for the implementation of cryogenics in the Kamioka GWD, KAGRAs [116]

Several experiments have been planned at the AEI 10 m facility although the initial major experiment that will be conducted is the measurement of the Standard Quantum Limit (SQL) to explore quantum-mechanical effects in macroscopic objects. The SQL is the quadrature sum of the quantum back-action noise of the interferometer mirrors and the photon shot noise. As no recycling techniques will be employed in the 10 m prototype immediately, in order to measure the SQL, we require high light power (arm cavities are designed to have a finesse of 675) with low mass mirrors (100 g) (see section 2.5.1 for a more detailed description of the SQL).

Shot noise or photon counting noise is known to limit the high frequency part of all advanced GWDs [118]. The low frequency limit where the radiation pressure noise is dominant has not been experimentally measured putting the prototype with its low mass mirrors in a unique position to do so. The low mass mirrors lead to an increased opto-mechanical coupling coefficient and the choice of 100 g is the minimum mass required in conjecture with other design parameters such as suspension thermal noise (which arises due to finite thickness of suspension fibers). Mirror thermal noise another predominant classical noise, is lowered by the choice of AlGaAs coatings over the conventional SiO_2TaO_5 coatings. These design choices of the experiment are such that the predicted sum of all classical noise sources lie below the sum of the quantum noise in the region

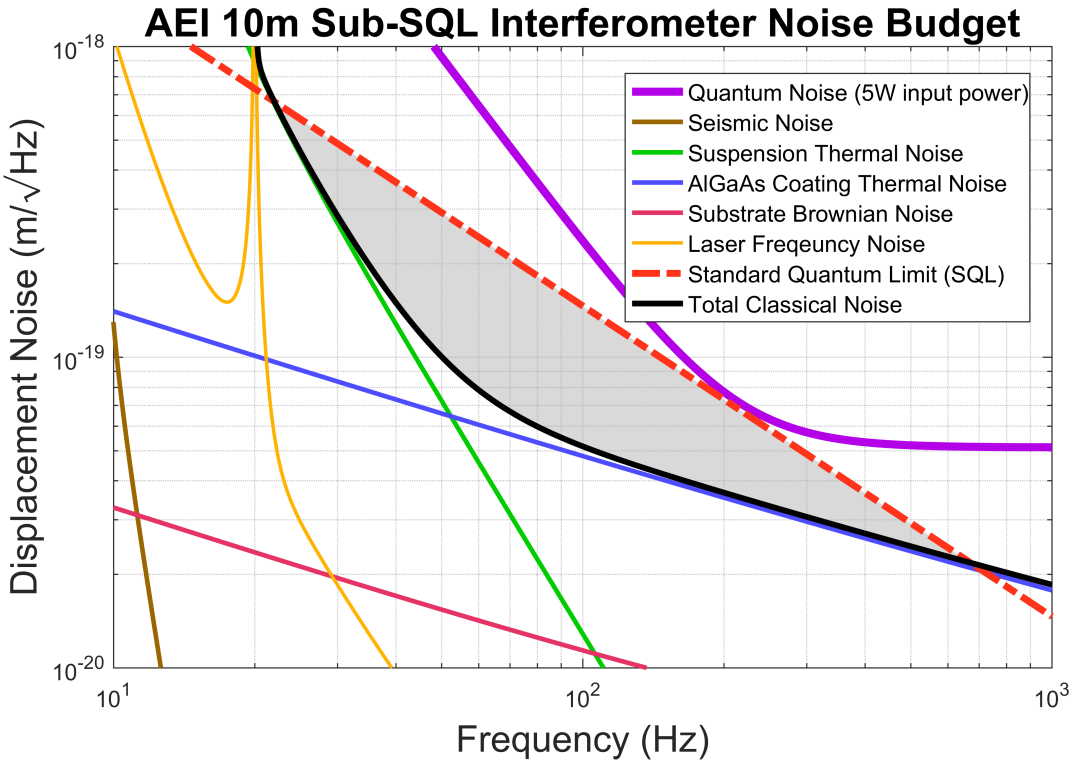

Figure 5.1: 10 m prototype displacement noise budget [117] which shows the predominant noise sources. The black solid line shows the sum of all the classical noise sources: seismic noise, suspension thermal noise, coating thermal noise, substrate Brownian noise, laser frequency noise (see section 2.5.1 for a detailed description of classical noise sources in GWDs). The standard quantum limit is indicated by the dashed red line and the grey shaded area between 25 Hz and 700 Hz is our region of interest.

of 25 Hz to several 100 Hz. Upon reaching the quantum noise limited sensitivity of the setup, experiments to improve the sensitivity below the SQL will be performed. These experiments could involve the injection of squeezed states of light [119] or back-action evasion techniques [120].

This chapter provides an overview of design goals and planned experiments at the 10 m prototype as well as provide an insight into the various individual sub-systems of the 10 m prototype that make the experiment work. These include the vacuum system, seismic isolation tables, the suspension platform interferometer and the main laser system along with the reference cavity for laser frequency stabilization, and the digital control and data system which is used to implement the digital feedback controls required by the 10 m prototype.

5.2 Sub-systems of the AEI 10 m prototype

The AEI 10 m prototype is not only planned to test technology of innovative interferometry concepts but is also planned to host experiments that have a wide application in future ultra-high precision interferometers. The optical layout of the 10 m prototype for measuring the SQL is shown in figure 5.2 and was first presented by Somiya et al in 2009 [121]. The study outlined the noise sources to be considered and mitigated in order to measure the SQL.

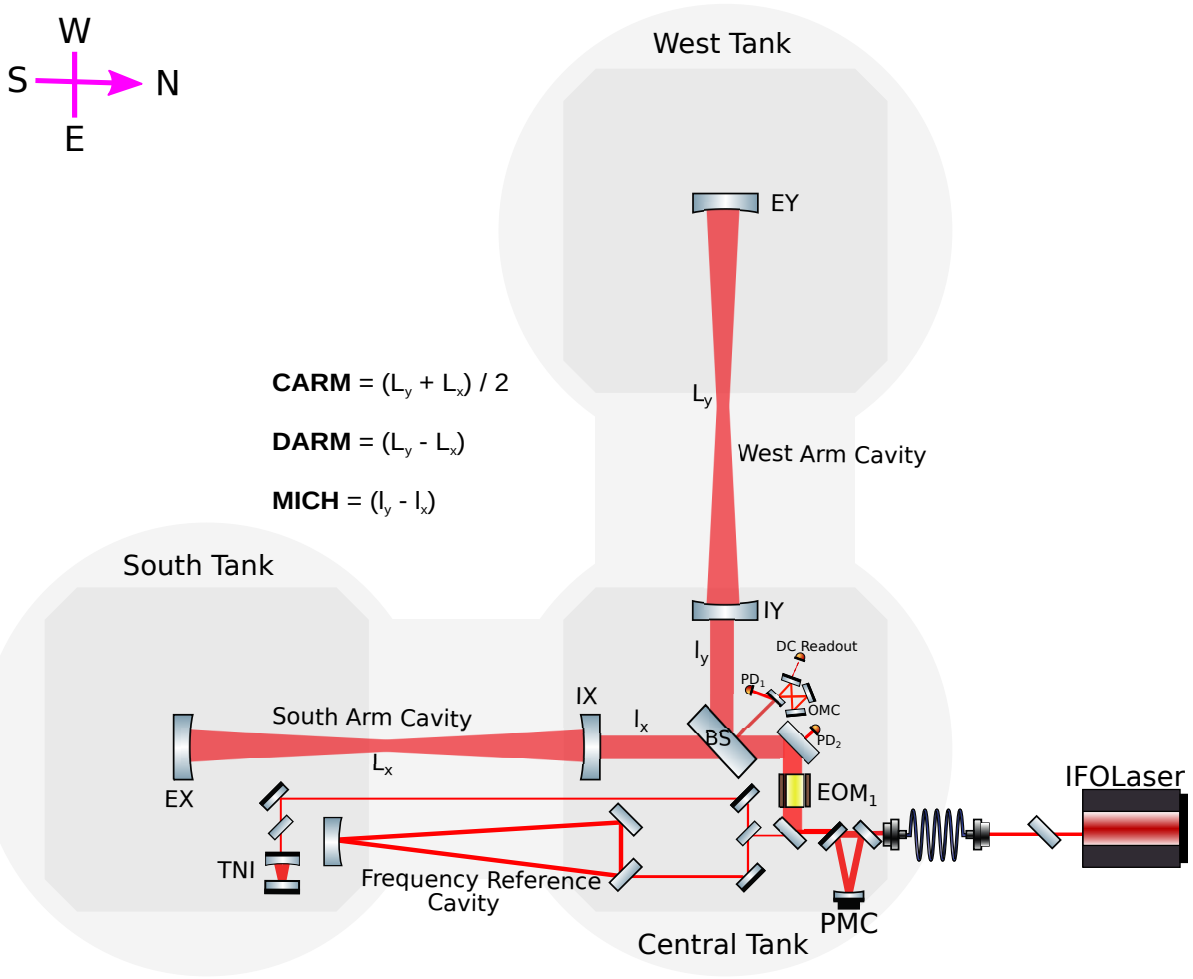

Figure 5.2: Simplified optical layout of 10 m SQL interferometer

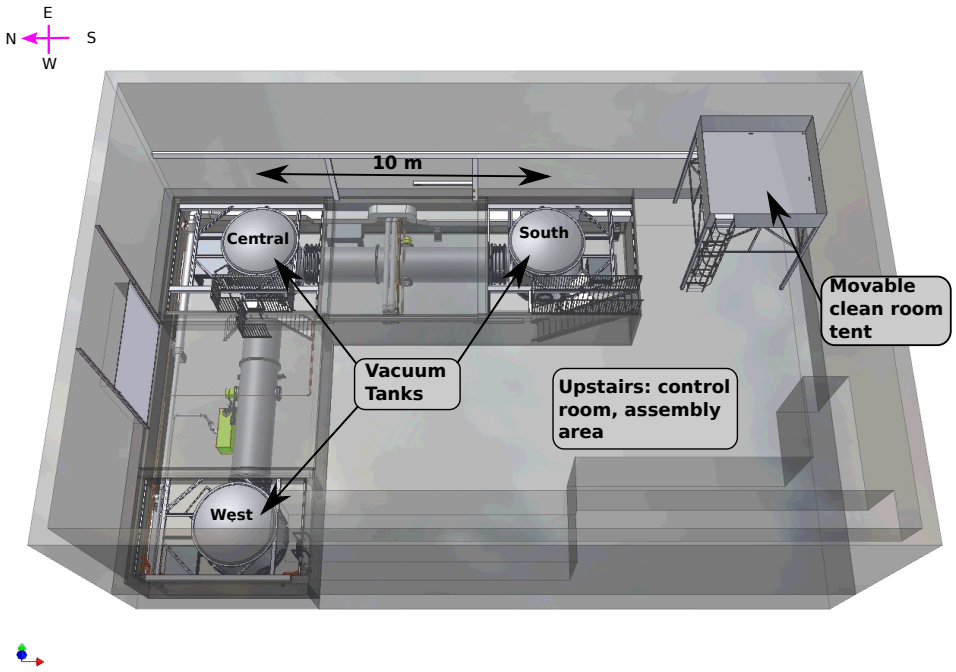

Figure 5.3: Inventor model of the 10 m prototype hall showing the entire infrastructure with the three vacuum tanks separated by a distance of about 10 m in the basement level and the upstairs area which houses the movable clean room tent which is currently under use to assemble the third table to go into the west tank. The L-shaped vacuum system, which will house the planned interferometry experiments, is located at basement level [122].

5.2.1 Vacuum system

The vacuum system provides a $100\,m^3$ ultra-high vacuum environment which ensures that environmental noise sources, such as acoustic coupling and refractive index fluctuations, are reduced to a level such that they do not impact the precision of future measurements. The L-shaped vacuum system designed in-house is composed of three stainless steel tanks with the dimensions 3.4 m × 3 m (h×d). These are interconnected by tubes which have a diameter of 1.5 m. The advantage of having tanks this large is the ability to 'walk-in' and they are large enough to host the optical tables and the SAS' described in the section 5.2.2.

The vacuum system is designed for rapid pump down with the help of screw pumps and two turbo-molecular pumps. The screw pumps operate at 175 l/s and pump the entire volume of the vacuum system from atmospheric pressure to 5 Pa in less than two hours. The turbo-molecular pumps rated at 2400 l/s are attached to each arm (shown in green in figure 5.3) and upon being switched on after the screw pumps, pump down to 10^{-6} hPa. These turbo pumps are backed by

scroll pumps. The 10 m prototype uses copper gaskets and double Viton® O-rings to reduce leaks. Although gate valves are not included in the design of the prototype as in the current advanced detectors [123], the fact that low pressures can be reached on relatively short time scales (approximately 1 day) makes the configuration well suited for the prototype as the system is vented frequently.

5.2.2 Seismic isolation

Seismic noise and gravity gradient noise limits all ground-based detectors at low frequencies (current detectors like aLIGO are limited by seismic noise below 10 Hz). The origin of both these noises have been discussed in section 2.5.1. At the 10 m prototype, ground motion, integrated over all frequencies has been measured to be approximately 300 nm rms [124]. In order to isolate the mirrors from ground motion, the AEI 10 m prototype uses a seismic attenuation system.

The AEI-SAS (AEI-Seismic Attenuation System) is based on the LIGO seismic attenuation system [125] but has been re-designed to meet the requirements of the 10 m prototype (which are as stringent as currently operational GWDs). An optical bench of the dimensions 175 cm × 175 cm × 40 cm ($l \times b \times h$) and mass 950 kg, will be installed in each of the three vacuum tanks which hosts all the suspensions and optics. At the time of writing this thesis, the central and south tables are in place and the west table is scheduled for installation soon. Two important design features of the SAS that provide vertical and horizontal isolation at very low frequencies are the geometric anti-springs filters and inverted pendulum (IP) legs respectively. These together, provide seismic isolation in all six degrees of freedom. The horizontal isolation stage comprises of three inverted pendulum legs [126, 127], that isolate a rigid platform (spring box in figure 5.4) from horizontal ground motion. The IP-leg is attached to the spring box via steel flexures. Above the roll-off frequency of the IP-legs, all horizontal ground motion is attenuated. The flexures (still flexure at the base plate and soft flexure at the spring box) constrain the pitch and roll motion of the IP-legs, thereby keeping them upright. The resonance frequency of the IP-legs is tuned down to $\approxeq 0.1$ Hz by loading the spring box.

The vertical isolation system of each table consists of three geometric anti-spring filters (GAS) [129] which in turn consist of eight cantilever blade springs which are bent and radially compressed

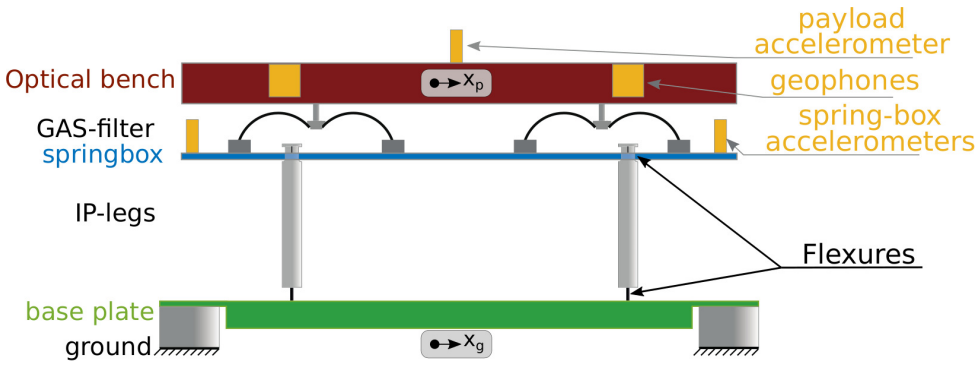

Figure 5.4: Simplified sketch of the original AEI-SAS design: The optical bench (payload) is supported by three GAS-filters providing vertical isolation. The GAS filters and IP-legs provide horizontal and vertical isolation respectively from ground motion. The spring box is supported by the IP-legs. The baseplate is connected to the 'feet' of the vacuum tank in a rigid fashion. Figure modified from [128].

against each other to form a crown of curved blades [124]. An anti-spring effect is created with the GAS filter blade springs and by altering the compression, the resonance frequency of the GAS filters can be tuned. This, along with the use of magic wands [125] which compensate for the inertia in the blade springs, provide isolation from vertical ground motion above 10 Hz.

The use of active feedback control improves the overall performance of the SAS and to facilitate this, the tables are equipped with numerous co-located sensors and actuators. Three kinds of sensors and actuators are used for reading out the motion of the table: linear variable differential transformers (LVDTs), accelerometers and geophones. The LVDTs are position sensors which measure the displacement of the table relative to the ground motion, accelerometers measure the horizontal inertial motion of the spring box and the geophones measure the residual motion of the optical bench. The two tables in the vacuum system employ commercial L22 vertical geophones manufactured by Geospace Technologies (these are put into suitable sealed vacuum cans for in-vacuum use) but these L22s are replaced by more sensitive L4Cs [130] for the third table which is scheduled to be installed into the west tank. The performance of the AEI-SAS is discussed in detail in [44, 128]. Stepper motors are used to fine tune the table positions and for alignment purposes.

5.2.3 Suspension platform interferometer

The relative motion of the three AEI-SAS' is sensed and mitigated with the help of an interferometric link, the suspension platform interferometer (SPI). The error signal measured by the SPI is fed-back to actuators in the south and west tables such that they all follow the motion of the central table at low frequencies and in this way, the three tables form a rigid platform. At low frequencies, in absence of passive isolation, the SPI can be used for active control of table position and angles thus creating an environment that would enable us to test techniques for space interferometry such as an experiment for a GRACE follow-on mission [131].

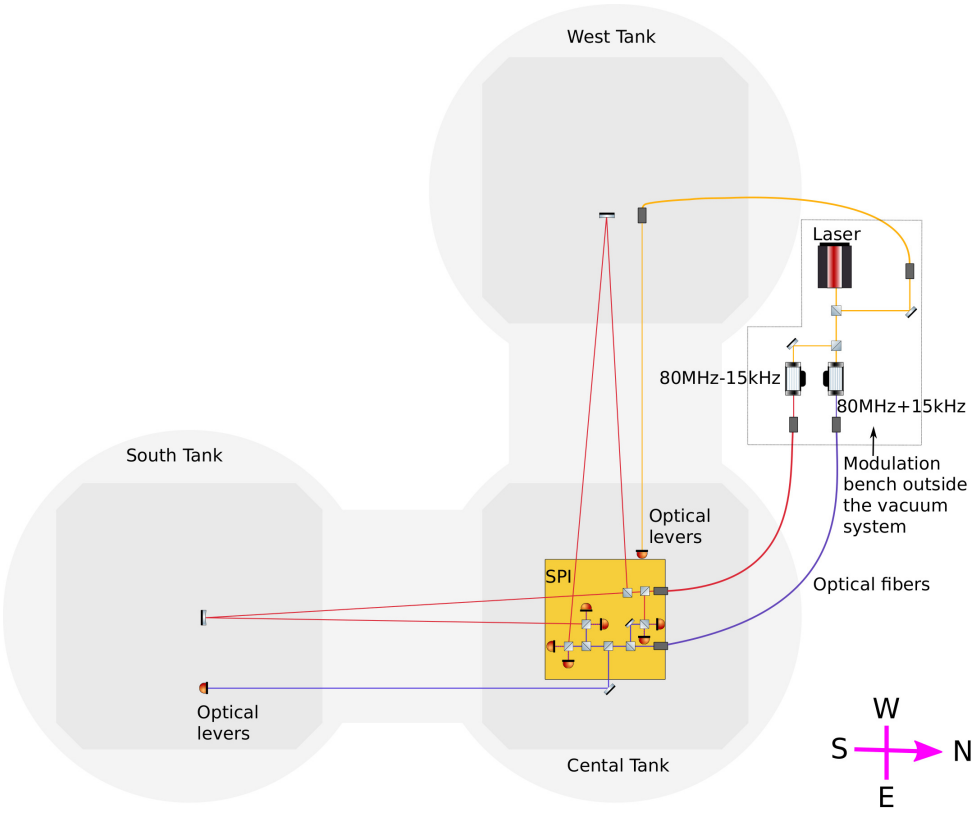

Figure 5.5: Simplified overview of the SPI with the central baseplate (yellow), located in the center of the table in the central tank. The dimensions of the same are $250 \times 250 \times 30\,\mathrm{mm}^3$. This baseplate, also called the measurement bench, hosts the four interferometers for measurement, diagnostics and reference. The baseplate is made of an ultra low thermal expansion glass. The figure also shows two of the four optical levers installed in parallel to the SPI to measure table tilt. Figure modified from [128].

The main laser of the SPI (iodine stablised, solid state laser from Prometheus) is set up on a modulation bench outside the vacuum system (see figure 5.5). The output of this laser is split into

two paths where the beams are frequency-shifted by $80\,\mathrm{MHz} \pm 15\,\mathrm{kHz}$ with the help of acousto-optic modulators and guided onto the central table via two optical fibres. The central table also hosts the measurement bench (shown in yellow in figure 5.5) on which optical components are set up. The measurement bench is a heterodyne Mach-Zehnder setup. The optical components are bonded via hydroxide-catalysis onto a CLEARCERAM R-Z HS baseplate [132]. As shown in figure 5.5, a curved mirror (of radius $-11.8\,\mathrm{m}$) is placed on the south and west tables to reflect the measurement beam back to the central table baseplate assembly.

The SPI consists of four interferometers: two measurement, one reference and one diagnostic. The reference interferometer signal is used to measure the common-mode signals from the other interferometers and the diagnostic interferometer as the name suggests is used for debugging purposes, out-of-loop measurements, thus enabling us to measure the sensitivity of the SPI. The measurement interferometers measure the relative position and orientation of the south and west tables with respect to the central table with the help of the beams reflected from the aforementioned curved mirrors. Quadrant photodiodes (QPDs) are used for reading out the signals from the measurement interferometers. The signal from the QPDs are processed via a phasemeter, the output of which is sent to the digital control system (CDS) via Ethernet and they are recombined here to yield error signals for feedback control.

The optical lever (OL) comprises of a collimated laser from the center of the central table onto a QPD on the south and west tables. A relative tilt between the tables corresponds to a motion of the spot on the QPD. The 10 m lever arm enhances the beam motion thus providing us with low noise tilt signals for the table tilts with respect to the central table.

In the frequency range between 10 mHz and 100 Hz, the design sensitivity of the SPI to measure inter-table distance is $100\,\mathrm{pm}/\sqrt{\mathrm{Hz}}$. The performance of SPI and OL will soon be published by S.Köhlenbeck [133].

5.2.4 Laser system and pre-mode cleaner

The laser system in the AEI 10 m prototype is developed by the AEI Hannover and LZH [118] following the design of the Advanced LIGO laser. It is a two stage system comprising of

a commercially available monolithic non-planar ring oscillator (NPRO) from Coherent (seed laser) [134] and an amplification stage. The 2 W output of the seed is amplified via the amplification stage consisting of four Nd:YVO_4 crystals. These crystals are pumped via fibre coupled diodes at 808 nm. The output of this system is a 35 W laser beam at a wavelength of 1064 nm.

95% of the light output is in the fundamental Gaussian mode (TEM_{00}). The laser beam is guided into the vacuum system via a 5 m photonic crystal fiber which further reduces the higher order mode content of the beam. The laser beam then passes through a pre-mode cleaner (PMC): a rigidly mounted three mirror cavity which provides further spatial mode filtering. The PMC (see figure 5.2) consists of three mirrors, two planar coupling mirrors and an end mirror with 1 m curvature radius, glued to a rigid spacer, forming a triangular cavity with a round-trip length of 53 cm, having a finesse of 1000.

The pointing noise at the input of the PMC is converted to power noise at its output and the power fluctuations thus sensed are used to set up a feedback loop via an intensity stabilisation system (ISS). This system stabilises the output to a relative intensity noise of 2×10^{-9} [135].

5.2.5 Frequency reference cavity

The frequency noise of a free running laser needs to be suppressed by seven orders of magnitude for the AEI 10 m prototype to not be limited by frequency noise, this noise would have to be mitigated. The isolated optical tables provide a stable length reference in the frequency range of interest for the 10 m prototype (25–700 Hz). A suspended triangular cavity of round trip length 21.2 m and a finesse of 3500 is used as a frequency reference cavity (see figure 5.2). The cavity is illuminated with 200 mW of input laser power and has a sensitivity of $10^{-4}\,\mathrm{Hz}/\sqrt{\mathrm{Hz}}$ at 20 Hz and falling off as $1/f$ (with f being the frequency) and $6 \times 10^{-6}\,\mathrm{Hz}/\sqrt{\mathrm{Hz}}$ at 1 kHz. To prevent susceptibility to radiation pressure effects and thermal noise effects, the mass of the mirrors is 850 g. The suspension cages have a weight of 13.5 kg and are within the allowed payload of the tables.

A Pound-Drever-Hall (see section 2.4) is employed to lock the laser frequency to the length of the suspended cavity. The laser is modulated at 8 MHz and these sidebands are not resonant in

the reference cavity providing us with an error signal for length change of the reference cavity which can then be fed back to the laser. Three kinds of actuators are used in the reference cavity for different frequency ranges; upto 1 Hz, the laser crystal temperature is used as an actuator to change the frequency; between 1 Hz and 10 kHz, a piezo-electric element is used; between 10 kHz and 250 kHz, a phase correcting EOM (electro optic modulator) is used as an actuator.

5.2.6 Thermal Noise Interferometer

The thermal noise interferometer (TNI) is a linear cavity (see figure 5.2) with a single pass length of 10 cm. The plane-concave geometry of the TNI puts the cavity close to instability along with the waist on the flat mirror and a larger spot on the curved input mirror. The intentional enhancement of coating thermal noise due to the choice in geometry and the design of the TNI puts it in a unique position to measure the coating thermal noise. The flat mirror which functions as the test mirror can be exchanged thus allowing us to study various experimental coatings for advanced GWDs. The TNI is also a triple suspended Fabry-Perot cavity [118] which like the reference cavity described in 5.2.5 can be locked with a PDH signal in reflection. The cavity is designed to be short to reduce the effect of frequency noise in the thermal noise measurement.

The TNI can also be used to study the effects of optical instability on coating Brownian noise, and as of yet this has not been experimentally verified (although there are several theoretical estimates). As this noise source will limit advanced GWDs at the TNI can be used to design and test novel coatings such as the AlGaAs coatings (crystalline coatings which will be tested at the prototype), the theoretical thermal noise contribution of which is plotted in figure 5.1.

5.2.7 CDS

The 10 m prototype has employed an aLIGO style digital control system which is based on real-time Linux and runs the EPICS software packages. CDS facilitates the co-ordinated functioning of all of the subsystems of the 10 m prototype and all the data is stored with a time stamp onto external hard disks at sample rates of up to 64 kHz [41] which allows the user to analyse the experimental results at a later time. The time-stamp is obtained via a GPS synchronised clock.

Over a hundred real-time control loops run with the CDS and are used for feedback control of mirror position (longitudinal position and angle).

The digital control loops are designed using Simulink-like blocks, the result of which is then complied into a Linux kernel module using a real-time code generator. All the parameters like filter coefficients, switches, control loop parameters, can be changed digitally by a graphical user interface called MEDM screens.

In order to put the data stored in a large scale detector into perspective, the total data collected by LIGO currently stands at over 4.5 Petabytes (Pb) of data, and is predicted to grow at a rate of about 0.8 Pb per year [136].

5.2.8 Single arm test

The Single Arm Test (SAT) is an intermediate step towards the final configuration of the 10 m prototype which would be used to measure the SQL. It is hosted on the existing optical tables in the vacuum system (central and south tables) and is designed to have the same infrastructure as the baseline final configuration of the AEI 10 m prototype. The mirrors of the SAT are designed to have the same mass, finesse and radii of curvature as the final configuration, thus making them susceptible to the same radiation pressure effects. The triple suspension currently used is designed at by University of Glasgow and has a metal penultimate mass. The last stage (test mass) is currently suspended by 50 μm wire and the parameters of this cavity are the similar to the final configuration and are summarised in the table 6.2. This stage will be exchanged for a monolithic assembly (this will be done at Glasgow) of fused silica masses with AlGaAs coatings (the coatings are obtained from G.Cole [137]).

The SAT will not be used to measure the SQL, and hence the optical losses in the SAT cavity are not as consequential as in the final configuration and hence lower quality mirrors are used. An important consequence of this decision in conjecture with marginally stable cavities (a configuration that could be tested), is increased shot noise due to increased higher order modes that arise from mirror imperfections which contribute to shot noise and not signal. Alignment sensing challenges can thus be investigated paving the way for research and development of novel

alignment sensing schemes which would benefit current and advanced GWDs.

A new concept for electro-static actuation using an electrostatic drive (ESD) [138] has been proposed for low noise control for the final configuration of the 10 m prototype. This ESD consists of two capacitor plates facing each other, which produces a force when a voltage is applied ($\approxeq$ 700 V is used currently to produce a force constant of about 6.4×10^{-7} N/V) [134] which can then be used to actuate on the mirrors. Some results of preliminary testing of the ESD have been used to model section 6.3.5 and arrive at tolerances for the maximum allowed mirror motion. The experience gained with the technical challenges that arise in the course of locking the SAT is transferable to the final configuration with ease.

Chapter 6

Controlling the longitudinal degrees of freedom in the AEI 10m prototype

6.1 Chapter overview

The AEI 10 m prototype is a test bed for new technologies for advanced detectors and is thus an ideal place to implement and test new control schemes. This chapter is broadly divided into four sub-sections:

- Building and validating a FINESSE model of the 10 m prototype (section 6.2)
- Length sensing and control modelling of the same (section 6.3)
- Comparison of BHD readout and DC readout for the 10 m prototype (section 6.4)
- Numerical modelling of optical springs in the single arm test (SAT) cavity (section 6.5)

The longitudinal sensing and control of the 10 m prototype is not different in complexity from advanced GWDs. Of the three longitudinal degrees of freedom (dofs) to be controlled (CARM, DARM and MICH), MICH and DARM are optically coupled. This chapter focuses on finding a sensing scheme that would allow us to sense and control the three dofs individually. To do so, the sub-carrier scheme proposed for SRCL control of ET-LF in chapter 4 is revisited and modified

for MICH sensing in the prototype. With this, it was possible to obtained an error signal for MICH completely dcoupled from DARM. This chapter also presents the advantages of balanced homodyne readout over the conventional DC readout for DARM sensing from the perspective of sensing noise. in particular this section shows how the CARM dof which couples to DARM via technical radiation pressure noise can be decoupled from DARM using balanced homodyne readout. The SAT cavity which is currently being commissioned, is in a unique position to measure radiation pressure effects. With the help of numerical 'experiments' a brief overview of the optical springs in provided in this section along with expected spring frequencies for various detunings of the SAT cavity.

All the results obtained for this chapter are a result of numerical modelling with FINESSE [92] and SimulinkNb [102].

6.2 Setting up the FINESSE model of the 10 m prototype

6.2.1 Parameter choices

For an interferometer with the topology of the AEI 10 m prototype sub-SQL interferometer, a total of three longitudinal degrees of freedom require feedback control: the lengths of the arm cavities (2 DOF: CARM, DARM), and the differential motion of the arm cavities (MICH) with respect to the central beam-splitter. All the macropscopic lengths in the optical setup are subject to spatial constraints due to limited number of components that can be populated onto an optical table of specific dimensions, payload of neighboring systems, load weights on the table to balance the table and so on. Although exact lengths have yet to be optimised, a working hypothesis has been developed assuming some parameters. The arm cavity length is assumed to be 10 m . The arm length of the small Michelson for the longer arm is 0.525 m and the for the shorter arm is 0.475 m thus setting the Schnupp asymmetry to be 0.05 m. The Michelson arm length is mainly determined by the need to extract pick-off beams and is limited by spatial constraints mentioned above. The lengths chosen for the purposes of the simulations presented in this chapter are subject to change.

The choice of dark fringe offset (DFO) for DC readout was made by choosing a microscopic offset to the positions of the end mirrors of the Fabry-Perot cavities (see figure 6.1) such that the circulating arm cavity powers are not too asymmetric but at the same time there is enough carrier at the dark port to readout the DARM dof. The DFO used here is applied differentially to the end mirrors of the arm cavities to utilise the power noise filtering of the carrier in the arm cavities (due to the cavity pole at rather low frequencies [33]; for comparision purposes, this frequency for the case of aLIGO is 41.66 Hz and in our case is 11.3 kHz). A consequence of this decision however is the appearance of optical spring due to detuned arm cavities. Using an offset to the beam splitter would also accomplish the same purpose. However, the former case requires a smaller detuning owing to the resonant enhancement of the arm cavities and the latter would require a larger to give the same power at the dark port. The larger detuning of the beam splitter has to be tested to check if we are able to obtain an error signal for MICH within its linear range around the operating point.

6.2.2 Model validation

Having thus optimised potential DFO, the Schnupp asymmetry and the modulation frequencies (see section 6.3.1 for details on this), the quantum noise limited sensitivity predicted by FINESSE was compared to analytic models based on the calculations of Danilishin [139] and Somaiya [121] [139] to validate the model. The results of the same are shown in the plot below. The quantum noise budget (see figure 6.2) is calculated for 3 W of input laser power and the cross-over of quantum radiation pressure and quantum shot noise is above 200 Hz . The analytic model made by Danilishin [139] is in agreement with the FINESSE model and varies slightly from the and Somaiya [121] [139] model due to a difference in assumption of the overall losses in the interferometer. The noise budget also has two lines predicted by FINESSE; one for the case where the transmission of the ETMs is 50 ppm (per ETM optic) thus representing the current SiO_2TaO_5 coatings and the second case being the new AlGaAs coatings (5 ppm losses per ETM optic). The cavity loss in both cases was simulated by changing the transmission of the ETMs (in our case increasing the transmission of the ETMs for SiO_2TaO_5 as opposed to the AlGaAs coatings). There is no significant difference between the two cases in terms of quantum noise limited sensitivity but the AlGaAs coatings are designed to have lower thermal noise contribution

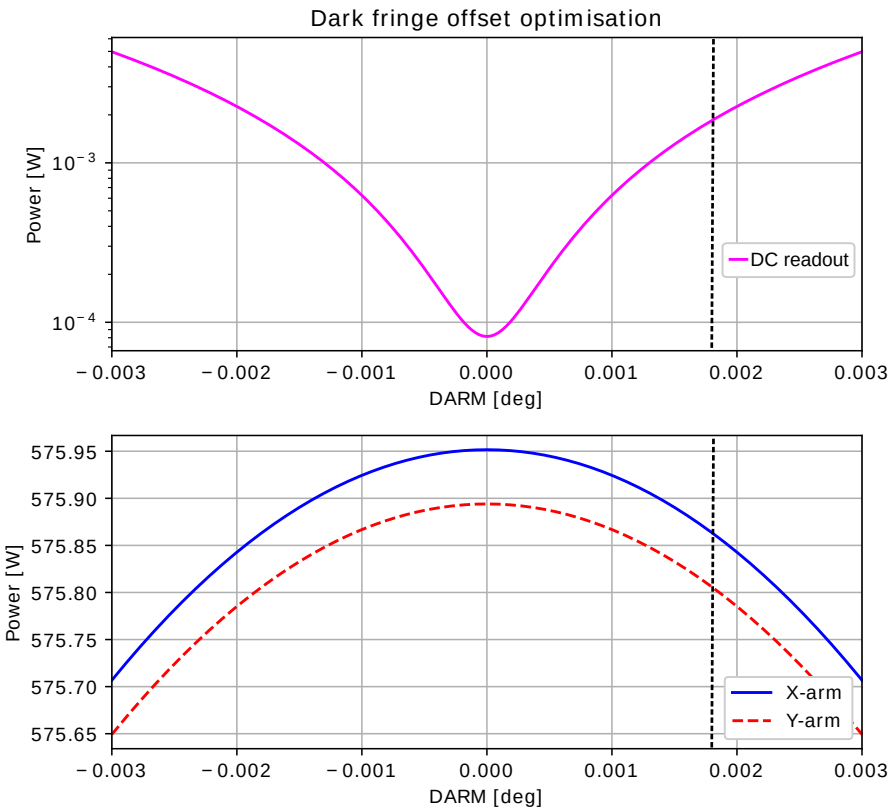

Figure 6.1: The dark fringe offset chosen for the 10 m prototype simulations (black dotted lines corresponding to 0.0018°) was chosen such that the asymmetry introduced in the arms due to off-setting the arms was minimal. The detuning corresponds to 5.32 pm. The power variation as a function of DARM offset in degree in shown in the first panel. The panel below is indicative of the arm cavity powers at the chosen DFO to get a power of 1.72 mW at the dark port after the OMC.

(see section 5.6). This allows us to have rather smaller beam sizes without necessarily pushing the cavities to instability or high g-factors. More details about the readout techniques and parameters used are in the following sections.

6.3 Length sensing and control modelling for the 10m prototype

6.3.1 Obtaining the error signals

Knowing the macroscopic lengths in our model, we then chose modulation frequencies for the longitudinal control of CARM and MICH. To produce sidebands which do not resonate in the arm cavities, we use a frequency which is far from an integer multiple of the arm cavity free

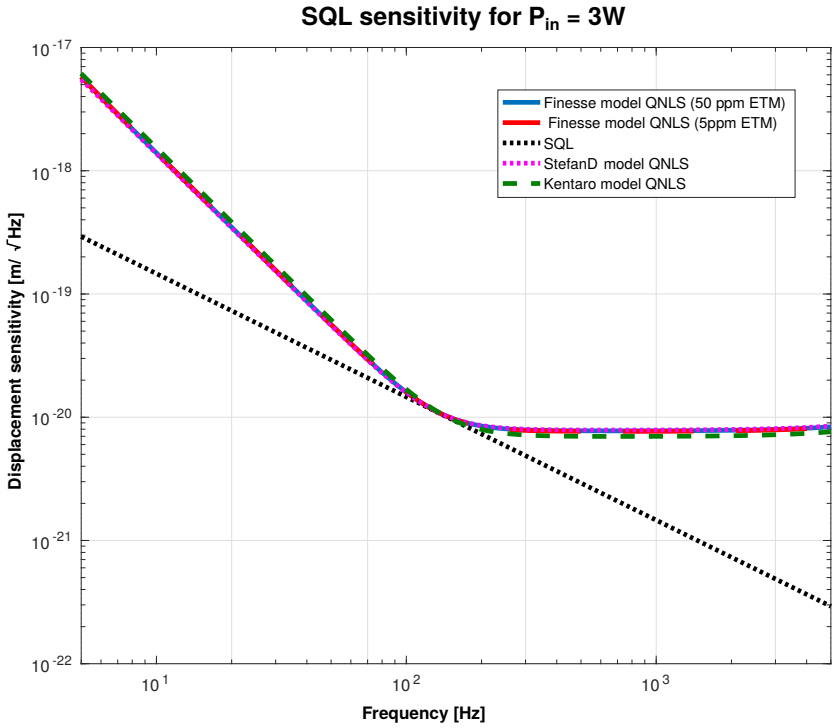

Figure 6.2: The 10m prototype Quantum Noise Budget as calculated by FINESSE (red) for the Fabry Perot Michelson layout with 5 ppm transmission end mirrors. For other simulation parameters see table 6.1. AlGaAs coatings which will be installed in the 10 m prototype are presumed to be lossier than the SiO_2TaO_5 coatings and hence the 50 ppm curve (blue) was calculated with the FINESSE model. The dashed pink and green lines are the quantum noise projections from analytic models of the 10 m prototype made by Danilishn and Somiya [139]. The SQL for a Fabry-Perot Michelson interferometer is shown by a dotted black line.

spectral range.

$$\mathrm{FSR}_{\mathrm{Arm}} = \frac{c}{2\,L_{Arm}} = 15\,\mathrm{MHz}, \tag{6.1}$$

where c is the speed of light and L_{Arm} is the arm cavity length.

The modulation frequency favored here is 20.44 MHz (f_1) and this is not resonant in the arm cavities and is transmitted via the Schnupp asymmetry to the dark port. Figure 6.4 shows the resonance conditions for the various modulation frequencies. Technically, any frequency that is not an integer multiple of the FSR of the arm cavities ($\mathrm{FSR}_{\mathrm{Arm}}$) could be chosen as a modulation frequency and the frequency we have chosen (20.44 MHz and shown in lime green in figure 6.4) for pure convenience and availability purposes.

A PDH error signal (as described in section 2.4), is obtained by taking the optical beat between two light fields at different frequencies. In the case of the 10 m prototype, the beat between

Parameters	10m PT
f_1	20.44 MHz
f_{gig}	1.527 GHz
L_{Arm}	10 m
$l_{schnupp}$	0.05 m
l_x	0.525 m
l_y	0.475 m
P_{in}	3 W
P_{aux}	1 mW
P_x	575.85 W
P_y	575.8 W
F_{cav}	660
$P_{OMC\text{-}REFL}$	9.9 mW
$P_{OMC\text{-}TRANS}$	1.72 mW
P_{f1}, OMC	20.6 nW
$P_{sub\text{-}carrier}$, in	0.01 W
$P_{sub\text{-}carrier}$, OMC	83.8 nW

Table 6.1: Parameters used in the 10 m prototype simulations. The table also shows the single sideband power in the modulation sidebands at the photodide used to measure DARM. 1.72 mW of DC carrier power is measured in transmission of the OMC after the removal of the modulation sidebands and the sub-carrier by the OMC.

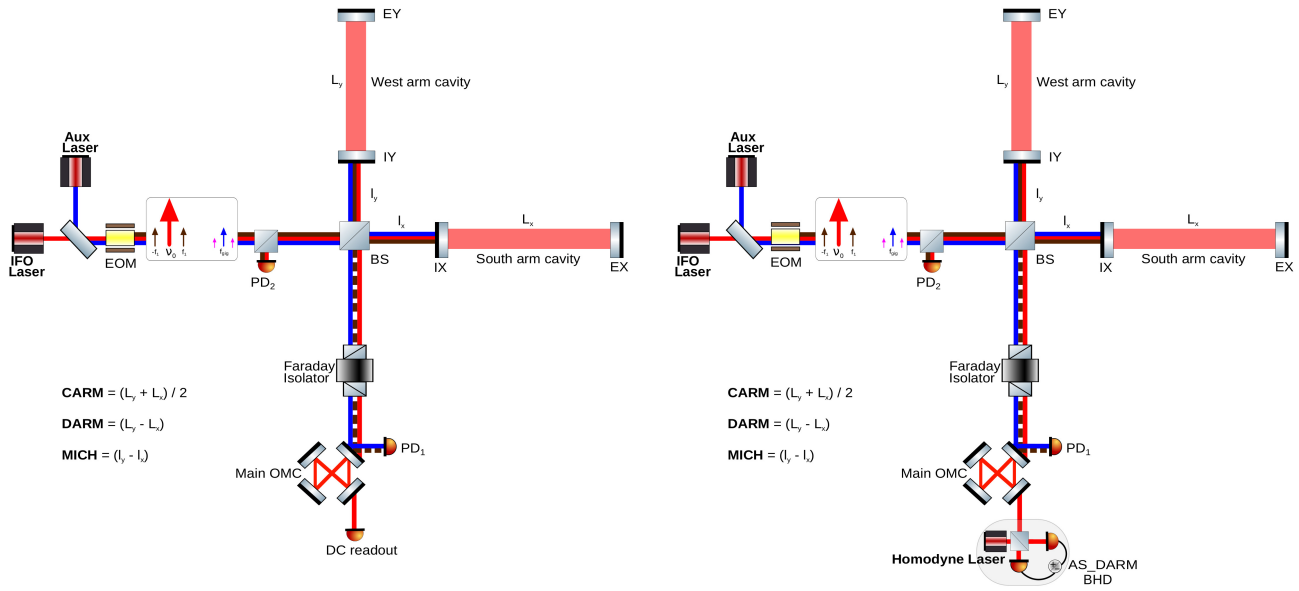

(a) Optical Layout with DC readout and sub-carrier

(b) Optical layout with BHD and sub-carrier

Figure 6.3: Simplified sketch of DARM readout options for the 10 m prototype. For both readout options, the use of an additional sub-carrier for sensing MICH dof has been considered. The advantages of using the same is detailed in the section 6.4

interferometer carrier light that senses the arm cavities and the non-resonant sidebands is demodulated at the sidebands frequency f_1 to obtain an error signal for the sensing the length

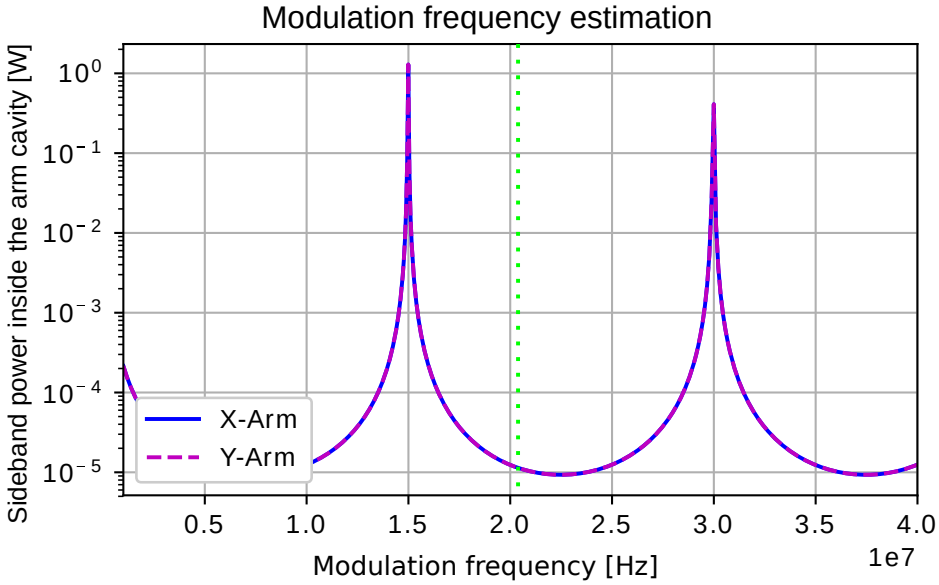

Figure 6.4: The figure shows the various potential modulation frequencies for sensing and control purposes in the 10 m prototype. As we want the modulation frequency to not be resonant in the arm cavities, we choose to avoid frequencies which are an integer multiple of the arm cavity FSR. The chosen modulation frequency of 20.44 MHz is indicated by the dashed lime green curve and it is not resonant in either arm cavities.

variations in the arm cavities. In order to sense CARM, we use the PDH error signal obtained at PD_2 by demodulating at f_1. For the DARM readout, as mentioned in section 6.1 there are two possibilities; DC readout or BHD readout. The advantages and disadvantages of both these techniques are discussed from the purview of sensing noise contamination from other dofs in section 6.5.

The MICH dof can be sensed at two ports, PD_1 (dark port) and PD_2 (input port), by taking the beat between the carrier and f_1. MICH motion, being a differential motion, is similar to DARM minus the amplification by the arm cavities i.e. MICH $= (\frac{4\times F}{\pi}) \times$ DARM where F is the finesse of the arm cavities. The Schnupp asymmetry leads to equal size sidebands at f_1 for MICH and dfo sensing at the dark port. The optical gain of MICH sensing signal is larger at PD_1 as opposed to that at PD_2. As the optical gain at DC is equivalent to the slope of the error signal (in other words the linear locking range of the error signal), using the frequency dependent transfer function of optical gain allows us to understand the coupling between the different dofs. For instance at the sensing ports available for MICH, the MICH signal is dominated by DARM and CARM respectively (see figure 6.5). If we were to use the signal of MICH from PD_2 to

control MICH length, the DARM and CARM signals need to be suppressed by 10^4 at 200 Hz to be able to sense MICH. If we were to use the error signal for MICH obtained at PD_1, both CARM and DARM motion need to be suppressed in order to sense MICH. In order to obtain an independent error signal for MICH that would not require gain hierarchy, we would need to employ a sub-carrier equivalent scheme presented for ET-LF SRCL control in Chapter 4. The

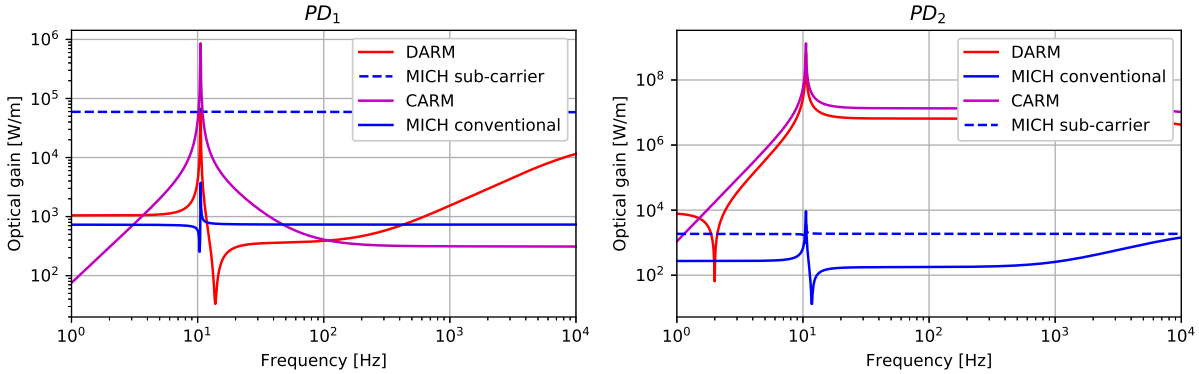

Figure 6.5: The optical gain of the conventional error signal for MICH at PD_1, a sensing port in reflection of the OMC, is very low. If instead, the sub-carrier (blue dashed lines) was used for MICH sensing, the optical gain of MICH is much larger than the conventional readout at PD_1. PD_2 at the input port of the interferometer is a popular readout port for MICH in advanced GWDs. The problem with the same is the low optical gain which can be seen in the figure above. We hence choose to readout MICH with the new sub-carrier to benefit from the high optical gain and the large signal separation

sub-carrier frequency has to be chosen such that it has a higher transmission to the dark port. For the sub-carrier to be transmitted efficiently to the dark port (see section 4.4.2 for a sample calculation) through a Schnupp asymmetry of 5 cm and be rejected by the OMC, the required frequency is in the GHz regime (see section 4.4.2). By using a 1.52 GHz sub-carrier, we can obtain an PDH-like error signal for MICH control at PD_1 by using the optical beat between the sub-carrier frequency and f_1. This sub-carrier is not resonant in the arm cavities and is outside the bandwidth of the OMC (hence not resonant in it either).

6.3.2 Potential injection scheme for the sub-carrier

Owing to spatial constraints, the sub-carrier would have to be injected from outside the vacuum system. In order to frequency shift the sub-carrier laser from the IFO carrier by 1.52 GHz, we could use a Rohde and Schwartz signal generator (see section 8.7.1). The technique of super-imposing

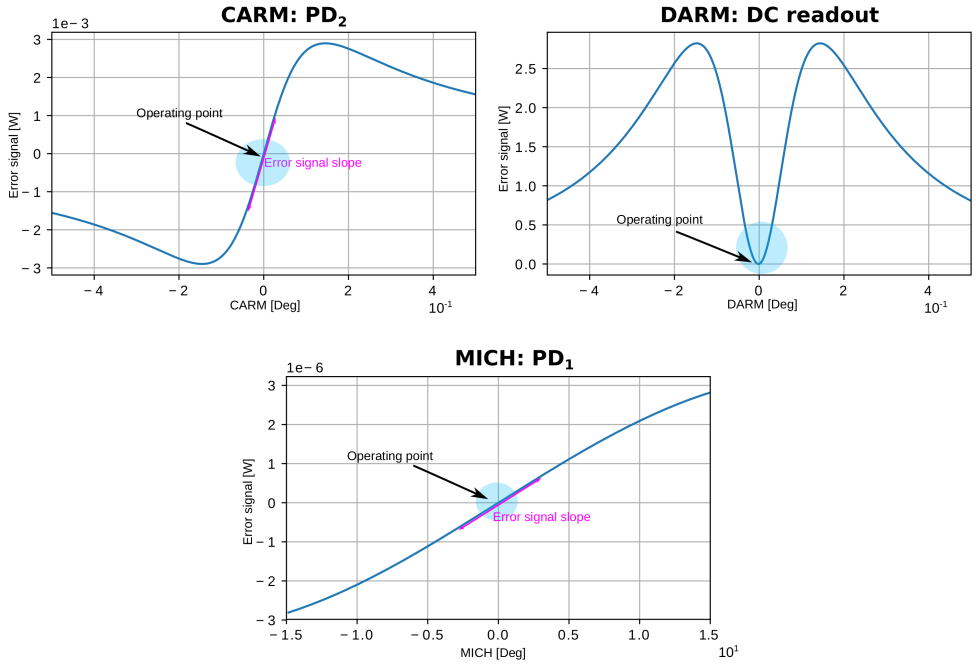

Figure 6.6: Error signals for CARM, DARM and MICH control. The error signal for CARM is sensed at PD_2, for MICH at PD_1 and DARM at DC readout photodiode from figure 6.3a. The optical gain in figure 6.5 at 0 Hz is the slope of the error signal at DC. To state approximately, the optical gain of the error signals is roughly equivalent to the slope of the error signal around the operating point. In the figure shown above, we have assumed MICH to not be the conventional readout but instead the sub-carrier readout.

a new laser beam onto the interferometer carrier can be employed here. This arrangement is shown in figures 6.3a, 6.3b and 6.7. The sub-carrier along with the interferometer pass through the PMC (for simplicity the PMC is not shown in the figures but is instead shown in figure 6.7) before passing through an EOM which phase modulates both these beams and adds 20.44 MHz sidebands on both the carrier and the sub-carrier. For MICH control, the optical beat between the sub-carrier and the 20.44 MHz sidebands can be used to derive an PDH equivalent error signal. This error signal would be similar in principle to the double-demodulation signals at aLIGO [140] with the added benefit of a higher optical gain. The sub-carrier laser is phase locked to the main IFO laser through an optical phase lock loop.

6.3.3 Shot noise limited noise budget for the 10m prototype

The definition of control loop noise and the factors affecting the level of loop noise in the final readout have been dealt with in section 4.1.3 and [91]. Having used FINESSE to build an optical

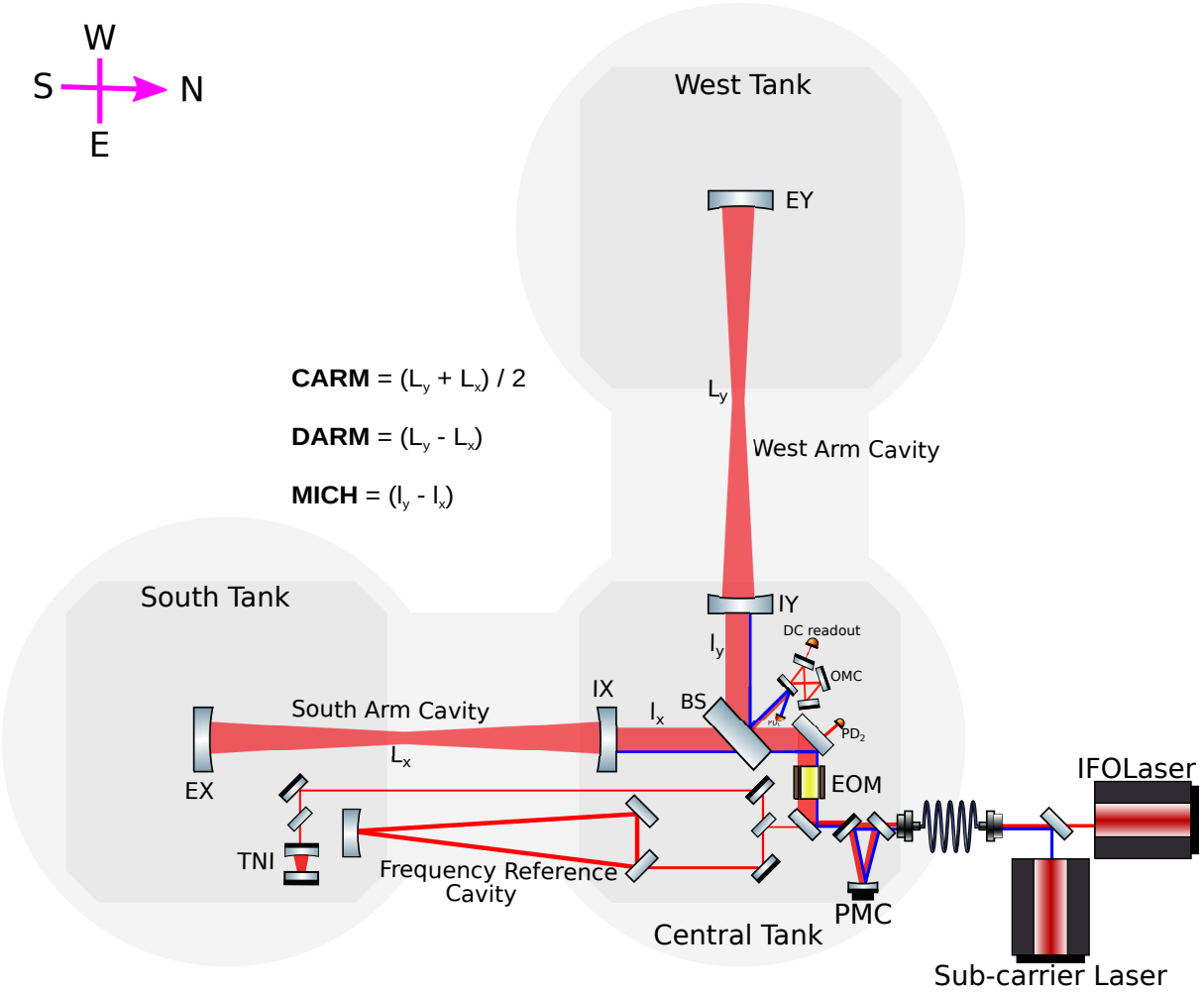

Figure 6.7: Simplified optical layout of the AEI 10 m interferometer including BHD path and an auxillary laser to introduce the sub-carrier. The Aux laser beam is superimposed onto the main interferometer beam and is offset from the same by 1.52 GHz. These two beams then enter the vacuum system through a fiber-coupler before passing through an EOM which introduced phase modulation sidebands at 20.44 MHz onto the IFO carrier and the sub-carrier. The sub-carrier laser can be phase locked to the IFO laser by either using a pick-off beam before it enters the vacuum system or by using the IFO carrier from the AR reflex of the main BS.

model and obtain a control matrix for the 10 m prototype, the loop noise model made with SimulinkNb [102] would potentially allow for fine tuning parameters like modulation depth, servo unity gain frequencies (ugfs), modulation frequencies [141].

In this section, the loop noise imposed via control is calculated in terms of displacement-equivalent shot noise limited sensitivity for DARM. In order to highlight the importance of optical gain and error signal separation on the readout photodiodes (because the level of control loop noise depends on these two parameters), two cases of MICH readout are compared. In both cases, the

basic assumption of DC readout is made for DARM. Sensing noise of each sensor (in our case, 3 dofs and 3 sensors) used to sense a particular dof, is propagated through the loops to obtain the effect on the DARM. The servos in all three control loops have a ugf of 200 Hz. Imposing this condition on the servos, allows us to imprint sensing noise onto the entire measurement band. The sensing noise from MICH and CARM couples to the DARM signal through the non-orthogonality of the optical plant. The scenario of imprinting sensing noise was used to set an upper limit for the influence of sensing noise. In fact, this would allow for modification of the servo design in order to prevent the DARM dof from being overwhelmed with control noise.

As mentioned earlier, MICH can be sensed by using an error signal obtained by demodulating at PD_2 using the beat between the carrier and f_1. Figure 6.8a is representative of the projected sensing noise from the closed CARM and MICH loops into the DARM loop. Ignoring the CARM loop noise and focussing on a bigger culprit, MICH sensing noise, it is possible to infer from the figure 6.8a that in order to be DARM shot-noise limited at the DARM readout port, the coupling from MICH sensing noise has to be smaller than a factor of approximately 10^5. Using the beat between the sub-carrier and f_1 to sense and control MICH at the port PD_1 allows us to obtain an error signal with a higher optical gain but with higher separation from DARM. This lowers the requirements on the suppression of MICH required in DARM be two orders of magnitude (see figure 6.8b).

For the new MICH readout, the principles of gain hierarchy [39, 63, 140] and servo design (see section 6.3.4) could be applied to mitigate the MICH sensing noise in DARM. For CARM control loop noise mitigation we could consider a feed-forward loop [142] to cancel the contribution of the same in DARM or eliminate the coupling path by using a new readout scheme for DARM (see section 6.4 for details).

6.3.4 Servo Design

To prevent the limiting of sensitivity of a detector by loop noise imposed by feed-back control, the control bandwidth is usually kept as small as possible (see chapter 4 for more details). The open loop gain of the loop is an indicator of the loop behaviour. It is the product of the transfer function of each 'component' in the loop (see appendix A for control loop basics). By modifying

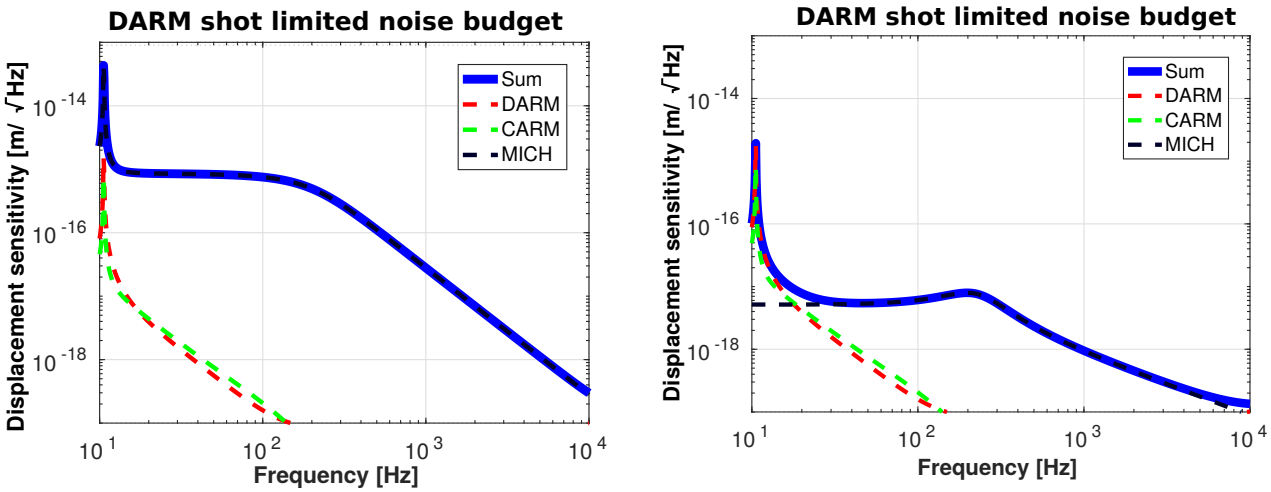

(a) Conventional MICH sensing

(b) MICH sensing using sub-carrier

Figure 6.8: Shot noise limited displacement noise budget comparisons for two MICH sensing schemes when DARM is readout using DC readout and CARM via a PDH error signal at PD_2. The sensing noise contamination from the MICH feedback control loop is two orders of magnitude lower for the case where MICH is sensed using the high optical gain error signal obtained by demodulating at the beat frequency of the sub-carrier and f_1 as opposed to the conventional MICH sensing using the beat between the IFO carrier and f_1.

the servo transfer function, the open loop gain can be modified thus changing the projected displacement-equivalent noise sensitivity. In general, the control loops in advanced gravitational wave detectors are designed to have a phase margin of 35°at the unity gain crossing [63, 143].

As a rule of thumb, at low frequencies the servo system is tailored to have large open loop gain at lower frequencies where displacement noises have a large magnitude and low gain at high frequencies in order to not imprint sensing noise into the GW measurement band. Assuming the new sub-carrier sensing scheme is employed for MICH length control, CARM and DARM length fluctuations are readout as described in section 6.3.1, figure 6.9a is indicative of the total displacement-equivalent shot noise in DARM. Figure 6.9b shows the condition where the ugf is lowered from 200 Hz to 12 Hz. Choosing a lower ugf for the MICH control loop lowers the sensing noise being fed into DARM. The choice of 12 Hz was not arbitrary but was made with the knowledge of all/any suspension resonances or SAS resonances (which are known to exist below 10 Hz) which may render the loop unstable.

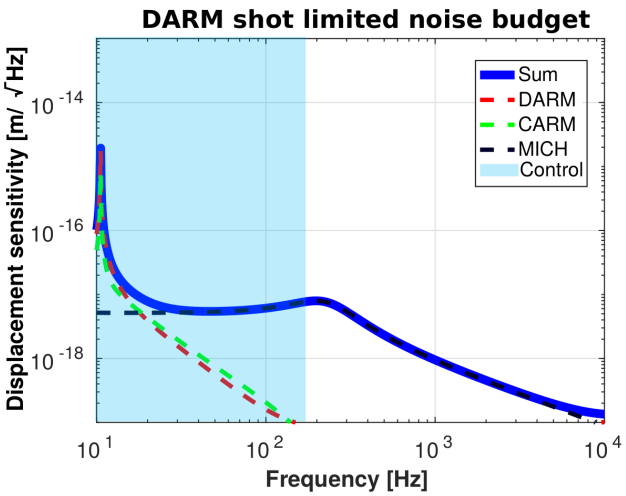

(a) SNLS for DARM : MICH ugf to 200 Hz

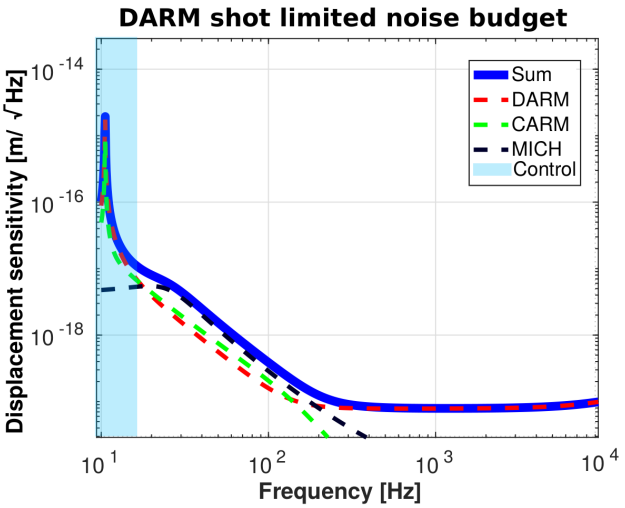

(b) SNLS noise budget for DARM : MICH ugf 12 Hz

Figure 6.9: Figures a) and b)show the shot noise limited displacement noise budget for the sensing scheme illustrated in section 7.5.2 and show the impact of servo design on the sensing noise contribution from the MICH control loop. The servo designed for MICH control will be modified during commissioning and will accommodate the more complex suspension transfer functions, actuator responses and other effects not modeled here. The shaded blue area indicates the region of active control for MICH.

6.3.5 Maximum tolerable rms motion

The residual motion of the mirrors can be estimated using the noise budget infrastructure that has been setup with SimulinkNb and FINESSE. If the DFO chosen for DC readout is in the range of picometers, experience with other GWDs has shown that the calibration does not vary by over 10 percent [142]. If were to take this for granted, the maximum tolerable length fluctuations in DARM can then calculated to be,

$$\Delta\mathrm{DARM} = \frac{10}{100} \times \mathrm{DFO} = 0.5 \times 10^{-12}\,\mathrm{m}\ ,$$

where, DFO is the dark fringe offset.

The relationship between DARM and MICH is the amplification factor due to the Fabry-Perot arm cavities. Without this factor, MICH and DARM are indistinguishable. Using this, the maximum tolerable length fluctuations in MICH can calculated as,

$$\Delta\mathrm{MICH} = \frac{2F}{\pi} \times \Delta\mathrm{DARM} = 2.1 \times 10^{-10}\,\mathrm{m}\ ,$$

where, $\frac{2F}{\pi}$ is the aforementioned amplification factor of the arm cavities having a finesse F (in our case, F=660).

The free swinging motion of the mirrors in the Single Arm Test (see section 5.8 for details on the aims and objectives of the SAT) as measured by the electrostatic drive (ESD which is used for actuation purposes) is $10^{-8}\,\mathrm{m}/\sqrt{\mathrm{Hz}}$ at 1 Hz [144]. At low frequencies, this motion is representative of actual mirror motion. This informs us that the MICH motion needs to be suppressed by two orders of magnitude in order to meet the aforementioned requirement. At low frequencies, the control loop forces the optic to move in order to cancel the sensing noise at the sensor and the rms motion of the total displacement-equivalent shot noise can be calculated and compared to ΔDARM (although arguably ΔMICH could be used, the requirements on DARM are higher and also it is our dof of interest).

At frequencies above 15 Hz, the assumption that the ESD measures actual mirror motion is no longer valid and for purposes of this simulation, the measured mirror motion is artificially rolled off as $1/f^6$ in order to not be limited by the seismic induced motion in the detection bandwidth (this assumption is valid and the combination of the seismic attenuation system and the suspensions function well enough for us to be limited by quantum noise and not seismic noise). The filtered seismic noise at frequencies greater than 15 Hz can then be added to the feed-back signal of the mirror control at frequencies below 15 Hz and the rms of the total displacement noise when all the control loops are closed can be calculated. Figure 6.10 is representative of the same and can be used to set an upper limit on the maximum tolerable motion. The residual motion of DARM dof has a root mean square of 1.441×10^{-14} m, integrated from 10 kHz to 10 Hz. This is below the requirement calculated for ΔDARM (and shown by a dotted black line in figure 6.10) thus showing that the control loop is does not cause the mirrors to move more than the calculated tolerances on DARM. This number is subject to change when suspension resonances will be added to the control model and the MICH servo would then require a much more sophisticated design.

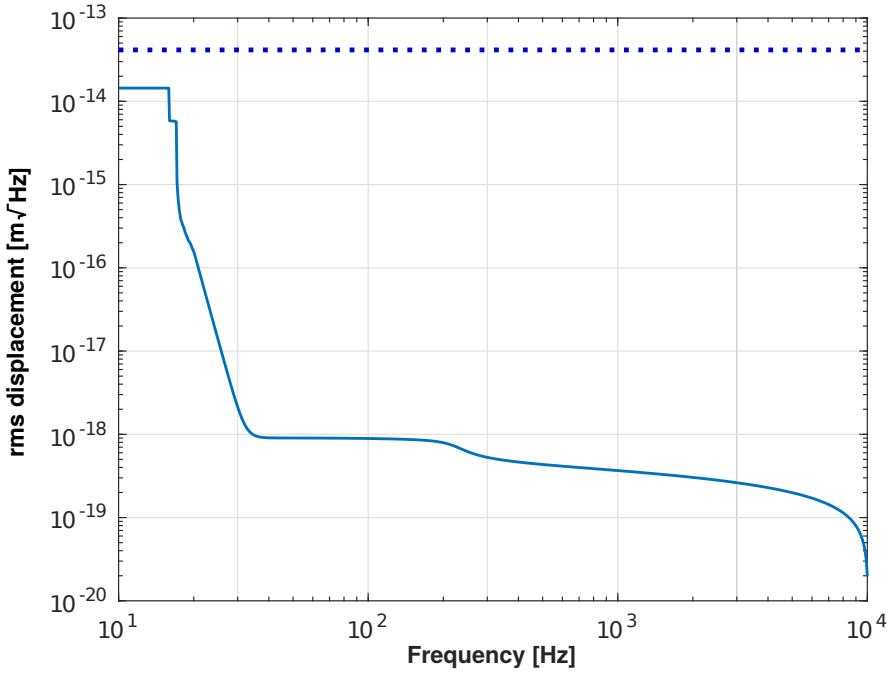

Figure 6.10: The maximum tolerable rms of mirror motion when all the control loops are closed at 10 Hz is $10^{-14}\mathrm{m}/\sqrt{\mathrm{Hz}}$. This motion is lower than the total tolerable DARM fluctuations which is indicated by the dotted blue line.

6.4 Consideration of DARM readout schemes for the 10m prototype

The most common readout technique for DARM in the current second generation detectors is DC readout which involves off-setting the position of the arms by a microscopic amount (of the order of picometers) in order to allow a small fraction of the carrier to leak into the dark port to provide a local oscillator (LO) for DARM readout with a stable phase reference [33]. This asymmetry of operating the arms slightly off resonance leads to couplings of the auxillary degrees of freedom (in our case, CARM and MICH) into the DARM channel via technical radiation pressure at low frequencies [90]. The displacement due to this effect can be calculated by:

$$\Delta x = \frac{1}{2mc(\pi f)^2}\sqrt{\frac{2hcP}{\lambda}}\ , \tag{6.2}$$

For the 10 m prototype with 100 g masses, this displacement is rather significant unlike in current advanced detectors like aLIGO (40 kg test masses) or ET (211 kg test masses). This served as the

motivation to use a different readout technique for DARM in the 10 m prototype.

Balanced homodyne (BHD) readout is considered as a potential readout scheme for DARM. In this readout scheme, the output signal is readout by taking the difference between two photodiode signals which are mixed with a local oscillator beam on another beam-splitter [87–89]. The local oscillator chosen here is a copy of the interferometer carrier. The most well known advantages of the scheme as demonstrated by several table top experiments [89] is the freedom to choose the readout angle and the the ability to change the phase of the LO relative to DARM and thereby optimising the sensitivity of the detector. In existing GWDs, this improved sensitivity at particular frequency would allow for specific sources to be studied in detail. Detuning the SRC is another way to achieve a similar sensitivity improvement at certain frequencies a detuned SRC is not an a priori requirement for BHD.

Figures 6.11a and 6.11b are indicative of the simulated displacement-equivalent shot noise limited sensitivities for the two DARM readouts schemes. The dashed green plot in both the figures is the CARM sensing noise projected into the DARM control loop. If a DFO were to be used to facilitate DC readout for DARM, the power imbalance in the arm cavities due to DFO allows CARM, which can be viewed as the dof that controls the arm cavity build up; to couple to DARM readout [85] [90]. If BHD readout (figure 6.11b) were to be used for DARM, the need for the DFO is eliminated thereby removing the coupling path for CARM in DARM. Although BHD readout has this distinct advantage of decoupling the CARM from DARM, for training and pedagogical purposes, the 10 m prototype will implement DC readout while preparations are being made for BHD readout.

Figure 6.12 is a comparision between the DC readout scheme and the BHD readout scheme for DARM with a varying homodyne angle for the BHD case. The 10 m prototype being a facility to test advanced techniques, is an ideal place to test the nuances of this technique. At 100 Hz, the sensitivity of BHD readout is better than DC readout but the local oscillator phase and the exact readout angle needs to be optimised in order to achieve the broad-band sensitivity of DC readout. The tolerable phase noise of the local oscillator due to mismatches in the finesse of the arm cavity mirrors, OMC length noise coupling into the readout and many other such influential factors need to be studied before implementing this readout scheme.

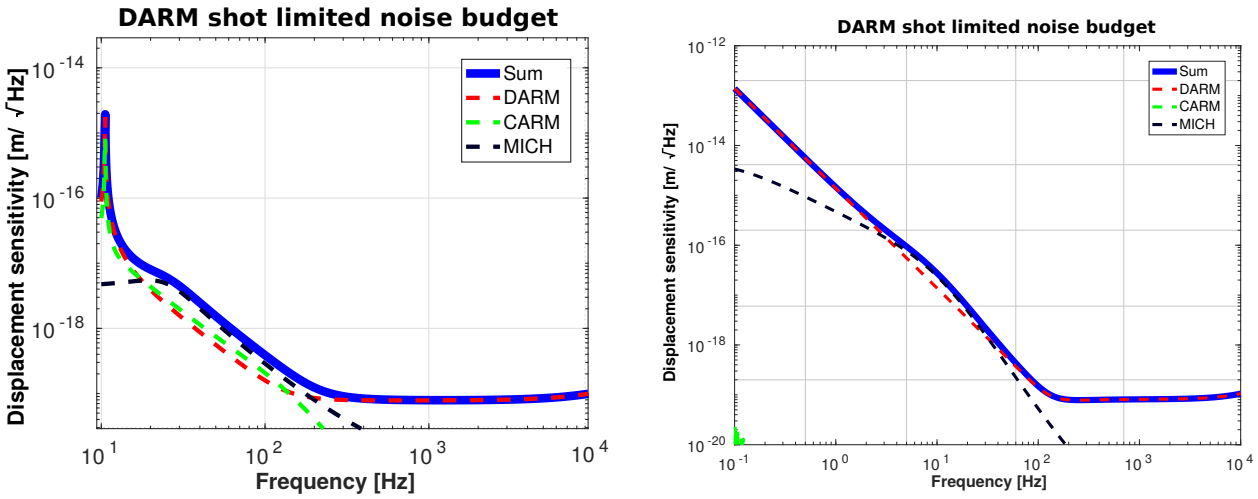

(a) (b)

Figure 6.11: a) SNL sensing noise budget using DC readout for DARM b) SNL sensing noise budget using BHD readout for DARM. The elimination of CARM sensing noise (dashed green lines) in BHD readout is the a motivator for the 10 m prototype to consider this readout scheme.

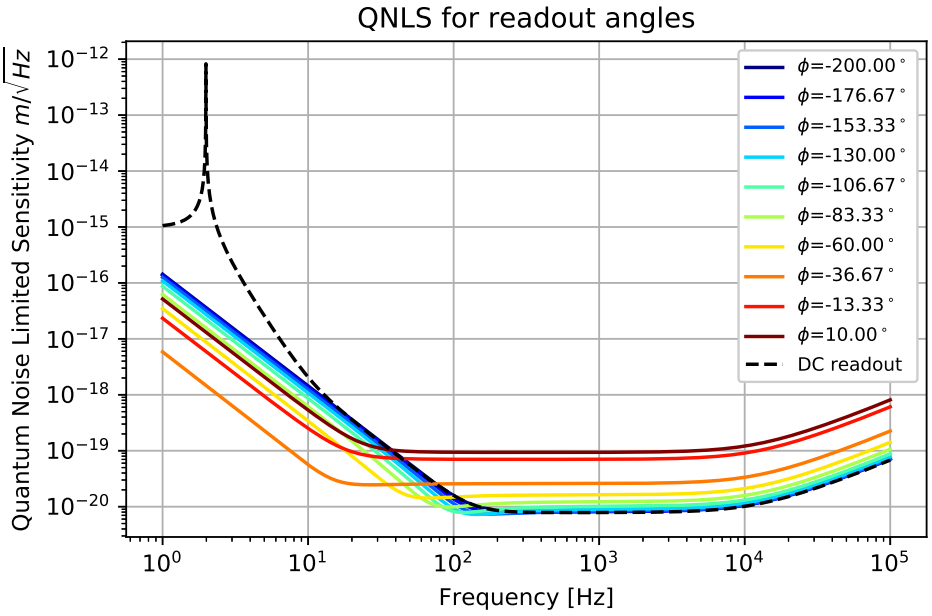

Figure 6.12: Comparision between DC readout with a dark fringe offset of 5.32 pm and BHD readout with varying homodyne readout angles. Choosing the 'wrong' homodyne readout phase can lead to poor sensitivity. The figure is only indicative of potential homodyne readout angles and to be able to use this in the experiment, a more thorough investigation is warranted.

6.5 Optical Springs in the single arm test

The main objectives of the 10 m prototype is to measure the SQL, after which it will be possible to demonstrate other techniques to overcome the same in current advanced detectors and

future detectors. The 'optical spring effect' which arises from detuning cavities is described mathematically and through experiments in [145–150]. The improvement in sensitivity in GWDs due to optical springs arising by detuning the SRC, have been discussed in detail in [151]. In this section, we present an overwiew of optical springs from the perspective of the single arm test. Theoretical and numerical 'experiments' to investigate the benefit of having differentially detuned cavities in the radiation pressure limited 10 m prototype are underway.

The SAT cavity which has been described in section 5.8 can be detuned to study optical spring effects (see figure 6.13 for a simplified sketch of the optical spring in the SAT). With FINESSE we have set up the infrastructure which has the capacity to not only calculate alignment signals and test the coupling of alignment control signals in length control signals [152], but can also be used to study radiation pressure effects. The demonstration of optical spring effects at the current stage would allow us to gain experience to deal with them in the in final configuration.

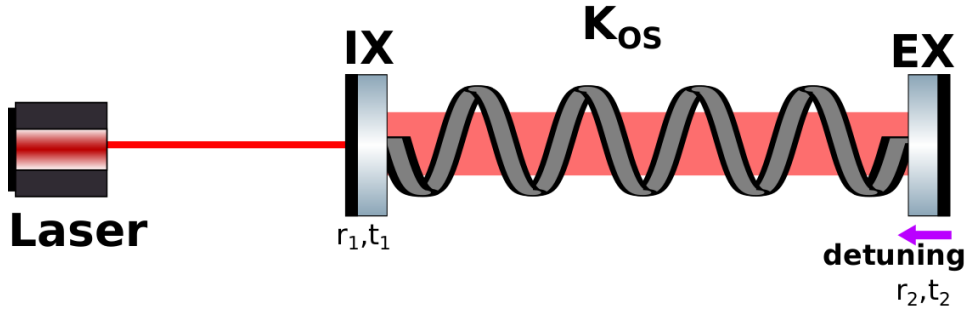

Figure 6.13: A cartoon sketch of the spring in the SAT cavity with input mirrors IX and EX and amplitude transmissions r_1 and r_2 respectively. The optical spring holds the mirrors IX and EX together and at low frequencies the cavity moves like an optical bar. The SAT cavity is detuned and the detuning shown in the figure is for the case when the cavity length decreases.

When a Fabry-Perot cavity is detuned, a linear coupling is introduced between the small fluctuations in the position of the cavity mirrors and the intra-cavity power [153]. The sign of detuning determines the nature of the optical spring. Figure 6.14 shows the optical transfer function of the SAT cavity from the cavity length fluctuations to the corresponding change in circulating power in the cavity for various detunings where the input cavity power is 200 mW, a finesse of 660 and a single pass length of 10.8 m (L_{Arm}).

For negative detunings when the cavity length gets longer (this is the convention we have adopted which is in accordance with the FINESSE convention), the optical spring has a negative spring

constant (using the mechanical analogy of a simple harmonic oscillator). In such a cavity, the radiation pressure forces push the cavity away from the resonance. In the alternative case where the detuning leads to a shorter cavity, the spring has a positive spring constant (a more comprehensive understanding of the consequences of a positive or negative spring constant can be found in [145, 146]). The radiation pressure force is the optical spring needs to be balanced by a second force. This force is normally provided by the control systems.

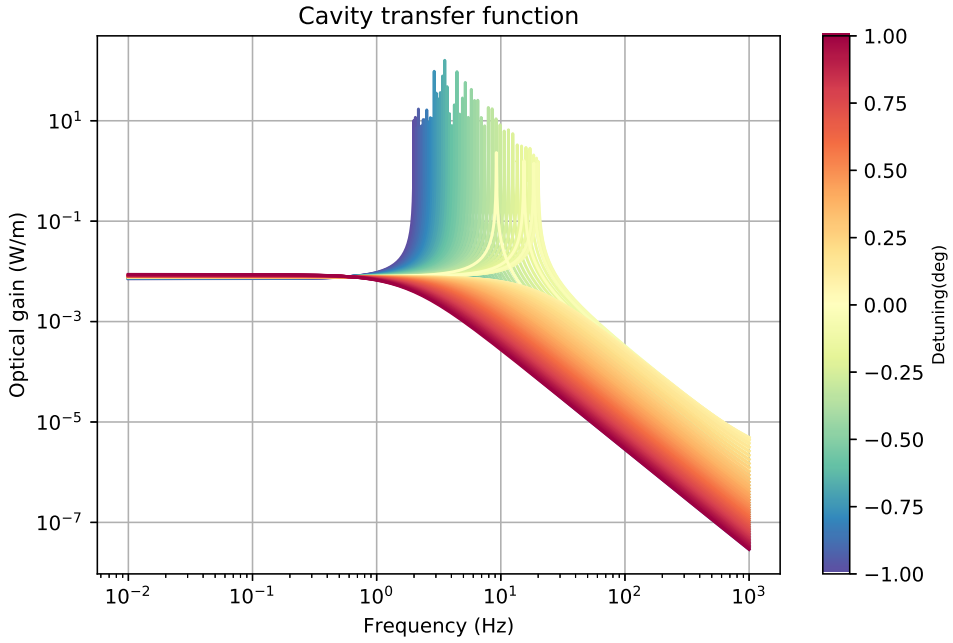

Figure 6.14: Optical transfer function of the detuned SAT cavity for different detunings which correspond to different macroscopic positions of EX.

The Young's modulus of diamond is $\approxeq 1.22 \times 10^{12}$ Pa and we can calculate the Youngs of the optical spring in SAT cavity (using equations from [147]) where the highest optical spring measurable is 20 Hz. For a mass (m), the rigidity of an optical spring at the resonance frequency can be calculated as:

$$K = (2\pi f_{os})^2 \times \mathrm{m} = 1579.136 \text{ N/m} \quad \text{where, m} = 100\text{g} \tag{6.3}$$

The radius of the beam entering the SAT cavity is $\approxeq$ 5 mm and thus setting the beam area to be $A = \pi r^2 = 7.8 \times 10^{-5}\,\mathrm{m}^2$. The Young's modulus of the optical spring holding the SAT mirrors

together can then be calculated to be :

$$Y = \frac{K L_{Arm}}{A} = 2.171 \times 10^8 \text{ Pa} . \tag{6.4}$$

With higher optical power and detuning, the Young's modulus of the cavity becomes closer to that of diamond implying that below the optical spring resonance, the cavity behaves as an rigid bar.

Parameters	SAT	Description
L_{arm}	10.8 m	Length of the cavity
F	660	Finesse of the cavity
FSR	1.5×10^7	Free spectral range
BW	$3\times10^5 Hz$	Bandwidth of the cavity
P_{in}	200 mW	input laser power
T_1	0.01	Power transmission of the input mirror
T_2	5 ppm	Power transmission of the output mirror
m	100 g	Mass of the mirror
λ	1064 nm	Laser wavelength
k	$\frac{2\pi}{\lambda}$	wave number
θ	0.1	cavity detuning in degrees

Table 6.2: Simulation parameters for the single arm test cavity

The radiation pressure dependent spring constant can be calculated as :

$$k_{opt} = \frac{-8\, P_{in}\, r_1\, r_2\, k\, T_1 \sin(\phi)}{c\,(1 + R_1 R_2 - 2 r_1 r_2 \cos(\phi))^2} \tag{6.5}$$

where, r_1 and r_2 are the amplitude reflectivities of the input and output mirrors of the SAT.

The parameter ϕ is the tuning of the cavity which can be calculated from $\phi = 2\,k\,\theta$. The spring frequency can then be calculated by :

$$k_{os} = \frac{1}{2\pi}\sqrt{\frac{k_{opt}}{m}} = 19.72 \text{ Hz} \tag{6.6}$$

Figure 6.15 shows the change in the spring frequency for varied detuning. A detuning of 0.1°corresponds to a length change of 2.96×10^{-10} m which corresponds to an optical spring at $\approxeq 20$ Hz. Using the parameters for the SAT highlighted in table 6.2, we can theoretically

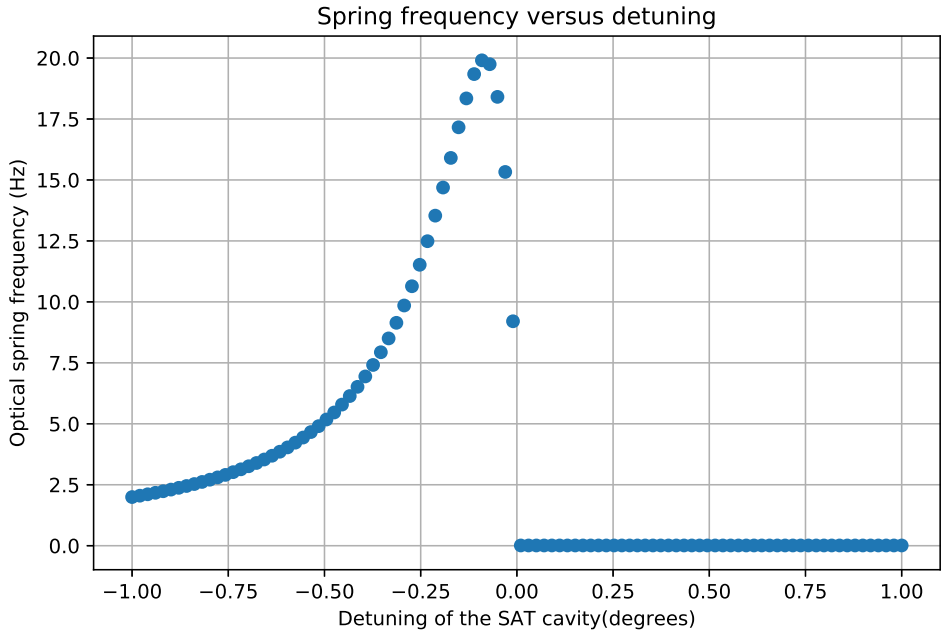

Figure 6.15: Change in optical spring frequency for a positive and negative detunings. As we go from a shorter cavity to a longer cavity(i.e. changing the sign of the detuning), the spring frequency is pushed lower owing to the change in the constant which depends on the detuning. For positive detunings, we do not see an optical spring.

estimate the spring frequency using equations from [5]. The spring frequency estimated from FINESSE is in good agreement with the theoretical prediction. The detuning of the cavity cannot be chosen arbitrarily. The detuning chosen to obtain an optical spring at the frequency $k_{os} = 20\,\mathrm{Hz}$ is $\approxeq 2.77 \times 10^{-4}$ times the laser wavelength. If this detuning were to be too large i.e if this detuning were to be larger than the cavity bandwidth, then the laser carrier would not be resonant in the cavity anymore. From our calculations, this detuning compared to the bandwidth of the cavity is 4.17 kHz which is well within the bandwidth of the SAT cavity.

In the course of modelling the full AEI 10 m interferometer with optical springs we discovered a notch in the interferometer response curve at low frequencies which arises from the phase difference between the light beams coming from the two arms. The notch frequency depends on the detuning of the arm cavities and the mass of the mirrors. Detailed investigations, both theoretical and FINESSE modelling are underway to understand the origin and the implications of this notch.

6.6 Discussions

6.6.1 DARM readout and longitudinal control of the AEI 10 m prototype

In this chapter a sensing and control scheme for the longitudinal control of the 10 m prototype which has a FPMI layout was presented. A new sensing scheme for the control of MICH dof was proposed which mitigates allows MICH to de sensed independently from DARM. This new sensing scheme for MICH along with BHD readout for DARM allows control of the interferometer within design specs.

6.6.2 Optical springs in the AEI 10 m prototype

An initial concern of optical springs being a problem during lock acquisition can be solved by using low powers during lock acquisition and then increasing the power slowly. The interesting 'feature' (a notch in the response transfer function of the Michelson interferometer) in the optical transfer function of the AEI 10 m prototype which arises due the differential detuning of the arm cavities is currently being studied with the help of both analytics and numerical modelling.

Chapter 7

GEO 600: testing new optical layouts and sensing schemes

Aerial view of the GEO 600. Picture courtesy Harald Lück.

7.1 Introduction to GEO 600

GEO 600 is the German-British GWD with the optical layout of a Dual Recycled Michelson interferometer (DRMI) with folded arms (see figure 7.2). The beam is folded once in the 600 m long arms, increasing the effective optical arm length to 1200 m. The current peak sensitivity of GEO 600 at 1 kHz was measured to be $2 \times 10^{-22} 1/\sqrt{\text{Hz}}$ [154]. The most promising signals to which GEO 600 would be sensitive to are signals with significant high frequency content such as transient burst signals arising from supernovae, gamma ray bursts etc. [155].

GEO 600 has been pioneering technologies for advanced GWDs for a long time. Some examples are the implementation of signal recycling in a large-scale interferometer, monolithic mirror suspensions, detuned signal recycling, ESD actuation etc. [156] [143] [157] [158] [159]. GEO 600 is also the first gravitational wave detector that uses squeezed light in order to improve sensitivity [13] [119] [160].

The sensitivity of advanced detectors all of which are larger has surpassed that of GEO 600 but the latter still participates in science runs by performing astrowatch with the other detectors and has also maintained astrowatch status when the other detectors were down for upgrades (for a measure, the sensitivity of GEO 600 is approximately that of Virgo high frequency during O2) thus enabling us to pay attention to the universe for cataclysmic events like supernova bursts. GEO 600 continues to explore new technology and is also undergoing upgrades to implement balanced homodyne detection as opposed to the existing DC readout in preparation for implementing EPR entanglement scheme. Testing this scheme in GEO 600 and analysing its merits and demerits would allow us to implement this technique in other advanced detectors thereby improving their sensitivity [161].

Having established the role of GEO 600 as a technology demonstrator, in this chapter the implementation of the new sensing scheme discussed for ET-LF in chapter 4 for controlling the length of the SRC in GEO is discussed. In this chapter I also consider the modification of the existing GEO 600 interferometer configuration from a DRMI to DRFPMI to explore the benefits of sensitivity improvement using the technique of 'twin-twin' signal recycling.

7.2 Quantum noise limited sensitivity of GEO 600: simulated and measured

A numerical model of GEO 600 was built in FINESSE based on the model made by Freise et.al. using parameters [162] which have been measured and estimated to investigate a alternative SRC length sensing scheme. The file was then modified to include the infrastructure required to test the new sensing scheme for GEO 600. Some of the parameters are mentioned in table 7.1. As a sanity check, the quantum noise limited sensitivity of GEO 600 predicted by FINESSE [92] was compared to the measured sensitivity (see figure 7.1). At low frequencies a deviation from the measured sensitivity is observed. This is because of two reasons; one, the current simulation model does not include any radiation pressure effects and two, GEO 600 is limited by several noise sources at these low frequencies: SRCL length noise, technical noises and a mystery noise [83]. Most of these noise sources are well understood.

Having validated the FINESSE model, the same model was used to find alternate error signals for SRCL control and also explore the aforementioned 'twin-twin Signal Recycling' configuration .

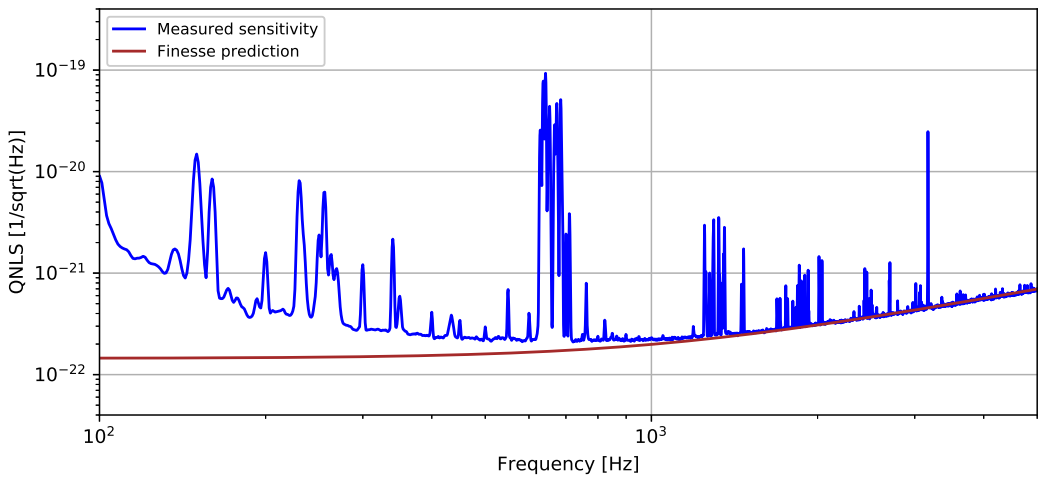

Figure 7.1: Comparison of the measured quantum noise limited sensitivity of GEO 600 and that predicted by a FINESSE model [163]. The reduction of quantum noise by using squeezing has not been considered here. Some of the line features in the spectra below 700 Hz are caused by excited violin modes, calibration lines and output mode cleaner alignment control lines.

7.3 GEO Length Sensing and Control

Having introduced the principles of length sensing and control in the previous chapters, this chapter focuses on the sensing and control of the three longitudinal degrees of freedom in GEO 600 – a dual recycled Michelson interferometer.

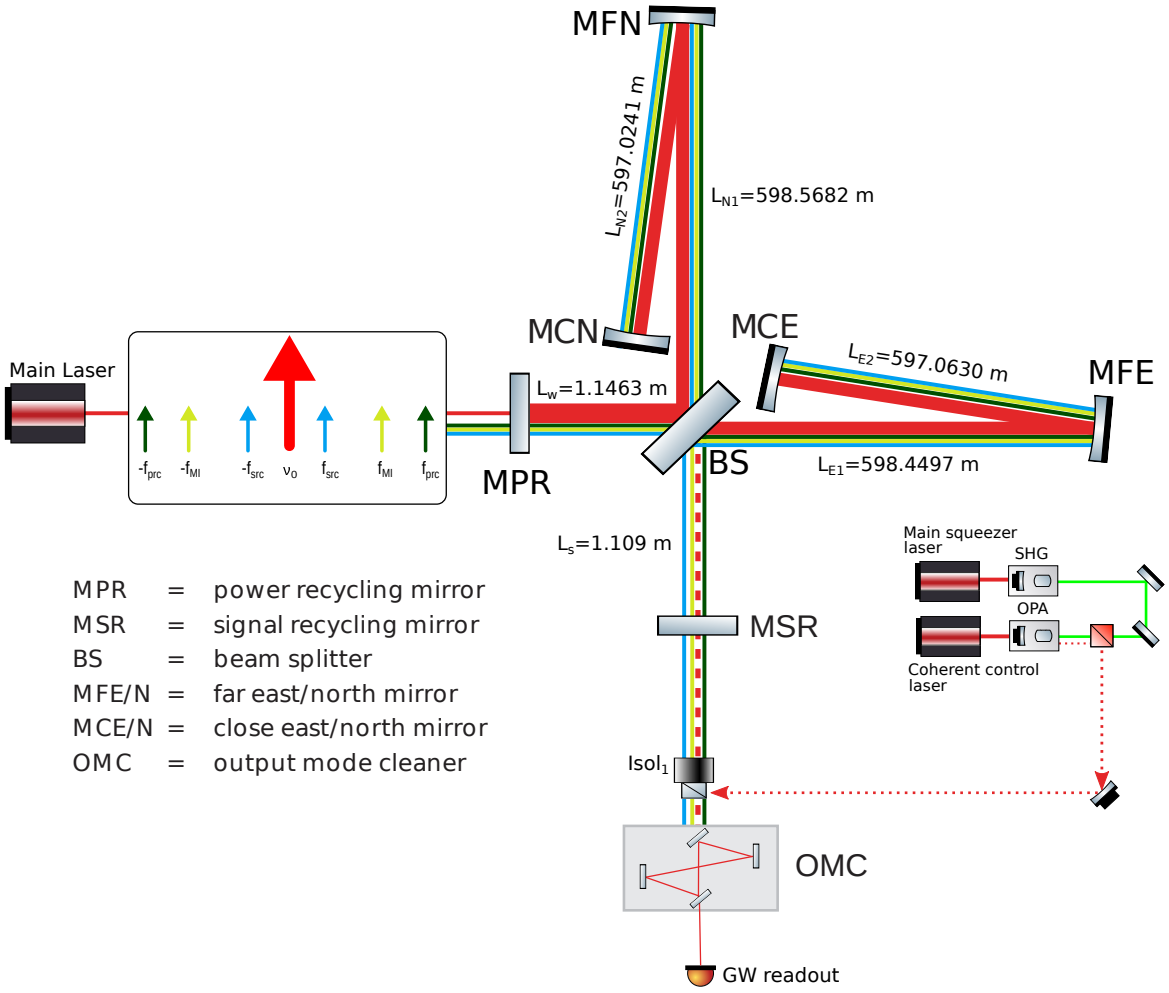

Figure 7.2: Visual of simplified optical layout of GEO 600 and depiction of different control sidebands. The sidebands chosen to be resonant in different parts of the interferometer. While the interferometer carrier is indicated in red, the sidebands are indicated by the different colors. f_{src} (solid green) and f_{prc} (solid blue) are resonant in the SRC and PRC respectively. The Michelson sidebands f_{MI} (lime) are resonant in the Michelson and even though the gravitational wave readout is done using DC readout, the Michelson sidebands are used in the process of lock acquisition. This figure is a modified version from [164].

The three DoFs (see figure 7.2 for a schematic of GEO 600) are:

- Length of the Power-Recycling cavity:

$$L_{PRC} = L_W + (L_E + L_N)/2$$

where L_E , L_N are the total lengths of the east and north arm respectively i.e. $L_E = L_{E1} + L_{E2}$ and $L_N = L_{N1} + L_{N2}$. L_W is the distance between the MPR and the BS.

- Differential length of the Michelson interferometer (this can be thought of as the dof that maintains the operating point of the interferometer):

$$\Delta L = L_E - L_N$$

- Length of the Signal-Recycling cavity:

$$L_{SRC} = L_S + (L_E + L_N)/2$$

with L_S as the length of the south arm i.e. the distance between the MSR and the BS.

7.4 Current GEO parameters and updated parameters

GEO 600 uses one modulation frequency for the longitudinal control of each of the aforementioned dofs : 37.16 MHz (L_{PRC}), 9 MHz (L_{SRC}), 14.90 MHz (L_{MI}). f_{SR} and f_{MI} are chosen to be multiples of the FSR of the PRC in order to be able to pass through the PRC. In GEO 600, the power recycling cavity is used as a reference for the frequency stabilisation of the main laser [143] [157] and the error signal to control PRCL is obtained in the reflection of the PRM by taking the optical beat between the interferometer carrier and the 37.16 MHz sideband. This modulation frequency is chosen to be resonant in the PRC only. The 14.90 MHz sidebands are used for lock acquisition of the differential Michelson (MID : science signal) and the final readout for the same is DC readout. The differential wavefront systems also use this 14.90 MHz sidebands for alignment control (the concept of alignment control is not dealt with in this thesis). The MI sidebands (f_{MI}) can also be used as a local oscillator in the event of switching to BHD for

Parameter	Existing value
$l_{schnupp}$	0.0796 m
l_{prc}-l_{src}	0.037 m
FSR_{SRC} and FSR_{PRC}	≈125 kHz
f_{MI}	14.905 MHz
f_{prc}	37.16 MHz
f_{SRC}	9017350 Hz
P_{PRC}	2.797 kW
P_{SRC}	0.675 W
P_{East}	1.433 kW
P_{North}	1.365 kW
Dark fringe offset	2.0984×10^{-10} m
P_{OMC} transmission	7.27 mW

Table 7.1: The table shown above is a list of the optical lengths and powers in the recycling cavities in GEO 600 assumed in the model.

GEO 600. These sidebands contain less HOM contamination since being being offset from the PRC resonance, they get bounced off the imperfect mirror surfaces less often. These sidebands can also be re-purposed to be the stable reference to phase lock any auxiliary lasers to the main interferometer laser (see the section 7.7.1 for more details).

The SRC length error signal is sensed and controlled using the carrier and the 9 MHz modulation sideband in reflection of the PRC (this could also be done by using a pick off from the beam-splitter). The predominant challenge with this technique in GEO 600 is the feedback noise introduced by this error signal into MID. The MID signal is plagued by noise from the current SRCL control loop up to 200 Hz [83].

To further investigate the noise from the SRC, the Finesse model described previously was used to compare the noise coupling from the SRC signal to the science signal, For completeness the same analysis is performed for the PRC. The figure 7.4 shows the coupling of SRCL into the MID signal up to 220 Hz. The main coupling mechanism is through the dark fringe offset which is a small offset in the position of the end mirrors which allows a small part of the interferometer beam to leak into the dark port to serve as the local oscillator for DC readout [90].

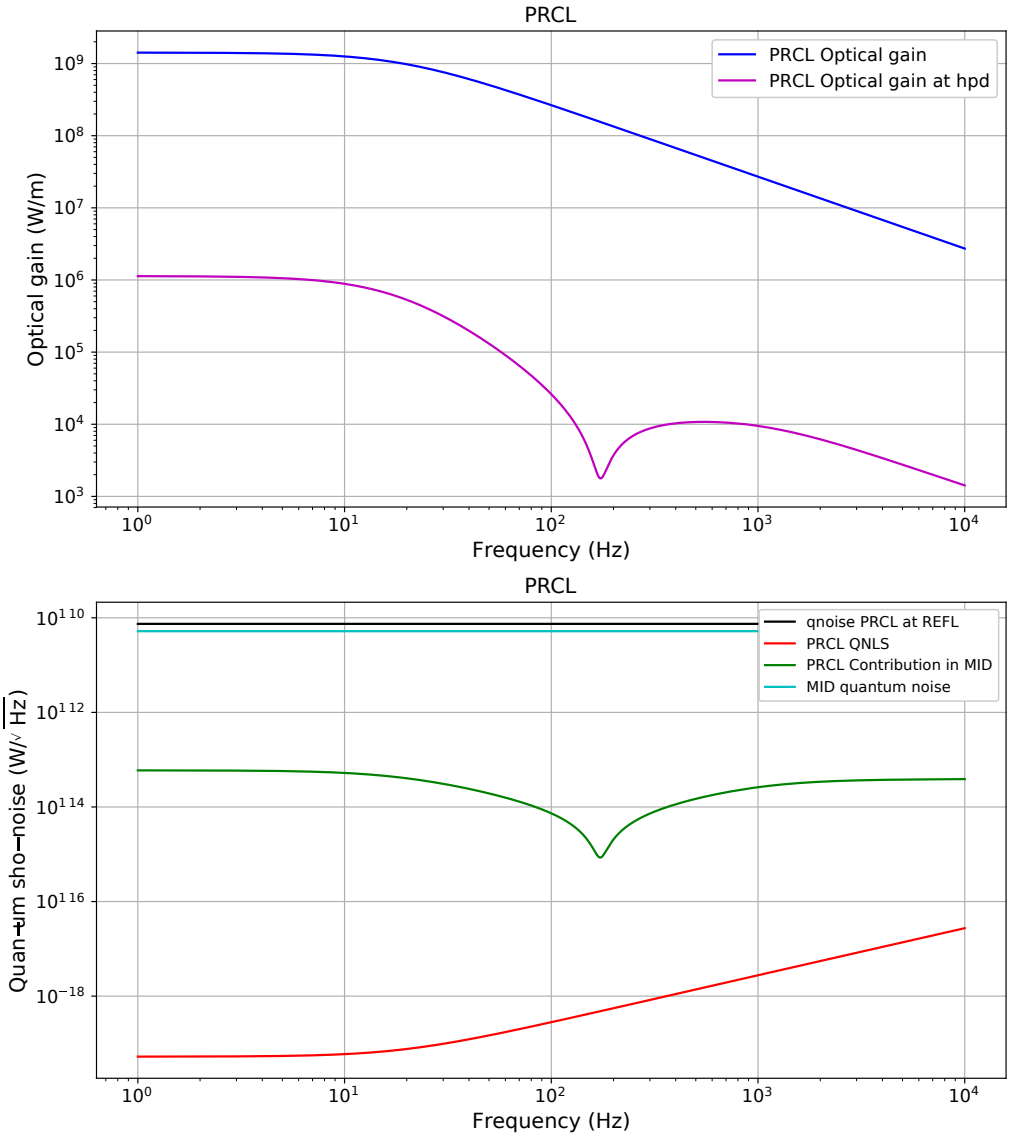

Figure 7.3: PRCL contribution to MID: PRCL readout is performed using the 37.16 MHz carrier

Figures 7.3 and 7.4 are aimed at providing an insight into the optical coupling of PRCL and SRCL into MID. The solid blue line in both the plots is indicative of the optical gains of PRCL and SRCL error signals at their respective readout points in W/m. This optical gain at low frequencies can be approximated to the slope of the error signal used to control the length of the PRC and SRC respectively. The purple line is the optical gain of PRCL and SRCL in W/m at the HPD (high power photodiode, used to readout the GW signal). This is indicative of the spurious amount of PRCL and SRCL motion that shows up at the sensing port of MID. The black line is the quantum shot noise at the PRCL and SRCL sensing ports respectively in $W/\sqrt{Hz}$. The quantum shot noise at the MID photodiode is shown in cyan and has the units $W/\sqrt{Hz}$ as

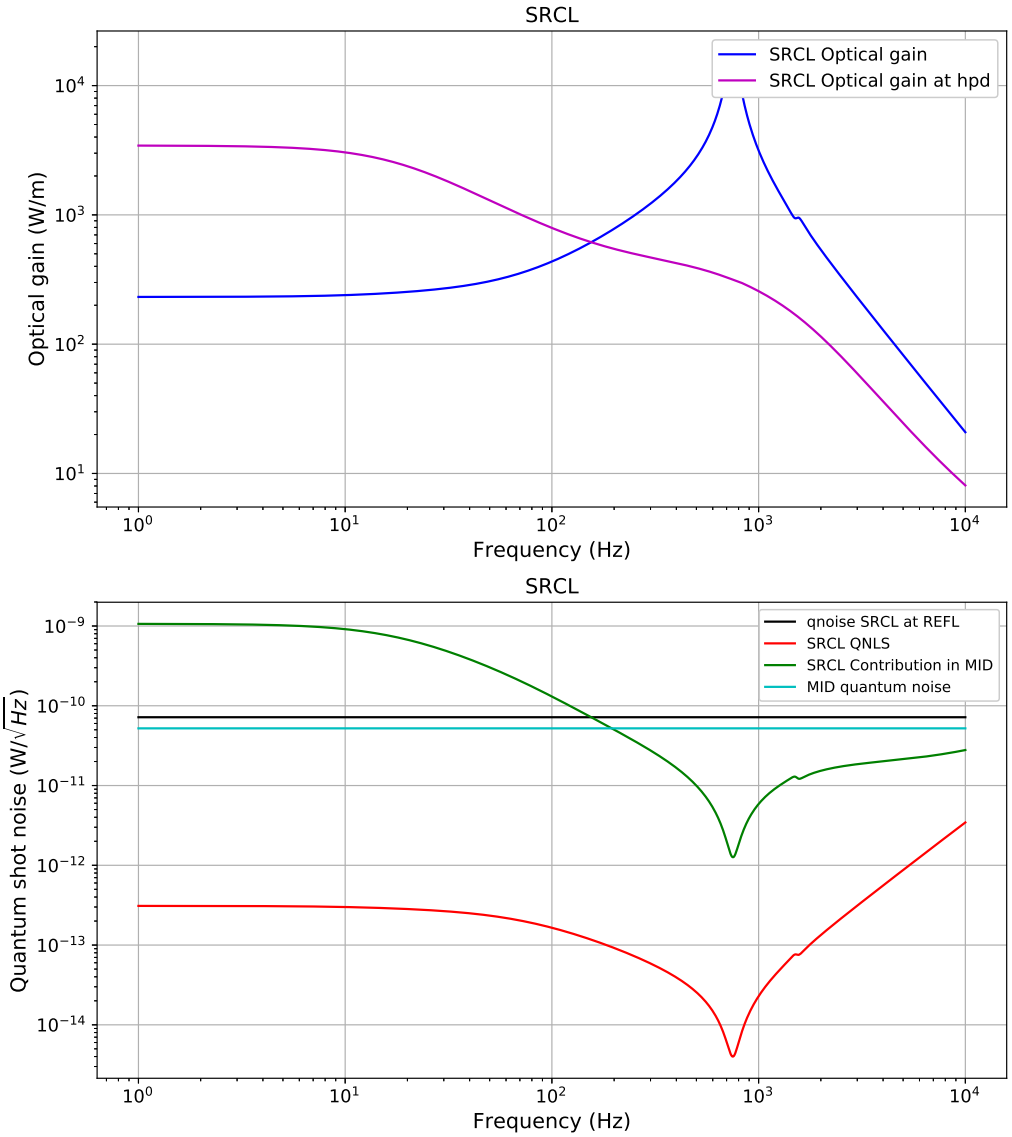

Figure 7.3

Figure 7.4: SRCL contribution to MID: using the current sensing scheme of 9 MHz modulation sidebands to produce an error signal for SRC length control.

well. The contribution of PRCL or SRCL in MID (dark green) can then be calculated in units of $W/\sqrt{Hz}$ in order to be able to compare it to the MID quantum shot noise. In the case of PRCL, one can understand from the plots that the shot noise contribution into MID is not a problem. However for SRCL, up to 220 Hz, the MID signal is dominated by the motion of the SRM if it were locked with the currently chosen error signal.

This SRCL error signal which has a low optical gain, is susceptible to changes in demodulation phase (see figure 7.5) to a degree. As a precursor to preparation for implementing the EPR

layout, the SRC will be detuned to increase the sensitivity to certain sources of gravitational waves [161]demonstrated previously [13] [82]. In combination with DC readout, this detuning of the SRC opens a coupling path for sensing noise to creep into the GW readout and till BHD is implemented in GEO 600, this could be a possible limiting noise source at low frequencies. These factors served as a motivator to find a solution to mitigate the SRCL length noise.

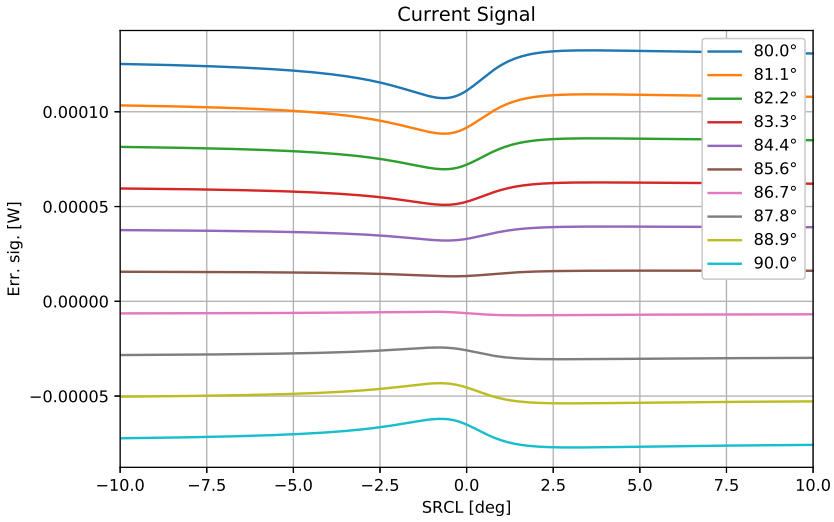

Figure 7.5: Susceptibility of simulated SRCL error signal to changes in demodulation phase. The plot demonstrates the change in operating point of the SRCL signal to small changes in the demodulation phase.

7.5 Proposed improvements to GEO LSC

Having established the nature of the problem with SRCL control, a potential way to mitigate the coupling into the MID signal can be considered. As proposed for control of the SRM in ET-LF (see chapter 4), the SRM in GEO 600 can also be controlled with a similar technique thus demonstrating the potential application in ET-LF and fulfilling it's role as a technology demonstrator for future gravitational wave detectors.

In order to obtain an error signal for SRCL control which is not influenced by the PRM, a phase modulated signal would have to be injected from the output side of the interferometer. This is the same side as the squeezer. Squeezed states are injected into the interferometer through the Faraday isolator indicated by Isol_1 in figure 7.2. An isolator is designed to allow propagation of

polarised light in one direction alone. As the input port of the Faraday is used for injection of squeezed states, an alternative injection point is required such that the squeezed states injected into the interferometer are not affected.

Figure 7.6 is a prospective injection scheme for the sub-carrier. The squeezed states produced by the OPA (indicated by the dotted purple lines) are in s-polarisation before being injected into the interferometer following the arrows.

Injection of the sub-carrier directly through the Faraday Isolator shown in Figure 7.2 is not possible owing to the squeezed vacuum states being injected through that port in order to minimise quantum noise in the interferometer. It is however possible to inject the sub-carrier using polarisation techniques without introducing additional lossy optical elements (e.g. a beam splitter) in order to not couple in additional anti-squeezing. We hence propose to inject an additional light field with an auxiliary laser (sub-carrier). The purple laser is phase locked to the GEO 600 main laser. This sub-carrier is injected at Isol_2 is injected in p-polarisation and is transmitted. The polarising beam splitter rotates the p-polarised beam by 45 °, and it passes through the faraday rotator and is rotated by another 45 °into s-polarised by the second polariser before being reflected by the OPA. Once reflected by the OPA and having been rotated to the correct polarisation earlier, the sub-carrier is now 'imprinted' onto the squeezed states and can be injected into the interferometer. The squeezed beam is aligned to the main interferometer with the help of a bright beam which is shuttered off when the squeezing is in operation.

This sub-carrier is chosen such that it is resonant only in the SRC and if GEO 600 were to switch between tuned and detuned operation, it would be easy to change the frequency of the sub-carrier. The justification behind choosing a GHz frequency (2.85 GHz) is the bandwidth of the OPA (squeezer cavity off which the sub-carrier is reflected) which has a bandwidth of about 100 MHz and in order to not interfere with the squeezed states coming out of the OPA, and also to be reflected off the OMC, a frequency of 2.85 GHz was chosen for the sub-carrier. The sub-carrier laser (see figure 7.6) is frequency shifted by the GHz frequency with the help of a signal generator and more details about the same are mentioned in the following sections.

A consequence of the current PRC parameters (i.e. the PRC is under-coupled as opposed to being impedance matched) is the fact that the PRC is co-resonant for the sub-carrier (at low frequencies:

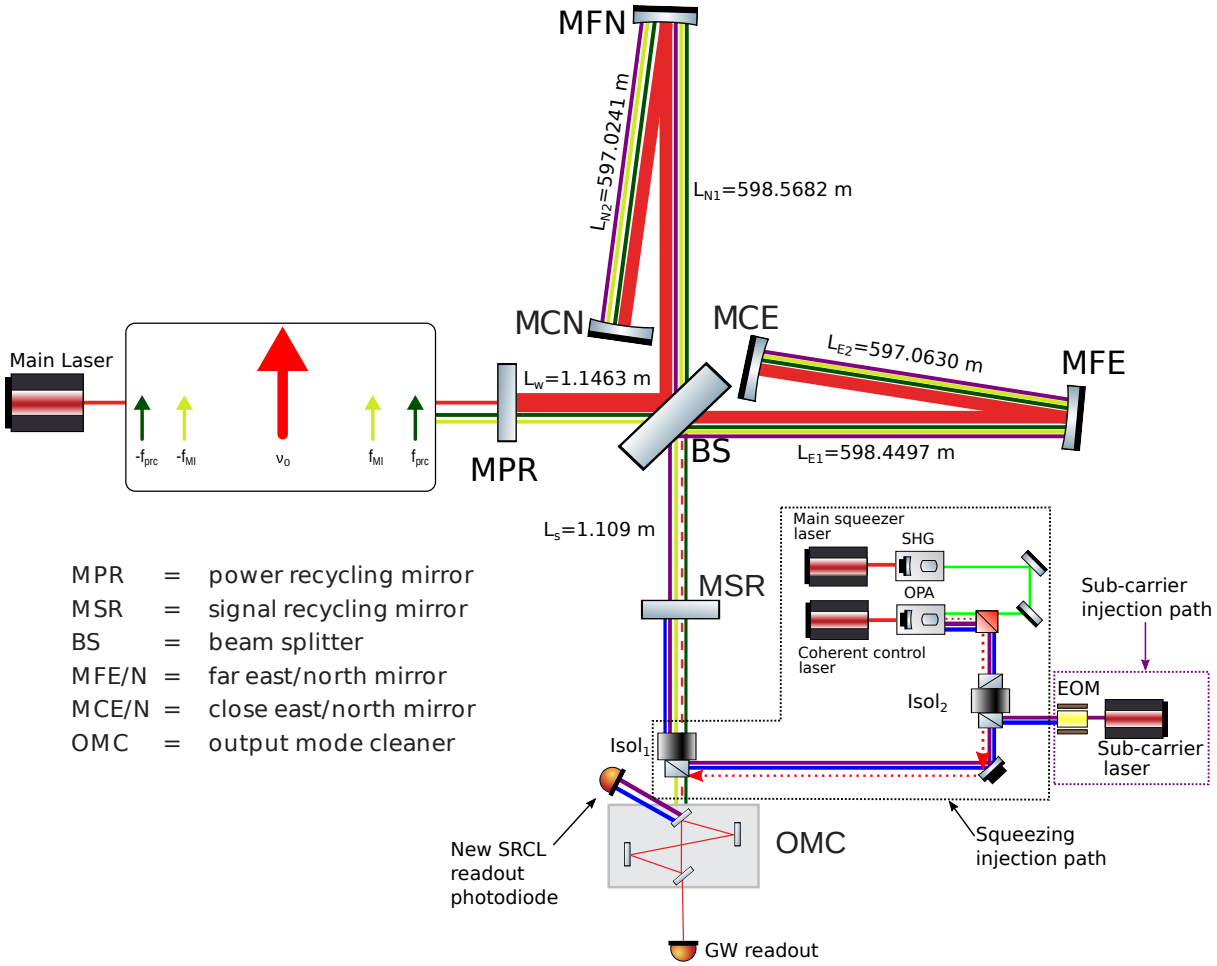

Figure 7.6: The sub-carrier shown in purple solid lines is reflected off the OPA, imprinted onto the squeezed states (dotted red line) and injected through $Isol_1$ into the interferometer. While the sub-carrier behaves as a stable phase reference for the SRCL error signal, in order to generate a PDH style error signal, a pair of phase modulation sidebands are required. These sidebands are shown in solid dark blue line in the figure and is not resonant in the SRC. The path of the squeezed states is highlighted by the dotted black box. The additional laser and phase modulator are shown by the purple box. The sub-carrier upon being injected through the isolator $Isol_2$, and reflected off the OPA, follows the same path as the squeezed states which had been pre-aligned to the interferometer.

see table 7.2 for the other frequencies that had been considered) leading to the condition that we would need extraordinarily large frequencies ($\approxeq$ 179 GHz) to be away from the influence of the sub-carrier, in the present scenario [165]. The PRC has a much larger gain than the SRC so unless the length of the SRC or the Schnupp asymmetry can be changed, we are stuck with this choice of modulation frequency. This is due to the large gain of the PRC (about a factor of 1000) which makes it so that the sub-carrier leaking into the PRC via the Schnupp coupling is resonantly enhanced. Another consequence of this is that the common mode of the Michelson

(which in principle needn't be controlled as it is essentially just the PRM motion) shows up rather strongly at the PRCL sensing port. However as this signal is degenerate with PRCL, it is sufficient to control PRCL.

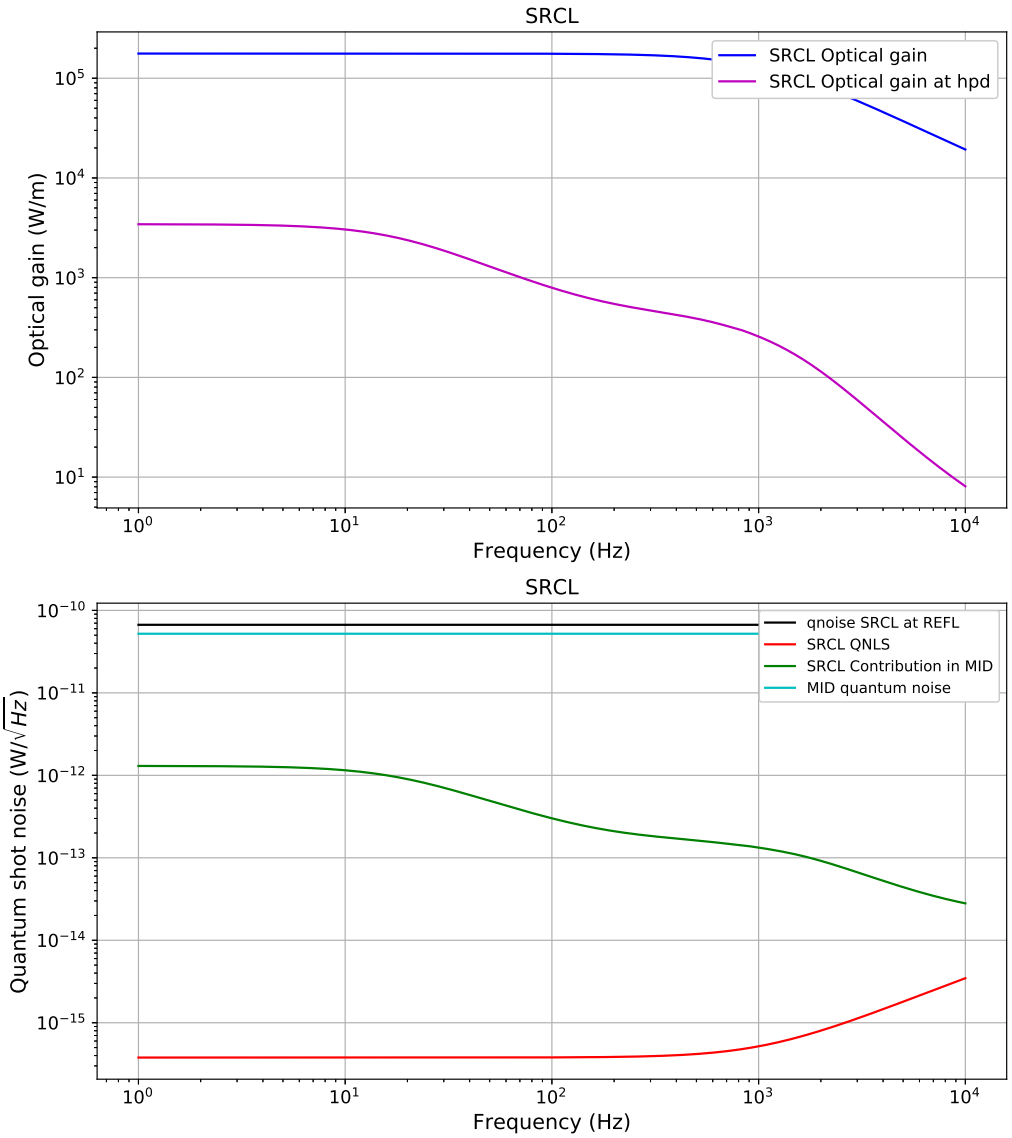

Figure 7.7: Using a the approach presented in section 7.4, the SRCL contribution to MID when using the GHz sub-carrier with the 15 MHz modulation sidebands to produce an error signal for SRM control. Compared to the present scenario of SRCL control, this scheme provides two orders of magnitude isolation from the shot noise of MID.

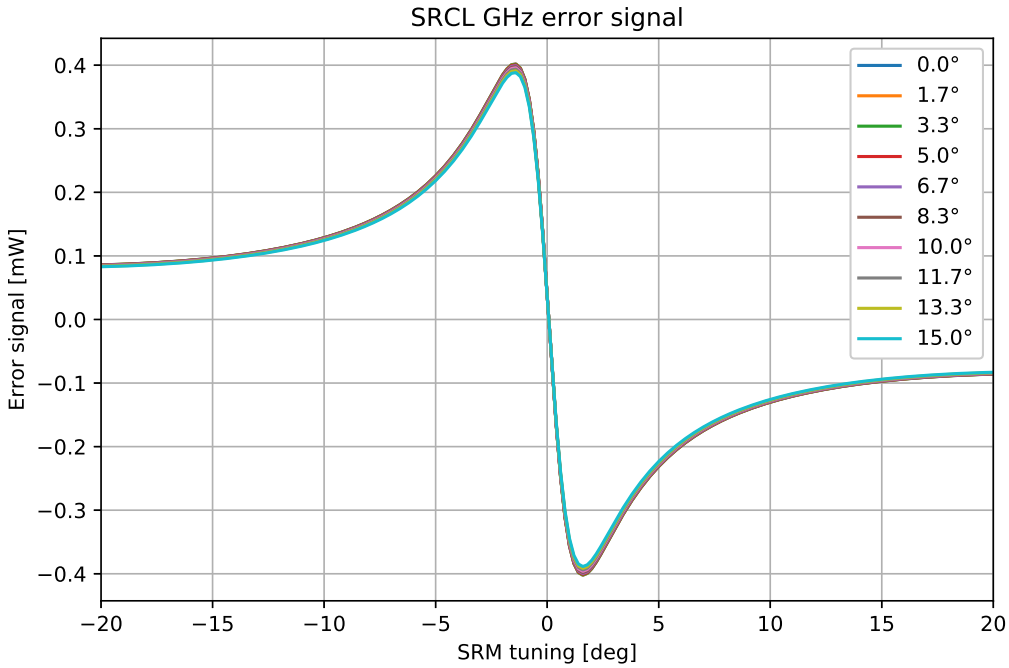

Figure 7.8: The error signal obtained with the new technique is robust to change in demodulation phase compared to the error signal obtained with the 9 MHz sidebands (see figure 7.5).

7.6 Sub-carrier parameters

To put the effect of the PRC into more perspective and to justify the use of the 2.85 GHz sub-carrier, I compared a few additional frequencies that had been initially considered for the sub-carrier frequency. From table 7.2 the undesirability of the lower modulation frequency can be reduced to two reasons: the enhancement by the PRC for the lower modulation frequencies (which leak to the common port of the interferometer via the Schnupp asymmetry) allows for a larger coupling from the common Michelson motion to the HPD; lower modulation sub-carriers are also not effectively rejected by the OMC thus contributing more to the shot noise on the HPD. Lower modulation frequencies also enter the OPA and might interfere with squeezing.

The sub-carrier frequency that has been chosen, 2.85 GHz is the offset frequency to the sub-carrier laser which is phase locked to the main GEO 600 laser. Although the details of the experimental implementation are presented in the following section, in the table 7.3 some of the essential parameters of the sub-carrier such as the resonance of the same in the Michelson arms, PRC and SRC are presented. Ideally, the OMC can de re-designed to completely reject the sub-carrier

Parameters	250.418 kHz	27.428 MHz
North Arm	0.01452 W	0.01025 W
East Arm	0.02162 W	0.0282 W
SRC	0.03562 W	0.03510 W
PRC	0.000542 W	0.0025 W
sub-carrier contamination on HPD	0.86 mW	2.34443 μW

Table 7.2: GHz frequencies were not popular in gravitational wave detectors because of the poor single sideband noise. The new signal generators for example the ones manufactured by Rohde and Schwartz [97] have very low single sideband noise thereby not contributing to additional shot noise and contaminating the science signal.

but judging by the power of the sub-carrier on the HPD, it can be concluded that this is an acceptable frequency to work with.

Parameters	Power of sub-carrier
North Arm	0.01838 W
East Arm	0.01800 W
SRC	0.03640 W
PRC	4.2354 μW
sub-carrier on HPD	9.50986×10^{-8} W
Carrier (1064 nm) on HPD	0.00723 W

Table 7.3: Sub-carrier (2.85 GHz) power at different points in the interferometer and contamination of the same on the HPD. If the configuration of GEO 600 were to be upgraded and arm cavities were to be included, the error signals can be separated like ET-LF using a second mode cleaner. The contamination of the MID signal at the HPD by the sub-carrier is minimal by the 2.85 GHz sub-carrier as this frequency is mostly rejected by the OMC.

7.7 Experimental implementation of the technique at GEO 600

While the principle of injection of an additional frequency from the output port has been discussed in the earlier, this section focuses on a detailed injection scheme and also provide some insight on the necessity of a new laser in order to generate this new sub-carrier as opposed to using a pick-off from the existing lasers on the squeezer table.

7.7.1 Phase locking sub-carrier laser to the main IFO laser

Although GEO 600 has been operating with a squeezer from a long time, additional optical components and electronics would be needed to experimentally implement the new scheme. The ingredients for producing and locking a frequency shifted sub-carrier to the interferometer carrier are listed below :

- Photodiode with a bandwidth of 3 GHz
- Cabling suitable for GHz signals
- Mixer, pre-amp electronics, servo to feedback to the sub-carrier NPRO
- GHz signal generator with good noise characteristics for example the Rohde and Schwarz model: SMA100A
- Phase lock loop (PLL) electronics to create an optical phase lock loop between the main interferometer laser and the sub-carrier laser

The optical PLL requires a stable phase reference for the auxiliary laser to have the same phase and frequency as the main interferometer laser. For this purpose the $2 \times f_{MID}$ frequency can be used as the reference frequency. This frequency can also serve as the local oscillator for balanced homodyne readout when GEO 600 would implement this technique. The implementation of BHD readout for GEO 600 is not discussed in this thesis. The phase noise of the PLL is not as crucial for us as it is in the case of BHD, and hence the Michelson sidebands could potentially be used as a phase reference to lock the sub-carrier laser to the interferometer. The phase noise of the GHz sub-carrier which is introduced via the GHz signal generator was initially a cause for concern but by calculations, it was shown that this number is small enough to not be a problem in MID (see section 7.7.2).

Assuming the unstabilised free running fiber noise of a 10 m fiber to be $1\,\mathrm{Hz}/\sqrt{\mathrm{Hz}}$ [166], and that the length of the signal recycling cavity cannot be controlled better than this, requirements for the local oscillator stability can be calculated and also the tolerable residual motion of the MSR if this GHz sub-carrier error signal is used to control it. The interferometer stability or the

MID sensitivity is about $10^{-22}\,1/\sqrt{\text{Hz}}$ and it would be safe to make the assumption that it is desirable to keep the MSR motion about a factor of 100 below this in order to not ruin strain sensitivity thus setting the SRCL length requirements at $10^{-20}\,1/\sqrt{\text{Hz}}$.

7.7.2 Generation and injection of f_{coh}

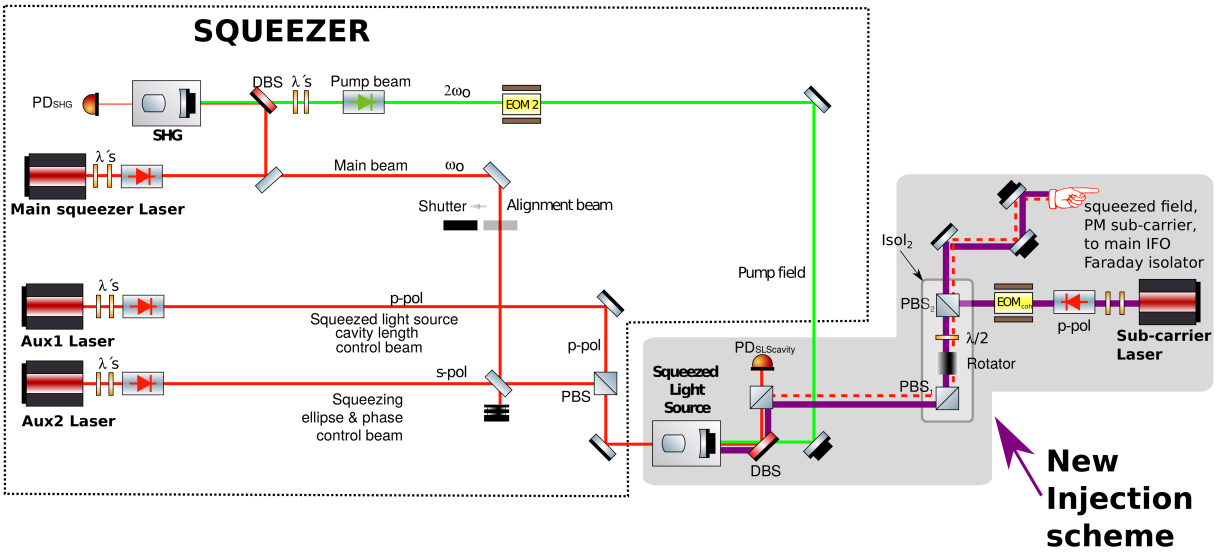

Figure 7.9: Simplified schematic shown here is the conceptual design of the optical setup for the GEO 600 squeezer and in purple is a possible path which can be implemented for the injection of the new sub-carrier. The sub-carrier which is generated from the sub-carrier Laser in the schematic, is frequency shifted such that it is resonant in the SRC and reflected by the OPA cavity [96].

In this section I present a potential way to implement the new control scheme for GEO SRCL control experimentally. Before doing this, it would be useful to understand the working of the various other lasers and the reasoning for the use of a new laser to produce the sub-carrier as opposed to using one of the existing lasers. A schematic of the squeezer path is shown in figure 7.9 with the proposed changed.

The main squeezer laser source in Figure 7.9 is the laser that provides the input field to the second harmonic generator that produces the squeezed states. This laser is phase locked to the main interferometer laser and is also used to align the squeezer to the interferometer. Two frequency shifted auxiliary lasers are in use (Aux1 and Aux2) in Figure 7.9 for the OPA cavity length control of the squeezed light source and the coherent control of the squeezing ellipse orientation [96].

Initially Aux1 or Aux2 lasers which pass through the OPA cavity were considered as candidates to be sub-carrier. These fields however have very negligible power at the MSR. Aux1 is resonant in the over-coupled OPA cavity and is transmitted. However, this transmitted Aux1 beam which has low power is used for OPA length control. Aux2 is non-resonant in the OPA cavity and has only a few μW of power being transmitted. For these reasons the use of an additional laser (sub-carrier laser in Figure 7.9), phase locked to the main interferometer laser has been proposed to produce a sub-carrier with considerable power. The frequency offset $f_{sub-carrier}$, with respect to the interferometer carrier, is chosen to be 2.85 GHz such that it is resonant only the SRC. The sub-carrier is phase modulated at 15 MHz to produce modulation sidebands which are not resonant in the SRC and can be used for Pound-Drever-Hall control of the MSR position.

Phase noise of this sub-carrier (w.r.t. the main interferometer carrier) must be low enough to not introduce additional noise in MID via cross-coupling. This phase noise will likely be limited by the phase noise of the frequency offset signal used in the phase lock loop for the sub-carrier. We estimate from the single sideband noise quoted by the manufacturers of state of the art signal generators [97] that the jitter of the SRM introduced by relative phase noise of the sub-carrier to be $4.0751 \times 10^{-18}\,\mathrm{m}/\sqrt{\mathrm{Hz}}$, which is not expected to have a noticeable influence on the science signal sensitivity.

7.8 Consideration of twin-twin signal recycling for GEO 600

Pure phase/amplitude squeezing improves the quantum noise limited sensitivity at a particular frequency [167]. While frequency dependent squeezing solves this problem, one would need one or more high finesse cavities (see filter cavities in appendix B) to rotate the squeezed states optimally to get a broad band reduction in quantum noise. These filter cavities have a very high finesse (hence a very small locking range) and need to be controlled with a lot of precision in order to provide optimal rotation of the squeezed states [12]. Any misalignment of the filter cavities causes anti-squeezing to couple into the interferometer [168]. The control of long filter cavities required for frequency dependent improvement in quantum noise limited sensitivity has not yet been demonstrated.

This tight requirement on the filter cavities coupled with the challenge of obtaining error signals for the longitudinal control of the detuned SRC (the problem can be mitigated with the new sensing scheme) served as motivators to find techniques that would relax the requirement on the number of filter cavities.

'Twin-twin' signal recycling was one of the potential upgrade options considered for GEO 600 was 'twin-twin' signal recycling [169]. A detailed investigation has not yet been performed for 'twin-twin' signal recycling configuration. It is based on a existing idea proposed by Thüring et. al. [170] for detuned GEO 600 without arm cavities i.e DRMI configuration. This configuration, which I call 'conventional' twin signal recycling, involves the addition of a second mirror in the signal output path of the interferometer thus forming an additional optically coupled cavity with the initial Signal Recycling (SR) cavity (see figure 7.10). In the new 'twin-twin' signal recycling along with changing the layout of GEO 600 form DRMI to DRFPMI, the addition of a mirror after the main signal recycling mirror called MSR in figure 7.11 has been proposed. The theory for twin-twin signal recycling is similar to the twin signal recycling case and in the following section I briefly describe the conventional twin signal recycling theory along with highlighting the minor change in theory for the twin-twin recycling case.

7.8.1 Theory of twin signal recycling

The resonance doublet which is a characteristic of coupled cavities can be seen in this case as well and the easiest way to visualise this would be to think of coupled mechanical oscillators. The frequency splitting f_{sp} of this resonance doublet is determined by the coupling of the two resonators, i.e. the MSR and TSR in figure 7.10 [171].

In a detuned signal recycling cavity where the interferometer carrier has an angular frequency of ω_0, a gravitational wave signal would modulate the same and produce upper and lower signal sidebands at $\omega_0 + \Omega$ and $\omega_0 - \Omega$ respectively. If the bandwidth of the signal recycling cavity is higher than the target frequency, then either the upper or lower signal sideband is recycled depending on the direction of the detuning. This leads to loss of half the signal owing to the suppression of the non-resonant sideband. In twin signal recycling where detuning of the MSR is not necessary, the two signal sidebands are equally enhanced before exiting the interferometer.

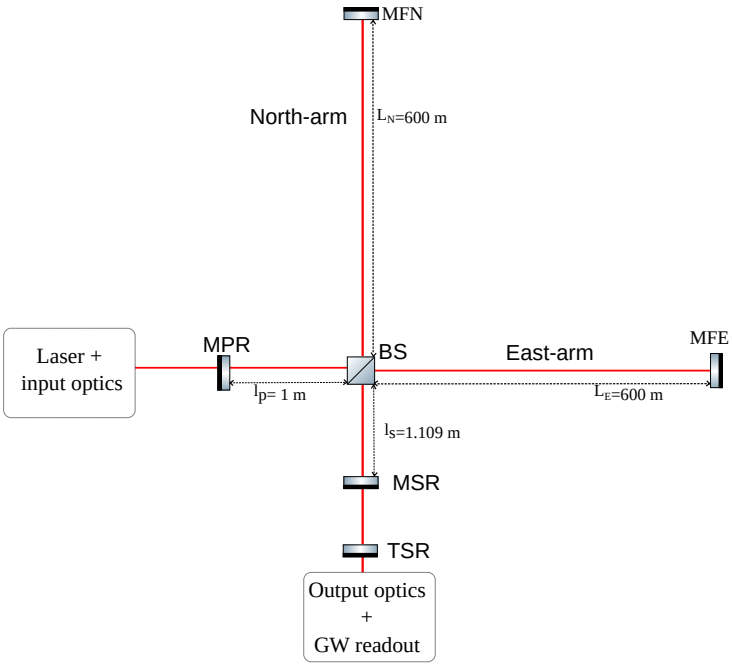

Figure 7.10: Conventional twin signal recycling concept in a DRMI configuration

The transmission T_c of the compound mirror formed by the MSR and TSR corresponding to this coupling can be obtained from the equation :

$$T_{\mathrm{c}} = 1 - \left(\frac{4\cos\left(2\frac{\omega_{\mathrm{sp}} L_{\mathrm{TSR}}}{c}\right) R_{\mathrm{end}}^2}{\left(1 + R_{\mathrm{end}}^2\right)^2} \right) \tag{7.1}$$

where, L_{TSR} is the length of the twin signal recycling cavity and R_{end} is the reflectivity of the end mirrors of the arm cavity.

This transmission T_c is chosen with respect to the required frequency splitting $\omega_{sp} = 2\pi f_{sp}$. The bandwidth of the resonances is given by the reflectivity of the TSR mirror (TSR) analogous to the interferometer bandwidth altering by the MSR.

Thüring et. al. [171] also investigated the possibility of increasing the sensitivity of GEO 600 in a broadband fashion without the use of filter cavities. In conventional twin signal recycling, owing to the symmetric arrangement of the upper and lower sidebands around the carrier frequency we do not have the optical spring effect [149] [150] [151] but instead having both the signal sidebands contributes to the improved sensitivity [171]. The sensitivity improvement with the use of TSR technique at high frequencies is well understood. It was also demonstrated by C.Graëf et. al. [172]

that the the additional mirror (TSR in figure 7.10) does not affect the controllability of the interferometer and all the longitudianl dofs can be sensed and controlled.

7.8.2 Twin-twin signal recyling: parameter choice and results

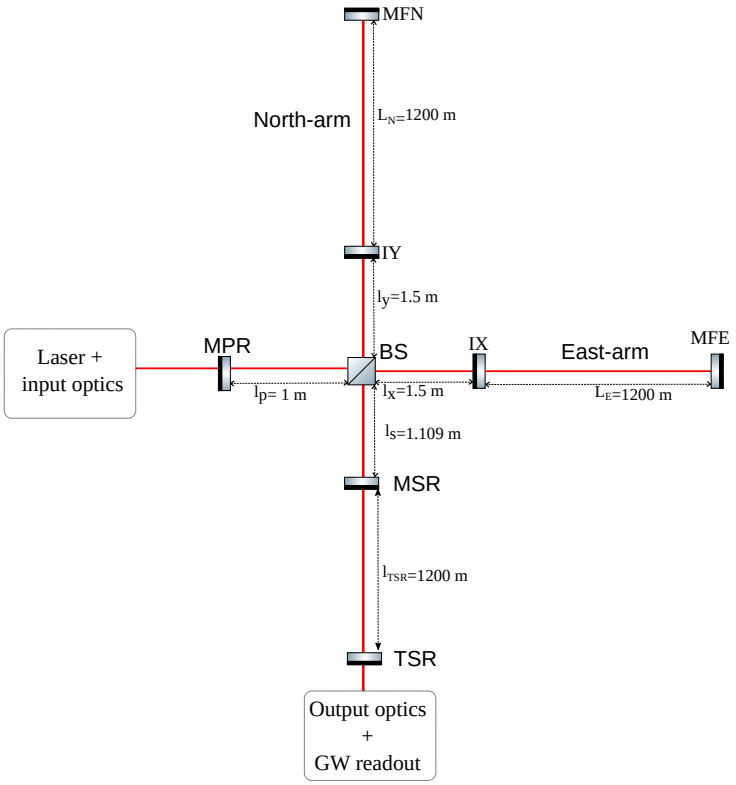

Figure 7.11: Twin-twin signal recycling configuration in a DRFPMI configuration where IX and IY are additional mirrors added to the east and north arms respectively to form arm cavities

Adding an additional signal recycling mirror (TSR in figure 7.11) to the DRFPMI configuration would create a new coupled cavity. In total, the system comprises of two coupled long cavities. One, formed by the MSR and the ITMs and the other formed by the TSR and the ITMs. Such a coupled optical system has a modal structure comprised of doublets of transmission peaks centred at the initial positions of the arm cavity resonances and separated by a gap defined by the transmissivity of the composite mirror formed by the MSR and the ITMs. The half-width at half maximum (HWHM) of the peaks is defined by the reflectivity of the TSR.

The parameters chosen for GEO 600 with arm cavities for purposes of our 'numerical experiments' are listed in the table 7.4. Using this the quantum noise limited sensitivity of GEO 600 for various cases was simulated.

Parameter	Power	Description
L_E and L_N	1200 m	Arm cavity length
L_{SRC}	1.109 m	BS-MSR distance
L_{PRC}	1.1463 m	BS-MPR distance
L_{TSR}	1200 m	MSR-TSR distance
T_{ETM}	0.999992	Transmisison of arm cavity end mirror
T_{MPR}	0.03	Transmisison of MPR
T_{MSR}	0.5	Transmisison of MSR
T_{TSR}	0.01	Transmisison of TSR
Intra-cavity power	510.971 kW	
Power entering the cavities	1.256 kW	
Power incident on the central BS	2.572 kW	
Input laser power	100 W	

Table 7.4: Parameters used for simulations of GEO 600 with arm cavities. Twin-twin signal recycling parameters were estimated to optimise sensitivity at 1.2 kHz (the required reflectivity can optimised depending on the science case).

The legend of the figure 7.12 is summarised in the following bullet points :

- Solid Green line: Current GEO 600 Sensitivity predicted by the Finesse model (see section 8.2).
- Solid Yellow line: GEO 600 with squeezing and Twin Signal Recycling from the paper presented by Thüring et.al.
- Solid Pink line: GEO 600 with a 1200 m long signal recycling cavity but with Arm Cavities (without squeezing) and 510.971 kW circulating arm cavity power.
- Solid Blue line: GEO 600 with arm cavities and 1200 m twin-twin Signal Recycling (without squeezing) and 510.971 kW of circulating arm cavity power.

In case of short signal recycling cavities, the phase accumulated by the signal sidebands can be ignored [173]. However when the length of the SRC is considerably long, the phase accumulated by the signal sidebands is $\Omega L_{sr}/c \approxeq 0$ where L_{sr} is the length of the SRC. Haixing et.al. [173] investigated the possibility of lengthening the SRC to allow the signal sidebands to pick up phase as they propagated through the SRC for aLIGO. The elongation of the SRC leads to enhancement of both upper and lower signal sidebands simultaneously at a certain frequency (depending on the length of the SRC). Their investigations confirm an improvement in the QNLS at high frequencies

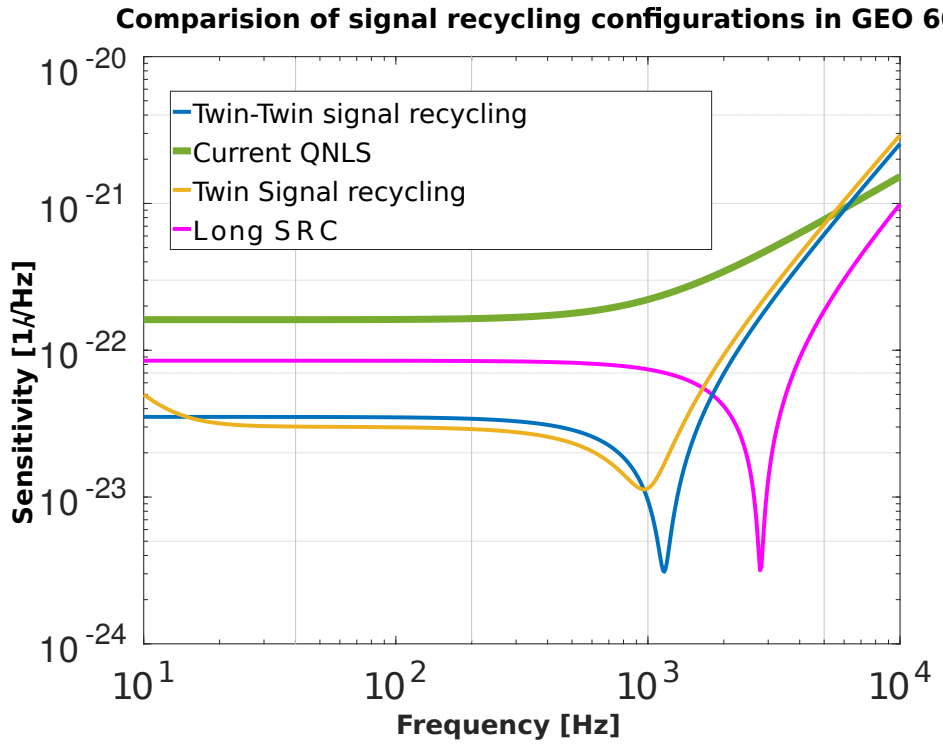

Figure 7.12: Sensitivities of GEO 600 for various twin and twin-twin signal recycling configurations. It can be seen that the sensitivity of both GEO 600 with a long SRC and GEO 600 with twin-twin recycling is better than the case of pure signal recycling presented by Thüring et. al. and current GEO 600. No squeezing is assumed for either curves. Except for the case of twin-twin signal recycling (where arm-cavities have been assumed for GEO 600), for all other cases shown above, GEO 600 has been simulated in its current DRMI layout. These plots are optimised for peak sensitivity. The other option is to optimise for same bandwidth and this is currently work in progress.

for aLIGO.

For GEO 600 with arm cavities, the sensitivity in the case of a long SRC arm cavities is comparable to the sensitivity with the twin-twin signal recycling and the same is indicated in the figure 7.12. The sensitivity of both the twin-twin recycled case and the long SRC can be improved with the use of squeezing. The sensitivity of a pure twin signal recycled Michelson was improved with the use of squeezed states. Even without filter cavities, it was possible to achieve broad band reduction in quantum noise. Without squeezing, the topological equivalence of twin-twin signal recycling to a long SRC in RSE at high frequencies questions the befit of introducing additional coupled cavities in the interferometer.

7.9 Discussions

In this chapter the problems with the current SRCL control in GEO 600 have been discussed. A potential option for mitigation of SRCL coupling into the GW channel has also been presented. Testing the new SRCL error signal proposed for SRCL control GEO 600 would benefit other GWDs with dual recycling configuration as well. The option of twin-twin signal recycling from the perspective of a third generation GWD has been explored for GEO 600 as a potential uogradeoption..

7.9.1 Suggested improvements to the current LSC of GEO 600

The challenges with the current SRCL control have been discussed in the chapter and a technique to obtain a dedicated, high optical gain signal has been highlighted in this chapter. The new technique which involves using a sub-carrier injected from the output port would benefit all GWDs with dual recycling. The error signal was shown to be impervious to demodulation phase changes to about 15°. This scheme has not been tested for sensing noise contamination in $h(t)$ and as future work, one could perform a noise budget analysis as done for ET-LF with SimulinkNb to demonstrate the benefit of using this new sensing scheme.

A possible injection scheme for the sub-carrier using the existing squeezing layout has been discussed in this chapter and it has been shown that the sub-carrier phase noise of the signal generator used for frequency shifting the sub-carrier is by far not a show-stopper. The use of polarisation tricks to introduce the sub-carrier into the interferometer ensures the non-interference of this beam with the squeezed states. While imprinting the sub-carrier onto squeezed states would be the most ideal and elegant way to introduce the sub-carrier into the interferometer, as a proof of principle, one could also introduce this sub-carrier through one of the beam directing optics in the output path and detect the PDH error signal for SRCL in reflection of the OMC.

7.9.2 Prospective upgrade for GEO 600

We have in this chapter also discussed a potential upgrade option for GEO 600 wherein a

numerical experiment was performed to predict the quantum noise limited sensitivity of a DRFPMI cofiguration with an additional signal recycling mirror ('twin-twin' signal recycling) and compared the same to a more conventional technique that has been investigated for aLIGO which involves elongating the SRC. This scheme needs to be vetted more thoroughly before making the case for advanced detectors.

Chapter 8

Summary and outlook

This thesis describes my work on designing and improving the longitudinal control systems of current and future gravitational wave detectors (GWD) in general and for ET-LF, GEO 600 and the AEI 10 m prototype in particular. A well designed control system is quintessential to hold the interferometer at its operating point, thus, ensuring that the GWD operates at full sensitivity. At the heart of such a control scheme is a sensing matrix which comprises of the frequency dependent optical gain of the error signals required for feed-back control. The sensing signals in current GWDs is strongly coupled making the gravitational wave (GW) readout channel susceptible to control noise contamination. In this thesis I propose and describe a new sensing scheme which decouples the error signals, thereby making the sensing matrix diagonal. The new scheme involves the injection of an additional frequency shifted phase modulated laser beam through the dark port of the interferometer. I also show that this additional beam can be generated and incorporated into the planned squeezing upgrade with minimal modifications to the planned infrastructure.

The Einstein Telescope (ET) is a proposed GW observatory planned to be built in Europe. The ET design study describes the ET observatory to consist of three detectors (and in total six interferometers) with a dual recycled Fabry-Perot Michelson configuration (see chapter 2 for a description) having an arm length of 10 km. The overall design sensitivity of ET is a factor of 10 better than the design sensitivity of current advanced GWDs like aLIGO and AdV. The design differences that allow for this improvement include techniques to split each of the three detectors

into two interferometers i.e. the 'xylophone design', one optimised for low frequencies and one optimised for high frequencies; cryogenics for lowering suspension thermal noise in ET-LF and beam shape change for ET-HF to mitigate thermal noise. More on ET and the important design differences can be found in chapter 3 .

The main challenge in controlling ET-LF is the known relatively high control noise in the low frequency band (7 Hz–32 Hz) where ET-LF is required to have high sensitivity. Thus, to be able to control the interferometer, this control noise must be mitigated. Since no current GWDs are designed to observe GWs at such low frequencies, this challenge had not previously been dealt with. In chapter 4, a novel control scheme for the low frequency part of the Einstein Telescope (ET-LF) is proposed that successfully meets the requirements for ET-LF. To the best of my knowledge, there are no previously proposed control schemes for ET-LF. Even though the control system is developed for ET-LF, it can be used in all GWDs with dual recycling.
The new control scheme proposed in my thesis sufficiently mitigates the control noise problem, and the key idea that makes this possible is the independent sensing signals with high SNR for all longitudinal degrees of freedom of ET-LF. Current GWDs are plagued by the control noise, mainly arising from the length control of the SRC. The new control scheme for ET-LF successfully mitigates this problem mainly due to a dedicated high gain, low noise error signal for SRCL. To obtain this error signal, a frequency shifted (GHz frequency range), phase modulated laser beam injected through the dark port of the interferometer. This beam, the sub-carrier is resonant only in the signal recycling cavity (SRC) of ET-LF while the phase modulation sidebands on it do not enter the interferometer. In order to not affect the squeezed states which are also injected through the dark port of the interferometer, the phase modulated sub-carrier is imprinted onto the squeezed states by reflecting it off the squeezing cavity. To test this sensing scheme a FINESSE model was built and used to generate the optical sensing matrix, that was fed into SimulinkNb together with various control loop transfer functions, to model and quantify the control noise couplings into the GW channel DARM. Future work involves making the model more realistic by including optical defects such as mirror imperfections and arm-cavity finesse imbalances. Further, it would be interesting to compare the current proposed interferometer design to competing interferometer designs such as speed-meters.

The 10 m prototype facility located at the Albert Einstein Institute (AEI) in Hannover, Germany.

It is a Fabry-Perot Michelson interferometer with an arm length of 10 m. The experiment is designed to be radiation pressure limited to measure the standard quantum limit (SQL) but also functions as a test bed for new technologies. More information on the facility is presented in chapter 5. Before implementing the new sensing scheme proposed for ET-LF in full-scale GWDs, this scheme could be tested at the AEI 10 m prototype. A modified version of the ET-LF control scheme is described and proposed for longitudinal sensing of the AEI 10 m prototype in chapter 6. The difference between implementing the scheme in ET-LF and the AEI 10 m prototype is the injection port for the sub-carrier. By super-imposing a frequency shifted laser beam (similar to the sub-carrier in ET-LF, this is also in the GHz frequency range) onto the main interferometer laser before it enters the interferometer and using this for sensing purposed, the differential Michelson degree of freedom (MICH) which is coupled to the arm cavity degrees of freedom can be decoupled from the latter.

Current GWDs use DC readout technique for the DARM degree of freedom, but another technique called balanced homodyne readout (BHD) has been proposed for advanced GWDs which is not susceptible to asymmetries in the interferometer. This technique, can be tested at the prototype. To further motivate the usage of BHD at the 10 m prototype, I have shown that the common arm motion of the arm cavities can be separated from the DARM readout by seven orders of magnitude. As the sub-carrier proposed for the control of ET-LF is also in the GHz regime, the prototype would be an ideal location to study realistic noise couplings of GHz frequency sub-carrier to the dark port which would be important for ET-LF as well. In addition the sub-carrier presented for MICH control, could potentially be used to readout the angular degrees of freedom of the interferometer. However, investigating this is beyond the scope of this thesis. Future work includes studying how the control signals are affected by cavity stability parameters.

GEO 600 is a German-British GWD located in Ruthe, outside Hannover, Germany which has the dual recycled Michelson interferometer layout (DRMI). GEO 600 has pioneered several technologies that are currently implemented into current advanced GWDs. One such technology (which is currently being implemented in aLIGO, AdV as well) is the utilisation of squeezed states to improve the quantum noise limited sensitivity of the interferometer. GEO 600 is limited by sensing noise from the length control of the SRC upto 220 Hz. This SRCL sensing noise can be mitigated by using the sensing scheme proposed for ET-LF. As GEO 600 employs squeezing as has

a DRMI layout (thereby having a cross-coupling situation similar to ET-LF), the sub-carrier can be injection from the dark port can be experimentally tested at GEO 600 and the infrastructure changes required to do so are detailed in chapter 7. Testing this scheme at GEO 600 would greatly benefit the technical design of ET-LF as the experience would allow us to set better requirements on the required stability of the sub-carrier.

Appendices

Appendix A

Control theory and control noise coupling

A.1 Basic Control Theory

Controls are used to modify the behaviour of a system. A system can be anything from shower temperature to an interferometer where we require to control/regulate something. The GW ifo, requires several control loops for smooth functionality for example, the length control loops keep the lengths of the cavities (CARM, DARM, MICH, SRCL, PRCL) in the linear range of the sensors. In this section we describe the basics of feedback control. We present the coupling path for MICH in DARM presented in section 4.6.1 in this section.

A.1.1 Feedback control

Around the operating point, the system can be approximated to a linear time invariant(LTI) system thereby allowing us to use linear control theory. Feedback control as the name suggests involves sensing a change in the system and the change is 'fed-back' with an inverted sign to the system to hold it at a predefined value (also called the operating point).

Figure A.1 outlines the essential components of a feedback loop. The Plant (P) is the object to be controlled . Any disturbances in the plant are measured by the sensor (S). The output of this sensor (b) is the error signal. The servo (G) determines the loop dynamics and the properties

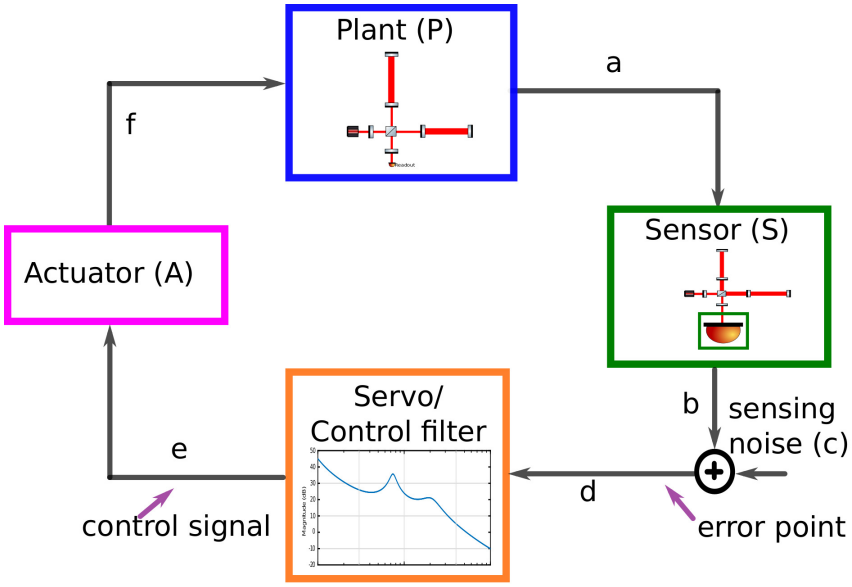

Figure A.1: A basic control loop showing the plant (system to be controlled), a sensor (that senses the change in the set point of the system), a servo (that generates an error signal) and actuators (that generate the feedback signal to the plant). While the set point is the desired operation point of the plant, the error point shows the actual position of the plant. Noise enters the system through both the sensing point (sensing noise) and the feedback point.

of the loop can be altered to achieve the desired behaviour. The servo signal (e) is the passed onto the actuators (A) which drive the plant with a feedback signal (f). It is common practice to represent the plant and the sensor as one system. A disturbance (c) say sensing noise is summed into the plant after the sensor.

For a plant that can be approximated to an LTI system [63], the output can be expressed as a linear combination of the inputs. In such LTI systems, the output frequency is always same as the input frequency. The ratio of the output to input is called a transfer function. Such trasnfer functions are used to calculate the sensitivity of the system adn the coupling of various noise sources [98].

Using Laplace domain algebra, the different equations in the loop can be written down as:

$$\begin{aligned} d &= c + b \ , \\ e &= G\, d \ , \\ f &= A\, e \ , \\ a &= P\, f \ , \\ b &= S\, a \ , \end{aligned} \tag{A.1}$$

Using the equation 8.1, b can be inferred to be:

$$b = (P\, S\, G\, A) \times d \ , \tag{A.2}$$

The quantity in the brackets, PSGA is the open loop gain of the system (G_{OL}) and it is the product of the loop elements which in practice would be the cascaded transfer functions of the individual blocks one time around the loop.

The effect of the feedback loop can be calculated by taking the transfer function from the disturbance to the error point i.e ,

$$\begin{aligned} \frac{d}{c} &= \frac{1}{(1 - PSGA)} \ , \\ &= \frac{1}{1 - G_{OL}} \ , \end{aligned} \tag{A.3}$$

Similarly the transfer function from the disturbance to the feedback point can be calculated:

$$\begin{aligned} \frac{f}{c} &= \frac{Ae}{(d - b)} \ , \\ &= \frac{A\, G}{1 - G_{OL}} \ , \end{aligned} \tag{A.4}$$

When the G_{OL} is larger than $1(|PSGA| > 1)$, the disturbance is suppressed in the feedback signal. The term $\frac{1}{1-G_{OL}}$ ic called the closed loop gain.

A.1.2 Servo design parameters

Although the optical plant to be controlled imposes the most stringent restrictions on the servo design, there are some common characteristics that are included in a servo:

- The servo is tailored to make a loop stable. A simple 1/f filter can make the system unconditionally stable but quite often in GWDs the servos are tailored to be conditionally stable or stable in a certain bandwidth to suppress noises in a certain bandwidth.
- In the high noise region, in GWDs typically at low frequencies (due to seismic noise), the servo gain is ensured to be high to suppress the noise.
- To prevent sensor noise from coupling into the control loop, the open loop gain of the plant is designed to be less than one after the unity gain crossing.

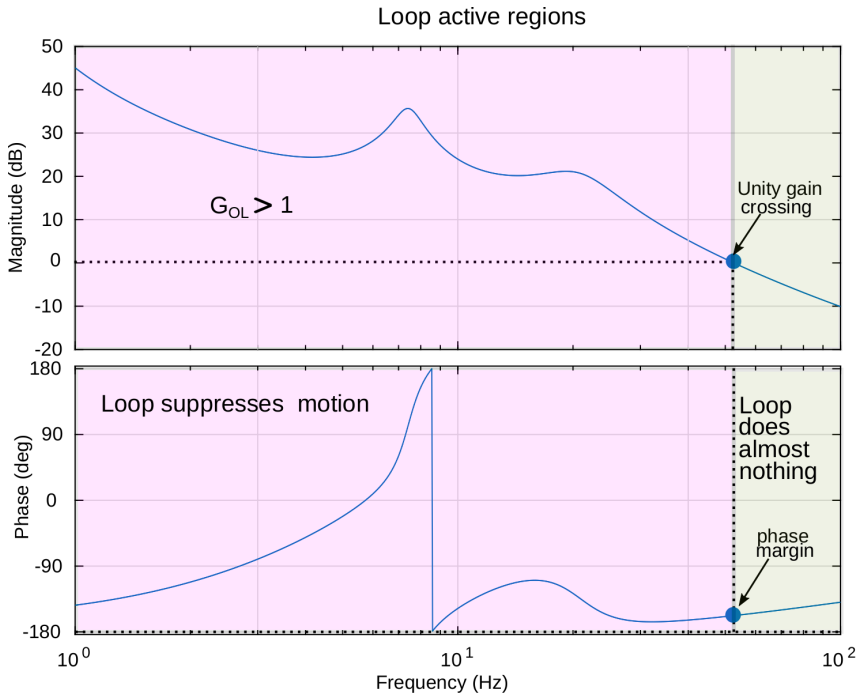

Figure A.2: Example Bode plot of the open loop gain of the DARM loop of a DRFPMI system inclusive of all the components listed in the earlier part of this appendix A.

Figure A.2 indicates the open loop gain of a system such as the one outlined in A.1. The unity gain crossing of the loop at $\approxeq 52\,\mathrm{Hz}$ is the point where the magnitude of the open loop gain is unity. This is also knows as the servo bandwidth. The phase margin indicates how far off is the loop from the -180°instability point at the unity gain crossing. At this point of -180°, the phase of

the error signal changes by -1 thus converting the negative feedback to a positive one rendering the loop instable. The pink shaded are shows the active region of the loop when G_{OL} is larger than one thereby suppressing all motion and the beige area indicates the region where the control loop does almost nothing.

A.2 MICH coupling in DARM

The math for the feed-forward filter implemented to eliminate the coupling of MICH in DARM presented in section 4.6.1 is detailed in [107]. From the sensing matrix presented in section

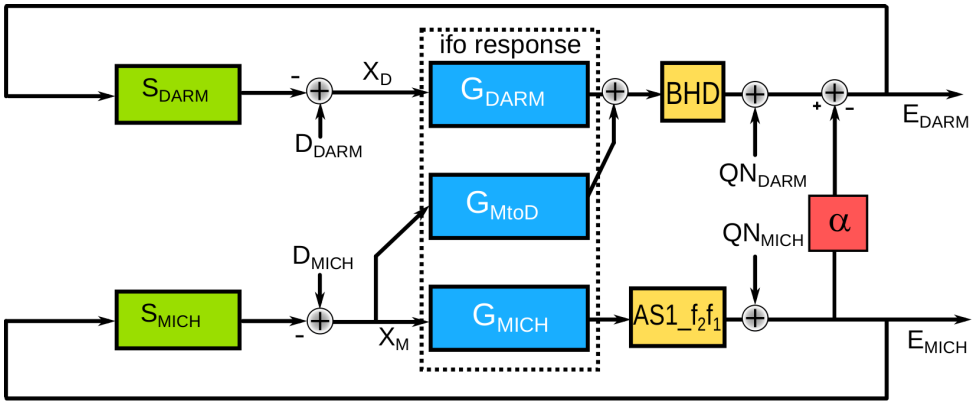

Figure A.3: Feed forwards of MICH into DARM in order to compensate for the optical coupling of MICH via G_{MtoD} in DARM.

4.5.2, we can see that the BHD sensor used to readout DARM also senses the MICH dof. If optical gains of the DARM and MICH dofs are denoted by G_{DARM} and G_{MICH} respectively, such that the resulting error signals to control them are E_{DARM} and E_{MICH}. The control signals generated by the servos to control the MICH (S_{MICH}) and DARM (S_{DARM}) dofs are X_M and X_D rspt. The optical gain for the MICH signal that appears in DARM is represented by G_{MtoD}. The disturbances to the MICH loop and DARM loop are shown by D_{MICH} and D_{DARM} rspt.

For MICH,

$$X_M = F_M \left(G_{MICH}\, X_M\, PD_M + QN_{MICH} \right) , \tag{A.5}$$

where QN_{MICH} is the sensing noise of the MICH control loop. Solving for X_M we get,

$$X_M = \frac{1 - F_M G_{MICH}}{P} D_M F_M QN_{MICH} , \tag{A.6}$$

The closed loop gain for the MICH dof can now be calculated to be,

$$CL_M = \frac{1}{1 - F_M G_{MICH} P_M} \ , \tag{A.7}$$

Using equation 8.7 in 8.6, we get

$$X_M = CL_M \, F_M \, QN_{MICH} \ , \tag{A.8}$$

The sensing noise of MICH in DARM which is sensed using a photodiode(BHD) can be calculated as:

$$BHD = (F_D \, G_{DARM} \, BHD) + (G_{MtoD} \, X_M) \ , \tag{A.9}$$

Solving for BHD,

$$\begin{aligned} BHD &= \frac{G_{MtoD}}{1 - (F_D \, G_{DARM})} \, CL_M \, F_M \, QN_{MICH} \ , \\ BHD &= CL_D \ CL_M \, F_M \, G_{MtoD} \, QN_{MICH} \ , \end{aligned} \tag{A.10}$$

The transfer function G_{MtoD} allows the sensing noise from MICH to creep into the DARM control loop.

Appendix B

A review of PDH locking

For a simple Fabry-Perot cavity, the operating point can be defined as the cavity condition that ensures that the desired optical fields are resonant or anti-resonant. Around this operating point the cavity can be approximated to a linear system. The linear regime around the operating point is determined by the line-width of the cavity. The cavity resonance conditions for the electric fields is maintained by means of an error signal obtained by the Pound-Drever-Hall (PDH) technique.

The PDH error signal is created by phase modulating (conventionally) the laser carrier at a radio frequency. Radio frequencies (RF) which are typically in the MHz range are chosen for the same (for comparison, the laser carrier is in the THz range). These RF sidebands are chosen to not be resonant in the cavity and therefor are not sensitive to cavity length fluctuations. The carrier is resonant in the cavity and is affected by any changes in the cavity length. A photodiode in reflection of the cavity would detect a beat signal of the modulation frequency and by demodulating at the modulation frequency and low pass filtering the signal, an error signal for the cavity length can be obtained.

The interferometer laser carrier field (before entering the cavity formed by mirrors IX and EX) can represented by

$$E_{in} = E_0 e^{i\omega t}\,, \tag{B.1}$$

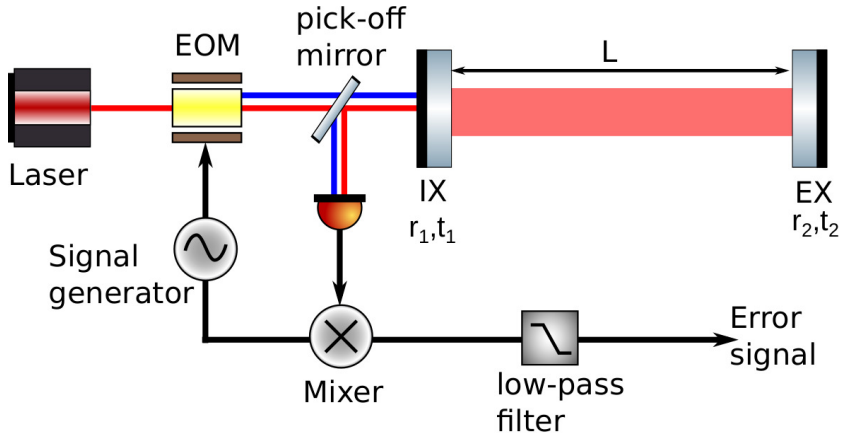

Figure B.1

where E_0 and ω are the amplitude and the angular frequency of the input laser field respectively. Upon phase modulating the laser output using an electro-optic modulator (EOM), at a frequency ω_m, the output of the electric field can now be written as,

$$E_{in} = E_0 e^{i\omega t} e^{i\Gamma \cos \omega_m t}\,, \tag{B.2}$$

where, Γ is the modulation depth. Using the Jacobi-Anger identity to expand equation B.2,

$$E_{in} = E_0 e^{i\omega t} \sum_{n=-\infty}^{\infty} i^n (-1)^n J_n(\Gamma) e^{i\omega_m t}\,, \tag{B.3}$$

where, J_n are Bessel functions of the n^{th} order.

By considering Bessel functions of the first order only,

$$\begin{aligned} E_{in} &= E_0 e^{i\omega t} \sum_{n=-1}^{1} i^n (-1)^n J_n(\Gamma) e^{i\omega_m t}\,, \\ &= E_0 e^{i\omega t} \left(J_0(\Gamma) - i J_1(\Gamma) e^{i\omega_m t} + i J_1(\Gamma) e^{-i\omega_m t} \right) \\ &= E_0 \left(J_0(\Gamma) e^{i\omega t} - i J_1(\Gamma) e^{i(\omega+\omega_m)t} + i J_1(\Gamma) e^{i(\omega-\omega_m)t} \right) \end{aligned} \tag{B.4}$$

If we were to use the pick-off mirror shown in figure above, to direct the reflected light (which is a combination of sidebands and carrier light), the electric field going towards the photodiode can

be written as,

$$E_{ref} = E_0 \left(J_0(\Gamma) e^{i\omega t} r_c(\omega) - i J_1(\Gamma) e^{i\omega_m t} r_c(\omega + \omega_m) + i J_1(\Gamma) e^{i\omega_m t} r_c(\omega - \omega_m) \right) \tag{B.5}$$

where r_c is the amplitude reflectivity of the cavity which is a function of the frequency of the carrier light.

Also, the total light field reflected off the cavity (the electric field leaking out and the promptly reflected field) is

$$E_{ref} = E_{in} r_c \,, \tag{B.6}$$

and

$$r_c(\omega) = -r_1 + \frac{t_i^2 r_2 e^{-i\frac{cL\omega}{c}}}{1 - r_1 r_2 e^{-i\frac{cL\omega}{c}}} \tag{B.7}$$

where, r_1 and r_2 are the amplitude reflectivities of the input and the end mirrors of the cavity separated by a distance L and c is the speed of light.

Photodiodes measure power and not electric fields. Hence, the output as measured by the photodiode in the figure is given by,

$$P_{meas} = E_{ref}^* E_{ref} \tag{B.8}$$

From equations B.5 and B.8,

$$\begin{aligned} P_{meas} = E_0^2 [& J_0^2(\Gamma) r_c^*(\omega) r_c(\omega) \\ & + J_1^2(\Gamma)(|r_c(\omega + \omega_m)|^2 + |r_c(\omega - \omega_m)|^2) \\ & - i J_0(\Gamma) J_1(\Gamma) e^{i\omega_m t} r_c^*(\omega) r_c(\omega + \omega_m) + i J_0(\Gamma) J_1(\Gamma) e^{-i\omega_m t} r_c^*(\omega) r_c(\omega - \omega_m) \\ & - i J_0(\Gamma) J_1(\Gamma) e^{i\omega_m t} r_c(\omega) r_c^*(\omega - \omega_m) + i J_0(\Gamma) J_1(\Gamma) e^{-i\omega_m t} r_c(\omega) r_c^*(\omega + \omega_m)] \end{aligned} \tag{B.9}$$

Assuming that the modulation sidebands reflected off the cavity have equal amplitude and by demodulating with a cosine function (here we call it an inphase signal) the voltage signal on the

photodiode after a low pass filtering function is applied is,

$$V^{I}_{meas} \propto J_0(\Gamma)J_1(\Gamma)Re\left[r^*_c(\omega)r_c(\omega+\omega_m) - r^*_c(\omega)r_c(\omega-\omega_m)\right] \tag{B.10}$$

Demodulating with the sine function (quadrature signal) gives us,

$$V^{Q}_{meas} \propto J_0(\Gamma)J_1(\Gamma)Im\left[r^*_c(\omega)r_c(\omega+\omega_m) + r^*_c(\omega)r_c(\omega-\omega_m)\right] \tag{B.11}$$

If the phase of the local oscillator is chosen correctly, the Q-phase signal will vanish, and all of the information about the cavity length change relative to the laser frequency will be contained in the I-phase signal. A detailed derivation of the above equation can be obtained from references [174] and [114].

Appendix C

Filter cavity optimisation for ET-LF

The use of squeezed states to improve the quantum noise limited sensitivity of the interferometer will soon be routine technology used in GWDs. ET will employ the use of squeezed states as well. As 15 dB (squeezing measured out of the squeezer) has already been demonstrated, it is not unrealistic to make the assumption that in ET, it would be possible to get a factor of 3 reduction in the quantum noise by employing squeezing.

The uncertainty on vacuum states according to the Heisenberg uncertainty principle is minimum. Vacuum states enter the interferometer from the open ports (the dark port). If we were to consider the Michelson interferometer layout shown in figure 2.1, the vacuum fluctuations couple into the interferometer through the unused port of the beam-splitter, where the photodetector is located (denoted by readout in the figure 2.1). The quantum noise in the phase quadrature (reduction in quantum shot noise limit at high frequencies) can be minimised by the use of phase squeezed states. This would however increase the quantum noise in the amplitude quadrature (i.e. increase radiation pressure noise at low frequencies). To achieve a broadband improvement in quantum noise, frequency dependent rotation of the squeezing ellipse is required. This frequency dependent rotation can be achieved by reflecting the squeezed states off a long, high finesse cavity [95]. Such filter cavities provide the correct frequency dependence (depending on the parameters of the cavity) for the injected squeezing state in order to obtain broad band quantum noise suppression in the main interferometer. The light reflected off these cavities needs to be injected into the

interferometer dark ports.

The quantum noise limited sensitivity plot for ET-LF features two resonances owing to the detuned SRC. One is the opto-mechanical resonance at 7 Hz and another at the optical spring resonance due to the detuned SRC at 25 Hz. For ET-LF to have a broadband reduction in quantum noise at all frequencies of interest, ET-LF would require two filter cavities. One filter cavity is required to rotate the squeezed states to compensate for the detuning of the SRC and the other filter cavity to compensate for the optical spring effect.

According to the laws of quantum mechanics, optical losses (like scattering, absorption, coupling of higher order laser beam modes) causes unsqueezed vacuum states to mix with the squeezed states thereby reducing the squeezing factor. Commonly referred to as squeezing degradation, this leads to a reduction and if too high, a decrease in sensitivity. The ET design stufy explains the choice of the filter cavity parameters. This section is aimed at presenting the challenge of optimising the filter cavity parameters thus motivating a future dedicated effort to optimise the parameters of the filter cavities. The position and angle of the filter cavity optics needs to be controlled with great precision without which, anti-squeezing would couple into the interferometer thereby degrading sensitivity.

C.1 Filter cavity and requirements

In case of a single filter cavity, the three parameters need to be optimised for frequency dependent squeezing are: detuning os the filter cavity (ϕ_{det}), its half-bandwidth (γ) and the round trip losses (L_{rt}) in the filter cavity. The round trip losses in the filter cavity are largely determined by the reflectivity of the in-coupler(R_c). The length of the filter cavity (L_{fc}) also plays a role in the rotation of the squeezed states with the desired angle. For two filter cavities the parameter space has now expanded from 4 to 8.

The design choices of the filter cavities chosen for ET-LF are described in the design study. The current set of parameters are:

Using the parameters mentioned in table C.1 in the ET-LF Finesse model, the desired broadband

Parameters	FC_1	FC_2
γ (Hz)	1.4	5.7
ϕ_{det} (degree)	0.136	0.3026
R_c	0.998864	0.995323
L_{fc}	10 km	10 km

Table C.1: Filter cavity parameters detailed in the design study

reduction in the quantum noise limited sensitivity of ET-LF was not obtained. Figure C.1 is a three dimensional plot of the sensitivity of ET-LF as a function of the input squeezing angle and frequency. The deep blue areas on this plot show the best sensitivity that can be obtained for each frequency and squeezing angle. By following the contour in the plot it can be seen that optimal squeezing starts at -90°and goes to zero at high frequencies hence justifying the need of a FC to get the correct rotation of the squeezing ellipse at other frequencies.

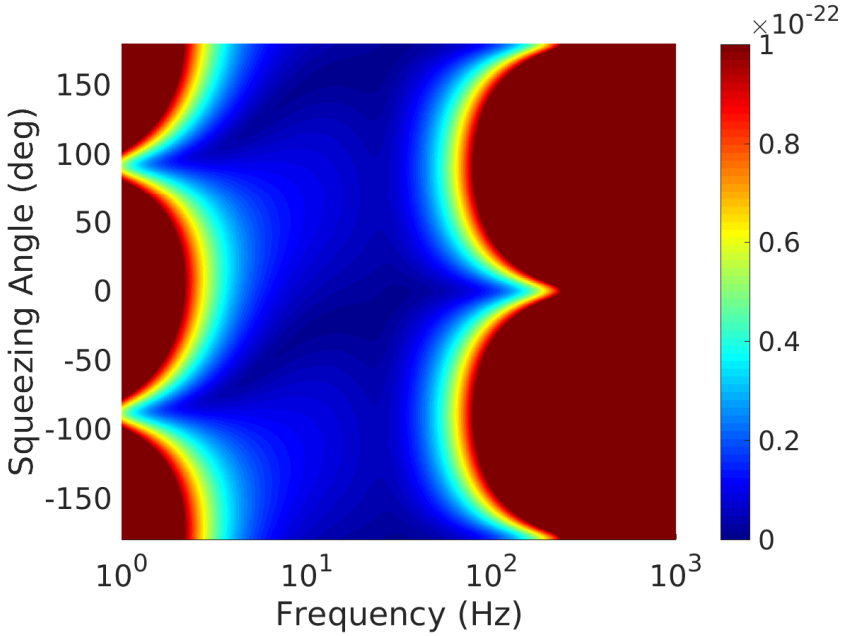

Figure C.1: 3-D plot of frequency dependent squeezing angle and the quantum noise limited sensitivity (QNLS) of ET-LF.

C.2 Estimation of filter cavity parameters for ET-LF

To find a new set of parameters for the filter cavity, a new feature of Pykat (the python wrapper [175] for Finesse) was used. The detunings of the two filter cavities, the reflectivities of the

in-couplers of the two filter cavities and also the input squeezing angle were used as variables. A brute force estimation where parakat, a Pykat package was used to run several parallel FINESSE jobs. A minimisation routine (using scipy.optimize.basinhopping algorithm) was also included to make sure that the chosen set of parameters led to optimal sensitivity. The new parameters obtained are listen in the table below:

Parameters	FC_1	FC_2	common
ϕ_{det} (degree)	0.243951	-0.090055	-
R_c	0.99612	0.99861	-
L_{fc}	10 km	10 km	-
Input squeezing angle	-	-	-140.920
Input squeezing level	-	-	15 dB

Table C.2: New optimised filter cavity parameters

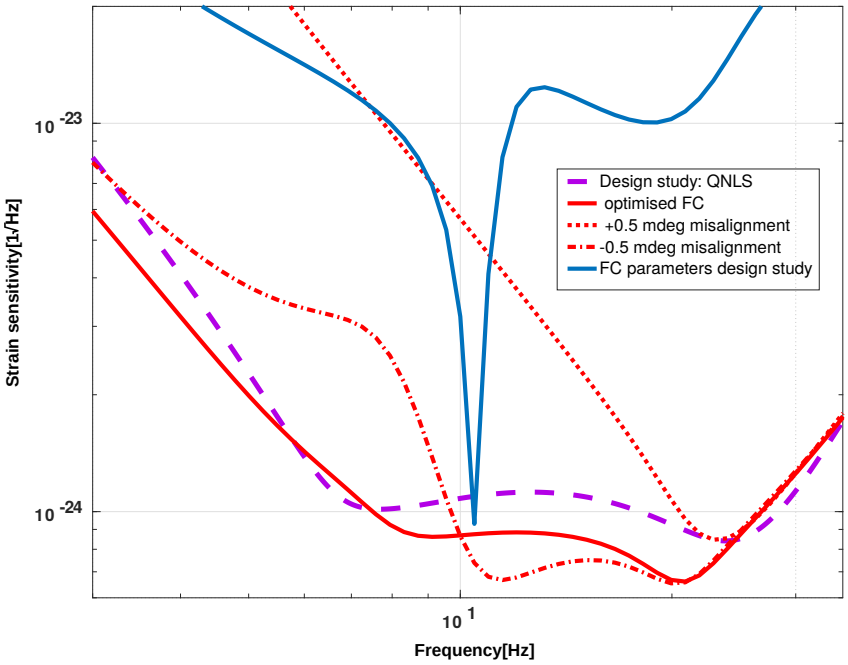

Figure C.2: Quantum noise limited strain sensitivity of ET-LF for filter cavity parameters assumed in the design study and the newly optimised parameters.

A preliminary result of this parameter estimation is shown in figure C.2 by the solid red line in the plot. A important point to be noted is that we have assumed balanced homodyne readout for the GW readout. The opening angle for the beam-splitter the ET-LF interferometer here is 60°. Once the filter cavity parameters were optimised, the homodyne readout angle was optimised separately. The solid blue line is indicative of the quantum noise limited sensitivity of ET-LF

with the filter cavity parameters taken from the design study. The pink dashed line shows the quantum noise limited sensitivity for one low frequency interferometer of ET-LF at 90°taken from the design study.

As mentioned earlier, the filter cavities are extremely high finesse cavities. The linear locking range of such cavities is very small thus making the control of such cavities challenging. Knowing the the maximum tolerance of the phase noise of the squeezing ellipse is of the order of a few mrad, the sensitivity of the filter cavities to 0.5 milli-degree longitudinal (100 µrad) misalignment was tested and shown by dashed red lines in figure C.2. It is evident from the plot that any small misalignments couple in anti-squeezing into the ifo thereby destroying squeezing. This preliminary investigation of the filter cavities only goes to show that the design study parameters cannot be used as such and need to be optimised during the technical review phase of ET.

Appendix D

Using SimulinkNB for Noise projections

D.1 SimulinkNb with FINESSE

SimulinkNb can be downloaded from here `https://github.com/cwipf/SimulinkNb/blob/master` and the one requirement is to add this to the matlab path so that your control loop model knows from where to import the packages required to do the modelling.

Once a control model is built, one can inject measured noise spectra at different points of the loop and project them through the loop. The simulinkNb page hosts an example to show the difference between open loop and closed loop modelling. One can use the live parts feature to automatically sync parameters like filters and servo transfer functions from the digital control system at specific GPS time.

Detailed information can be found in [176]

D.1.1 Some components of SimulinkNb

The generic blocks of SimulinkNb are described here:

- noises: generated noise budget terms from the simulink model with the given frequency vector

- sys: contains the calibrated Transfer functions and is a linearised simulink model.

- NbNoiseSource: user defined amplitude spectral density of the noise where the source is summed into the model.

- NbNoiseSink and NbNoiseCal: these are user defined degrees of freedom. For every degree of freedom there should be only one sink and one calibration block. The calibration block has to be connected to the signal to be measured.

- linflexTf: liniearises the simulink block

- prescale: improves the numerical accuracy

D.2 Finesse

Frequency domain INterfErometer Simulation SoftwarE as the name suggests is an interferometer simulation tool that can be used to obtain the optical response of the interferometer and also obtain the quantum noise limited sensitivity of the same. It can be downloaded and installed using the instructions from here: `http://www.gwoptics.org/finesse`. The extensive manual available on the same webpage is a great starting point for people who have never used this before.

D.3 File Location

All the files for the simulation of a control noise budget for ET-LF are located in this git repository: `https://gitlab.aei.uni-hannover.de/sean.leavey/ET-ISC/tree/master/projects/ETLF_simulink`

D.4 Details of using SimulinkNb

D.4.1 Inputs and outputs

SimulinkNb is integrated with Optickle [177] another frequency domain interferometer simulation tool and inorder to be able to use FINESSE outputs in our control loop model, this was the only block that needed to be replaced. In figure D.1, the blocks that take in a Finesse input are highlighted by the blue box called Finesse FRD. All the other components are obtained from the NbLibrary and Matlab control toolbox.

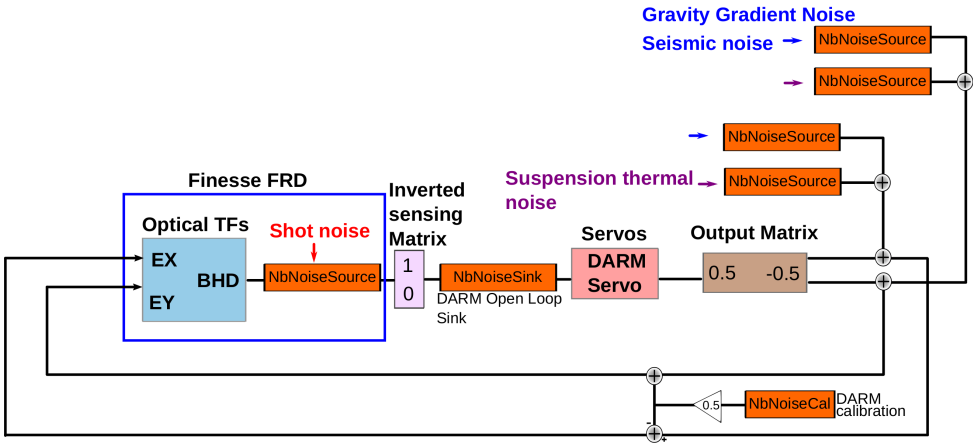

Figure D.1: Simplified noise budget for only the DARM loop using the optical plant transfer functions from FINESSE. These transfer functions are stored in the Finesse FRD block. We also get the shot noise at the detection port for DARM from FINESSE. The orange blocks: NbNoiseSource, NbNoiseSink, NbNoiseCal can be copied over from the NBLibrary of SimulinkNb.

To get your control model started the following components are quintessential:

1. A list of 'drives' and 'probes' or in other words the inputs and outputs of the opto-mechanical plant to be simulated. This is used to generate a Simulink subsystem with the appropriate input-output ports and noise blocks.

2. Matrix of transfer functions from drives to probes. This is given in the frequency domain and stored in a matlab 'frd' object ('frequency response data'). The units are typically W/m and if otherwise, one can use conversion blocks to convert the units as required.

3. The ASD of the noise spectra for instance the shot noise associated with the BHD sensor

to measure DARM is in units of $W/\sqrt{Hz}$ and is obtained from the FINESSE model.

For (1), the sub-system can be generated by explicitly listing the drives and probes as,

```
buildOptickleSys('modelName', 'freqVector', driveArray, probeArray)
```

where driveArray and probeArray are cell arrays of strings naming the drives (mirrors in our case) and probes (photodiodes).

A matlab auto-generated editable sub-system then opens for us to start summing in the different noise blocks as shown as shown in figure D.1. To incorporate the FINESSE outputs, this block has to be edited by hand to point to items 2 and 3.

For 2, the FINESSE transfer functions are loaded into an frd object in the workspace. If it is called finesseFrd, then by following 'sub-system→Properties→block description→flexTF: optickleFrd(modelName,freqVector)' should be replaced with 'flexTF: finesseFrd'.

For 3, the noise spectra is loaded as a matlab matrix and by using the orange NbNoiseSource blocks we can incorporate all the noise sources. To assign a path for the noise source, the block parameters obtained from opening the NbNoiseSource dialog box can be edited to refer to the relevant matlab variable.

D.4.2 Transfer functions from FINESSE

- frd() creates pseudo-LTI objects from a frequency response, and freqresp() extracts the frequency response from LTI objects. They are inverses of each other.
- The transfer functions obtained from FINESSE should be complex valued i.e to model the TF correctly, information about the magnitude and phase is required.
- The shape of the noise curves is determined by two things: the shape of the input spectrum as set in the noise source block; and the calibration transfer function, given by the TF from the noise block to the sink divided by the TF from the cal block to the sink.
- to get 2: this portion can be included in the script (this is present in the notebook in the

repository).

```
pd2 ASD_offResQ $fMod2 90 $fs nmeasure
fsig darm EX 0.01 0
fsig darm EY 0.01 180
xaxis darm f log 0.01 100 1000
yaxis abs:deg
scale meter
```

- to get 3: this needs to be incorporated into the FINESSE code

```
fsig darm EX 0.01 0
fsig darm EY 0.01 180
qnoised ASD_offResQ 1 $fs nmeasure
xaxis signal f log 0.01 100 1000
yaxis log abs
```

Bibliography

[1] A. Einstein. Näherungsweise Integration der Feldgleichungen der Gravitation. *Sitzungsberichte der Königlich Preußischen Akademie der Wissenschaften (Berlin), Seite 688-696.*, 1916.

[2] R. A. Hulse and J. H. Taylor. Discovery of a pulsar in a binary system. *Apjl*, 195:L51–L53, January 1975.

[3] B. P. Abbott, R. Abbott, T. D. Abbott, F. Acernese, K. Ackley, C. Adams, T. Adams, P. Addesso, R. X. Adhikari, V. B. Adya, and C. et.al. Affeldt. Gw170817: Observation of gravitational waves from a binary neutron star inspiral. *Phys. Rev. Lett.*, 119:161101, Oct 2017.

[4] Tobin Thomas Fricke. *Homodyne detection for laser-interferometric gravitational wave detectors*. PhD thesis, Louisiana State University and Agricultural and Mechanical College, 2011.

[5] Daniel David Brown. *Interactions of light and mirrors: Advanced techniques for modelling future gravitational wave detectors*. PhD thesis, University of Birmingham, 2016.

[6] B. S. Sathyaprakash and Bernard F. Schutz. Physics, astrophysics and cosmology with gravitational waves. *Living Reviews in Relativity*, 12(1):2, Mar 2009.

[7] B P Abbott, R Abbott, T D Abbott, M R Abernathy, K Ackley, C Adams, P Addesso, R X Adhikari, V B Adya et.al. (LIGO Scientific Collaboration), and J Harms. Exploring the sensitivity of next generation gravitational wave detectors. *Classical and Quantum Gravity*, 34(4):044001, 2017.

[8] F Acernese, T Adams, M Agathos, K Agatsuma, A Allocca, P Astone, G Ballardin, F Barone, M Barsuglia, A Basti, Th S Bauer, V Bavigadda, M Bejger, and C Belczynski et.al. The advanced virgo detector. *Journal of Physics: Conference Series*, 610(1):012014, 2015.

[9] Masaki Ando and the TAMA collaboration. Current status of tama. *Classical and Quantum Gravity*, 19(7):1409, 2002.

[10] Yoichi Aso, Yuta Michimura, Kentaro Somiya, Masaki Ando, Osamu Miyakawa, Takanori Sekiguchi, Daisuke Tatsumi, and Hiroaki Yamamoto. Interferometer design of the kagra gravitational wave detector. *Phys. Rev. D*, 88:043007, Aug 2013.

[11] The kagra collaboration. kagra website, 2017.

[12] Abernathy M et al and ET Science Team 2010 Technical Report No. ET-0106C-10. 2010.

[13] K L Dooley, J R Leong, T Adams, C Affeldt, A Bisht, C Bogan, J Degallaix, C Gräf, S Hild, J Hough, A Khalaidovski, N Lastzka, J Lough, H Lück, D Macleod, L Nuttall, M Prijatelj, R Schnabel, E Schreiber, J Slutsky, B Sorazu, K A Strain, H Vahlbruch, M Wąs, B Willke, H Wittel, K Danzmann, and H Grote. Geo 600 and the geo-hf upgrade program: successes and challenges. *Classical and Quantum Gravity*, 33(7):075009, 2016.

[14] B. P. Abbott, R. Abbott, T. D. Abbott, M. R. Abernathy, F. Acernese, K. Ackley, C. Adams, T. Adams, P. Addesso, R. X. Adhikari, V. B. Adya, C. Affeldt, M. Agathos, K. Agatsuma, and N. et.al. Aggarwal. Binary black hole mergers in the first advanced ligo observing run. *Phys. Rev. X*, 6:041015, Oct 2016.

[15] B. P. Abbott, R. Abbott, T. D. Abbott, M. R. Abernathy, F. Acernese, K. Ackley, C. Adams, T. Adams, P. Addesso, R. X. Adhikari, V. B. Adya, C. Affeldt, M. Agathos, K. Agatsuma, and N. et.al. Aggarwal. Gw150914: The advanced ligo detectors in the era of first discoveries. *Phys. Rev. Lett.*, 116:131103, Mar 2016.

[16] `https://www.ligo.caltech.edu/news/ligo20170825`.

[17] B. P. Abbott, R. Abbott, T. D. Abbott, M. R. Abernathy, F. Acernese, K. Ackley, C. Adams, T. Adams, P. Addesso, R. X. Adhikari, V. B. Adya, C. Affeldt, M. Agathos, K. Agatsuma, and N. et.al. Aggarwal. Gw151226: Observation of gravitational waves from a 22-solar-mass binary black hole coalescence. *Phys. Rev. Lett.*, 116:241103, Jun 2016.

[18] Tito Dal Canton, Alexander H. Nitz, Andrew P. Lundgren, Alex B. Nielsen, Duncan A. Brown, Thomas Dent, Ian W. Harry, Badri Krishnan, Andrew J. Miller, Karl Wette, Karsten Wiesner, and Joshua L. Willis. Implementing a search for aligned-spin neutron star-black hole systems with advanced ground based gravitational wave detectors. *Phys. Rev. D*, 90:082004, Oct 2014.

[19] B. P. Abbott, R. Abbott, T. D. Abbott, F. Acernese, K. Ackley, C. Adams, T. Adams, P. Addesso, R. X. Adhikari, V. B. Adya, C. Affeldt, M. Afrough, B. Agarwal, M. Agathos, K. Agatsuma, and N. et.al. Aggarwal. Gw170104: Observation of a 50-solar-mass binary black hole coalescence at redshift 0.2. *Phys. Rev. Lett.*, 118:221101, Jun 2017.

[20] B. P. Abbott, R. Abbott, T. D. Abbott, F. Acernese, K. Ackley, C. Adams, T. Adams, P. Addesso, R. X. Adhikari, V. B. Adya, C. Affeldt, M. Afrough, B. Agarwal, M. Agathos, K. Agatsuma, and N. et.al. Aggarwal. Gw170814: A three-detector observation of gravitational waves from a binary black hole coalescence. *Phys. Rev. Lett.*, 119:141101, Oct 2017.

[21] V. Savchenko, C. Ferrigno, E. Kuulkers, A. Bazzano, E. Bozzo, S. Brandt, J. Chenevez, T. J.-L. Courvoisier, R. Diehl, A. Domingo, L. Hanlon, E. Jourdain, A. von Kienlin, P. Laurent, F. Lebrun, A. Lutovinov, A. Martin-Carrillo, S. Mereghetti, L. Natalucci, J. Rodi, J.-P. Roques, R. Sunyaev, and P. Ubertini. Integral detection of the first prompt gamma-ray signal coincident with the gravitational-wave event gw170817. *The Astrophysical Journal Letters*, 848(2):L15, 2017.

[22] B. P. Abbott, R. Abbott, T. D. Abbott, M. R. Abernathy, F. Acernese, K. Ackley, C. Adams, T. Adams, P. Addesso, R. X. Adhikari, V. B. Adya, C. Affeldt, M. Agathos, K. Agatsuma, and N. et.al. Aggarwal. Observation of gravitational waves from a binary black hole merger. *Phys. Rev. Lett.*, 116:061102, Feb 2016.

[23] `https://alog.ligo-wa.caltech.edu/aLOG/index.php?callRep=12836`.

[24] `https://alog.ligo-wa.caltech.edu/aLOG/index.php?callRep=36123`.

[25] `https://alog.ligo-wa.caltech.edu/aLOG/index.php?callRep=36711`.

[26] `https://alog.ligo-wa.caltech.edu/aLOG/index.php?callRep=36703`.

[27] Hang Yu M. Kasprzack. Beam Position from Angle to Length minimization, DCC: LIGO T1600397, 2017.

[28] B. P. Abbott, R. Abbott, T. D. Abbott, F. Acernese, K. Ackley, C. Adams, T. Adams, P. Addesso, R. X. Adhikari, V. B. Adya, C. Affeldt, M. Afrough, B. Agarwal, M. Agathos, K. Agatsuma, N. Aggarwal et.al., (LIGO Scientific Collaboration, and Virgo Collaboration). Gw170608: Observation of a 19 solar-mass binary black hole coalescence. *The Astrophysical Journal Letters*, 851(2):L35, 2017.

[29] Samantha A Usman, Alexander H Nitz, Ian W Harry, Christopher M Biwer, Duncan A Brown, Miriam Cabero, Collin D Capano, Tito Dal Canton, Thomas Dent, Stephen Fairhurst, Marcel S Kehl, Drew Keppel, Badri Krishnan, Amber Lenon, Andrew Lundgren, Alex B Nielsen, Larne P Pekowsky, Harald P Pfeiffer, Peter R Saulson, Matthew West, and Joshua L Willis. The pycbc search for gravitational waves from compact binary coalescence. *Classical and Quantum Gravity*, 33(21):215004, 2016.

[30] Cody Messick, Kent Blackburn, Patrick Brady, Patrick Brockill, Kipp Cannon, Romain Cariou, Sarah Caudill, Sydney J. Chamberlin, Jolien D. E. Creighton, Ryan Everett, Chad Hanna, Drew Keppel, Ryan N. Lang, Tjonnie G. F. Li, Duncan Meacher, Alex Nielsen, Chris Pankow, Stephen Privitera, Hong Qi, Surabhi Sachdev, Laleh Sadeghian, Leo Singer, E. Gareth Thomas, Leslie Wade, Madeline Wade, Alan Weinstein, and Karsten Wiesner. Analysis framework for the prompt discovery of compact binary mergers in gravitational-wave data. *Phys. Rev. D*, 95:042001, Feb 2017.

[31] Nicolas Arnaud, Matteo Barsuglia, Marie-Anne Bizouard, Violette Brisson, Fabien Cavalier, Michel Davier, Patrice Hello, Stephane Kreckelbergh, and Edward K. Porter. Coincidence and coherent data analysis methods for gravitational wave bursts in a network of interferometric detectors. *Phys. Rev. D*, 68:102001, Nov 2003.

[32] A. Effler. *Performance Characterization of the Dual-Recycled Michelson Subsystem in Advanced LIGO*. PhD thesis, Louisiana State University and Agricultural and Mechanical College, 2014.

[33] Tobin T Fricke, Nicolás D Smith-Lefebvre, Richard Abbott, Rana Adhikari, and Katherine L Dooley et.al. Dc readout experiment in enhanced ligo. *Classical and Quantum Gravity*, 29(6):065005, 2012.

[34] Rana Adhikari. *Sensitivity and Noise Analysis of 4 km Laser Interferometric Gravitational Wave Antennae*. PhD thesis, California Institute of Technology Pasadena, California, 2004.

[35] Lisa Barsotti. *The control of the Virgo interferometer for gravitational wave detection*. PhD thesis, Scuola Normale Superiore di Pisa, 2006.

[36] D.Toeyrae. Fabry Perot Cavities. `https://www.gwoptics.org/learn/02_Plane_waves/01_Fabry_Perot_cavity/04_Linewidth.html`.

[37] Evan D Hall. *Long-baseline laser interferometry for the detection of binary black-hole mergers*. PhD thesis, CALIFORNIA INSTITUTE OF TECHNOLOGY Pasadena, California, 2017.

[38] K. A. Strain and B. J. Meers. Experimental demonstration of dual recycling for interferometric gravitational-wave detectors. *Phys. Rev. Lett.*, 66:1391–1394, Mar 1991.

[39] Kenneth A. Strain, Guido Müller, Tom Delker, David H. Reitze, David B. Tanner, James E. Mason, Phil A. Willems, Daniel A. Shaddock, Malcolm B. Gray, Conor Mow-Lowry, and David E. McClelland. Sensing and control in dual-recycling laser interferometer gravitational-wave detectors. *Appl. Opt.*, 42(7):1244–1256, Mar 2003.

[40] R. W. P. Drever, J. L. Hall, F. V. Kowalski, J. Hough, G. M. Ford, A. J. Munley, and H. Ward. Laser phase and frequency stabilization using an optical resonator. *Applied Physics B*, 31(2):97–105, Jun 1983.

[41] T. Westphal, G. Bergmann, A. Bertolini, M. Born, Y. Chen, A. V. Cumming, L. Cunningham, K. Dahl, and C. et.al. Gräf. Design of the 10 m aei prototype facility for interferometry studies. *Applied Physics B*, 106(3):551–557, Mar 2012.

[42] S Hild, H Grote, J Degallaix, S Chelkowski, K Danzmann, A Freise, M Hewitson, J Hough, H Lück, M Prijatelj, K A Strain, J R Smith, and B Willke. DC-readout of a signal-recycled gravitational wave detector. *Classical and Quantum Gravity*, 26(5):055012, 2009.

[43] Gravitational wave interferometer noise calculator, v3.1. 2016.

[44] G Bergmann, C M Mow-Lowry, V B Adya, A Bertolini, M M Hanke, R Kirchhoff, S M Köhlenbeck, G Kühn, P Oppermann, A Wanner, T Westphal, J Wöhler, D S Wu, H Lück, K A Strain, and K Danzmann. Passive-performance, analysis, and upgrades of a 1-ton seismic attenuation system. *Classical and Quantum Gravity*, 34(6):065002, 2017.

[45] S M Aston, M A Barton, A S Bell, N Beveridge, B Bland, A J Brummitt, G Cagnoli, C A Cantley, L Carbone, A V Cumming, L Cunningham, R M Cutler, R J S Greenhalgh, and G D Hammond et.al. Update on quadruple suspension design for advanced ligo. *Classical and Quantum Gravity*, 29(23):235004, 2012.

[46] S Hild, S Chelkowski, A Freise, J Franc, N Morgado, R Flaminio, and R DeSalvo. A xylophone configuration for a third-generation gravitational wave detector. *Classical and Quantum Gravity*, 27(1):015003, 2010.

[47] Braccini S. Presentation at GWADW 2010 (Kyoto), DCC:LIGO P1200121. `http://gw.icrr.u-tokyo.ac.jp/gwadw2010/program/2010_GWADW_Braccini.ppt`, 2010.

[48] Ryan DeRosa, Jennifer C Driggers, Dani Atkinson, Haixing Miao, Valery Frolov, Michael Landry, Joseph A Giaime, and Rana X Adhikari. Global feed-forward vibration isolation in a km scale interferometer. *Classical and Quantum Gravity*, 29(21):215008, 2012.

[49] Jan Harms. Terrestrial gravity fluctuations. *Living Reviews in Relativity*, 18(1):3, Dec 2015.

[50] Jan Harms and Stefan Hild. Passive newtonian noise suppression for gravitational-wave observatories based on shaping of the local topography. *Classical and Quantum Gravity*, 31(18):185011, 2014.

[51] B W Barr, G Cagnoli, M M Casey, D Clubley, D R M Crooks, K Danzmann, and E J Elliffe et.al. Silica research in glasgow. *Classical and Quantum Gravity*, 19(7):1655, 2002.

[52] G D Hammond, A V Cumming, J Hough, R Kumar, K Tokmakov, S Reid, and S Rowan. Reducing the suspension thermal noise of advanced gravitational wave detectors. *Classical and Quantum Gravity*, 29(12):124009, 2012.

[53] `https://alog.ligo-wa.caltech.edu/aLOG/index.php?callRep=37523`.

[54] Carlton M. Caves. Quantum-mechanical radiation-pressure fluctuations in an interferometer. *Phys. Rev. Lett.*, 45:75–79, Jul 1980.

[55] Rana X Adhikari. Gravitational radiation detection with laser interferometry, DCC: LIGO P1200121, 2012.

[56] V B Braginsky, Yu Levin, and S P Vyatchanin. How to reduce suspension thermal noise in ligo without improving the q of the pendulum and violin modes. *Measurement Science and Technology*, 10(7):598, 1999.

[57] V.B. Braginsky, M.L. Gorodetsky, and S.P. Vyatchanin. Thermo-refractive noise in gravitational wave antennae. *Physics Letters A*, 271(5):303 – 307, 2000.

[58] Yu. Levin. Internal thermal noise in the ligo test masses: A direct approach. *Phys. Rev. D*, 57:659–663, Jan 1998.

[59] Gabriela González. Suspensions thermal noise in the ligo gravitational wave detector. *Classical and Quantum Gravity*, 17(21):4409, 2000.

[60] M. Evans, S. Ballmer, M. Fejer, P. Fritschel, G. Harry, and G. Ogin. Thermo-optic noise in coated mirrors for high-precision optical measurements. *Phys. Rev. D*, 78:102003, Nov 2008.

[61] Garrett D. Cole, Ignacio Wilson-Rae, Katharina Werbach, Michael R. Vanner, and Markus Aspelmeyer. Phonon-tunnelling dissipation in mechanical resonators. *Nature Communications*, 2:231 EP –, Mar 2011. Article.

[62] Garrett D. Cole, Wei Zhang, Michael J. Martin, Jun Ye, and Markus Aspelmeyer. Tenfold reduction of brownian noise in high-reflectivity optical coatings. *Nature Photonics*, 7:644 EP –, Jul 2013. Article.

[63] Sean Stephan Leavey. *Enhancing the sensitivity of future laser-interferometric gravitational wave detectors*. PhD thesis, University of Glasgow, 2017.

[64] Gregory M Harry and the LIGO Scientific Collaboration. Advanced ligo: the next generation of gravitational wave detectors. *Classical and Quantum Gravity*, 27(8):084006, 2010.

[65] A Freise, S Chelkowski, S Hild, W Del Pozzo, A Perreca, and A Vecchio. Triple michelson interferometer for a third-generation gravitational wave detector. *Classical and Quantum Gravity*, 26(8):085012, 2009.

[66] P Ajith, M Hewitson, and I S Heng. Null-stream veto for two co-located detectors: implementation issues. *Classical and Quantum Gravity*, 23(19):S741, 2006.

[67] M Hewitson and P Ajith. Using the null-stream of geo 600 to veto transient events in the detector output. *Classical and Quantum Gravity*, 22(22):4903, 2005.

[68] `http://einsteintelescope.ulg.ac.be/index30.html`.

[69] Gianni Conforto and Riccardo DeSalvo. Proposal for lower frequency companions for the advanced ligo gravitational wave interferometric detectors. *Nuclear Instruments and Methods in Physics Research Section A: Accelerators, Spectrometers, Detectors and Associated Equipment*, 518(1):228 – 232, 2004. Frontier Detectors for Frontier Physics: Proceedin.

[70] Tomek D.Keitel, M.Chan. ET design study update meeting, 2017. `https://gilsay.physics.gla.ac.uk/dokuwiki/doku.php?id=et_update_2017`, 2017. [Internal meeting page].

[71] Jo van den Brand et.al. KNAW-Agenda Einstein Telescope proposal. `https://www.knaw.nl/shared/resources/adviezen/bestanden/KNAWAgendaEinsteinTelescope.pdf`, 2017. [available online].

[72] C J Moore, R H Cole, and C P L Berry. Gravitational-wave sensitivity curves. *Classical and Quantum Gravity*, 32(1):015014, 2015.

[73] Haixing Miao Stefan Hild. ET design study update meeting, 2017. https://gilsay.physics.gla.ac.uk/dokuwiki/doku.php?id=et_update_2017, 2017. [Internal meeting page].

[74] Paul Fulda, Keiko Kokeyama, Simon Chelkowski, and Andreas Freise. Experimental demonstration of higher-order laguerre-gauss mode interferometry. *Phys. Rev. D*, 82:012002, Jul 2010.

[75] Kentaro Somiya and Kazuhiro Yamamoto. Coating thermal noise of a finite-size cylindrical mirror. *Phys. Rev. D*, 79:102004, May 2009.

[76] S.Hild. Talk at IOPNPDD, DCC number : LIGO G1100435, 2011.

[77] Jun Mizuno. *Comparison of optical configurations for laser-interferometric gravitational-wave detectors*. PhD thesis, Gottfried Wilhelm Leibniz Universität Hannover Hannover, Germany, 1995.

[78] Henning Vahlbruch, Moritz Mehmet, Karsten Danzmann, and Roman Schnabel. Detection of 15 db squeezed states of light and their application for the absolute calibration of photoelectric quantum efficiency. *Phys. Rev. Lett.*, 117:110801, Sep 2016.

[79] Virgo Collaboration et al. Advanced Virgo technical design report, 2012.

[80] R.L.Ward. *Length Sensing and Control of a Prototype Advanced Interferometric Gravitational Wave Detector*. PhD thesis, California Institute of Technology Pasadena, California, 2010.

[81] Kentaro Somiya, Peter Beyersdorf, Koji Arai, Shuichi Sato, Seiji Kawamura, Osamu Miyakawa, Fumiko Kawazoe, Shihori Sakata, Aya Sekido, and Norikatsu Mio. Development of a frequency-detuned interferometer as a prototype experiment for next-generation gravitational-wave detectors. *Appl. Opt.*, 44(16):3179–3191, Jun 2005.

[82] S Hild, H Grote, M Hewitson, H Lück, J R Smith, K A Strain, B Willke, and K Danzmann. Demonstration and comparison of tuned and detuned signal recycling in a large-scale gravitational wave detector. *Classical and Quantum Gravity*, 24(6):1513, 2007.

[83] H.Wittel. SRC length contol loop improvements in GEO600, DCC number: LIGO G1700418, 2017.

[84] D. V. Martynov, E. D. Hall, B. P. Abbott, R. Abbott, T. D. Abbott, C. Adams, R. X. Adhikari, R. A. Anderson, S. B. Anderson, K. Arai, M. A. Arain, S. M. Aston, L. Austin, S. W. Ballmer, M. Barbet, D. Barker, B. Barr, L. Barsotti, J. Bartlett, M. A. Barton, I. Bartos, J. C. Batch, A. S. Bell, I. Belopolski, J. Bergman, J. Betzwieser, G. Billingsley, and et.al. Birch. Sensitivity of the advanced ligo detectors at the beginning of gravitational wave astronomy. *Phys. Rev. D*, 93:112004, Jun 2016.

[85] Ballmer S Barsotti L et.al. Abbott R, Adhikari R. Advanced ligo length sensing and control final design. *LIGO DCC*, (T060272), 2010.

[86] Vaishali Adya, Sean Leavey, Harald Lück, Christian Gräf, and Stefan Hild. Length sensing and control for einstein telescope low frequency. *Journal of Physics: Conference Series*, 716(1):012030, 2016.

[87] Peter Fritschel, Matthew Evans, and Valery Frolov. Balanced homodyne readout for quantum limited gravitational wave detectors. *Opt. Express*, 22(4):4224–4234, Feb 2014.

[88] Teng Zhang, Stefan L. Danilishin, Sebastian Steinlechner, Bryan W. Barr, Angus S. Bell, Peter Dupej, Christian Gräf, Jan-Simon Hennig, E. Alasdair Houston, Sabina H. Huttner, Sean S. Leavey, Daniela Pascucci, Borja Sorazu, Andrew Spencer, Jennifer Wright, Kenneth A. Strain, and Stefan Hild. Effects of static and dynamic higher-order optical modes in balanced homodyne readout for future gravitational waves detectors. *Phys. Rev. D*, 95:062001, Mar 2017.

[89] Sebastian Steinlechner, Bryan W. Barr, Angus S. Bell, and Danilishin et.al. Local-oscillator noise coupling in balanced homodyne readout for advanced gravitational wave detectors. *Phys. Rev. D*, 92:072009, Oct 2015.

[90] Kiwamu Izumi and Daniel Sigg. Advanced LIGO: length sensing and control in a dual recycled interferometric gravitational wave antenna. *Classical and Quantum Gravity*, 34(1):015001, 2017.

[91] Kentaro Somiya and Osamu Miyakawa. Shot-noise-limited control-loop noise in an interferometer with multiple degrees of freedom. *Appl. Opt.*, 49(23):4335–4342, Aug 2010.

[92] A Freise, G Heinzel, H Lück, R Schilling, B Willke, and K Danzmann. Frequency-domain interferometer simulation with higher-order spatial modes. *Classical and Quantum Gravity*, 21(5):S1067–S1074, 2004. Finesse is available at `http://www.gwoptics.org/finesse`.

[93] Lise Schnupp. Presentation at European Collaboration Meeting on Interferometric Detection of Gravitational Waves, Sorrent. 1988.

[94] P. Kwee, J. Miller, T. Isogai, L. Barsotti, and M. Evans. Decoherence and degradation of squeezed states in quantum filter cavities. *Phys. Rev. D*, 90:062006, Sep 2014.

[95] P. Kwee, J. Miller, T. Isogai, L. Barsotti, and M. Evans. Decoherence and degradation of squeezed states in quantum filter cavities. *Phys. Rev. D*, 90:062006, Sep 2014.

[96] Henning Vahlbruch. *Squeezed light for gravitational wave astronomy.* PhD thesis, Gottfried Wilhelm Leibniz Universität Hannover Hannover, Germany, 2008.

[97] `https://www.rohde-schwarz.com/us/product/smb100a-productstartpage_63493-9379.html`.

[98] Andreas Freise and Kenneth Strain. Interferometer techniques for gravitational-wave detection. *Living Reviews in Relativity*, 13(1):1, Feb 2010.

[99] K.Arai. Interferometer Length Sensing in Gravitational Wave Detectors, LIGO G1401386, 2014.

[100] Joshua Ryan Smith. *Formulation of Instrument Noise Analysis Techniques and Their Use in the Commissioning of the Gravitational Wave Observatory, GEO 600.* PhD thesis, Gottfried Wilhelm Leibniz Universität Hannover Hannover, Germany, 2006.

[101] Lisa Barsotti. The Advanced LIGO detectors at the beginning of the new gravitational wave era, DCC: LIGO G1600324, 2016.

[102] `https://github.com/cwipf/SimulinkNb`.

[103] `https://www.gik.uni-karlsruhe.de/en/bfo.html`.

[104] S Hild, M Abernathy, F Acernese, P Amaro-Seoane, N Andersson, K Arun, F Barone, B Barr, M Barsuglia, M Beker, N Beveridge, S Birindelli, and S Bose et.al. Sensitivity studies for third-generation gravitational wave observatories. *Classical and Quantum Gravity*, 28(9):094013, 2011.

[105] F Acernese, M Agathos, K Agatsuma, D Aisa, N Allemandou, A Allocca, J Amarni, P Astone, et al. Advanced Virgo: a second-generation interferometric gravitational wave detector. *Classical and Quantum Gravity*, 32(2):024001, 2015.

[106] `https://alog.ligo-la.caltech.edu/CSWG/index.php?callRep=11217`.

[107] Vajente G Barsotti L Swinkels B, Campagna E and Evans M. Longitudinal noise subtraction: the alpha-, beta- and gamma-technique. *Virgo Note*, (VIR-0050A-08), 2008.

[108] `https://de.mathworks.com/matlabcentral/fileexchange/7444-nyquist-plot-with-logarithmic-amplitudes`.

[109] G. Heinzel, J. Mizuno, R. Schilling, W. Winkler, A. Rüdiger, and K. Danzmann. An experimental demonstration of resonant sideband extraction for laser-interferometric gravitational wave detectors. *Physics Letters A*, 217(6):305 – 314, 1996.

[110] G. Heinzel, K. A. Strain, J. Mizuno, K. D. Skeldon, B. Willke, W. Winkler, R. Schilling, A. Rüdiger, and K. Danzmann. Experimental demonstration of a suspended dual recycling interferometer for gravitational wave detection. *Phys. Rev. Lett.*, 81:5493–5496, Dec 1998.

[111] R L Ward, R Adhikari, B Abbott, R Abbott, D Barron, R Bork, T Fricke, V Frolov, J Heefner, A Ivanov, O Miyakawa, K McKenzie, B Slagmolen, M Smith, R Taylor, S Vass, S Waldman, and A Weinstein. dc readout experiment at the caltech 40m prototype interferometer. *Classical and Quantum Gravity*, 25(11):114030, 2008.

[112] Lisa Barsotti. LIGO-VIRGO plans towards O3,LIGO G1800136, 2018.

[113] Kiwamu Izumi, Koji Arai, Bryan Barr, Joseph Betzwieser, Aidan Brooks, Katrin Dahl, Suresh Doravari, Jennifer C. Driggers, W. Zach Korth, Haixing Miao, Jameson Rollins, Stephen Vass, David Yeaton-Massey, and Rana X. Adhikari. Multicolor cavity metrology. *J. Opt. Soc. Am. A*, 29(10):2092–2103, Oct 2012.

[114] K.Izumi. *Multi-Color Interferometry for Lock Acquisition of Laser Interferometric Gravitational-wave Detectors*. PhD thesis, Department of Astronomy, The University of Tokyo, 2012.

[115] K Yamamoto, T Uchiyama, S Miyoki, M Ohashi, K Kuroda, H Ishitsuka, and T Akutsu et.al. Current status of the clio project. *Journal of Physics: Conference Series*, 122(1):012002, 2008.

[116] Kentaro Somiya. Detector configuration of kagra–the japanese cryogenic gravitational-wave detector. *Classical and Quantum Gravity*, 29(12):124007, 2012.

[117] D.S.Wu. Noise Budget, 10 m prototype logbook page =2961, 2018. [Internal logbook].

[118] Tobias Westphal. *A Coating Thermal Noise Interferometer for the AEI 10 m Prototype facility*. PhD thesis, Gottfried Wilhelm Leibniz Universität Hannover Hannover, Germany, 2016.

[119] H. Grote, K. Danzmann, K. L. Dooley, R. Schnabel, J. Slutsky, and H. Vahlbruch. First long-term application of squeezed states of light in a gravitational-wave observatory. *Phys. Rev. Lett.*, 110:181101, May 2013.

[120] V. B. Braginsky and F. Ya. Khalili. Quantum nondemolition measurements: the route from toys to tools. *Rev. Mod. Phys.*, 68:1–11, Jan 1996.

[121] Kentaro Somiya et.al. Conceptual design of the hannover 10m interferometer for sub sql measurement. (LIGO-G0900438-v1).

[122] K.Mossavi. Design ideas for vacuum system of the 10m prototype, pg 1. [Internal logbook].

[123] `https://alog.ligo-wa.caltech.edu/aLOG/index.php?callRep=40281`.

[124] Christian Gräf. *Optical Design and Numerical Modeling of the AEI 10 m Prototype sub-SQL Interferometer*. PhD thesis, Gottfried Wilhelm Leibniz Universität Hannover Hannover, Germany, 2013.

[125] Thomas Corbitt, Yanbei Chen, Farid Khalili, David Ottaway, Sergey Vyatchanin, Stan Whitcomb, and Nergis Mavalvala. Squeezed-state source using radiation-pressure-induced rigidity. *Phys. Rev. A*, 73:023801, Feb 2006.

[126] G. Losurdo, M. Bernardini, S. Braccini, C. Bradaschia, C. Casciano, V. Dattilo, and R. De Salvo et.al. An inverted pendulum preisolator stage for the virgo suspension system. *Review of Scientific Instruments*, 70(5):2507–2515, 1999.

[127] A. Takamori, P. Raffai, S. Márka, R. DeSalvo, V. Sannibale, H. Tariq, A. Bertolini, G. Cella, N. Viboud, K. Numata, R. Takahashi, and M. Fukushima. Inverted pendulum as low-frequency pre-isolation for advanced gravitational wave detectors. *Nuclear Instruments and Methods in Physics Research Section A: Accelerators, Spectrometers, Detectors and Associated Equipment*, 582(2):683 – 692, 2007.

[128] Gerald Bergmann. *Improving the isolation for the AEI 10 m prototype*. PhD thesis, Gottfried Wilhelm Leibniz Universität Hannover Hannover, Germany, 2018.

[129] G Cella, R DeSalvo, V Sannibale, H Tariq, N Viboud, and A Takamori. Seismic attenuation performance of the first prototype of a geometric anti-spring filter. *Nuclear Instruments and Methods in Physics Research Section A: Accelerators, Spectrometers, Detectors and Associated Equipment*, 487(3):652 – 660, 2002.

[130] R. Kirchhoff, C. M. Mow-Lowry, V. B. Adya, G. Bergmann, S. Cooper, M. M. Hanke, P. Koch, S. M. Köhlenbeck, J. Lehmann, P. Oppermann, J. Wöhler, D. S. Wu, H. Lück, and K. A. Strain. Huddle test measurement of a near johnson noise limited geophone. *Review of Scientific Instruments*, 88(11):115008, 2017.

[131] Marina Dehne, Felipe Guzmán Cervantes, Benjamin Sheard, Gerhard Heinzel, and Karsten Danzmann. Laser interferometer for spaceborne mapping of the earth's gravity field. *Journal of Physics: Conference Series*, 154(1):012023, 2009.

[132] Katrin Dahl. *From design to operation: a suspension platform interferometer for the AEI 10 m prototype*. PhD thesis, Gottfried Wilhelm Leibniz Universität Hannover Hannover, Germany, 2013.

[133] S.Köhlenbeck et. al. paper in preparation. 2018.

[134] Kenneth Strain. Electrostatic drive (ESD) results from GEO and application in Advanced LIGO, DCC: LIGO T060015-00-K, 2006.

[135] J.Junker. Laser power stabilization for the AEI 10m prototype, Master thesis, Gottfried Wilhelm Leibniz Universität Hannover, Germany, 2016.

[136] `https://www.ligo.caltech.edu/page/faq`.

[137] Janis Wöhler. Thermal Noise Interferometer in the AEI 10 m Prototype facility, DCC number: LIGO P1600260, 2016.

[138] S. Hild H. Wittel and K. A. Strain. Design ideas for the electrostatic drives of the AEI 10 m, 2012. [Internal logbook].

[139] S.Danilishn V.Adya. 10 m prototype internal logbook page 7261.

[140] The LIGO Scientific Collaboration, J Aasi, B P Abbott, R Abbott, T Abbott, M R Abernathy, K Ackley, C Adams, T Adams, P Addesso, R X Adhikari, and et al. V Adya. Advanced LIGO. *Classical and Quantum Gravity*, 32(7):074001, 2015.

[141] Peter Fritschel Kentaro Somiya, Osamu Miyakawa and Rana Adhikari. Length sensing and control for adligo. (LIGO-G0900438-v1).

[142] Gabriele Vajente. *Analysis of sensitivity and noise sources for the Virgo gravitational wave interferometer*. PhD thesis, Scuola Normale Superiore di Pisa, 2008.

[143] Andreas Freise. *The Next Generation of Interferometry: Multi-Frequency Optical Modelling, Control Concepts and Implementation*. PhD thesis, Gottfried Wilhelm Leibniz Universität Hannover Hannover, Germany, 2003.

[144] S.Köhlenbeck. personal communication. 2017.

[145] Yiqiu Ma. *Optomechanical Physics in the Design of Gravitational Wave Detectors*. PhD thesis, The University of Western Australia, 2015.

[146] Neil Andrew Gordon. *Characterisation and Control of Coupled Optical Springs for Future Gravitational Wave Detectors*. PhD thesis, University of Glasgow, 2014.

[147] Matthew Patrick Edgar. *Experimental Investigations into Diffractive Optics and Optomechanical Systems for Future Gravitational Wave Detectors*. PhD thesis, University of Glasgow, 2011.

[148] Benjamin S. Sheard, Malcolm B. Gray, Conor M. Mow-Lowry, David E. McClelland, and Stanley E. Whitcomb. Observation and characterization of an optical spring. *Phys. Rev. A*, 69:051801, May 2004.

[149] James D. Lough. *Optical Spring Stabilization*. PhD thesis, Syracuse University, 2014.

[150] Stefan L. Danilishin and Farid Ya. Khalili. Quantum measurement theory in gravitational-wave detectors. *Living Reviews in Relativity*, 15(1):5, Apr 2012.

[151] Alessandra Buonanno and Yanbei Chen. Optical noise correlations and beating the standard quantum limit in advanced gravitational-wave detectors. *Classical and Quantum Gravity*, 18(15):L95, 2001.

[152] A.Freise. Alignment coupling with large beams, LIGO-G1702391-v1, 2017.

[153] Kentaro Somiya. *Investigation of radiation pressure effect in a frequency-detuned interferometer and development of the readout scheme for a gravitational-wave detector*. PhD thesis, The University of Tokyo, 2004.

[154] Stefan Hild. *Beyond the first Generation: Extending the Science Range of the Gravitational Wave Detector GEO 600.* PhD thesis, Gottfried Wilhelm Leibniz Universität Hannover Hannover, Germany, 2007.

[155] Ajith Parameswaran. *On aspects of gravitational-wave detection: Detector characterisation, data analysis and source modelling for ground-based detectors.* PhD thesis, Gottfried Wilhelm Leibniz Universität Hannover Hannover, Germany, 2007.

[156] Gerhard Heinzel. *Advanced optical techniques for laser-interferometric gravitational-wave detectors.* PhD thesis, Gottfried Wilhelm Leibniz Universität Hannover Hannover, Germany, 1999.

[157] Hartmut Grote. *Making it Work: Second Generation Interferometry in GEO 600 !* PhD thesis, Gottfried Wilhelm Leibniz Universität Hannover Hannover, Germany, 2003.

[158] Christoph Affeldt. *Laser power increase for GEO 600 Commissioning aspects towards an operation of GEO 600 at high laser power.* PhD thesis, Gottfried Wilhelm Leibniz Universität Hannover Hannover, Germany, 2014.

[159] H Wittel, S Hild, G Bergmann, K Danzmann, and K A Strain. New design of electrostatic mirror actuators for application in high-precision interferometry. *Classical and Quantum Gravity*, 32(17):175021, 2015.

[160] E. Schreiber, K. L. Dooley, H. Vahlbruch, C. Affeldt, A. Bisht, J. R. Leong, J. Lough, M. Prijatelj, J. Slutsky, M. Was, H. Wittel, K. Danzmann, and H. Grote. Alignment sensing and control for squeezed vacuum states of light. *Opt. Express*, 24(1):146–152, Jan 2016.

[161] Daniel D. Brown, Haixing Miao, Chris Collins, Conor Mow-Lowry, Daniel Töyrä, and Andreas Freise. Broadband sensitivity enhancement of detuned dual-recycled michelson interferometers with epr entanglement. *Phys. Rev. D*, 96:062003, Sep 2017.

[162] D.D.Brown et. al. Finesse file for GEO 600, page 1798. `https://intranet.aei.uni-hannover.de/geo600/geohflogbook.ns`.

[163] E.Schreiber. GEO 600, page 7261. `https://intranet.aei.uni-hannover.de/geo600/geohflogbook.nsf?OpenDatabase`.

[164] H Wittel, H Lück, C Affeldt, K L Dooley, H Grote, J R Leong, M Prijatelj, E Schreiber, J Slutsky, K Strain, M Was, B Willke, and K Danzmann. Thermal correction of astigmatism in the gravitational wave observatory geo600. *Classical and Quantum Gravity*, 31(6):065008, 2014.

[165] V.Adya. Finesse file for GEO 600, page 7616. https://intranet.aei.uni-hannover.de/geo600/geohflogbook.ns.

[166] Benno Wilke. Personal communication.

[167] S S Y Chua, B J J Slagmolen, D A Shaddock, and D E McClelland. Quantum squeezed light in gravitational-wave detectors. *Classical and Quantum Gravity*, 31(18):183001, 2014.

[168] Vaishali Adya. Twin signal recycling for the Einstein Telescope, DCC: LIGO G1601171, 2016.

[169] H.Lueck. Twin signal recycling, Crystalline coatings, GEOHF+Meeting, Crieff, 2015. [Internal document].

[170] André Thüring. *Investigations of coupled and Kerr non-linear optical resonators*. PhD thesis, Gottfried Wilhelm Leibniz Universität Hannover Hannover, Germany, 2009.

[171] André Thüring, R. Schnabel, H. Lück, and K. Danzmann. Detuned twin-signal-recycling for ultrahigh-precision interferometers. *Opt. Lett.*, 32(8):985–987, Apr 2007.

[172] Christian Gräf, André Thüring, Henning Vahlbruch, Karsten Danzmann, and Roman Schnabel. Length sensing and control of a michelson interferometer with power recycling and twin signal recycling cavities. *Opt. Express*, 21(5):5287–5299, Mar 2013.

[173] Haixing Miao, Huan Yang, Rana X Adhikari, and Yanbei Chen. Quantum limits of interferometer topologies for gravitational radiation detection. *Classical and Quantum Gravity*, 31(16):165010, 2014.

[174] Jennifer Clair Driggers. *Noise Cancellation for Gravitational Wave Detectors*. PhD thesis, California Institute of Technology Pasadena, California, 2015.

[175] Daniel David Brown and Andreas Freise. Pykat, July 2017. http://www.gwoptics.org/pykat.

[176] C.Wipf. Building the aLIGO Noise Budget,LVC Meeting, Stanford, DCC:LIGO-G1401000 , 2014.

[177] https://github.com/Optickle/Optickle.

Curriculum vitae

Personal Data

Name:	Vaishali Badrish Adya
Address:	Schaufelder straße 30167 Hannover
Nationality:	Indian
Date and place of birth:	31.03.1990, Gulbarga, India

Academic career

09/2013 – 03/2018	PhD Thesis at Leibniz Universität Hannover Albert Einstein Institue *Ways to stop mirrors from moving unnecessarily: design of advanced gravitational wave detectors*
05/2011 – 05/2013	MSc at National Institute of Technology, Karnataka, India MSc thesis at National Institute of Technology *Red Organic Light Emitting Diodes : Fabrication and testing efficiency*
05/2008 – 05/2011	BSc at Christ University, Karnataka, India

Extra curricular activities and academic achievements

2017	Princess of Asturias Award for Technical and Scientific Research
2016	Gruber Cosmology prize
2016	Special Breakthrough prize in Fundamental Physics
11/2013-07/2017	PhD student representative at the *Albert Einstein Institute*
01/2016	Seminar *"Listen to me! Promote yourself authentically!"*
06/2013	Score of 8.0 in *"Overall International English Language Test"*
11/2013	Science Magazine editor ("Physics Prime"), National Institute of Technology Karnataka, Surathkal, India
2012	Summer research fellow at *Aryabhatta Research Institute of Observational Sciences (ARIES)*

05/2008-05/2011	Sir C V Raman Scholarship (2008-11) at Christ University

Collaborations

09/2013 – present	Member of *LIGO Scientific Collaboration* (LSC)
02/2017-06/2017	Research stay at LIGO Hanford as *LIGO fellow*

Education

2005 – 2006	10th Grade Carmel High School, Bangalore Karnataka
2006 – 2008	Pre-University degree K.L.E. Society's S. Nijalingappa Pre-University College
2011 – 2013	Bachelors in Physics, Chemistry and Mathematics, Christ University Bangalore
2013 – 2015	Masters in Physics, NITK Surathkal

Publications

Publications with direct contribution

[1] R. Kirchhoff, C. M. Mow-Lowry, V. B. Adya, G. Bergmann, S. Cooper, M. M. Hanke, P. Koch, S. M. Köhlenbeck, J. Lehmann, P. Oppermann, J. Wöhler, D. S. Wu, H. Lück, and K. A. Strain. Huddle test measurement of a near johnson noise limited geophone. *Review of Scientific Instruments*, 88(11):115008, nov 2017.

[2] G Bergmann, C M Mow-Lowry, V B Adya, A Bertolini, M M Hanke, R Kirchhoff, S M Köhlenbeck, G Kühn, P Oppermann, A Wanner, T Westphal, J Wöhler, D S Wu, H Lück, K A Strain, and K Danzmann. Passive-performance, analysis, and upgrades of a 1-ton seismic attenuation system. *Classical and Quantum Gravity*, 34(6):065002, feb 2017.

[3] Vaishali Adya, Sean Leavey, Harald Lück, Christian Gräf, and Stefan Hild. Length sensing and control for einstein telescope low frequency. *Journal of Physics: Conference Series*, 716(1):012030, 2016.

[4] P. B. Covas, A. Effler, E. Goetz, P. M. Meyers, A. Neunzert, M. Oliver, B. L. Pearlstone, V. J. Roma, R. M. S. Schofield, V. B. Adya, and et al. Identification and mitigation of narrow spectral artifacts that degrade searches for persistent gravitational waves in the first two observing runs of Advanced LIGO. *ArXiv e-prints*, January 2018.

Collaboration Publications

[1] J. Aasi et al. Advanced LIGO. *Classical and Quantum Gravity*, 32(7):074001, mar 2015.

[2] J. Aasi et al. Searching for stochastic gravitational waves using data from the two colocated LIGO hanford detectors. *Physical Review D*, 91(2), jan 2015.

[3] J. Aasi et al. Searches for continuous gravitational waves from nine young supernova remnants. *The Astrophysical Journal*, 813(1):39, oct 2015.

[4] J. Aasi et al. Directed search for gravitational waves from scorpius x-1 with initial LIGO data. *Physical Review D*, 91(6), mar 2015.

[5] J Aasi et al. Characterization of the LIGO detectors during their sixth science run. *Classical and Quantum Gravity*, 32(11):115012, may 2015.

[6] J. Aasi et al. Narrow-band search of continuous gravitational-wave signals from crab and vela pulsars in virgo VSR4 data. *Physical Review D*, 91(2), jan 2015.

[7] J Aasi et al. Characterization of the LIGO detectors during their sixth science run. *Classical and Quantum Gravity*, 32(11):115012, may 2015.

[8] J. Aasi et al. Searching for stochastic gravitational waves using data from the two colocated LIGO hanford detectors. *Physical Review D*, 91(2), jan 2015.

[9] B. P. Abbott et al. Results of the deepest all-sky survey for continuous gravitational waves on LIGO s6 data running on the einstein@home volunteer distributed computing project. *Physical Review D*, 94(10), nov 2016.

[10] and B. P. Abbott et al. The basic physics of the binary black hole merger GW150914. *Annalen der Physik*, 529(1-2):1600209, oct 2016.

[11] B. P. Abbott et al. Upper limits on the rates of binary neutron star and neutron star black hole mergers from advanced ligos first observing run. *The Astrophysical Journal*, 832(2):L21, nov 2016.

[12] B. P. Abbott et al. Localization and broadband followup of the gravitational-wave transient gw150914. *The Astrophysical Journal*, 826(1):L13, jul 2016.

[13] B. P. Abbott et al. Supplement: "localization and broadband follow-up of the gravitational-wave transient gw150914". *The Astrophysical Journal Supplement Series*, 225(1):8, jul 2016.

[14] B P Abbott et al. Characterization of transient noise in advanced LIGO relevant to gravitational wave signal GW150914. *Classical and Quantum Gravity*, 33(13):134001, jun 2016.

[15] B. P. Abbott et al. Search for transient gravitational waves in coincidence with short-duration radio transients during 2007–2013. *Physical Review D*, 93(12), jun 2016.

[16] B. P. Abbott et al. Binary black hole mergers in the first advanced LIGO observing run. *Physical Review X*, 6(4), oct 2016.

[17] B. P. Abbott et al. GW151226: Observation of gravitational waves from a 22-solar-mass binary black hole coalescence. *Physical Review Letters*, 116(24), jun 2016.

[18] B. P. Abbott et al. Properties of the binary black hole merger GW150914. *Physical Review Letters*, 116(24), jun 2016.

[19] B. P. Abbott et al. Properties of the binary black hole merger GW150914. *Physical Review Letters*, 116(24), jun 2016.

[20] B. P. Abbott et al. Observing gravitational-wave transient GW150914 with minimal assumptions. *Physical Review D*, 93(12), jun 2016.

[21] B. P. Abbott et al. Improved analysis of GW150914 using a fully spin-precessing waveform model. *Physical Review X*, 6(4), oct 2016.

[22] B. P. Abbott et al. Directly comparing GW150914 with numerical solutions of einstein's equations for binary black hole coalescence. *Physical Review D*, 94(6), sep 2016.

[23] B. P. Abbott et al. Tests of general relativity with GW150914. *Physical Review Letters*, 116(22), may 2016.

[24] B. P. Abbott et al. Comprehensive all-sky search for periodic gravitational waves in the sixth science run LIGO data. *Physical Review D*, 94(4), aug 2016.

[25] B. P. Abbott et al. First targeted search for gravitational-wave bursts from core-collapse supernovae in data of first-generation laser interferometer detectors. *Physical Review D*, 94(10), nov 2016.

[26] B. P. Abbott et al. GW151226: Observation of gravitational waves from a 22-solar-mass binary black hole coalescence. *Physical Review Letters*, 116(24), jun 2016.

[27] S. Adrián-Martínez, , et al. High-energy neutrino follow-up search of gravitational wave event GW150914 with ANTARES and IceCube. *Physical Review D*, 93(12), jun 2016.

[28] B. P. Abbott et al. Observation of gravitational waves from a binary black hole merger. *Physical Review Letters*, 116(6), feb 2016.

[29] B. P. Abbott et al. Astrophysical implications of the binary black hole merger gw150914. *The Astrophysical Journal*, 818(2):L22, feb 2016.

[30] B. P. Abbott et al. GW150914: First results from the search for binary black hole coalescence with advanced LIGO. *Physical Review D*, 93(12), jun 2016.

[31] B. P. Abbott et al. The rate of binary black hole mergers inferred from advanced ligo observations surrounding gw150914. *The Astrophysical Journal*, 833(1):L1, nov 2016.

[32] B. P. Abbott et al. GW150914: Implications for the stochastic gravitational-wave background from binary black holes. *Physical Review Letters*, 116(13), mar 2016.

[33] B. P. Abbott et al. GW150914: The advanced LIGO detectors in the era of first discoveries. *Physical Review Letters*, 116(13), mar 2016.

[34] B. P. Abbott et al. All-sky search for long-duration gravitational wave transients with initial LIGO. *Physical Review D*, 93(4), feb 2016.

[35] J. Aasi et al. First low frequency all-sky search for continuous gravitational wave signals. *Physical Review D*, 93(4), feb 2016.

[36] J. Aasi et al. Search of the orion spur for continuous gravitational waves using a loosely coherent algorithm on data from LIGO interferometers. *Physical Review D*, 93(4), feb 2016.

[37] B. P. Abbott et al. Prospects for observing and localizing gravitational-wave transients with advanced LIGO and advanced virgo. *Living Reviews in Relativity*, 19(1), feb 2016.

[38] B. P. Abbott et al. First narrow-band search for continuous gravitational waves from known pulsars in advanced detector data. *Physical Review D*, 96(12), dec 2017.

[39] B. P. Abbott et al. Erratum: "first search for gravitational waves from known pulsars with advanced LIGO" (2017, ApJ, 839, 12). *The Astrophysical Journal*, 851(1):71, dec 2017.

[40] B. P. Abbott et al. Search for post-merger gravitational waves from the remnant of the binary neutron star merger GW170817. *The Astrophysical Journal*, 851(1):L16, dec 2017.

[41] B. P. Abbott et al. On the progenitor of binary neutron star merger GW170817. *The Astrophysical Journal*, 850(2):L40, dec 2017.

[42] B. P. Abbott et al. GW170608: Observation of a 19 solar-mass binary black hole coalescence. *The Astrophysical Journal*, 851(2):L35, dec 2017.

[43] B. P. Abbott et al. Gravitational waves and gamma-rays from a binary neutron star merger: GW170817 and GRB 170817a. *The Astrophysical Journal*, 848(2):L13, oct 2017.

[44] B. P. Abbott et al. A gravitational-wave standard siren measurement of the hubble constant. *Nature*, oct 2017.

[45] B. P. Abbott et al. Estimating the contribution of dynamical ejecta in the kilonova associated with GW170817. *The Astrophysical Journal*, 850(2):L39, dec 2017.

[46] B. P. Abbott et al. Multi-messenger observations of a binary neutron star merger. *The Astrophysical Journal*, 848(2):L12, oct 2017.

[47] B. P. Abbott et al. Gravitational waves and gamma-rays from a binary neutron star merger: GW170817 and GRB 170817a. *The Astrophysical Journal*, 848(2):L13, oct 2017.

[48] B. P. Abbott et al. GW170817: Observation of gravitational waves from a binary neutron star inspiral. *Physical Review Letters*, 119(16), oct 2017.

[49] B. P. Abbott et al. GW170814: A three-detector observation of gravitational waves from a binary black hole coalescence. *Physical Review Letters*, 119(14), oct 2017.

[50] B. P. Abbott et al. First narrow-band search for continuous gravitational waves from known pulsars in advanced detector data. *Physical Review D*, 96(12), dec 2017.

[51] B. P. Abbott et al. Upper limits on gravitational waves from scorpius x-1 from a model-based cross-correlation search in advanced LIGO data. *The Astrophysical Journal*, 847(1):47, sep 2017.

[52] B. P. Abbott et al. All-sky search for periodic gravitational waves in the o1 LIGO data. *Physical Review D*, 96(6), sep 2017.

[53] B. P. Abbott et al. First low-frequency einstein@home all-sky search for continuous gravitational waves in advanced LIGO data. *Physical Review D*, 96(12), dec 2017.

[54] A. Albert et al. Search for high-energy neutrinos from gravitational wave event GW151226 and candidate LVT151012 with ANTARES and IceCube. *Physical Review D*, 96(2), jul 2017.

[55] A. Albert et al. Search for high-energy neutrinos from gravitational wave event GW151226 and candidate LVT151012 with ANTARES and IceCube. *Physical Review D*, 96(2), jul 2017.

[56] A. Albert et al. Search for high-energy neutrinos from binary neutron star merger GW170817 with ANTARES, IceCube, and the pierre auger observatory. *The Astrophysical Journal*, 850(2):L35, nov 2017.

[57] B. P. Abbott et al. First low-frequency einstein@home all-sky search for continuous gravitational waves in advanced LIGO data. *Physical Review D*, 96(12), dec 2017.

[58] B. P. Abbott et al. GW170104: Observation of a 50-solar-mass binary black hole coalescence at redshift 0.2. *Physical Review Letters*, 118(22), jun 2017.

[59] B. P. Abbott et al. Search for gravitational waves associated with gamma-ray bursts during the first advanced LIGO observing run and implications for the origin of GRB 150906b. *The Astrophysical Journal*, 841(2):89, may 2017.

[60] B. P. Abbott et al. Search for gravitational waves associated with gamma-ray bursts during the first advanced LIGO observing run and implications for the origin of GRB 150906b. *The Astrophysical Journal*, 841(2):89, may 2017.

[61] B. P. Abbott et al. Search for intermediate mass black hole binaries in the first observing run of advanced LIGO. *Physical Review D*, 96(2), jul 2017.

[62] B. P. Abbott et al. Search for gravitational waves from scorpius x-1 in the first advanced LIGO observing run with a hidden markov model. *Physical Review D*, 95(12), jun 2017.

[63] B. P. Abbott, , et al. First search for gravitational waves from known pulsars with advanced LIGO. *The Astrophysical Journal*, 839(1):12, apr 2017.

[64] B. P. Abbott et al. Directional limits on persistent gravitational waves from advanced LIGO's first observing run. *Physical Review Letters*, 118(12), mar 2017.

[65] B. P. Abbott et al. Upper limits on the stochastic gravitational-wave background from advanced LIGO's first observing run. *Physical Review Letters*, 118(12), mar 2017.

[66] B. P. Abbott et al. All-sky search for short gravitational-wave bursts in the first advanced LIGO run. *Physical Review D*, 95(4), feb 2017.

[67] Benjamin P Abbott et al. The basic physics of the binary black hole merger gw150914. *Annalen der Physik*, 529(1-2), 2017.

[68] B P Abbott, , et al. Effects of waveform model systematics on the interpretation of GW150914. *Classical and Quantum Gravity*, 34(10):104002, apr 2017.

[69] B. P. Abbott et al. All-sky search for short gravitational-wave bursts in the first advanced LIGO run. *Physical Review D*, 95(4), feb 2017.

[70] B P Abbott et al. Exploring the sensitivity of next generation gravitational wave detectors. *Classical and Quantum Gravity*, 34(4):044001, jan 2017.

[71] B. P. Abbott et al. Search for continuous gravitational waves from neutron stars in globular cluster NGC 6544. *Physical Review D*, 95(8), apr 2017.

[72] B. P. Abbott et al. First search for nontensorial gravitational waves from known pulsars. *Physical Review Letters*, 120(3), jan 2018.

[73] B P Abbott et al. All-sky search for long-duration gravitational wave transients in the first advanced LIGO observing run. *Classical and Quantum Gravity*, 35(6):065009, feb 2018.

[74] BP Abbott et al. Localization and broadband follow-up of the gravitational-wave transient gw150914. pages –, 2018.